An investigation into the flow fields around bluff bodies and artificial heart valves

Andrew Kenneth Hind

Doctor of Philosophy
University of Edinburgh
1997

EX BIBL. UNIV. EDINBURGEN.

Declaration

The work described in this thesis is the original work of the author and was carried out without the assistance of others, except where explicit credit is given in the text. It has not been submitted, in whole or in part, for any other degree at any University.

Andrew Kenneth Hind
Edinburgh

June 27, 1997

Acknowledgements

I would like to thank the following people and organisations for their assistance in the undertaking of the experimental work and support during the period over which the work was carried out.

Dr. John Christy for supervising the experimental programme and the preparation of this thesis.

My parents and family for their moral and occasional financial support.

Shell Expro for the funding of a three year demonstrator's post during which a significant proportion of the experimental work was completed.

The workshop for their technical assistance and workmanship in preparing the experimental equipment, and, in particular, the careful construction of the test sections and pulsatile pump by Mr. Tommy Murray, and Mr. M. Ree for the development of various key bits of electronic equipment.

Mr. Frank "Superman" Johnston for his advice, skill and perseverance in developing and printing PIV recordings.

Dr. Neil Skilling and Mr. Geoff Ballinger for programming advice and their exemplary maintenance of the computing system used for running the PIV analysis software.

Abstract

The replacement of diseased heart valves with biological or mechanical prostheses constitutes a significant proportion of cardiac surgery. Neither category of prosthesis is ideal. The problems are exemplified by the calcification of tissue valves and the increased risk of thrombosis produced by mechanical prostheses; the latter is commonly treated using anti-coagulant drugs. For mechanical valve prostheses, with which this work is largely concerned, haemolysis and thrombosis arise as a result of the non-physiological flows produced in the vicinity of the valve. These may be characterised by stasis, stagnation, elevated shear stresses, the surface impingement of fluid, and enhanced mass transfer. Each factor has been correlated with thrombosis or haemolysis but the relative importance of each remains uncertain.

A milk analogue for clotting blood was developed by Lewis. This was then used by Christy, and subsequently Marosek, to investigate the clot deposited in the region of a series of bluff bodies and heart valves in both steady and pulsatile flows. Bodies of revolution, such as a teardrop, were used to simplify the flow structures present in the flow, making the relation of flow features to the deposition of clot more amenable to analysis. Christy concluded that stasis was a necessary but not sufficient condition for thrombus deposition.

A quantitative flow visualisation technique known as particle image velocimetry (PIV) has been developed and applied to the flows investigated by Christy but with water as the test fluid. This required the development of a method to reduce the errors arising from velocity gradients within areas of the PIV recording analysed by autocorrelation. This method produced a significant improvement in the accuracy of velocities determined from simulated PIV recordings. However, the approach was less successful in experimental recordings, where the lower signal-to-noise ratio reduces the probability of obtaining a valid velocity measurement at a given point and also increases the error associated with a given valid velocity measurement. As a result, it is more likely that the analysable regions will be separated in real PIV recordings. The interpolation scheme used as part of the procedure was not optimal: a thin shell spline technique might have offered improvement.

Christy found that in steady flow, clot filled the stable wake region behind the upstream apex large teardrop. For the other test bodies Christy found that the clot formed in regions of stagnation in the wake. The shape of the clot observed by Christy correlates with the iso-velocity contours of lowest magnitude predicted in steady flow computational fluid dynamics simulations. This supports the conclusion of Christy that stasis plays a dominant role in thrombus deposition. A periodic ejection of material was observed from the recirculation zone for all but the teardrop shaped test body. The stability of the wake behind the tear-drop shaped test body may explain its anomalous behaviour in that the formed clot fills the wake region. In pulsatile flows, it was found that flow structures that developed during the stagnant phase of the pulsatile cycle directed material from both the wall and the wake region onto the surface of the test body. The position of impingement correlated with the location of a thicker layer of clot deposited on the teardrop shaped test body as observed by Christy.

Steady flow PIV investigations around a Björk-Shiley valve showed significant three dimensional structure which varied markedly over time. In pulsatile flows, both at and below physiologically relevant flowrates, significant variation was observed between recordings made at the same point in successive pulse cycles. This may indicate that the assumptions underlying the sampling methods used in LDA investigations to estimate the Reynolds stresses downstream of heart valve prostheses in pulsatile flows are flawed. In pulsatile flows of a period of 1 Hz and a mean volumetric flowrate of 6.7×10^{-5} m^3/s, the maximum bulk viscous shear stresses determined using PIV were of the order of 0.05 N/m^2 with maximum values of 0.5 N/m^2 near the wall, well below the value expected to cause lysis of red blood cells even for extended exposure. In the same physiologically relevant flow conditions, the maximum viscous shear stress at the trailing tip of the valve designed by Dr Norman Macleod was again of the order of 0.5 N/m^2. This level of wall shear is at the lower end of the range over which behavioural and shape changes are induced in endothelial cells and the adhesion of platelets to endothelial cells may be promoted.

Particle image velocimetry is a powerful augmentation to the range of techniques available for assessing the performance of heart valve prostheses *in vitro*.

Contents

1 Introduction **1**

1.1 Prolegomena 1

1.2 Previous work 4

1.2.1 The aim of extending earlier work 5

1.3 Particle Image Velocimetry 5

1.4 Applying PIV to flows in the circulatory system 6

1.5 Comments in the format of this thesis 7

1.6 Publications 8

2 Literature Review **9**

2.1 Fluid Mechanical Factors in Heart Valve Design 9

2.1.1 Introduction 9

2.1.2 Damage to Blood Components 11

2.1.3 Damage to wall cells 17

2.1.4 A milk analogue for blood 19

2.1.5 Flow visualisation and velocity measurements 20

2.1.6 LDA Measurements 26

2.1.7 CFD calculations 33

2.1.8 Discussion 34

2.2 Particle Image Velocimetry 37

2.2.1 Introduction 37

2.2.2 The basic technique 38

2.2.3 Early development of LSV and PIV and the Young's fringe analysis technique 40

2.2.4 Seeding particles 46

2.2.5 Illumination 49

2.2.6 Recording parameters 50

2.2.7 The analysis of PIV recordings 55

2.2.8 Errors 60

2.2.9 Directional Ambiguity 67

2.2.10 Post Processing 71
2.2.11 Related techniques 81
2.3 Discussion 85

3 Analysis, simulation and developments ... 88
3.1 Introduction 88
3.2 Simulating PIV recordings 89
3.2.1 Introduction 89
3.2.2 Flows simulated 90
3.2.3 Method 90
3.3 Analysis system 92
3.3.1 Introduction 92
3.3.2 The analysis of digital PIV images 93
3.3.3 Peak location 95
3.3.4 Performance 97
3.4 Validating and orienting velocity vectors 101
3.4.1 Introduction 101
3.4.2 Method 104
3.4.3 Results 109
3.4.4 Discussion 113
3.4.5 Experimental Application 119
3.4.6 Conclusions 122
3.5 Reducing the error from velocity gradients in the auto-correlation analysis of PIV images 123
3.5.1 Introduction 123
3.5.2 Method 124
3.5.3 Applying the technique to a simulated Oseen vortex 129
3.5.4 Discussion 132
3.5.5 Conclusions 141
3.6 Analysing two-phase flow data 141
3.6.1 Method 142
3.6.2 Discussion 143

4 Experimental Equipment 145
4.1 Flow system 145
4.2 Illumination System 151
4.3 Seeding particles 154
4.4 Recording system 156
4.5 Description of test bodies and valves 159

4.5.1 Experimental procedure 161

5 Experimental Results **164**

5.1 Laminar Flow 164

5.1.1 Test section 164

5.1.2 Bluff bodies 168

5.1.3 Heart Valves 199

5.2 Pulsatile flow 199

5.2.1 Test section 200

5.2.2 The valve designed by Dr. Norman Macleod 205

6 Discussion **210**

6.1 The PIV technique 210

6.1.1 Steady Flow 210

6.1.2 Pulsatile flow 211

6.1.3 Damage to erythrocytes and endothelial cells 213

6.1.4 Developments of the PIV technique 214

6.1.5 Improved PIV recordings about artificial heart valves 215

6.1.6 Potential developments of the PIV technique 216

6.2 The experimental flow system 217

6.3 Relating flow features to clot deposition 218

6.3.1 Steady Flow 218

6.3.2 Pulsatile Flow 221

7 Conclusions and future work **224**

7.1 Conclusions 224

7.2 Further Work 226

Appendices **228**

A **228**

A.1 The performance of the analysis algorithm for ideal PIV recordings . . . 228

A.2 Volume moment peak location method 230

A.3 Gaussian moment peak location method 234

A.4 Whittaker's method for peak location 238

B **242**

B.1 Bias in the measurement of fractional displacements 242

B.2 Bias arising from an alternative calculation of the volume moment . . . 246

B.3 Bias in the measurement of fractional displacements, including the bias from loss of pairs 247

C **248**

C.1 Maple script showing the derivation of the methods used to correct velocity gradients 248

D **253**

D.1 The flow patterns downstream of the Björk-Shiley valve in steady flow . 253

D.1.1 Iterative analysis of the first image 253

E **260**

E.1 The flow patterns downstream of Dr. Norman Macleod's valve in pulsatile flow 260

References **269**

List of Figures

1.1 The heart. 2

1.2 A selection of heart valve prostheses: **a)** and **b)** show trileaflet valves constructed from biological material, **c)** a Starr-Edwards mechanical valve, and **d)** a Björk-Shiley mechanical valve. 3

2.1 The flow through an arterial stenosis. 13

2.2 The idealised flow features produced by a disk normal to a uniform flow. 28

2.3 The idealised flow features produced by a disk at a high angle of incidence to a uniform flow. 29

2.4 The idealised flow features produced by a disk at a low angle of incidence to a uniform flow. 29

2.5 A pulsed light sheet illuminating a section of fluid. 38

2.6 A typical high image density PIV recording of a flow. 39

2.7 A schematic of a typical fringe analysis system. 40

2.8 The interference pattern produced by coherent waves from two point sources - Young's experiment. 41

2.9 A light sheet generated by expanding a collimated light source with a diverging lens and a second collimating lens. 50

2.10 A light sheet generated by a rotating mirror and collimating parabolic mirror 50

2.11 The spectral sensitivity curve for Kodak Technical Pan. (Reproduced with permission) 53

2.12 The spectral sensitivity curve for Kodak T-Max 100 53

2.13 The spectral sensitivity curve for Kodak T-Max 400 54

2.14 The range of displacements recorded and the range of measurable displacements. 69

2.15 The range of measurable velocities and the range of displacements recorded after judicious use of image shifting and choice of recording parameters. 70

2.16 The rotating mirror image shifting system. $\overrightarrow{I_1I_2}$ represents the real displacement of the particle images, $\overrightarrow{I_2I_3}$ the superimposed displacement, and $\overrightarrow{I_1I_3}$ the measured displacement 70

2.17 Particle tracking: black images are in the first frame, red in the second, blue in the third and purple in the fourth. 82

3.1 Peak location criteria 95
3.2 Definition of points for Gaussian fit to correlation peak 96
3.3 The validation procedure 107
3.4 Simulated velocity field. 110
3.5 The velocity vectors produced after the analysis of Figure (3.4), with no validation of the results. 110
3.6 As Figure (3.5), after applying conventional multi-pulse validation criteria. 111
3.7 As Figure (3.5), after applying the new validation algorithm. 111
3.8 As Figure (3.7), after applying the algorithm to resolve directional ambiguity. 112
3.9 u_r as a function of distance from the centre of the vortex for the conventional validation method. 112
3.10 u_θ as a function of distance from the centre of the vortex for the conventional validation method (compared with the expected value). 113
3.11 u_r as a function of distance from the centre of the vortex for the proposed validation method. 113
3.12 u_θ as a function of distance from the centre of the vortex for the proposed validation method (compared with the expected value). 114
3.13 $u_\theta - u_{\theta\ expected}$ as a function of distance from the centre of the vortex for the conventional validation method. 114
3.14 $u_\theta - u_{\theta\ expected}$ as a function of distance from the centre of the vortex for the proposed validation method. 115
3.15 Simulated PIV recording using an 'ideal' image shifting technique. . . . 115
3.16 The velocity vectors produced from analysis of the image shifted recording shown in Figure(3.4) 116
3.17 The velocity vectors produced from analysis of the image shifted recording shown in Figure(3.4) with the shift velocity subtracted 116
3.18 u_r as a function of distance from the centre of the vortex for the image shifting technique. 117
3.19 u_θ as a function of distance from the centre of the vortex for the image shifting technique (compared with the expected value). 117
3.20 $u_\theta - u_{\theta\ expected}$ as a function of distance from the centre of the vortex for the image shifting technique. 118
3.21 A PIV image of the flow downstream of an artificial heart valve. 119
3.22 A schematic diagram of the flow shown in Figure (3.21) 120
3.23 The new validation and orientation algorithm applied to a series of velocity fields produced in analysing (3.21). 121
3.24 The iterative procedure used to correct the velocity fields produced from multi-pulse PIV recordings that include significant velocity gradients. . 129
3.25 A simulated PIV image of an Oseen vortex - see text for details 131

3.26 **a)** A PIV analysis area before correction for velocity gradients and **b)** the analysis area after correction 131

3.27 **a)** The auto-correlation function from the PIV analysis area before correction for velocity gradients and **b)** the auto-correlation function after correction 132

3.28 The result of conventional PIV analysis: **a)** the raw velocity field, **b)** the velocity field after validation, **c)** the variation of u_r with r, and **d)** the variation of u_θ with r. 133

3.29 The results after one iteration of the analysis method including deformation: **a)** the raw velocity field, **b)** the velocity field after validation, **c)** the variation of u_r with r, and **d)** the variation of u_θ with r. 134

3.30 The results after five iterations of the analysis method including deformation: **a)** the raw velocity field, **b)** the velocity field after validation, **c)** the variation of u_r with r, and **d)** the variation of u_θ with r. 135

3.31 The results after ten iterations of the analysis method including deformation: **a)** the raw velocity field, **b)** the velocity field after validation, **c)** the variation of u_r with r, and **d)** the variation of u_θ with r. 136

3.32 The results after ten iterations of the analysis method including deformation: **a)** the velocity field after validation and smoothing, **b)** the variation of u_r with r, and **c)** the variation of u_θ with r. 137

3.33 **a)** The variation in the standard deviation of u_r and **b)** the fraction of invalid vectors detected after each iteration step. 138

3.34 The ratio of the measured value for u_θ divided by that expected as a function of r, Figures a), b), c), and d) show the results after normal analysis, five iterations, ten iterations, and ten iterations with smoothing. 139

3.35 The variation of u_θ and its first and second derivative with respect to r as a function of r. 139

3.36 The variation in the detected value for u_θ divided by the expected value as a function of the dimensionless velocity gradient. 140

3.37 **a)** the variation of vorticity with r calculated after ten iterations, **b)** the variation in vorticity calculated after ten iterations and smoothing. The expected value for vorticity is shown for comparison. 140

3.38 A simulated two phase recording and the separated seeding phases . . . 143

4.1 Steady flow arrangement of the test rig. 146

4.2 Construction of the test section. 148

4.3 The dismantled head of the positive displacement pump used to generate pulsatile flows. 149

4.4 The mechanical chopper used in the initial experiments. 152

4.5 The scanning mirror system with the parabolic mirror to the left hand side. 152

4.6 A schematic diagram of the experimental equipment, approximately to scale. 153

4.7 The test bodies used (excluding the one on the far right). Reproduced from Christy[1]. 160

4.8 A schematic of the long downstream apex tear-drop mounted in the test section. 160

4.9 A selection of heart valve prostheses investigated: **a)** a Björk-Shiley mechanical valve and **b)** a Starr-Edwards mechanical valve. 161

4.10 A schematic of a valve mounted before the test section. 162

5.1 A PIV recording of laminar flow through the short test section, Re = 300. 165

5.2 A PIV recording of developing laminar flow through the short test section, Re=800. 165

5.3 The mean velocity profile over the test section determined at a Reynolds number of 330 from the image shown in Figure (5.1). The points marked with an 'x' are from the initial analysis and those marked with an '+' after 10 iterations of the procedure to correct for velocity gradients. The solid line represents the expected fully-developed laminar for the measured flowrate of 8.3×10^{-6} m^3/s. 167

5.4 The mean developing velocity profile over the test section determined at a Reynolds number of 800 from the image shown in Figure (5.2). The points marked with an 'x' are from the initial analysis and those marked with an '+' after 10 iterations of the procedure to correct for velocity gradients. The solid line represents the expected fully-developed laminar for the measured flowrate of 2×10^{-5} m^3/s. 167

5.5 **a)** the clot formed about the downstream-apex large tear-drop -see Christy[1] for experimental details. **b)** The boundary layer to the same scale. 169

5.6 **a)** A PIV recording of the flow round the downstream-apex test body at a Reynolds number of 250, based on the projected diameter of the test body. **b)** The vorticity map and velocity field produced after one iteration of the procedure to correct for velocity gradients. The maximum velocity is indicated by a white vector which represents 0.0473 m/s. **c)** as b) but after the velocity field was smoothed with a low pass filter. Again, the maximum vector is indicated in white and represents 0.0444 m/s. 170

5.7 An enlarged view of the section around the test body **a)** from Figure (5.6:b) and **b)** from Figure (5.6:c). 171

5.8 Predictions of the flow around the tear-drop shaped test body made using FLUENT v4.3 at a Reynolds number of 250 based on the diameter of the test body: **a)** the computational grid, **b)** the velocity vectors, **c)** contours of the stream-function, **d)** the out of plane, or z-component, of vorticity. 172

5.9 As Figure (5.8) but with the number of grid points halved in each direction: **a)** the computational grid, **b)** the velocity vectors, **c)** contours of the stream-function, **d)** the out of plane, or z-component, of vorticity. 173

5.10 Recordings of seeding particles in the recirculation region distal to the tear-drop shaped test body at a Reynolds number of 800 based on the pipe diameter. The images are recorded at one second intervals and follow a sequence as numbered. 174

5.11 Estimated particle concentration from the scattered light intensity weighted with radius and normalised to the first recording. 175

5.12 **a)** A PIV recording of the flow round the spherical test body at a Reynolds number of 250 based on the projected diameter of the test body. **b)** The vorticity map and velocity field produced after normal PIV analysis and interpolation. The maximum velocity is indicated by a white vector which represents 0.050 m/s. 178

5.13 The clot formed around the sphere in steady flow as reported by Christy[1]. 178

5.14 Predictions of the flow around the sphere made using FLUENT v4.3 at a Reynolds number of 250 based on the diameter of the test body: **a)** the computational grid, **b)** the velocity vectors, **c)** contours of the stream-function, **d)** the out of plane, or z-component, of vorticity. . . . 179

5.15 Predictions of the flow around the sphere made using FLUENT v4.3 at half the grid resolution used in Figure (5.14): **a)** the computational grid, **b)** the velocity vectors, **c)** contours of the stream-function, **d)** the out of plane, or z-component, of vorticity. 180

5.16 Recordings of seeding particles in the recirculation region distal to the oblate shaped test body at a Reynolds number of 800 based on the pipe diameter. The blanks represent partially illuminated recordings that have been omitted. The images are recorded at one second intervals and follow a sequence as numbered. 182

5.17 The clot formed around the disk shaped test body in steady flow as reported by Christy[1]. 182

5.18 **a)** A PIV recording of the flow round the disk at a Reynolds number of 250 based on the projected diameter of the test body. **b)** The vorticity map and velocity field produced after normal PIV analysis and interpolation. The maximum velocity is indicated by a white vector which represents 0.0508 m/s. **c)** The shear stress map and velocity field produced after normal PIV analysis. 183

5.19 Predictions of the flow around the oblate shaped test body made using FLUENT v4.3 at a Reynolds number of 250 based on the diameter of the test body: **a)** the computational grid, **b)** the velocity vectors, **c)** contours of the stream-function, **d)** the out of plane, or z-component, of vorticity. 184

5.20 Predictions of the flow around the oblate shaped test body made using FLUENT v4.3, with the grid density doubled in the radial direction compared with Figure (5.19): **a)** the computational grid, **b)** the velocity vectors, **c)** contours of the stream-function, **d)** the out of plane, or z-component, of vorticity. 185

5.21 Recordings of seeding particles in the recirculation region distal to the upstream-apex cone at a Reynolds number of 800 based on the pipe diameter. The images are recorded at one second intervals and follow a sequence as numbered. 187

5.22 The clot formed around the upstream apex cone in steady flow as reported by Christy[1]. 188

5.23 **a)** A PIV recording of the flow round the upstream apex cone at a Reynolds number of 250 based on the projected diameter of the test body. **b)** The vorticity map and velocity field produced after normal PIV analysis, interpolation and the application of a low pass filter. The maximum velocity is indicated by a white vector which represents 0.0445 m/s. **c)** The shear stress map and velocity field produced after normal PIV analysis. 189

5.24 Predictions of the flow around the upstream apex cone made using FLUENT v4.3 at a Reynolds number of 250 based on the projected diameter of the test body: **a)** the computational grid, **b)** the velocity vectors, **c)** contours of the stream-function, **d)** the out of plane, or z-component, of vorticity. 190

5.25 Predictions of the flow around the upstream apex cone made using FLUENT v4.3, with the grid density doubled in the axial direction compared with Figure (5.24): **a)** the computational grid, **b)** the velocity vectors, **c)** contours of the stream-function, **d)** the out of plane, or z-component, of vorticity. 191

5.26 Recordings of seeding particles in the recirculation region distal to the downstream-apex cone at a Reynolds number of 800 based on the pipe diameter. The images are recorded at one second intervals and follow a sequence as numbered. 193

5.27 **a)** A PIV recording of the flow round the downstream apex cone at a Reynolds number of 250 based on the projected diameter of the test body. **b)** The vorticity map and velocity field produced after normal PIV analysis, interpolation and the application of a low pass filter. The maximum velocity is indicated by a white vector which represents 0.0468 m/s. **c)** The shear stress map and velocity field produced after normal PIV analysis. 194

5.28 Predictions of the flow around the down-stream apex cone made using FLUENT v4.3 at a Reynolds number of 250 based on the projected diameter of the test body: **a)** the computational grid, **b)** the velocity vectors, **c)** contours of the stream-function, **d)** the out of plane, or z-component, of vorticity. 195

5.29 Predictions of the flow around the down-steam apex cone made using FLUENT v4.3, with the grid density doubled in the axial direction compared with Figure (5.28): **a)** the computational grid, **b)** the velocity vectors, **c)** contours of the stream-function, **d)** the out of plane, or z-component, of vorticity. 196

5.30 Recordings of seeding particles in the recirculation region distal to the upstream apex small tear-drop at a Reynolds number of 800 based on the pipe diameter. The images are recorded at one second intervals and follow a sequence as numbered. 197

5.31 Recordings of seeding particles in the recirculation region distal to the upstream-apex large tear drop at a Reynolds number of 800 based on the pipe diameter. The images are recorded at one second intervals and follow a sequence as numbered. 198

5.32 The velocity profiles produced at eight equally spaced intervals in the cycle of pulsatile pipe flow. The first profile was obtained at the peak flowrate. The legend indicates the dimensionless time at which the profile is obtained by taking the recording time (relative to the peak volumetric flowrate) and dividing by the period of the pulse. 201

5.33 Predictions of the flow in the empty test section for an ideal rectified sinusoidal volumetric flowrate. Re = 530, α=25. The images a) through h) are at the respective dimensionless times of 0, 0.125, 0.25, 0.375, 0.5, 0.625, 0.75 and 0.875. These results are taken from the fifth cycle in the simulation. 203

5.34 The clots observed by Christy[1] in pulsatile flow. The mean flowrate was 2 $\times 10^{-5}$ m^3/s and the pulse frequency 1.167 Hz. 204

5.35 A series of 8 PIV recordings made around the short, upstream-apex teardrop in a pulsatile flow of 1.3×10^{-5} m^3/s with a frequency of 0.4 Hz. The images reading from top to bottom and then left to right were made at dimensionless times of 0, 0.125, 0.25, 0.375, 0.5 0.625. 0.75 and 0.875. The flow was seeded with 6 μm aluminium oxide particles and illuminated using the HeNe laser with the scanning beam system. The light sheet was pulsed at 40 Hz. 205

5.36 A series of 4 PIV recordings made around the downstream-apex teardrop in a pulsatile flow of 2×10^{-5} m^3/s with a frequency of 1.0 Hz. Images were recorded at random times, these represent those at various points in the stagnant phase. The illumination frequency was 75 Hz. 206

5.37 Close up sections of the PIV recordings around Dr. Norman Macleod's valve. 208

5.38 **a)** PIV recording made downstream of the Björk-Shiley Valve in a rectified sinusoidal pulsatile flow of 6.7 $\times 10^{-5}$ m^3/s and a pulsation frequency of 1 Hz. Re (based on the tube diameter) = 2700 and α = 40. The flow was seeded with 6 μm aluminium oxide particles and illuminated using the scanning beam system with the light sheet pulsed at 300Hz. The recording was made at a dimensionless time of 1/8. **b)** The resulting velocity field. The maximum velocity is 0.371 m/s. 209

6.1 A comparison of the simulated velocity magnitude with the location of clot formation for the downstream apex teardrop in steady flow. The Reynolds number based on the test body diameter is 250. The two images are shown to the same scale. 218

6.2 A comparison of the simulated velocity magnitude with the location of clot formation for the sphere. The Reynolds number based on the test body diameter is 250. The two images are shown to the same scale. . . 219

6.3 A comparison of the simulated velocity magnitude with the location of clot formation for the oblate. The Reynolds number based on the test body diameter is 250. The two images are shown to the same scale. . . 219

6.4 A comparison of the simulated velocity magnitude with the location of clot formation for the upstream apex cone. The Reynolds number based on the test body diameter is 250. The two images are shown to the same scale. 220

A.1 Results for two pulses and an image diameter of 1 pixel. 230

A.2 Results for two pulses and an image diameter of 1 pixel. (Magnified view) 230

A.3 Results for two pulses and an image diameter of 2 pixels. 230

A.4 Results for two pulses and an image diameter of 2 pixels. (Magnified view) 230

A.5 Results for two pulses and an image diameter of 4 pixels. 230

A.6 Results for two pulses and an image diameter of 6 pixels. 230

A.7 Results for two pulses and an image diameter of 10 pixels. 231

A.8 Results for two pulses and an image diameter of 16 pixels. 231

A.9 Results for three pulses and an image diameter of 1 pixel. 231

A.10 Results for three pulses and an image diameter of 1 pixel. (Magnified view) 231

A.11 Results for three pulses and an image diameter of 2 pixels. 231

A.12 Results for three pulses and an image diameter of 2 pixels. (Magnified view) 231

A.13 Results for three pulses and an image diameter of 4 pixels. 232

A.14 Results for three pulses and an image diameter of 6 pixels. 232

A.15 Results for three pulses and an image diameter of 10 pixels. 232

A.16 Results for three pulses and an image diameter of 16 pixels. 232

A.17 Results for four pulses and an image diameter of 1 pixel. 232

A.18 Results for four pulses and an image diameter of 1 pixel. (Magnified view) 232

A.19 Results for four pulses and an image diameter of 2 pixels. 233

A.20 Results for four pulses and an image diameter of 2 pixels. (Magnified view) 233

A.21 Results for four pulses and an image diameter of 4 pixels. 233

A.22 Results for four pulses and an image diameter of 6 pixels. 233

A.23 Results for four pulses and an image diameter of 10 pixels. 233

A.24 Results for four pulses and an image diameter of 16 pixels. 233

A.25 Results for two pulses and an image diameter of 1 pixel. 234

A.26 Results for two pulses and an image diameter of 1 pixel. (Magnified view) 234

A.27 Results for two pulses and an image diameter of 2 pixels. 234

A.28 Results for two pulses and an image diameter of 2 pixels. (Magnified view) 234
A.29 Results for two pulses and an image diameter of 4 pixels. 234
A.30 Results for two pulses and an image diameter of 6 pixels. 234
A.31 Results for two pulses and an image diameter of 10 pixels. 235
A.32 Results for two pulses and an image diameter of 16 pixels. 235
A.33 Results for three pulses and an image diameter of 1 pixel. 235
A.34 Results for three pulses and an image diameter of 1 pixel. (Magnified view) 235
A.35 Results for three pulses and an image diameter of 2 pixels. 235
A.36 Results for three pulses and an image diameter of 2 pixels. (Magnified view) 235
A.37 Results for three pulses and an image diameter of 4 pixels. 236
A.38 Results for three pulses and an image diameter of 6 pixels. 236
A.39 Results for three pulses and an image diameter of 10 pixels. 236
A.40 Results for three pulses and an image diameter of 16 pixels. 236
A.41 Results for four pulses and an image diameter of 1 pixel. 236
A.42 Results for four pulses and an image diameter of 1 pixel. (Magnified view) 236
A.43 Results for four pulses and an image diameter of 2 pixels. 237
A.44 Results for four pulses and an image diameter of 2 pixels. (Magnified view) 237
A.45 Results for four pulses and an image diameter of 4 pixels. 237
A.46 Results for four pulses and an image diameter of 6 pixels. 237
A.47 Results for four pulses and an image diameter of 10 pixels. 237
A.48 Results for four pulses and an image diameter of 16 pixels. 237
A.49 Results for two pulses and an image diameter of 1 pixel. 238
A.50 Results for two pulses and an image diameter of 1 pixel. (Magnified view) 238
A.51 Results for two pulses and an image diameter of 2 pixels. 238
A.52 Results for two pulses and an image diameter of 2 pixels. (Magnified view) 238
A.53 Results for two pulses and an image diameter of 4 pixels. 238
A.54 Results for two pulses and an image diameter of 6 pixels. 238
A.55 Results for two pulses and an image diameter of 10 pixels. 239
A.56 Results for two pulses and an image diameter of 16 pixels. 239
A.57 Results for three pulses and an image diameter of 1 pixel. 239
A.58 Results for three pulses and an image diameter of 1 pixel. (Magnified view) 239
A.59 Results for three pulses and an image diameter of 2 pixels. 239
A.60 Results for three pulses and an image diameter of 2 pixels. (Magnified view) 239
A.61 Results for three pulses and an image diameter of 4 pixels. 240

A.62 Results for three pulses and an image diameter of 6 pixels. 240
A.63 Results for three pulses and an image diameter of 10 pixels. 240
A.64 Results for three pulses and an image diameter of 16 pixels. 240
A.65 Results for four pulses and an image diameter of 1 pixel. 240
A.66 Results for four pulses and an image diameter of 1 pixel. (Magnified view) 240
A.67 Results for four pulses and an image diameter of 2 pixels. 241
A.68 Results for four pulses and an image diameter of 2 pixels. (Magnified view) 241
A.69 Results for four pulses and an image diameter of 4 pixels. 241
A.70 Results for four pulses and an image diameter of 6 pixels. 241
A.71 Results for four pulses and an image diameter of 10 pixels. 241
A.72 Results for four pulses and an image diameter of 16 pixels. 241

B.1 Bias for two pulse recordings with images of diameter 1 pixel and analysed with no padding of the data in the analysis region. 243
B.2 Bias for two pulse recordings with images of diameter 2 pixel and analysed with no padding of the data in the analysis region. 243
B.3 Bias for two pulse recordings with images of diameter 3 pixel and analysed with no padding of the data in the analysis region. 243
B.4 Bias for two pulse recordings with images of diameter 1 pixel and analysed with padding equal to half the length of analysis size added to the data in the analysis region. 243
B.5 Bias for two pulse recordings with images of diameter 2 pixel and analysed with padding equal to half the length of analysis size added to the data in the analysis region. 243
B.6 Bias for two pulse recordings with images of diameter 3 pixel and analysed with padding equal to half the length of analysis size added to the data in the analysis region. 243
B.7 Bias for two pulse recordings with images of diameter 1 pixel and analysed with padding equal the length of analysis size added to the data in the analysis region. 244
B.8 Bias for two pulse recordings with images of diameter 2 pixel and analysed with padding equal the length of analysis size added to the data in the analysis region. 244
B.9 Bias for two pulse recordings with images of diameter 3 pixel and analysed with padding equal the length of analysis size added to the data in the analysis region. 244
B.10 Bias for three pulse recordings with images of diameter 1 pixel and analysed with no padding of the data in the analysis region. 244
B.11 Bias for three pulse recordings with images of diameter 2 pixel and analysed with no padding of the data in the analysis region. 244

B.12 Bias for three pulse recordings with images of diameter 3 pixel and analysed with no padding of the data in the analysis region. 244

B.13 Bias for three pulse recordings with images of diameter 1 pixel and analysed with padding equal to half the length of analysis size added to the data in the analysis region. 245

B.14 Bias for three pulse recordings with images of diameter 2 pixel and analysed with padding equal to half the length of analysis size added to the data in the analysis region. 245

B.15 Bias for three pulse recordings with images of diameter 3 pixel and analysed with padding equal to half the length of analysis size added to the data in the analysis region. 245

B.16 Bias for three pulse recordings with images of diameter 1 pixel and analysed with padding equal the length of analysis size added to the data in the analysis region. 245

B.17 Bias for three pulse recordings with images of diameter 2 pixel and analysed with padding equal the length of analysis size added to the data in the analysis region. 245

B.18 Bias for three pulse recordings with images of diameter 3 pixel and analysed with padding equal the length of analysis size added to the data in the analysis region. 245

B.19 Bias for two pulse recordings with images of diameter 1 pixel and analysed with no padding of the analysis region. The area for the volume moment calculations extended as described at the start of the chapter. . 246

B.20 Bias for two pulse recordings with images of diameter 2 pixel and analysed with no padding of the analysis region. The area for the volume moment calculations extended as described at the start of the chapter. . 246

B.21 Bias for two pulse recordings with images of diameter 3 pixel and analysed with no padding of the analysis region. The area for the volume moment calculations extended as described at the start of the chapter. . 246

B.22 Bias for two pulse recordings with images of diameter 1 pixel and analysed with no padding of the analysis region. The velocity is not corrected for the bias arising from loss of image pairs. 247

B.23 Bias for two pulse recordings with images of diameter 2 pixel and analysed with no padding of the analysis region. The velocity is not corrected for the bias arising from loss of image pairs. 247

B.24 Bias for two pulse recordings with images of diameter 3 pixel and analysed with no padding of the analysis region. The velocity is not corrected for the bias arising from loss of image pairs. 247

D.1 A schematic indicating the location of the PIV recordings. 253

D.2 A series of nine PIV recordings made distal to the mount of the Björk-Shiley Valve. The recordings were made at one second intervals. The number in each figure indicates the time at which each recording was made. Re=800 (based on the pipe diameter). 254

D.3 **A)** The vector field produced by analysing the first image. **B)** The vector field produced after validating the vector field shown in A) using the method described in the text. 255

D.4 **A)** The validated velocity field after no iterations; **B)** after one iteration **C)** after two iterations; **D)** and after three iterations. 255

D.5 **A)** The unvalidated velocity field after no iterations; **B)** after five iterations; **C)** the validated velocity field after five iterations; **D)** and the interpolated and validated velocity field after five iterations. 256

D.6 **A)** PIV recording at time 0 s. **B)** The vector field produced after five iterations to correct for velocity gradients and validation. The maximum velocity vector represents 0.0620 m/s: the maximum shear stress is 0.023 N/m^2. 256

D.7 **A)** PIV recording at time 1 s. **B)** The vector field produced after five iterations to correct for velocity gradients and validation. The maximum velocity vector represents 0.0528 m/s: the maximum shear stress is 0.018 N/m^2. 257

D.8 **A)** PIV recording at time 2 s. **B)** The vector field produced after the initial analysis. The maximum velocity vector represents 0.0529 m/s: the maximum shear stress is 0.035 N/m^2. 257

D.9 **A)** PIV recording at time 3 s. **B)** The vector field produced after five iterations to correct for velocity gradients and validation. The maximum velocity vector represents 0.0479 m/s: the maximum shear stress is 0.020 N/m^2. 257

D.10 **A)** PIV recording at time 4 s. **B)** The vector field produced after five iterations to correct for velocity gradients and validation. The maximum velocity vector represents 0.0393 m/s: the maximum shear stress is 0.012 N/m^2. 258

D.11 **A)** PIV recording at time 5 s. **B)** The vector field produced after five iterations to correct for velocity gradients and validation. The maximum velocity vector represents 0.0419 m/s: the maximum shear stress is 0.014 N/m^2. 258

D.12 **A)** PIV recording at time 6 s. **B)** The vector field produced after five iterations to correct for velocity gradients and validation. The maximum velocity vector represents 0.0511 m/s: the maximum shear stress is 0.017 N/m^2. 258

D.13 **A)** PIV recording at time 7 s. **B)** The vector field produced after five iterations to correct for velocity gradients and validation. The maximum velocity vector represents 0.0472 m/s: the maximum shear stress is 0.025 N/m^2. 259

D.14 **A)** PIV recording at time 8 s. **B)** The vector field produced after five iterations to correct for velocity gradients and validation. The maximum velocity vector represents 0.0564 m/s: the maximum shear stress is 0.019 N/m^2. 259

E.1 **A)** PIV recording at a dimensionless time of 0/8 **B)** The vector field produced after five iterations to correct for velocity gradients and validation. The maximum velocity vector represents 0.0242 m/s. **C)** PIV recording at a dimensionless time of 0/8 **D)** The vector field produced after five iterations to correct for velocity gradients and validation. The maximum velocity vector represents 0.0223 m/s. 261

E.2 **A)** PIV recording at a dimensionless time of 1/8 **B)** The vector field produced after five iterations to correct for velocity gradients and validation. The maximum velocity vector represents 0.0298 m/s. **C)** PIV recording at a dimensionless time of 1/8 **D)** The vector field produced after five iterations to correct for velocity gradients and validation. The maximum velocity vector represents 0.0250 m/s. 262

E.3 **A)** PIV recording at a dimensionless time of 2/8 **B)** The vector field produced after five iterations to correct for velocity gradients and validation. The maximum velocity vector represents 0.0221 m/s. **C)** PIV recording at a dimensionless time of 2/8 **D)** The vector field produced after five iterations to correct for velocity gradients and validation. The maximum velocity vector represents 0.0181 m/s. 263

E.4 **A)** PIV recording at a dimensionless time of 3/8 **B)** The vector field produced after five iterations to correct for velocity gradients and validation. The maximum velocity vector represents 0.0176 m/s. **C)** PIV recording at a dimensionless time of 3/8 **D)** The vector field produced after five iterations to correct for velocity gradients and validation. The maximum velocity vector represents 0.0164 m/s. 264

E.5 **A)** PIV recording at a dimensionless time of 4/8 **B)** The vector field produced after five iterations to correct for velocity gradients and validation. The maximum velocity vector represents 0.0130 m/s. **C)** PIV recording at a dimensionless time of 4/8 **D)** The vector field produced after five iterations to correct for velocity gradients and validation. The maximum velocity vector represents 0.0126 m/s. 265

E.6 **A)** PIV recording at a dimensionless time of 5/8 **B)** The vector field produced after five iterations to correct for velocity gradients and validation. The maximum velocity vector represents 0.0105 m/s. **C)** PIV recording at a dimensionless time of 5/8 **D)** The vector field produced after five iterations to correct for velocity gradients and validation. The maximum velocity vector represents 0.0117 m/s. 266

E.7 **A)** PIV recording at a dimensionless time of 6/8 **B)** The vector field produced after five iterations to correct for velocity gradients and validation. The maximum velocity vector represents 0.0090 m/s. **C)** PIV recording at a dimensionless time of 6/8 **D)** The vector field produced after five iterations to correct for velocity gradients and validation. The maximum velocity vector represents 0.0101 m/s. 267

E.8 **A)** PIV recording at a dimensionless time of 7/8 **B)** The vector field produced after five iterations to correct for velocity gradients and validation. The maximum velocity vector represents 0.0243 m/s. **C)** PIV recording at a dimensionless time of 7/8 **D)** The vector field produced after five iterations to correct for velocity gradients and validation. The maximum velocity vector represents 0.0292 m/s. 268

List of Tables

2.1 The resolving power of various films 52

4.1 Seeding particle data: ❶ determined using a Malvern Instrument's Mastersizer S (long bed), ① the terminal velocity calculated using Stokes' Law given by equation (2.5), ② The slip velocity calculated using Adrian's method[2] given by equation (2.7) and estimating the maximum acceleration to be of the order of 1 m/s^2 , ③ the slip velocity calculated according to the method of Agüí and Jiménez[3] given by equation (2.11) and estimating the lowest turnover rate of the largest structures to be of the order of the pulsation frequency (1 Hz), ④ the macro scale of turbulence expected to be resolved by the seeding particles according to the method of Lim *et al.*[4] given by equation (2.10). 154

4.2 The depth of field as calculated from equation(2.14) for HeNe illumination at 633 nm. The depth of field would be expected to be around 80% of these value for Argon ion illumination with a wavelength of 500 nm. . 157

4.3 The particle image size as a function of the recording magnification and aperture for 8 μm seeding particles illuminated with an Argon ion laser. Recorded image sizes indicated in type face will be under-sampled using the digitisation system, those in type face are approaching the required digitisation resolution. 157

4.4 The particle image size as a function of the recording magnification and aperture for 50 μm seeding particles illuminated with an Argon ion laser. Recorded image sizes indicated in type face will be under-sampled using the digitisation system, those in type face are approaching the required digitisation resolution. 158

4.5 The particle image size as a function of the recording magnification and aperture for 8 μm seeding particles illuminated with a HeNe laser. Recorded image sizes indicated in type face will be under-sampled using the digitisation system, those in type face are approaching the required digitisation resolution. 158

4.6 The particle image size as a function of the recording magnification and aperture for 50 μm seeding particles illuminated with a HeNe laser. Recorded image sizes indicated in type face will be under-sampled using the digitisation system, those in type face are approaching the required digitisation resolution. 158

Chapter 1

Introduction

1.1 Prolegomena

The surgical implantation of heart valve prostheses to replace diseased valves within the heart constitutes a significant proportion of cardiac surgery[5]. This is illustrated by the implantation of some 51,000 artificial cardiac valves in the US during 1988[6]. The valves implanted fall into two distinct categories: mechanical prostheses that are constructed from man-made materials, and biological prostheses that are based on human or other animal tissue and reflect the trileaflet construction of the heart valves which they replace. A number of complications arise from the implantation of both types of valve. These stem from several factors, including: the non-physiological flows developed through the valves, mechanical failure, and other significant changes in the behaviour of the materials of construction. Surgical and immediate post-operative complications are also significant but outside the scope of the discussion presented here. The factors that should be considered in the design of an artificial valve are discussed by Christy[1] and Marosek[6].

This work is largely concerned with the investigation of two specific problems that arise after the implantation of mechanical heart valve prostheses; haemolysis and thrombosis. Both are produced as a consequence of the non-physiological flows that are developed through artificial valves. Haemolysis refers to the damage of red blood cells and plate-

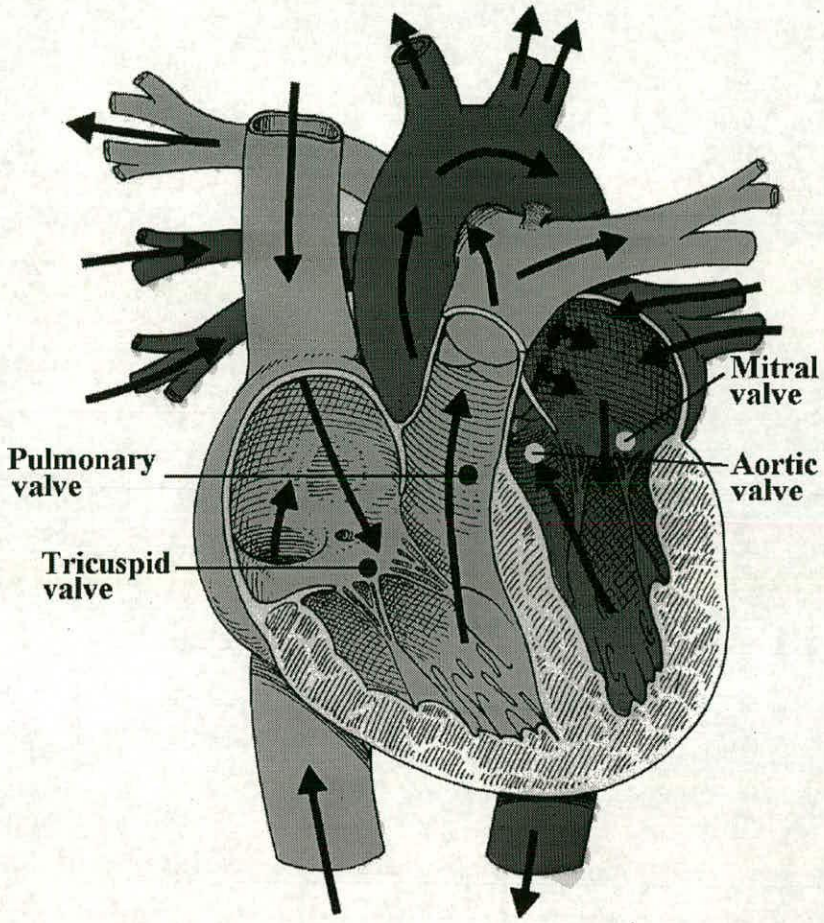


Figure 1.1: The heart.

lets in the high shear[7] and turbulent flows[8] generated in the immediate vicinity of implanted valves. This damage can lead to thrombosis through the release of pro-coagulant factors into the blood promoting the subsequent formation and deposition of clot in the valve region. The mechanism and location of clot deposition, and mass transfer influences on the clotting reaction are obviously dependent on the flows produced in the region of a given valve[9]. Once thrombus has formed there is always a possibility that the clot becomes mobile, leading to thrombo-embolism[10], with potentially fatal consequences.

A realistic assessment of the fluid mechanical influences on haemolysis and thrombus deposition should take into account the possible locations of the implanted valve and

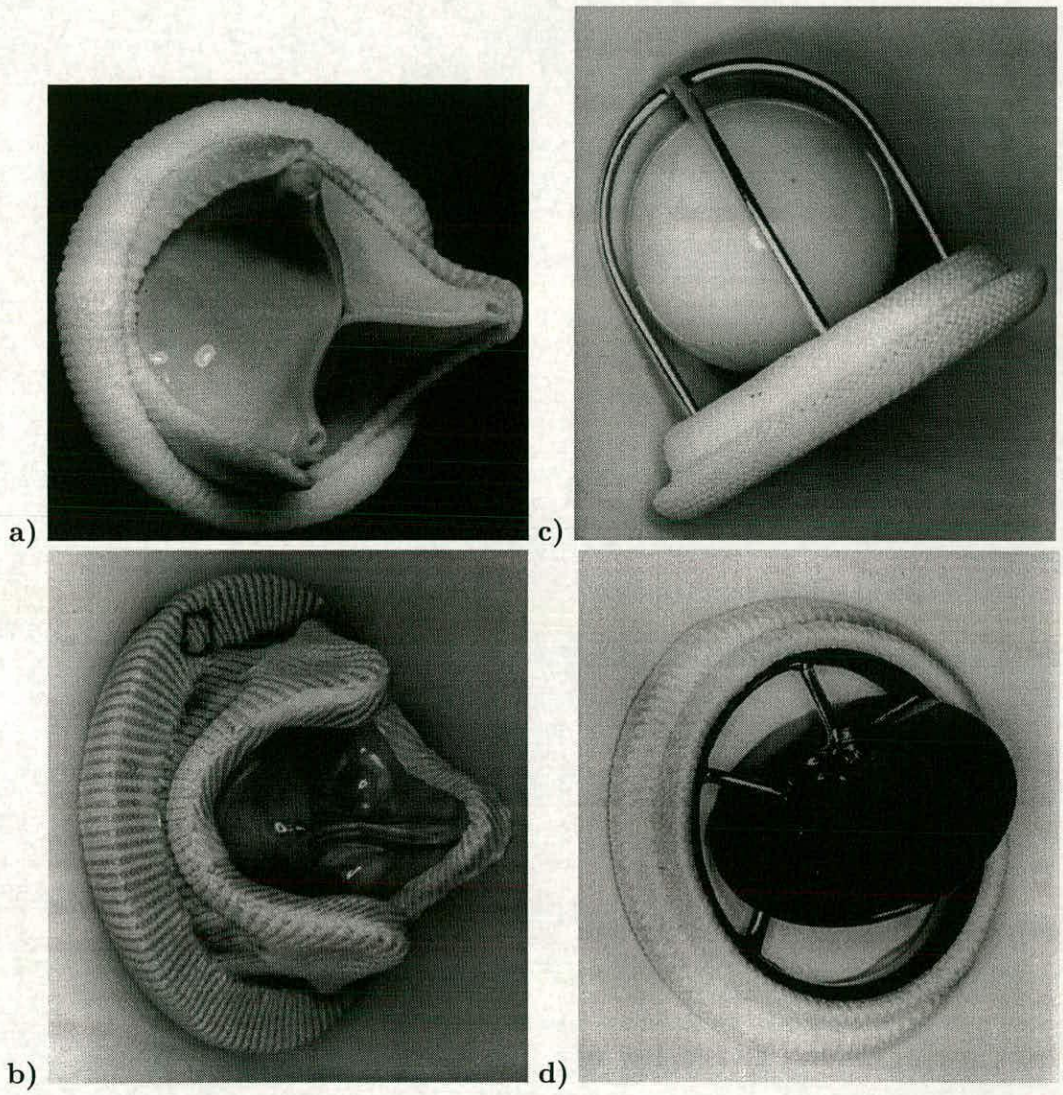


Figure 1.2: A selection of heart valve prostheses: **a)** and **b)** show trileaflet valves constructed from biological material, **c)** a Starr-Edwards mechanical valve, and **d)** a Björk-Shiley mechanical valve.

the construction and operation of the valve itself. Figure (1.1) shows a diagram of the heart and in particular the position of the aortic and mitral valves, which the vast majority of implanted valves are used to replace. Figure (1.2) shows a selection of heart valve prostheses that have been employed for this purpose.

In most investigations a mock circulatory loop is used to simulate the circulation system around the body. This usually includes a flow resistance and a compliance chamber to model the elastic nature of the arterial system[11]. The flow in the region of the

valve is often modelled by constructing a pipe section the diameter of which reflects the hydrodynamic mean diameter of the flow before and aft of the valve[12]. Alternatively, the valve might be mounted in an artificial heart to simulate the flows encountered *in vivo*[13]. Particular attention is often paid in reproducing the flow in the aortic arch. The investigations reported here, however, were carried out in a cylindrical pipe section. This was to duplicate the flow regimes in which Christy[1] and Marosek[6] performed their assessments of a coagulable fluid to mimic the clotting behaviour exhibited by whole blood. This is a promising, non-clinical method to compare the thrombogenetic performance of prosthetic valves.

The advantages of a method for assessing the thrombogenetic performance of artificial valves without the use of blood or *in vivo* experiments are obvious. Any method that allows the clotting behaviour of blood to be modelled or simulated would permit a greater range of potential valve designs and minor modifications to these designs to be assessed with regard to thrombus formation. Repeatable, *in vitro* tests, also allow valves to be compared without the variation that is inherent with *in vivo* investigations[14]. Although *in vivo* experimentation can not be avoided, its use may be reduced with the availability of such techniques.

1.2 Previous work

There have been a series of investigations carried out by Lewis[15], Christy[1], and Marosek[6] to assess the performance of a milk analogue fluid to reproduce the clotting behaviour of blood. The work demonstrated that there are some similarities in the clotting reactions of blood and rennetised milk[15,16] and congruous microscopic and macroscopic clotting behaviour was observed[1,15]. Christy[1] used a series of simple test bodies in both steady and pulsatile pipe flows in an initial study of the fluid mechanical factors affecting the clotting behaviour of the analogue fluid. His objective was to simplify the flows in which deposition was studied thus rendering the relationship between coagulation results and flow phenomena more amenable to analysis. The results supported the hypothesis that areas of stagnation - where the residence time

is greater than the mean residence time - are a necessary but not sufficient condition for clot to be deposited. It was proposed that the other important factors influencing clot deposition were: the prolonged contact time between clotting material and the test body surface, the advection of coagulable material by the flow, and the subsequent impingement of this material upon the test body.

Marosek[6] described an ultrasound system that was used to investigate the growth of milk clot over time about some of the same test bodies used by Christy[1]. Although it proved possible to measure the development of clot at the tube wall it was not possible to infer the morphology of the coagulum forming on the test bodies. Comparisons between the investigations performed by Christy and those carried out by Marosek are difficult as there were a number of important differences in the experimental conditions[6] that each used. These included: the concentrations of reagents; the shape, diameter and material of the test body and support; and the variation of the flow with time.

1.2.1 The aim of extending earlier work

The initial aim of this work was to make a more detailed analysis of the fluid behaviour around the test bodies used by Christy[1] in both steady and pulsatile flows. A secondary goal was the application of a quantitative flow visualisation technique to resolve the flows around prosthetic valves. In pulsatile flows it was hoped to resolve both how structures developed within the pulsatile cycle and the variation of these structures from cycle-to-cycle. A better understanding of the fluid mechanical factors important in haemolysis and the deposition of thrombus would allow the possibility of designing out valve features that promote such effects.

1.3 Particle Image Velocimetry

Particle Image Velocimetry, often abbreviated to PIV, is a quantitative flow visualisation technique[2]. Small seeding particles are added to a flow and illuminated using a

thin sheet of pulsed light. Normal to the light sheet individual particles appear as a series of dots as they are illuminated by successive pulses. This view can be recorded in a short exposure to capture essentially instantaneous velocity information over the illumination plane. If the time between illumination pulses is known and the local spacing between successive particle images can be determined, local velocities can be obtained. If the density of seeding particles is low, then the motion of individual particles can be followed using particle tracking techniques. For high densities of seeding particles statistical methods are used to determine the mean particle spacing within a small area.

The velocity field produced from a PIV analysis allows the calculation of derived quantities such as vorticity, certain components of the deformation tensor[17], and, with some limitations, the statistical quantities that characterise turbulence[18]. It is also possible to use the information to calculate values for the stream function and local pressure variations. In addition, the velocity profiles obtained from a PIV recording can be interpolated to give an estimate of the wall shear stress, in much the same way as is common with LDA measurements[19]. Indeed, the instantaneous measurement of the velocity profile should improve the accuracy of this procedure.

1.4 Applying PIV to flows in the circulatory system

The following observations make PIV an attractive tool to resolve some of the fluid mechanical influences on clot formation and deposition within the circulatory system:

- flow features such as stasis and recirculation should be immediately apparent;
- some components of the rate of strain tensor can be determined and related to haemolysis - especially as the generated vector field might be used to predict the position of a moving pocket of fluid and estimate its time exposure to different shear levels;

- the technique promises to divulge the velocity field and shear stress distribution required to calculate the red blood damage index (RBDI) for artificial valves proposed by Giersiepen[7];
- the damage to endothelial cells could be inferred from estimates of the wall shear stress and by identifying jet flows that are likely to impinge on the arterial wall;
- the decay in seeding particle concentration in the vicinity of obstructions within the flow should allow residence time measurements to be made;
- there is potential to make measurements close to the surfaces of valves, test bodies, and the wall;
- detailed velocity fields can be used in the validation of CFD simulations.

The technique may profitably be applied to resolve the same information in other related areas, for example, the study of stenosis and of arterial branching.

1.5 Comments in the format of this thesis

The literature review in the following chapter falls into two distinct sections. The first considers the fluid mechanical factors thought to be significant in the lysis of red blood cells and platelets. Flow induced damage and behavioural changes induced in endothelial cells are also reviewed. The factors thought to be important in the formation and deposit of coagulum are also discussed. Various techniques used to determine these factors are then described along with the associated measurements. The second half of the literature review is concerned with the PIV technique, both in its development and application.

Chapter 3 represents a compilation of developments made to the PIV techniques in response to observations made during the experimental programme of work. This includes: a comprehensive analysis of the errors associated with a program developed to analyse PIV recordings, carried out by simulating PIV images; an algorithm to validate and orient the velocity vectors produced from PIV analysis; an algorithm to

deform analysis areas to reduce the bias that arises when velocity gradients imply that there is a significant change in the inter-image spacing in the area used to determine the mean displacement; and some initial comments from applying the PIV technique to investigate two phase flows.

The remaining chapters describe the experimental equipment, the results, a discussion of the experimental results and in particular how they might help to explain the clot deposition observed by Christy[1] and Marosek[6]; and finally, conclusions and further work.

1.6 Publications

An initial investigation of the PIV technique and its application to pipe flow and the steady flow downstream of a Björk-Shiley valve was reported by Hind and Christy[20]. This included an analysis technique based on a binary representation of a PIV recording to decrease the processing time required. This approach has been rendered obsolete by the increasing computing power delivered by modern desk-top workstations. For this and copyright restrictions reprints of this work are not bound with this thesis.

Initial considerations pertinent to the application of PIV to two-phase flows were presented by Hind *et al.*[21] and McCluskey *et al.*[22]. Again, copyright restrictions prevent their inclusion. The involvement in the work of Yianneskis *et al.*[23] was solely in carrying out the analysis of PIV recordings made by Dr D.R. McCluskey and is omitted. Other less detailed publications[24,25] are omitted but did report initial observations of the complex structure in the steady flow downstream of a Björk-Shiley valve[24] and cycle-to-cycle variations observed in pulsatile flows[25].

Ultrasound measurements of clot growth around a teardrop shaped test body were compared with the predictions of clot growth from residence time measurements and the results of PIV investigations by Christy and Hind[26]. The deformation algorithm to correct for velocity gradients within PIV analysis areas and the results from simulated PIV recordings were presented by Hind and Christy[27]. Reprints of both are bound at the end of the thesis.

Chapter 2

Literature Review

This review falls into two distinct sections: a discussion of the fluid mechanical factors affecting prosthetic heart valve design and the use of a quantitative flow visualisation technique known as particle image velocimetry, or simply as PIV.

2.1 Fluid Mechanical Factors in Heart Valve Design

2.1.1 Introduction

The replacement of heart valves by mechanical and biological prostheses now constitutes a significant proportion of cardiac surgery, following the first implant of the Starr-Edwards ball-and-cage valve in 1960[5]. Since that time, there has been continued development of valves to improve their haemodynamic performance and biological compatibility. In particular, mechanical heart valve prostheses can lead to embolism and thrombosis, and patients implanted with these valves require anti-coagulation therapy[28–33]. The non-physiological flows produced around valve implants can result in damage to red blood cells, platelets, and endothelial cells; and the presence of certain flow features and surfaces may favour the formation and deposition of thrombus. The continued improvement of the design of prosthetic heart valves requires that a range of techniques are available to allow the comparison and assessment of valve performance, both clinically and in the laboratory.

A personal and informative account of the development of the artificial heart valve was given by Björk[30]. In discussing recent advances, a porous coated mono-strut valve was described that performed well in animal trials without anti-coagulation treatment. It was suggested that this may be the next step forward to enhance the quality of life of patients who undergo valve replacement surgery. In contrast, Schoen *et al.*[29] gave a detailed account of the pathology of bioprosthetic heart valves and concluded that the technological difficulties in developing near anatomical trileaflet prostheses are surmountable. This suggests that the way forward is by no means clear and improvements in prosthetic valve design may be made in a number of related areas.

A wide range of factors are considered in the design of mechanical heart valve prostheses. For valves of the same size, a crude assessment of haemodynamic performance can be made by measuring the mean pressure drop across a valve as a function of the r.m.s. flow[34–37]. Similar methods for comparing valves of differing diameters were proposed by Yoganathan *et al.*[38], and Tindale and Trowbridge[39]; both based on the orifice flow equations. Other important factors in comparing heart valve designs include: the volume of fluid that flows backwards during the closing of the valve, the back-flow or leakage of fluid once the valve is closed, the energy losses during forward flow, the energy losses during the closure of the valve, and the energy losses associated with back-flow. Several valves have been compared using these criteria by Knott *et al.*[35], Willshaw *et al.*[40], Lee and Chandran[41], Wendt *et al.*[42], She *et al.*[43], and Reul *et al.*[36]. Other, less obvious, factors may also have a significant effect on the performance of artificial heart valves. For example, Köhler and Wirtz[44] investigated sticking of the occluder associated with the deformation of the valve rim, a problem that arises for larger valve sizes as the valve ring stiffness decreases. The sticking of valves was associated with an increased likelihood of thrombosis.

The interaction of artificial surfaces and blood is also of importance and discussed extensively in the literature, for example see Forbes *et al.*[45], and Kaplan[32]: it will not be discussed in any detail here. Other clinical issues such as valve endocarditis[33,46] and the properties of the materials from which artificial heart valves are made, such as pyrolytic carbon[31,47–49], are also outside the scope of this work and mentioned only

for completeness.

The aim of this first section of the literature review is to compare the techniques that have been used to make quantitative measurements of the flows around heart valve prostheses, and to concentrate on the relation of flow structures and features to thrombus formation and the damage of blood components.

2.1.2 Damage to Blood Components

Mechanical Haemolysis

Blood damage in the form of the lysis of red blood cells (RBCs) and platelets has been associated with the presence of artificial heart valves within the circulatory system. This damage may be caused by a number of flow related phenomena including: shear within the bulk flow, shear close to surfaces, and cavitation. An extensive discussion of mechanical haemolysis is given by Blackshear and Blackshear[50]. In summary, they stated that the presence of foreign materials, injurious wall contact, flow through contractions, high shear stresses, turbulent flow, accelerating flow, and pressure gradients are all potential sources of traumatic stress for RBCs and platelets.

Blackshear and Blackshear[50] also reviewed the measurements of haemolysis as a function of shear stress made in conventional viscometers. They conclude that shear stress alone is not sufficient to predict haemolysis and that cell shape and tumbling are also important factors. Elongated, tank treading cells [1] can be produced when the spacing between the surfaces of the viscometer approaches the size of a RBC. For suspensions made from a small number of RBCs and other filler material, the tumbling of cells is inhibited and tank treading motion observed. The formation of elongated cells was reported in turbulent flows and it was noted that RBCs seem to be more easily damaged by viscous shear stresses than turbulent shear stresses of the same magnitude.

Haemolysis in pipe flow was also reviewed by Blackshear and Blackshear[50]. It was

[1] "Cells that are behaving on a similar manner to the tracks on a tank."

noted that wall roughness on the same scale as RBCs correlated with haemolysis. Surface-induced, osmotic haemolysis of RBCs was reported under flow conditions that would not be expected to give haemolysis in the bulk flow. However, it should be noted that surfaces in contact with blood become coated with material over a period of time, effectively reducing the surface roughness and its influence on the haemolysis process. In the bulk flow, extremely rapid haemolysis was reported when RBCs were exposed to shear stresses of 10^3 - 10^4 N/m^2: at these shear stresses RBCs are distorted to such a degree that they are simply ripped apart. The responses of RBCs and platelets to sub-lethal shear levels were also discussed; in particular, it was noted that the transport properties of the cell membrane alter with shear.

Wurzinger *et al.*[9,51] also present an overview of mechanical blood trauma. After identifying typical *in vivo* shear levels and exposure times, an on-line viscometry method was developed to expose RBCs and platelets to four shear stresses over four exposure times. Their results showed that shear stresses of 120 N/m^2 acting for 700 ms produced significant lysis rates; in contrast, only 14 ms exposure times were required to produce significant lysis rates at shear stresses over 450 N/m^2. They concluded that both platelet and RBC lysis are approximately linearly dependent on exposure time, that the lysis of RBC varies with the square of the shear stress to which they are exposed, and that the lysis of platelets varies as the cube of the applied shear stress.

A possible sequence of events leading to thrombus formation was proposed[9] for blood flowing rapidly through an arterial stenosis, as depicted in Figure (2.1). At the stenosis there is a local increase in shear that leads to the damage of platelets and red blood cells. In the downstream recirculation zone there is a decrease in convective mass transport and a rapid reduction in the shear stress; cells are trapped and release products after being activated upstream; there is an auto-catalytic amplification of the pro-coagulation process; and optimal conditions exist for platelet aggregation. At the reattachment point, the stagnation point flow velocity component is normal to the wall giving rise to the primary adhesion of platelets that may, in turn, lead to secondary aggregation. A very low level of lysis could, by this feedback mechanism, lead to a significant thrombogenic potential. *In vivo* observations support this hypothesis. Wurzinger

et al.[9] noted that the sites of thrombus formation found clinically were characterised by a local increase in the wall shear stress and secondary flow phenomena, including recirculating regions and pockets of stagnant fluid. These were confirmed as contributing factors[51] but not ranked in any order of importance. Christy[1] drew similar conclusions after a more detailed survey of the available literature.

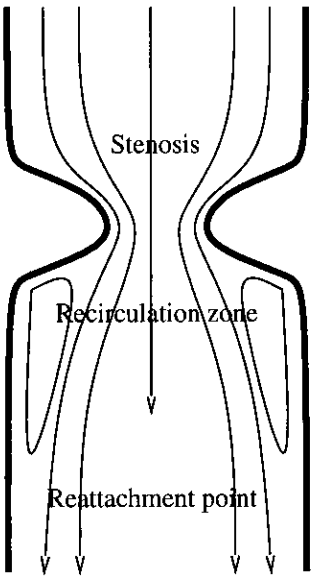


Figure 2.1: The flow through an arterial stenosis.

Giersiepen *et al.*[7] used the results of the previous work by Wurzinger *et al.*[9,51] to develop a simple expression for the percentage of cytoplasm enzyme (LDH) released by platelets and the percentage of haemoglobin (Hb) released by red blood cells as a function of shear and exposure time. The results of this curve fitting and parameter estimation exercise are given in equations (2.1) and (2.2).

$$\%LDH = 3.31\ 10^{-6}\ t_{exp}^{0.77}\ \tau^{3.075} \tag{2.1}$$

$$\%Hb = 3.62\ 10^{-5}\ t_{exp}^{0.785}\ \tau^{2.416} \tag{2.2}$$

where t_{exp} is the exposure time in seconds and τ is the shear stress in N/m^2.

LDA measurements made around twenty five heart valve prostheses were used to obtain values for Reynolds stresses and velocities and to estimate the time of exposure to particular stresses. The damage to RBCs and platelets was estimated using the mathematical model of haemolysis and by integrating over the pulse cycle to give a relative blood damage index (RBDI). For most of the valves tested there was good agreement between the calculated RBDI and clinical observations of flow induced haemolysis. However, the prediction of haemolysis for the Björk-Shiley mono-strut valve was over-estimated by a factor of six. There was no given, or obvious, explanation for this discrepancy.

Jones[8] observed that it is common practice to relate erythrocyte damage to Reynolds stresses, usually measured using LDA. It was proposed that viscous shear stress be used as an alternative indicator of turbulence and the induced damage to blood cell components. The power spectrum of the velocity fluctuations downstream of an 89% constriction of the flow area with a flow Reynolds number of 3,400 was reported. This indicated that the majority of the power was contained in the high frequencies associated with viscous shearing. Assuming that the turbulence is in equilibrium with viscous dissipation and that the overall spectrum of turbulent energy does not change over time, the production of turbulent kinetic energy is equal to the viscous dissipation of this energy. Using this simple model, Reynolds stress measurements can be related to the root mean square viscous shear stress. Jones went on to review a selection of haemolysis measurements and to estimate the Kolmogorov length and time scales associated with the flows. The Reynolds number, the characteristic shear rate, the root mean square shear stress, and the viscous dissipation rate were also estimated. The Kolmogorov length scales were comparable with the size of red blood cells suggesting that the viscous dissipation of the energy associated with turbulence was an important haemolytic mechanism in the investigations considered. The characteristic time scale associated with these turbulence measurements was of the order of 10 μs. It was observed that root mean square shear stress values of the order of 100 N/m^2 were required to give significant damage to blood cell components at a Reynolds number of around 6,000, and 10 N/m^2 for Reynolds numbers of 33,000 and 42,000. This is consistent with the increase in the ratio of the maximum stress to the root mean square shear

stress as a function of the Reynolds number[8,52]. It was noted that larger Kolmogorov length scales would be expected *in vivo* than those found in the experimental analysis of haemolysis and that a careful approach is required to understand the mechanisms by which turbulence can damage erythrocytes. The anomalous result obtained by Giersiepen *et al.*[7] for the Björk-Shiley mono-strut valve was used to emphasise this point. The characteristic length scales found in these experiments supports the proposition that blood cells are damaged by the viscous dissipation of the energy associated with turbulence.

In vitro measurements of haemolysis, for a range of valves, were reported by Häussinger *et al.*[53] and Wendt *et al.*[54]. Both made lysis measurements in a pulsating system using blood. Wendt *et al.* predicted the survival times of erythrocytes in patients implanted with artificial valves, and obtained reasonable agreement with clinical observations. Clinical accounts of haemolysis are given, for example by Barmada and Starr[55], but most of the clinical comparisons with *in vitro* experiments are made in respect of authors' experience and are usually reported along with other measurements.

Cavitation

Cavitation refers to the formation of vapour or gas filled bubbles associated with either the vaporisation of fluid as the local pressure falls below the fluid's vapour pressure or the discharge of absorbed gas from the liquid. When these bubbles collapse, in regions of higher pressure, they generate pressure waves and jets that may contribute to material erosion and the damage of blood components. Cavitation is discussed in more detail by Knapp *et al.*[56] and flow visualisation studies[57] clearly show the micro-jets and shock waves produced when these bubbles collapse. The cavitation potential of mechanical heart valve prostheses was investigated by Graf *et al.*[58] and the causes cited as:

1. the fluid downstream of the valve separating from the closing valve body due to sudden deceleration at valve closure (generating a negative pressure proportional to the deceleration);

2. negative pressures generated in accelerated flow regions;

3. the generation of alternating fields of positive and negative pressures at valve closure due to natural frequency oscillations of the occluder.

Graf *et al.*[58] investigated the cavitation behaviour of ten valves in a mock circulatory loop using water as a blood analogue, the cavitation behaviour was recorded on video. It was expected that the conditions at the mitral valve would be most likely to produce cavitation as a result of high closing body velocities, fast temporal variations in pressure, and the associated accelerations. Cavitation was expected from nearly all the valves considered under physiological flow conditions and it was found that as the leakage rate of the valve decreased the cavitation potential increased. The formation of bubbles with an initial radius of approximately 10μm and short bubble collapse times were reported indicating that vapour cavitation had been observed. Based on this information, theoretical predictions of the bubble collapse time of about 0.1 ms were made in reasonable agreement with the experimental results. The measured fluid jet velocity was around 100 m/s, and the water hammer pressure was calculated to be 140 MPa acting for 3.5×10^{-7} s.

A similar study was carried out by Lee *et al.*[59] using an aqueous glycerol mixture as the blood analogue fluid. They suggested that the erosion of valve material by cavitation may produce favourable sites for thrombus deposition. Three sources of cavitation initiation were identified in the nine valves investigated: the stop, the inflow strut, and the clearances. In particular, where the occluder impacts against the stop an accelerated flow develops with an associated reduction in pressure, sufficient to initiate cavitation. Large pressure differentials across clearances as the valve closes are also cited as causes of cavitation. To overcome these problems Lee *et al.*[59] proposed that stops are located away from the edges of the major orifice flows and that clearances should have rounded entrances. It was also noted that the use of "floating" valve occluders would help to distribute the erosion damage over the surface of the occluder and minimise local erosion.

The cavitation behaviour of four blood analogue fluids was investigated by Zapanta *et al.*[60]. The fluids used were: distilled water, an aqueous glycerol mixture, a polyacrylamide solution, and a xantham gum solution. The investigation concentrated on the performance of a Medtronic-Hall valve mounted in a mock circulatory loop. Two types of cavitation behaviour were observed, both deemed to be vapour cavitation from the short bubble collapse times. Bubble cavitation was observed as well as cavitation in the cores of vortices where the local pressure is low and where there is high shear. The Newtonian fluids gave the same cavitation behaviour but the degree of cavitation was reduced for the xantham gum solution, and further reduced for the polyacrylamide solution. This reduction in cavitation was associated with a higher elastic component of the complex viscosity for the polyacrylamide solution: both solutions having nearly identical viscous components of the complex viscosity. Of the four solutions used, the rheological properties of xantham gum are the most similar to those of blood; as a result, the authors conclude that cavitation is likely to be a problem *in vivo*, in spite of the reduction in intensity arising from the non-Newtonian behaviour of blood.

2.1.3 Damage to wall cells

Fry[14] studied the effect of acutely induced mechanical stresses on endothelial cells in the circulatory systems of dogs. The stress giving the greatest rate of change from normal to abnormal cells, termed the critical yield stress, was less than 42 N/m^2. In a similar manner, the erosion stress was defined as the stress at which endothelial cells are eroded at the greatest rate, and reported in the range 43-161 N/m^2. A previous study by the same author quoted the erosion stress as 37.9 ± 8.5 N/m^2. Although several factors were uncontrolled and unmeasured in the *in vivo* experiments, the author is confident in his observation that increased shear stresses at the wall produces structural damage to endothelial cells, with some changes observable even for low shear exposure.

Dewey *et al.*[61] stated that wall shear stresses between 0.2 and 10 N/m^2 are expected in the circulatory system and investigated the change in endothelial cell structure and function when exposed to shear stresses within this range. The experiments were performed by mounting a cell sample in a cone and plate viscometer. When endothelial

cells were exposed to shear levels of 0.8 N/m^2 the usual polygonal cell shape developed into an ellipsoidal form over a period of twenty-four hours, with the cell alignment in the direction of shear. Effects on cell regeneration were also reported but proved inconclusive. Dewey *et al.* also postulate a shear induced increase in the adhesion between platelets and endothelial cells for wall shear stress as low as 0.8 N/m^2.

Herkes and Lloyd[62] used an electro-chemical technique to determine the wall shear stresses in flows around mechanical heart valve prostheses. Maximum values of 48 N/m^2 and 17 N/m^2 were found for model caged-disk and caged-ball valves, respectively. The investigation only covered flow through a fully open valve and did not consider the effects of valve opening and closure. In particular, jet flows during the opening of valve prostheses are likely to impinge on arterial surfaces giving higher wall shear stresses than reported in this case.

Tillmann *et al.*[63] compare a range of valves with respect to the wall shear at the valve ring and sinus measured by hot-wire anemometry in a mock circulatory loop. Readings were averaged over 64 pulse cycles. The values of shear stress obtained compare well with those reported in LDA measurements, in which the velocity profile is extrapolated to give the velocity gradient at the wall. Wall shear stresses in the range 10-500 N/m^2 were obtained for the Starr-Edwards 1260, Björk Shiley 27ABP and Lillehei-Kaster valves at various locations. The results agreed with clinical observations that ball valves have a worse haemodynamic performance than disk valves. A peak wall shear stress of 180 N/m^2 was measured 70 ms after systole for the ball valve. For the Björk-Shiley valve wall shear stresses as high as 500 N/m^2 were reported, depending on the measurement location. However, the Lillehei-Kaster valve gave wall shear stress values below 50 N/m^2 at all measurement locations. The wall shear stresses for the caged ball valve reported in this investigation are higher than those given by Herkes and Lloyd[62] as would be expected in a pulsatile flow. High shear stresses between the ring and the disk of the Björk Shiley valve were reported and explained by valve leakage after closure, typically 5-9% of the forward flow. This was correlated with clinical observations of the formation of thrombus in the area of the disk groove. Regions of stasis were also reported to correlate with clot deposition. The authors concluded that

the wall shear stress values exceed the threshold values for blood damage, quoted in the literature, under physiological resting conditions for the ball valves, whereas the disk based valves do not exceed this value even under exercise conditions. The possible damage to endothelial cells as a result of these stress levels is not discussed.

Measurements of wall shear stress are given in many LDA and other investigations and are reported along with the other results from these particular studies.

2.1.4 A milk analogue for blood

Jollés[16] compared the enzymatic milk clotting process with the blood clotting process. Lewis and Macleod[15], noting some similarities discussed in this work, proposed the use of clotting milk as a blood analogue fluid for studying flow related thrombosis around prosthetic heart valves. Their aim was to produce an *in vitro* method to compare the thrombogenetic nature of alternative prosthetic heart valve designs. Microscopically, the two clotting processes showed a remarkable resemblance and similar clot features, not readily explained by the fluid mechanics. A milk mixture with similar clotting behaviour to blood was developed: one exhibiting the same characteristics according to the simple Lee-White test of the time dependence of clot rheology. This blood analogue was then used in a reconstruction of an earlier blood clotting experiment in which essentially the same macroscopic behaviour was observed. This was confirmed by the resemblance of the milk and blood clots formed around artificial heart valves under similar flow conditions.

In discussing their results, Lewis and Macleod observed that the sites of thrombus deposition correlated with pockets of stasis and not with regions of turbulence and high disturbance. They proposed that the initial stages of clot formation would be promoted by the enhanced mass transfer arising from turbulence with the induction phase of the reaction thereby reduced. It was also noted that turbulence would strongly influence the aggregation of particles within the flow.

The continuation of this work was reported by Christy and Macleod[64]. In order to

investigate further the similarity between milk and blood clot formation, the deposition of clot around a series of bluff bodies was examined in both steady and pulsatile flows. The flows around these bodies could be more easily determined than those around prosthetic valves and the correlation between flow structures and the deposition observed made easier. The authors concluded that stasis is a necessary, but not sufficient, condition for the formation of clot. The effect of local turbulence on clot deposition was investigated using a modified Lee-White test. This showed agitation to have little effect during the initiation of the milk clotting reaction, in contrast to the earlier hypothesis of Lewis and Macleod[15], and agitation after this period to produce an extremely adherent clot. A more detailed account of this work was given by Christy[1].

Christy and Hind[26] developed a simplified deposition model around one of the bluff bodies used in the work of Christy and Macleod[64]. The separation and reattachment points of the boundary layer were determined by injecting small particles into the flow. These particles were also used to estimate the mean residence time of fluid in the recirculation zone bounded by the test body and boundary layer. This and a simple kinetic model based on the Lee-White clotting test were used to model the recirculation zone as a well mixed region. The predictions agreed with experimental observations. This will be discussed in greater detail later.

2.1.5 Flow visualisation and velocity measurements

In general, a wide range of techniques have been used in fluid mechanical investigations to study the fields of velocity, temperature, density, and chemical concentration. In particular, flow patterns have been studied qualitatively using flow visualisation. The techniques include, among others: dye tracers, schlieren photography, hydrogen bubble wires, smoke wires, and surface tufts. Merzkirch[65] discusses these techniques and others in detail and many examples of the use of these techniques can be found in the compilations of photographs produced by van Dyke[66] and by the Japanese Society of Mechanical Engineers[57]. Gad-el-Hak[67] reviews many of the same techniques and their use in unsteady flows. Optical techniques, such as laser Doppler anemometry (LDA) and particle imaging techniques are now common ways of obtaining quantitative

information about fluid flows[2,68,69]. The advantage of these techniques over other common methods of velocity measurement - such as the use of pitot-tubes, hot-wire anemometry, and hot-film anemometry - is that they are non-invasive, although the introduction of small seeding particles into the flow is required. Other developments include ultrasonic velocimetry techniques, NMR based techniques, and pulsed laser fluorescence.

The majority of the techniques mentioned have been applied to investigate the flows around artificial heart valves. Comment here is limited to a few illustrative examples in which quantitative measurements have been made. The results of LDA investigations are reported in some detail in the following section. Particle imaging techniques are covered extensively in the second half of this literature review although the results of their application to the flows in the vicinity of prosthetic heart valves are summarised here.

Hot wire measurements

Figliola and Mueller[70] used hot wire anemometry to make turbulent shear stress measurements in the vicinity of disk, ball, and tilting disk prosthetic heart valves. The valves were tested in the fully open position at Reynolds numbers of 2000, 4000, and 6000, based on the tissue sewing ring diameter of approximately 26 mm. Maximum Reynolds stresses of 394, 410, and 690 N/m^2 were measured for the Kay-Shiley uncovered caged disk, the Starr-Edwards uncovered caged-ball, and the Björk-Shiley uncovered tilting disk valves, respectively, at the maximum Reynolds number of 6000. The corresponding maximum shear components of the stress were found by translating the measurement probe and reported as 170, 101 and 50 N/m^2 at maximum values of 24,000, 14,400 and 7000 s^{-1} for the shear component of the rate of strain. Maximum normal components of the shear stress of 100, 75 and 20 N/m^2 were also reported with the corresponding maximum normal components of the shear rate of 14,400, 10,500 and 2900 s^{-1}.

Hot film measurements

Chandran *et al.*[71] measured velocity profiles and Reynolds stresses for two Starr-Edwards valves and a Björk-Shiley valve in pulsatile flows using a hot film technique. Peak turbulent normal stresses of 110 N/m^2 were observed for the silastic ball valve 108 ms after the opening of the valve, 45 mm downstream of the ball; peak turbulent normal stresses of 35 N/m^2 were measured for the stellite ball valve. Turbulent shear stresses as high as 150 N/m^2 were obtained in the minor flow region of the Björk-Shiley valve.

Hasenkam *et al.*[72] used hot-film anemometry to measure the turbulence profiles downstream of a selection of aortic valves. Different measurement locations make comparisons with other work difficult but the variations between valves closely follow the LDA results of Yoganathan *et al.*[11]. The shear stress values reported are lower than those measured by Yoganathan *et al.* as they are measured further downstream from the valve.

Nygaard *et al.*[13] used hot-film anemometry to determine the flow profile and turbulent shear stresses downstream of artificial heart valves. This information was used, as suggested in earlier work[7], to calculate a relative blood damage index (RBDI) for two bioprosthetic valves. Maximum turbulent shear stresses of 154 N/m^2 and 194 N/m^2 were observed for the Ionescu-Shiley pericardial standard valve and the Hancock Porcine valve, respectively. The RBDI for both valves was calculated to be 1.8, over double the maximum reported in the original work. The discrepancy was explained as the RBDI is very much dependent on the axial distance downstream of the valve where the measurements are made: the results are thus difficult to compare directly. The RBDI is put forward as a useful indicator of valve performance that can be calculated when the velocity and shear-stress distributions are measured simultaneously.

Christy[1] reviews other hot-film measurements in which Reynolds stresses in the range 15-82 N/m^2 and turbulence intensities in the range 20-50% are reported.

Flow visualisation

Yurechko *et al.*[73] used photo-chromic flow visualisation to investigate the flow downstream of artificial heart valves. A line was "burnt" into the photo-chromic fluid using a laser and then followed using a high speed camera. Velocity profiles relative to the burn line were produced and gave reasonable agreements with LDA measurements made in the same system.

Affeld *et al.*[74] used a PIV cross-correlation method to investigate the flows behind Björk-Shiley standard and St. Jude valves using a flow system scaled up tenfold. The size enlargement allowed the use of lower velocities and comparatively large seeding particles overcoming some illumination problems. A thirty-five fold reduction in the maximum velocity was achieved as a result of the ratio of the kinematic viscosity of blood to that of the test fluid (water) of 3.5:1 and the use of model valves with a diameter of 220 mm. The Reynolds number, the Strouhal number, and the Archimedes number were kept constant in scaling up the experimental equipment. The Strouhal number, Str, is a dimensionless frequency and is the ratio of the diameter of the valve, d, over the product of the mean velocity, u, and the period of the pulsatile flow, t. Thus the Strouhal number, $\mathrm{Str} = \frac{d}{ut}$, represents the relation of the stroke volume to the size of the test valve. The Archimedes number takes into account the difference in density between the occluder and the test fluid and is defined as, $\mathrm{Arch} = \frac{\rho_{occluder} - \rho_{fluid}}{\rho_{fluid}\, u^2}\, d\, g$. The effective framing rate of the video was about 9000Hz taking the scaling into account. The video images were digitised using a conventional frame grabber (768 lines by 512 pixels) and processed using 16 by 16 pixel interrogation areas. The method is claimed to have an accuracy comparable with that of LDA although no support for this statement was given. The method does, as stated, have the advantage of avoiding averaging techniques allowing individual flow phenomena to be observed and quantified.

Cassot *et al.*[75] used classic flow visualisation behind a series of valves in a mock circulatory system. This allowed a quantitative interpretation of flow phenomena and a comparison with numerical simulations. Ultrasound Doppler velocimetry was also used to obtain 2D profiles of the axial component of the flow behind the same series

of valves. This information is difficult to compare with other work because of the lack of an obvious scale on the velocity diagrams. The results were also compared with numerical simulations.

Hirt *et al.*[76] used PIV to study the flow of an aqueous glycerol solution in a mock circulatory loop downstream of a bileaflet valve. Sodium iodide was added to the mixture to match the refractive index of the fluid to that of the test section in order to minimise refractive distortions. No comment was made about the increased density of the test fluid. The results showed appreciable velocity gradients over individual analysis areas that increase the error associated with each measurement[2], although no comment is made in reference to this topic. Features in the flow were analysed using a critical point technique, previously discussed by Chong *et al.*[77]. The second invariant of the rate of strain tensor is linked to the shear rate (as would be expected[78]) and thereby to the shear stress. Large local strains are associated with large negative values of the second invariant. The rates of strain observed at the mitral valve position were approximately double those observed at the aortic valve position.

Lim *et al.*[79] discussed the development of a PIV system to make measurements around prosthetic heart valves. An aqueous glycerol solution was adopted as the blood analogue fluid. A hybrid method incorporating both PIV and particle tracking velocimetry was developed to contend with the wide range of velocities present in the flows. These range from the relatively high velocities within jet flows to the velocities associated with recirculation zones and near stagnation points. The seeding densities used in these experiments are obviously too low giving a poor data yield compared with those normally obtained using similar techniques. Thus, the interpolated results from these few, spatially well separated velocity vectors are unlikely to be meaningful.

Other features of the circulatory system have also been investigated using flow visualisation. Ojha *et al.*[80] used a multiple trace photo-chromic method to visualise the flow produced by modelled arterial stenosis. The wall shear stress was estimated by fitting a curve to the velocity profiles obtained and estimating the velocity gradient at the wall. Lynch *et al.*[19] used flow visualisation to identify recirculation regions,

separation and reattachment points, and other features in pulmonary arterial models.

Ultrasound velocimetry measurements

Farahifar *et al.*[81] investigated the influence of the orientation of a Björk-Shiley valve prosthesis on the downstream velocity field using pulsed Doppler ultrasound velocimetry. Valve orientation was shown to influence the location of the maximum velocity and the direction of rotation of vortices.

David *et al.*[82] analysed the behaviour of regurgitant jets produced during valve closure and produced good agreement with ultrasound measurements in a simplified experiment.

Colour Doppler echocardiography was used by Chao *et al.*[83] to investigate the influence of the Coanda effect on the measurement of the regurgitant jet area and flows downstream of artificial heart valves made using this technique. The great advantage of this and other ultrasound techniques is their use *in vivo*. For example, colour Doppler echocardiography is used to give a qualitative measure of valvular disease in which the area of the regurgitant jet is an important indicator, see Mohan *et al.*[84].

Nygaard *et al.*[85] used a perivascular pulsed Doppler ultrasound system to evaluate the spatial distribution and temporal development of turbulent stresses 5-6 cm downstream of implanted valves. For the St. Jude Medical valves the maximum values of the estimated Reynolds normal stress were in the range 27-63 N/m^2 with the maximum value occurring along the central slit near the vessel wall. CarboMedics valves gave similar results to the St. Jude valves with the maximum Reynolds normal stress in the range 11-72 N/m^2. The Starr-Edwards silicone rubber ball valves gave maximum Reynolds normal stress values in the range 11-56 N/m^2 with the maximum occurring in the annulus between the ball and the vessel wall. Turbulent shear stresses measured *in vivo* using hot-film anemometry are also summarised. Values for the maximum Reynolds normal stress are given in the range 38-113 N/m^2 for the St. Jude Medical valve and in the range 37-120 N/m^2 for the Starr-Edwards silicone rubber ball valve.

The estimated magnitudes of the turbulent shear stresses and exposure times are believed to be sufficient to give rise to sub-lethal and possible lethal damage of RBCs and platelets. The low turbulent shear stresses measured for the Starr-Edwards valve were discussed: the combination of skew mounting of the valve and post-stenotic dilation was suggested as a possible explanation.

Other measurements

Galanga and Lloyd[86] investigated flow induced mass transfer in the vicinity of artificial heart valves using an electro-chemical technique. Regions of high mass transfer were found in both high and low shear regions and correlated with reports of thrombus formation *in vivo*.

2.1.6 LDA Measurements

The Laser Doppler Anemometry (LDA) technique is based on measuring the Doppler shift of laser light reflected/scattered by small seeding particles moving in a flow; the shift is proportional to the particle velocity. The work of Tritton[87], and Merzkirch[65] provide introductory material on the LDA technique. For a more detailed discussion see the work of Drain[88], Durst *et al.*[89], and the wealth of literature devoted to the theory and application of LDA. The technique gives a time series of one, two or three components of the velocity from a probe volume within a fluid. From these results various turbulence statistics can be obtained; in particular, values for Reynolds normal and shear stresses. This assumes that Taylor's hypothesis is valid; ie that spatial velocity fluctuations around the mean velocity are carried downstream at the mean velocity and appear as temporal fluctuations in the measured velocity. The technique can be used to measure a wide range of velocities and allows the resolution of the direction of motion.

Unless stated otherwise, the following investigations have used a mock circulatory system with an aqueous mixture of glycerine as the blood analogue fluid, have determined

the position of the probe volume in an appropriate way (commonly by ray tracing), and have made measurements under physiologically plausible fluid mechanical conditions.

Measurements made in steady flows

Yoganathan and Corcoran[90] measured wall shear stresses of the order of 100 N/m^2 in the vicinity of the Starr-Edwards 1260-12A, Björk-Shiley 27XMBRP, Smeloff-Cutter A-5, Cooley-Cutter A-25, and Starr-Edwards 6520-1M valves. The investigations were made using a steady flow of Pluracol solution and a single component LDA system operating in the dual beam, forward scattering mode. Maximum turbulence intensities were measured in the range 25-50% decaying to 15-20% 0.12 m downstream from the valves. Bulk turbulent shear stresses were estimated in the range 10-100 N/m^2 but are likely to be higher as a result of acceleration effects in pulsatile flow. It was concluded that damage to blood elements and to the endothelial lining of the aorta was likely. Experimental correlation between the location of thrombus formation and pockets of stasis observed in steady flow was reported.

Figliola and Mueller[91] measured the axial component of the velocity downstream of several valve types in steady flow using a single component LDA system operating in the backscattering mode. Maximum wall shear stresses were reported in the range 70-300 N/m^2, maximum turbulent shear stresses in the range 11-82 N/m^2, and maximum turbulence intensities of 40-50% decaying to 12-25% further downstream. Turbulent shear stresses in the annular flow region near the occluder, where measurements are difficult, were estimated in the range 60-170 N/m^2. Viscous stresses of 45 N/m^2 were also reported. Regions of separated slow flow were correlated with the formation of thrombus in clinical observations.

Chandran *et al.*[92] compared the velocity and turbulence measurements made using an aqueous glycerol solution and a dilute sodium chloride solution. A single component LDA system operating in the dual beam, forward scattering mode was used. Variations in velocity profiles were obtained for the two solutions at the same Reynolds number. This was explained by the different viscous interaction between the fluids and the

occluder and its supports.

Lei *et al.*[93] measured velocities in the vicinity of a Björk-Shiley valve in steady flow. A kerosene and oil mixture was used for Reynolds numbers up to 800 and water for Reynolds numbers up to 4000. The single component LDA measurements (operating in the forward scattering mode) support the existence of two nearly symmetric spiral vortices downstream of the valve, show no recirculation in the downstream aorta, and no obvious stagnation region in the vicinity of the minor orifice. The results were used to validate 2D FEM numerical calculations in which the valve was approximated as a circular disk. Good agreement was observed at low Reynolds numbers. At higher Reynolds numbers, deviations between the observed flow and the predictions were explained as the full three dimensional nature of the flow was not modelled. Attention was drawn to the work of Thwaites[94] showing the idealised flow pattern produced by a uniform flow past a flat, circular plate. Figure (2.2) shows the flow with the plate normal to the stream, Figure (2.3) at a large angle of incidence, and Figure (2.4) at a small angle of incidence. These flow patterns indicate the presence of spiral vortices, evident in the work of Lei *et al.*[93] and others[74,95,96].

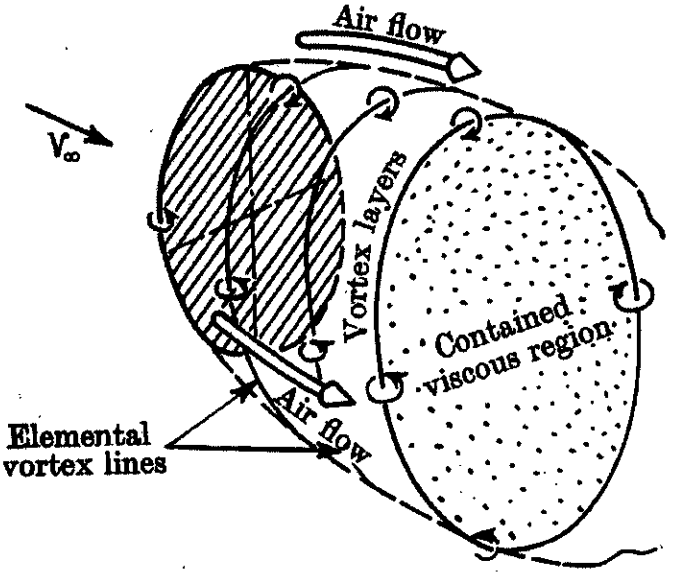


Figure 2.2: The idealised flow features produced by a disk normal to a uniform flow.

Chew *et al.*[97] made measurements in steady flow downstream of three prosthetic heart valves using a two-component LDA system operating in the forward scattering mode.

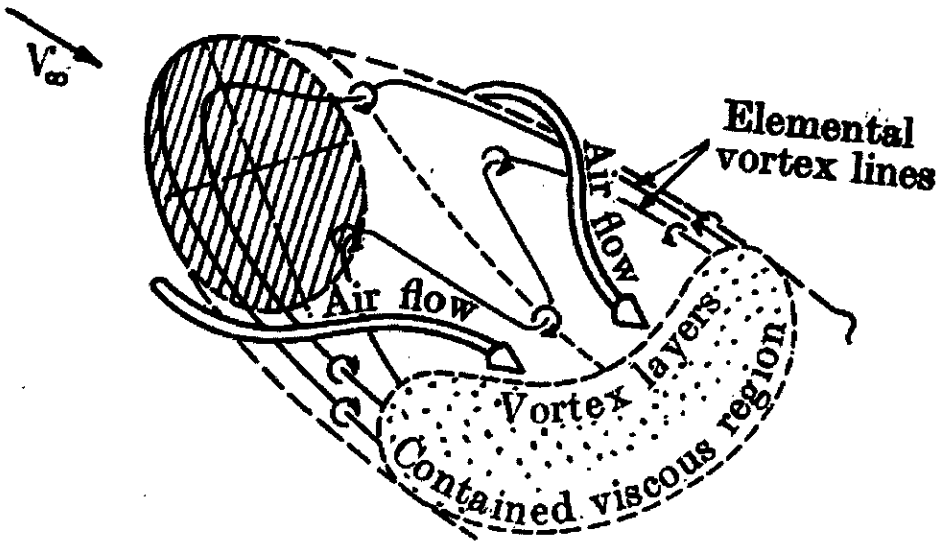


Figure 2.3: The idealised flow features produced by a disk at a high angle of incidence to a uniform flow.

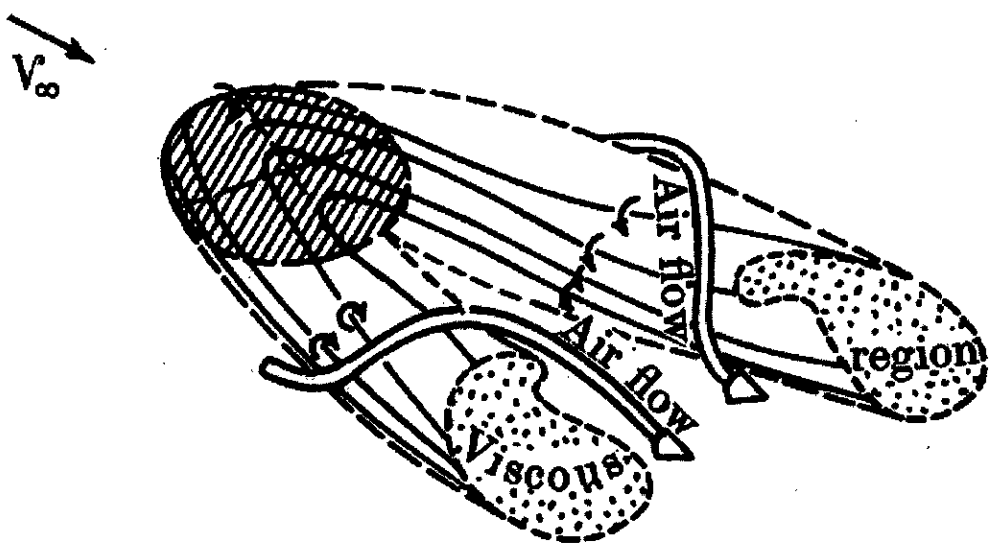


Figure 2.4: The idealised flow features produced by a disk at a low angle of incidence to a uniform flow.

For flowrates of 30 l/min, wall shear stresses in the range 3-5 N/m^2 were measured two diameters downstream from the valve, significantly lower than those obtained by Yoganathan and Corcoran[90] and others[62,63]. The difference is explained as the shear stresses in steady flows are expected to be lower than those in the accelerating flow with

the same peak velocity, as mentioned earlier. At one diameter downstream from the valve, maximum Reynolds normal stresses were observed in the range 160-310 N/m^2.

Measurements made in pulsatile flows

Walburn *at al.*[98] made turbulent stress measurements in the region of a Hancock porcine prosthetic valve using a two channel LDA system in the differential Doppler mode with forward scattering for flowrates in the range 2.3-5.2 l/min. Peak shear stresses were reported in the range 90-190 N/m^2 although the average over the cycle was only 4 N/m^2. Normal stresses with a peak value of 675 N/m^2 and a mean value of 38 N/m^2, averaged over the cycle, were also reported. Peak values of the turbulence intensity, measured axially, were reported in the range 5-19%. It was noted that the measurement axes differed from the axes associated with the principal stresses by approximately two degrees.

Tiederman *et al.*[96] studied pulsatile flows in a mock circulatory loop that did not include a model sinus region. Velocity profiles were produced by averaging data over 200, 15 ms windows at the peak systolic flow. Ensemble average turbulent shear stresses of 282 N/m^2 and 207 N/m^2 were measured downstream of trileaflet and tilting disk valves, respectively. The measured turbulent shear stress values decreased more rapidly with axial distance for the tilting disk valve. A four beam, two colour, two component LDA system operating in the forward scattering mode was used in the investigation allowing the determination of turbulent statistics without making assumptions about correlation coefficients; a significant advantage over the simpler, single component techniques.

Yoganathan *et al.*[11] measured the turbulent shear stresses downstream of a number of aortic heart valve prostheses at various axial and radial positions using a three beam, two component LDA system operating in both forward-scattering and backscattering modes[99]. The bioprostheses investigated produced lower turbulent shear stresses than reported previously for mechanical prostheses but all the valves gave rise to shear stresses sufficient to cause sub-lethal and/or lethal damage to blood components. Peak turbulent shear stresses (at peak systole) were in the range 200-450 N/m^2 depending

on the valve and the measurement location. Similar results are presented by Woo and Yoganathan[100] from measurements made in the vicinity of mitral heart valve prostheses using the same LDA technique. Peak shear stresses (at peak diastole) in the range 20-195 N/m^2 were reported, again dependent on the measurement position.

Woo and Yoganathan[12] produced a more detailed account of the behaviour of the St. Jude Medical valve in both the mitral and aortic positions. Flow visualisation as well as LDA results were presented. The same LDA technique was used as that by Yoganathan *et al.*[11,99]. In the mitral position, the maximum turbulent shear stress measured was 76 N/m^2. After valve closure, turbulent shear stresses of the order of 12 N/m^2 were found upstream of the central pivot associated with backflow through the valve. In the aortic position, the highest turbulent shear stresses were observed at the edges of the jet like flow fields, with a maximum value of the order of 200 N/m^2. Turbulent stresses of 33 N/m^2 were measured in back flow. A Maximum wall shear stress value of 63 N/m^2 was also reported. The valve leaflets were observed to open asynchronously.

Schwarz *et al.*[101] investigated the influence of cardiac flow rate on the turbulent shear stress measurements made in the vicinity of a mono-strut, disk valve using a four beam, two colour, two component LDA system operating in the dual beam forward scattering mode. Shear stresses up to 99 N/m^2 were measured. The maximum shear stress was found to scale with the flowrate to the power 0.72. The exponent is thought to depend on the valve geometry and the opening angle of the valve. It was also noted that as the flow accelerated through the major orifice of the valve a "starting" vortex developed and was then shed from the disk.

Giersiepen *et al.*[102] used a two component LDA system to measure the velocity and shear stress distributions downstream of ten mechanical valves. At a distance of 0.55 times the diameter of the aorta downstream from the valve the maximum shear stress was observed at peak systole, whereas at a distance of 1.5 times the diameter of the aorta downstream from the valve the shear stress peaked during the deceleration phase of the flow. Velocities up to 1.5 m/s and turbulent shear stresses up to 150 N/m^2 were

measured during systole. Recirculation in the aortic sinus produced turbulent shear stresses of the order of 25 N/m^2 for all the valves studied. Shear stress levels were highest at the edges of the jet flow. It was shown that exposure times of 150 ms to turbulent stresses of the order of 80 N/m^2 would be expected at the border of the jets in the recirculation zone. It was noted that the results agreed well with those found in earlier work[11,96].

Walker and Yoganathan[103] measured, amongst other things, velocities and turbulent shear stresses downstream of five mechanical heart valves prostheses using a three beam, two component, LDA system operating in both the forward-scattering and backscattering modes. For the Medtronic-Hall tilting disk valve maximum forward velocities of the order of 2 m/s were measured at a volumetric flowrate of 7.5 l/min. The maximum reversed flow velocity was 0.25 m/s. The fluid adjacent to the wall near the minor orifice of the valve was stagnant in both the accelerating and decelerating phases of the flow. In the larger orifice area, turbulent stresses of 120 to 150 N/m^2 were measured 7 and 13 mm downstream of the valve at peak systole. In the minor orifice region, a peak turbulent shear stress of 145 N/m^2 was reported 15 mm downstream from the valve. It was suggested that higher values occur closer to the valve where measurements are difficult. Similar velocities were found downstream of the St. Jude Medical bileaflet valve and turbulent shear measurements of the order of 170 N/m^2 made distal to the central orifice. Again, higher shear stresses would be expected nearer to the valve. The Björk-Shiley mono-strut valve gave similar maximum fluid velocities. High turbulent shear stresses correlated with high velocity gradients such as those found at the edges of jets. Maximum values of the turbulent shear stress of 125 and 80 N/m^2 were measured 11 and 17 mm downstream from the valve. A slightly higher maximum velocity of 2.25 m/s was observed with the Omni-Carbon tilting disk valve and maximum values for the turbulent shear stress in the range 125-170 N/m^2 were found 8-14 mm downstream of this valve. A maximum turbulent shear stress of 180 N/m^2 occurred at the central edge of the minor orifice jet. The Duromedics bileaflet valve gave a maximum turbulent shear stress of 220 N/m^2. The velocity and turbulent shear stress fields for the five valves were similar and all induced turbulent shear stresses high enough to cause lethal and/or sub-lethal damage to blood elements. The problems of haemolysis, thrombosis,

and thromboembolic complications were not eliminated in these new designs.

Van Son *et al.*[104] investigated the velocity profiles of four bileaflet heart valve prostheses using a two-channel LDA system operating in forward scatter, polarised mode. The data was averaged over 64 cardiac cycles. Three peaks in the velocity profile were exhibited by all of the valves with the flatter velocity profiles associated with the valves with the widest opening angle.

Baldwin *et al.*[105] described a filtering technique and a method for determining the principal Reynolds stresses from measurements made in pulsatile flows. Reynolds normal stresses and Reynolds shear stresses of 298 and 120 N/m^2 are respectively reduced to 41 and 17 N/m^2 by the filtering technique. Large variations were observed in transforming from the measured coordinates to the principal axes. This seems to have been disregarded so far in biofluid-mechanical investigations, except in the comments made by Walburn *at al.*[98]. It was also noted that researchers in this field have not given enough consideration to the number of cycles over which data is averaged and the length of measurement window used to give pseudo-steady flow. Velocity bias is also briefly discussed and solutions proposed to correct for this. In view of these comments it seems likely that a number of the studies reported in this section could have over estimated the shear stresses but a lack of detail regarding the exact processing of the data makes this difficult to substantiate.

2.1.7 CFD calculations

The role of computational fluid dynamics (CFD) in the analysis of prosthetic heart valve flows was discussed by Tansley *et al.*[10]. A concise account of the fluid mechanical problems associated with heart valve design was given and the experimental flow analysis techniques that have been used described and contrasted. The major advantage in using CFD simulations over the experimental techniques is that full flow field information can be obtained, the major drawback is the lack of suitable turbulence models for use in pulsatile flows.

Early attempts to simulate the pulsatile flow around heart valve prostheses used 2D geometries and the $\Psi - \Omega$ (stream function-vorticity) formulation. The work of Cheng *et al.*[106,107] explains the formulation and gives example results. The superposition model used makes shear stress predictions difficult. More complex geometries were modelled as grid generation and solution techniques advanced[93,108]. Thalassoudis *et al.*[109] included a turbulence model in their 2D simulations of the flow around a caged-ball valve prosthesis. The results clearly showed flow separation, high and low velocities, and gave predictions for the turbulent shear stresses in the flow. The computed turbulent shear stress values at the sewing ring tip of 6-50 N/m^2 for flows of 5-20 l/min are significantly lower than those found experimentally by Figliola *et al.*[91] and Woo and Yoganathan[100]. Similar simulations without turbulence models gave much lower predictions for the shear stress. This may be due to an experimental over-estimate of the shear stresses, as discussed in the previous section, or inadequacies in the turbulence models used.

A more complex 3D time-dependent formulation[110] was applied to predict the flow through an artificial heart by Rogers *et al* [111]. The moving boundary of a piston was included in the model. An imaginative model of the movement of elastic and rigid surfaces within cardiac fluid mechanics was discussed by Peterson[112] and by Cheng *et al* [113]. Vesier *et al* [114] extended the method to three dimensions to model pulsatile flow within compliant vessels. Peskin and McQueen[115] presented a complex simulation of the flow within the heart but at flowrates below those encountered physiologically. This model has been used to provide insight into the flows around valves in an attempt to assess and improve possible designs.

2.1.8 Discussion

It is apparent from a range of measurements, both *in vitro*[1,11–13,62,63,71,72,90–93,96,100–103,105] and *in vivo*[85], that artificial heart valves produce turbulent stresses high enough to cause sub-lethal and/or lethal damage to RBCs and platelets[1,7–9,50,51]. Heart valve prostheses may also produce viscous shear stresses at or near the wall[1,12,62,63,90,91,97] that can cause structural changes,

damage, and erosion of endothelial cells[14]; as well as damage to erythrocytes enhanced by the presence of foreign surfaces[10,50]. This process is more important for valve designs that produce fluid jets that impinge upon the arterial wall. It is clear that cavitation in the vicinity of valves should also be considered as a mechanism for erythrocyte damage and erosion of valve materials[58–60]. It is apparent that regurgitant jets and the edges of jet type flows in systole are associated with turbulent shear stresses and exposure times sufficient to damage erythrocytes. This is evident where recirculation could prolong the exposure time of blood components to modest shear stresses in the vicinity of the jet type flows[102], particularly in the sinus region.

The comments of Baldwin *et al.*[105] suggest that LDA measurements should be viewed with some caution. In particular, the averaging method, the filtering of results, and the time window in which measurements are made require adequate consideration; in addition to other measurement problems that apply to steady as well as pulsatile flows. The suggestion is that turbulent shear stresses may well be over-estimated, although the evidence is that the results from LDA and other anemometry techniques are in broad agreement[11–13,62,63,71,72,90–93,96,100–103]. However, the assumption that the stress pattern is repeated from cycle-to-cycle is debatable and that the averaging procedure may include variations, particularly on larger scales, that are not due to turbulence. LDA and other anemometry techniques that average over several cycles may give the same results, all including cycle-to-cycle variations in any estimates of turbulence statistics. For example, the hot wire investigation by Chandran *et al.*[71]divided the pulse into small segments and found turbulent statistics by averaging the readings for each segment over sixteen cycles. It seems doubtful that Taylor's hypothesis applies to the averaging techniques used over sections of the pulse cycle. This view is supported by the reduction in the measured shear stress produced by the filtering technique of Baldwin *et al.*[105] removing only a small number of measurements.

Quantitative flow visualisation techniques - such as particle tracking, particle image velocimetry, and related techniques - have the potential to give a large number of simultaneous velocity measurements[2]. It may also be appropriate to use these techniques to visualise coherent structures and estimate turbulent statistics but such discussion

is deferred until later. The potential to make measurements of the quantities required to calculate a RBDI for a valve is clear. However, several important considerations in using these techniques, such as the effect of velocity gradients, have not been considered in the works to date. These techniques, and the results from ultrasound Doppler techniques, provide useful validation material for numerical simulations and they have an obvious role to play in the development and assessment of turbulence models for pulsatile flows.

The damage to erythrocytes through exposure to shear is well accepted[1,7,9,50,51], although there are obvious problems in relating viscous shear stresses, as measured in a number of experiments, to turbulent stresses. The work of Jones[8] in linking Reynolds stress measurements to viscous shear stresses is a first step and provides a convincing explanation for the variation of the threshold shear values required to damage erythrocytes as the distribution of the turbulent velocity fluctuations broadens with increasing Reynolds number. The analysis of characteristic length and time scales provides useful information in determining the recording parameters for quantitative flow visualisation experiments.

The mechanism for thrombus formation proposed by Wurzinger *et al.*[9]is appealing: the damage of RBCs and platelets releasing clotting agents; this material being trapped in a recirculating flow; and clotting material being convected to a surface where thrombus formation is favourable. This mechanism is supported in steady flow by a variety of work [1] but is more difficult to assess in pulsatile flows. However, the mechanism of clot formation is more complex as high shear can prevent clot formation and deposits are found at upstream stagnation points under some conditions, on the the valve mounting and surfaces [1]. The convective and diffusive mass transport of blood components and clotting agents also have an important effect, but are difficult to determine conclusively. Tansley *et al.*[10] describe the aggregation of cells within turbulent eddies, where erythrocytes have been damaged, as another mechanism of thrombus formation clearly associated with enhanced mass transport. The mechanism proposed by Wurzinger *et al.*[9] is also supported by the experiments using the milk analogue fluid where stasis is shown to be a necessary, through not sufficient, prerequisite for clot formation[1,15,64].

The modified Lee-White test results also indicate that mass transport is important in the areas of stasis where clotting occurs[1,64].

The impingement of jets on endothelial cells and cavitation related erosion may produce sites that favour the initiation of thrombus formation[14,58–60]. Thrombus itself is not a major concern unless it gives rise to valve disfunction or stenosis. It is the mobilisation of thrombus leading to thrombo-embolism at another location in the circulatory system that can not be tolerated[10].

2.2 Particle Image Velocimetry

2.2.1 Introduction

Particle image velocimetry (PIV) is a quantitative flow visualisation technique, which provides instantaneous velocity information throughout an illuminated plane within a flow. The velocities are typically accurate to within 1-2% [2], often good enough for meaningful values of derived quantities, such as vorticity, to be calculated. The technique compliments, and is distinct from, point measurement techniques, such as LDA, from which a time series of readings can be obtained at one point but a series of such measurements are required to determine the whole flow field. PIV, like LDA, is non-invasive and does not disturb the flow to the same extent as, for example, hot wire investigations; although small light scattering particles have to be introduced into the flow, as with LDA.

This second section of the literature review is concerned with the basic PIV technique, its development, the requirements to produce good experimental recordings, the methods of analysis and their accuracy, sources of errors, and post processing of the velocity field.

2.2.2 The basic technique

The flow under study is seeded with small, light scattering particles that accurately follow the motion of the fluid. A pulsed light sheet is used to illuminate a plane within this flow, usually chosen so that the velocity normal to the illuminated plane is small, as shown in Figure (2.5). Viewing perpendicular to the light sheet, particle images are seen as a series of dots as they move along particle tracks, as shown in Figure (2.6). This view is commonly recorded onto photographic film or digitally using a CCD camera and typically contains 2 to 5 images of each particle. If the spacing between the particle images in the recording is known, as well as the illumination frequency, local mean velocity vectors can be determined in small areas throughout the illuminated plane, typically giving around 50,000 data points per PIV recording. The technique has been discussed in several review articles including those by Lauterborn and Vogel[68], Adrian[2,116], Dudderar *et al.*[117], Grant[118], Hesselink[69] and Buchhave[119]. A compendium of significant papers related to PIV is also available, edited by Ian Grant[120].

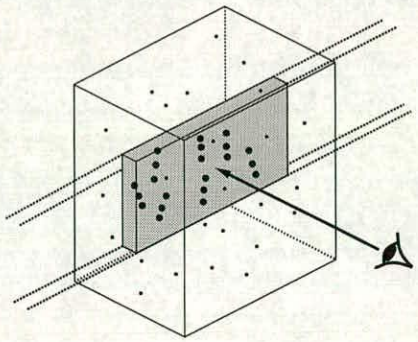


Figure 2.5: A pulsed light sheet illuminating a section of fluid.

A classification of the various "PIV" techniques was proposed by Adrian[2] and will be adopted here. Although there is a tendency to refer to the technique in general as *Particle Image Velocimetry* it falls into the broader category of *Pulsed Light Velocimetry*. The first division of *Pulsed Light Velocimetry* is between techniques that use *molecular markers* and those that use *particulate markers*. This work is involved with the latter branch, which is sub-divided into *speckle pattern methods* and *particle image methods*. Again, the latter branch is divided into techniques giving recordings with low

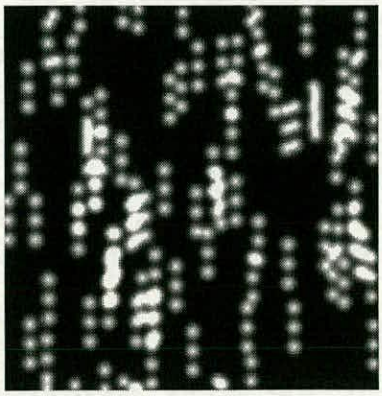


Figure 2.6: A typical high image density PIV recording of a flow.

image densities, often referred to as *particle tracking velocimetry*, and those giving high image density recordings, referred to as *particle image velocimetry*.

As discussed by Adrian[2], for large seeding densities, the images in the recording overlap and phase differences between the images of different particles produce a random interference pattern known as laser speckle[121]. Velocity measurements with such recording densities are referred to as laser speckle velocimetry, or LSV. The speckle pattern associated with groups of particles is roughly constant and can be used to trace the motion of the fluid.

For very low seeding densities, particle images are unlikely to overlap and the series of images recorded are small in length compared with the distance between seeding particles. This implies that individual images are easily identified. As the number of images is small it is possible to track the paths of individual particles. This is usually termed particle tracking velocimetry, or PTV.

Between these two extremes lie recordings in which the image density is too low to give speckle but in which there are enough images to make particle tracking prohibitively time consuming. The displacement of groups of images is measured instead, in a similar way to measuring the speckle displacement in LSV. This mode of operation is referred to as high-image-density PIV.

Adrian's notation[2] will be used wherever possible in the following discussion.

2.2.3 Early development of LSV and PIV and the Young's fringe analysis technique

The PIV technique has its origins in the pioneering work of Willis and Deardorff[122], Barker and Fourney[123], Grousson and Mallick[124],and Dudderar and Simpkins[125]. Willis and Deardorff[122] used the technique with low seeding particle concentrations and manually digitised the coordinates of particle centres to determine inter-image spacings. The illumination was arranged to give an initial particle streak to determine the direction of motion of the fluid: an issue that will be discussed in more detail later. Barker and Fourney[123], Grousson and Mallick[124], and Dudderar and Simpkins[125] applied speckle analysis methods[121,126–132], previously used almost exclusively to study surface motion, to their photographic recordings. The LSV recording was analysed by illuminating a small section of the negative with a parallel beam of monochromatic light. A converging lens is placed after the negative and a series of Young's fringes are observed in the back focal plane of the lens, as shown in Figure (2.7).

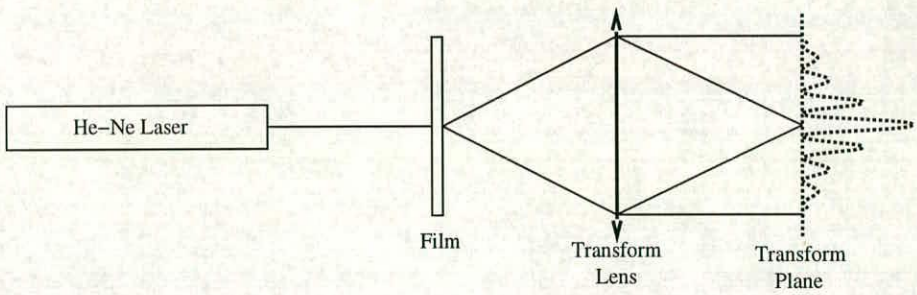


Figure 2.7: A schematic of a typical fringe analysis system.

Young observed that for waves originating from two points sources an interference pattern is observed and that if the waves from the point sources are in phase, or coherent, then a particular interference pattern is produced, as shown in Figure (2.8). The solid and dashed lines represent the maxima and minima of the emitted waves. Where maxima associated with the waves originating from the different sources meet there is constructive interference. Where maxima and minima meet there is destructive interference. When observations of the wave amplitude are made in a plane parallel to the line separating the two point sources a series of maxima and minima are observed. The spacing of the maxima, Δy, is governed by the wavelength of the waves, λ; the

separation between the two point sources, a; and the distance to the observation plane, s. The relationship[133] is given below. It can also be shown that the maxima and minima ideally follow a cosine squared form.

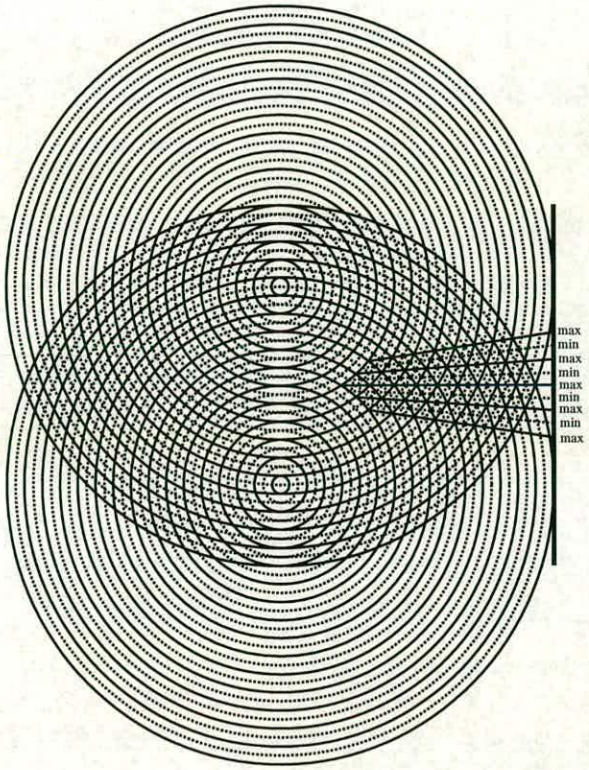


Figure 2.8: The interference pattern produced by coherent waves from two point sources - Young's experiment.

$$\Delta y = \frac{s}{a}\lambda \tag{2.3}$$

When a small section of a PIV image is illuminated with coherent light each pair of images produces an interference pattern similar to that described above. Most image pairs are oriented at random and produce diffraction patterns oriented at random. However, in the flow direction the interference pattern from each double image of a seeding particle produces an identical, or very similar, interference pattern. As the number of image pairs is increased these diffraction patterns constructively interfere and become increasingly distinct compared with the background interference pattern. It is this overall pattern that is observed in the optical analysis if PIV images. The period

of the fringes is related to the mean velocity vector in the illuminated area by equation (2.4) with the orientation of the fringes normal to the direction of the mean fluid motion, assuming that the velocity is both spatially and temporally constant over the illuminated area. The negative is usually mounted on a computer controlled translation stage to select the analysis area. All three groups of early investigators[123–125] proved the technique in steady, laminar pipe flows, obtaining good agreement with theory.

$$\Delta X = \frac{\lambda f}{M|\mathbf{v}|T} \tag{2.4}$$

where ΔX is the fringe spacing normal to the fringes (m), λ is the wavelength of the illumination (m), f is the focal length of the lens (m), $|\mathbf{v}|$ is the magnitude of the mean velocity in the analysis area (m/s), T the time between illumination pulses (s), and M the magnification of the PIV recording.

Iwata *et al.*[134], Ewan[135], and Meynart[136] applied the technique in more complex situations, for example in convection driven flows and spray atomisers. Baker *et al.*[137] were the first workers to investigate the accuracy of the technique by recording particles fixed to a rotating drum. The velocity vectors produced were within 2-3% of the expected values. The streaming velocities of biological samples were also measured to within $\pm 10\%$ of the values determined using optical microscopy.

Kaufmann[132] was the first to consider the effect of the diffraction halo[138] on the accuracy of fringe location. The pattern seen in the transform plane is the diffraction halo modulated by a pattern of equally spaced, cosine square fringes. The diffraction halo introduces a small shift in the location of fringe maxima. Kaufmann showed that measuring the spacing of fringe minima, as opposed to fringe maxima, reduces the error by half; although other errors, for example, those associated with lens aberration, remain the same. It was suggested that "dividing out" the diffraction halo or using a Fourier transform based analysis of the fringes would remove the effect of the diffraction halo. A similar "dividing out" procedure was suggested by Georgieva[139]. This was investigated by Kaufmann *et al.*[140] who used a linear photo detector array, attached to a potentiometer for angle measurement, to analyse the fringe pattern.

Perpendicular to the fringe direction the fringe spacing was recorded and parallel to the fringes the diffraction halo was recorded. The first results were then divided by the second to remove the diffraction halo and a fast Fourier transform (FFT) routine used to determine the fringe spacing. A 1D theoretical analysis of the diffraction halo was carried out by Kaufmann[141] who concluded that the 1D FFT technique could be used without dividing out the diffraction halo.

Following this work, Meynart[142] described the difficulties involved with obtaining experimental and theoretical measurements of the diffraction halo due to the non-Gaussian statistics of the speckle produced by a small number of independent particles. A "cepstrum" technique was proposed that involved the Fourier transform of the logarithm of the 1D digitisation of the fringe pattern but this gave a significant decrease in the signal-to-noise ratio. Alternatively, the use of windowing techniques in calculating Fourier transforms was suggested. The proposed methods were used in an unsteady gas flow to measure velocities over 1 m/s[143,144] and to estimate vorticity, calculated using a difference scheme, with an uncertainty of 15% of the maximum vorticity[136]. Robinson[145] digitised the fringe pattern and used an automated system to obtain the fringe orientation and averaged the fringe data parallel to the fringes. Meynart[146] highlighted a problem seen in several derivations of theoretical predictions for the diffraction halo, for example, that given by Yamaguchi[147], and gives the correct analysis. He also comments that the correct theoretical expression is subject to inaccuracy as it does not take into account the non-linear response of the photographic film. Pedestal removal, that is, removing the effects of the diffraction halo, was also addressed by Pickering and Halliwell[148] in a similar manner.

Erbeck[149] calculated the 1D cross correlation function along directions at 45^o and used these six results to give the fringe orientation and spacing. Collicott and Hesselink[150] used a novel anamorphic optical processor to measure one component of the flow along a line in the recording: a method for producing velocity profiles. Other automated procedures for determining the fringe spacing and orientation were discussed by Pickering and Halliwell[151], and Kirita *et al.*[152]; and reviewed by Kirita *et al.*, [153] and Huntley[154]. It can be concluded from these works that the 2D FFT transform of

the fringe pattern, to give the auto-correlation function of the illuminated region of the photograph according to the Wiener-Khinchin theorem[155], gave the lowest random error in the mean displacement and produced more reliable results when only a small number of fringes were present, compared with the methods already mentioned. Kim[156] was very critical of the methods used to remove the diffraction halo and from a detailed analysis believes that although such methods are attractive they do not take into account the complexity of the problem. The effect is an arbitrary modification of the speckles from the specklegram. Kim recommended the use of 2D FFT processing to yield the auto-correlation function. It was also suggested that corrections could be made to reduce the effects of velocity gradients on PIV measurements and that the measurement of small displacements will be affected by the diffraction halo if they are less than one speckle diameter.

Alternative analysis techniques were proposed by Takai and Asakatura[157] and by Adrian and Yao[158]. The latter involved taking a 2D image of the analysis area and projecting all the points in two orthogonal directions, thus compressing the amount of information and decreasing the amount of processing time required to analyse the image.

Pickering and Halliwell[159] considered the effect of photographic film noise in fringe patterns due to variations in film thickness and refractive index. These effects, as might be expected, were more important for faster films. The phase noise from varying film thickness was removed using a liquid gate[160]. In a further refinement, it was proposed that a positive transparency be produced from the original recording. Analysis of this positive recording gave fringes with an improved signal-to-noise ratio[161], in agreement with earlier theoretical predictions[162].

Compensation for the diffraction halo in speckle photography has recently been reported using a negative mask - a negative of the diffraction halo used as a density filter at the observation plane. A similar method is investigated for improving the fringe quality produced in PIV investigations by Ganesan *et al.*[163]. The new method is compared with the contact print approach and gives a greater number of fringes and sharper

peaks in the auto-correlation function. This increases the maximum magnitude of the velocities that can be measured. The combination of the negative mask method with contact printing gave further improvements[163].

Iwata *et al.*[134] were the first to comment on the decrease of fringe visibility as the velocity gradient over the analysis area increases. The results of Pearson *et al.*[164] show velocities underestimated where velocity gradients are significant and the degradation of fringe quality with turbulence. Related to this is the proposal by Hinsch *et al.*[165] that any spatial variation in velocity should be correlated with the fringe pattern. This was realised in the work of Arnold and Hinsch[166] who related fringe visibility with turbulence, although the turbulence levels measured using this technique were higher than those obtained by hot-wire anemometry. Erbeck and Merzkirch[167] report similar conclusions. Later, Grant and various co-workers[168,169] made turbulence estimates to within 10% of those measured using other techniques using a similar correlation with fringe visibility.

Other factors affecting the accuracy of the PIV technique were noted during this developmental period, and will be covered in detail in later sections. Jacquot and Rostig[170] considered the effect of out of plane motion when studying solid surfaces and proposed a stereo-scopic technique to resolve all three components of the direction of motion. Meynart[171] was the first to consider the optimum number of particle pairs that should be contained in an interrogation area and suggested this to be between 5 and 20.

Experimental applications of the technique over this development period, not already mentioned, include: Binnington *et al.*[172,173] who studied laminar fluid flow and concluded that the scope for application of the technique to non-Newtonian flows was great; Bernabeu[174] who studied convection driven flows; Kaufmann[175] who used double pulsed white light speckle velocimetry for fluid flow measurements; Gartner *et al.*[176] who studied the motion of an internal gravity wave; Pearson *et al.*[164] who studied the motion in a simplified gas jet; Meynart[177] who studied buoyancy driven recirculation; and Kawahashi and Hosoi[178] who studied the flow in a water channel.

2.2.4 Seeding particles

Seeding particles must follow the motion of the flow, that is they must be neutrally buoyant or have an insignificant slip velocity. The maximum slip velocity may be calculated using Stoke's equation (2.5) (valid for $Re < 2$) as the particle sizes are generally small.

$$u_t = \frac{g\, d_p^2\, (\rho_p - \rho_f)}{18\, \mu} \tag{2.5}$$

where u_t is the slip velocity in m/s, d_p is the particle diameter in m, ρ_p is the particle density in kg/m^3, ρ_f is the density of the fluid in kg/m^3, and μ is the viscosity of the fluid in Ns/m^2.

Adrian[2] derives the result given in equation(2.6) for the slip velocity between a seeding particle and the fluid as a function of the acceleration of the particle. This applies to non-interacting particles and ignores the added mass of the fluid, unsteady drag forces, pressure gradients, and non-uniform fluid motion. These assumptions are valid for heavy solid or liquid particles used to seed a gas flow.

$$|\mathbf{v} - \mathbf{u}| = \sqrt{\frac{2}{3}\frac{\rho_p}{\rho}\frac{d_p}{C_D}|\dot{\mathbf{v}}|} \tag{2.6}$$

where $\mathbf{v}$ is the particle velocity (m/s), $\mathbf{u}$ is the fluid velocity (m/s), ρ is the fluid density (kg/m^3), ρ_p is the particle density (kg/m^3), d_p is the particle diameter (m), C_D is the drag coefficient, and $\dot{\mathbf{v}}$ is the particle acceleration (m/s^2).

Equation(2.6) simplifies to equation(2.7) when the particle Reynolds number is much less than 1.

$$|\mathbf{v} - \mathbf{u}| = \frac{\rho_p d_p^2 |\dot{\mathbf{v}}|}{36\rho\mu} \tag{2.7}$$

The equation of motion for a small rigid sphere in a non-uniform flow, including the terms excluded in the previous result, was given by Maxey and Riley[179] and the behaviour of solid particles in turbulent flows have been simulated by Brown and Hutchinson[180]. This, and other work, has been used by Lim *et al.*[4] in determining the macro-scales of turbulence which seeding particles may be expected to resolve. The result is given in equation (2.8).

$$\frac{d_p}{\Lambda} = \left[\frac{u'\Lambda}{v}\left(\frac{\rho_p}{\rho} + \beta\right)\right]^{\frac{1}{2}} \tag{2.8}$$

where v is the kinematic viscosity of the fluid (m^2s^{-1}), Λ is the macro-scale of the turbulence (m), u' is the rms velocity fluctuation (m/s), and β is given by

$$\beta = 1 + \frac{\rho}{2\rho_p} \tag{2.9}$$

Solving for Λ:

$$\Lambda = \frac{v\,\rho\,\rho_p\,\sqrt[3]{2}\left(\dfrac{d_p\,u'\left(2\,{\rho_p}^2 + 2\,\rho\,\rho_p + \rho^2\right)}{v\,\rho\,\rho_p}\right)^{2/3}}{u'\left(2\,{\rho_p}^2 + 2\,\rho\,\rho_p + \rho^2\right)} \tag{2.10}$$

Dadi *et al.*[181] compared a linearised model and a pseudo-linear empirical model for particle motion with experimental results. The linear model is valid when the relative motion of the particle and fluid is small, as above, and the pseudo-linear model for particle motion when the relative Reynolds number ($Re = |\mathbf{u} - \mathbf{v}|\,\frac{d\rho}{\mu}$) is greater than one but not very large. For relative Reynolds numbers up to 40 the pseudo-linear model gave a good representation of reality; and for Reynolds numbers below one, little difference between the two models was observed.

Agüí and Jiménez[3] also discussed the motion of seeding particles when discussing the performance of particle tracking. Assuming that the density of the seeding particles is similar to the density of the fluid, the expected difference between the fluid velocity and particle velocity was given as equation (2.11).

$$\frac{|\mathbf{v}-\mathbf{u}|^2}{|\mathbf{u}|^2} \approx 1.8 \times 10^{-2} \left(\frac{\rho_p}{\rho} - 1\right)^2 \frac{\omega_0}{v} d_p^2 \tag{2.11}$$

where ω_0 corresponds roughly to the lowest turnover rate of the large eddies in the flow (Hz).

The scattering power of seed materials was discussed by Adrian and Yao[182–184]. The smallest particles that can be photographed were determined for both air and water by Mie scattering calculations. Using Kodak Technical Pan 2415 film, a range of apertures and light of wavelength $\lambda = 0.6943\ \mu m$: polystyrene particles of diameter, $d_p \approx 10\ \mu m$, were recommended for use in water; and oil or glass particles of diameter, $d_p \approx 5\ \mu m$, for use in air. Adrian[183] showed that seeding particles with a diameter less than 1 μm exhibit Rayleigh scattering (expected when $d_p \ll \lambda$), where the scattered light intensity is proportional to d_p^4 and the recorded image diameter is given by the point response function of the recording optics. For seeding particles above 10 μm in diameter, geometric scattering is observed (expected when $d_p \gg \lambda$) where the scattered light intensity is proportional to d_p^2 and the size of the recorded image is proportional to d_p. For seeding particle sizes in the range 1 and 20 μm, transitional scattering behaviour is expected, the scattered light intensity is proportional to d_p^2 but the image diameter is largely independent of d_p. It was also shown, as expected, that the scattered light intensity depends on the ratio of the refractive indices of the fluid and seeding material, although comparisons between different fluids and seeding materials were found difficult.

A wide range of seeding materials have been used by different researchers. Of note are seeding materials with their scattering properties enhanced by metallic coatings, available through Birral in the UK, and the hollow glass micro-spheres manufactured by

Potter's Ballotini Ltd (UK) that have more than one surface from which light may be scattered. A silver coating procedure for hollow glass spheres is described by Schmitt *et al.*[185]. Careful selection of the density and size range of the starting material and the amount of silver deposited on the surface of the spheres can be used to generate seeding particles with an appropriate density range tailored for a particular application. For a more detailed analysis of scattering from small particles refer to van de Hulst[186], Adrian[2], and Grant[120].

2.2.5 Illumination

The light sheets used in PIV investigations are typically generated from coherent light sources using expanding optics, and a mechanical or electro-optical chopper if the light source is continuous[2]. An optical fibre beam delivery system was considered by Anderson *et al.*[187] and demonstrated to be a safe way to guide the output from high powered lasers to a beam expansion system at an experimental rig. A small number of researchers have used white light sources[170,175,188] suitably collimated, to take speckle photographs of flow fields or when using encapsulated liquid crystals as the seeding material[189].

The use of a rotating, polygon mirror illumination system is becoming more common and has several advantages over the conventional optical train, which are discussed by Gray *et al.*[190]. The light beam from a laser is directed onto a rotating, polygon mirror producing a light sheet that is collimated through a reflection in a parabolic mirror: similar results can be produced using an oscillating mirror. These and acousto-optical beam deflection techniques are compared by Rockwell *et al.*[191]. The conventional and rotating mirror systems are shown in Figures (2.9) and (2.10), respectively.

As Gray *et al.*[190] conclude for continuous emission lasers, the rotating mirror system can increase the energy available for exposing the particles, typically by a factor of 20, as all the laser energy is available for illumination, compared with a small fraction when using an optical chopper. Particle images are illuminated by a shorter, higher intensity, light pulse compared with the conventional technique; this ensures that the particle

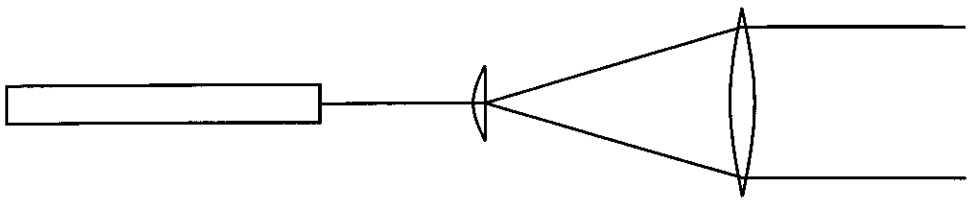


Figure 2.9: A light sheet generated by expanding a collimated light source with a diverging lens and a second collimating lens.

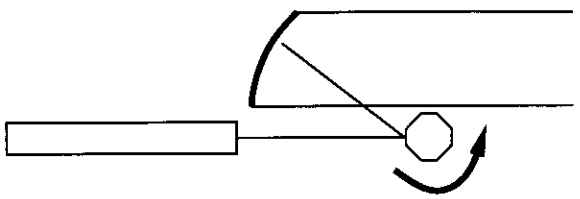


Figure 2.10: A light sheet generated by a rotating mirror and collimating parabolic mirror

motion is frozen and blurred images are less likely. For a particular application, the scanning technique allows the use of lower power lasers, the investigation of higher speed flows or the illumination of larger areas of the flow. A light sheet of even intensity can be produced; in contrast to a light sheet that retains the Gaussian intensity distribution of the source beam using the conventional method. This avoids the over exposure of particles in the centre of PIV recordings and under exposure at the edges.

A novel extension to the rotating mirror system was used by Post *et al.*[192]. The multi-line output from an Argon ion laser was dispersed and the prominent green (512 nm) and blue (488 nm) lines selected to make two colour PIV recordings using a single laser. This resolves the directional ambiguity inherent in some forms of the PIV technique that will be discussed later. The two coloured beams may be offset slightly and the colour intensity used to define the third component of velocity[193].

2.2.6 Recording parameters

The PIV image may be recorded onto photographic film or digitally using a CCD. In both cases a lens with minimal distortion and flat focal field is required to introduce

as little aberration as possible into the recording.

Adrian[2] discusses the relationship between the diameter of the seeding particles, d_p, and the particle image diameter, d_e. The approximate formula for the image diameter is given in equation (2.12) below.

$$d_e = \sqrt{M^2 d_p^2 + d_s^2 + d_r^2} \tag{2.12}$$

where M is the recording magnification, d_s the diameter of the point response function of the recording optics, and d_r is the resolution of the recording medium. d_p, d_e, d_s, d_r should all be in metres. d_s is given by:

$$d_s = 2.44(1 + M)f^{\#}\lambda \tag{2.13}$$

where $f^{\#}$ is the f number of the recording optics (dimensionless) and λ is the wavelength of the light source (m).

The previous two results are valid when the particle is within the depth of field of the recording optics, δz, given by

$$\delta z = 4\left(1 + \frac{1}{M}\right)^2 f^{\#2}\lambda \tag{2.14}$$

Outside this range, the particle image is blurred by an amount exceeding 20% of the in-focus diameter[2].

Film

Recordings made on photographic film require subsequent processing. This may include the development of the film, the production of a contact print to increase fringe

EX BIBL. UNIV. EDINBURGEN

Film	ASA No	Resolving Power lines/mm
Technical Pan	50	125-320
T-Max 100	100	63-200
T-Max 400	400	50-125

Table 2.1: The resolving power of various films

visibility[160–162], and possibly the production of prints. Negatives and prints can be transformed into digital images for computer-based analysis using commercial scanners. The flatbed scanners available have optical resolutions in the range 300-1200 dots per inch and the negative scanners in the range 600-2700 dots per inch, although this technology is still under rapid development. A wide range of film is available for which the manufacturers provide data sheets. The quality and nature of the negatives and prints produced depend greatly on the processing stages and chemicals used and the manufacturers' guidelines should be followed. For example, see the Kodak publications regarding T-Max[194] and Technical Pan[195] films.

The spectral sensitivity curves for Kodak T-Max 100, Kodak T-Max 400 and Kodak Technical Pan are shown in Figures (2.12,2.13,2.11). The sensitivity of most panchromatic black and white films, like the T-Max films, tails off between 600 and 650 nm making these films suitable for green, blue or white light sources. The spectral sensitivity curves show that the Technical Pan films should be used for red light sources. The speed of the film does not affect the shape of the curve significantly.

Lourenco[196] compares KODAK Technical Pan 2415 and KODAK Royal X Pan for recording PIV images noting that the sensitivity for the latter declines beyond 620nm making this film unsuitable for He-Ne illumination (633 nm). Workers using red light sources have tended to use KODAK Technical Pan 2415[197–199].

The resolving power of various films is given in Table (2.1) where the information is taken from the manufacturers' data sheets. A 35 mm negative can resolve around 5000 lines assuming a 25mm image and 200 lines/mm.

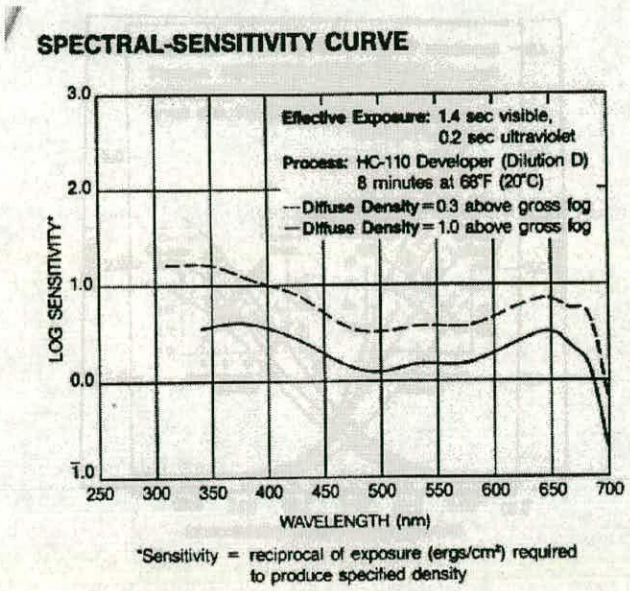


Figure 2.11: The spectral sensitivity curve for Kodak Technical Pan. (Reproduced with permission)

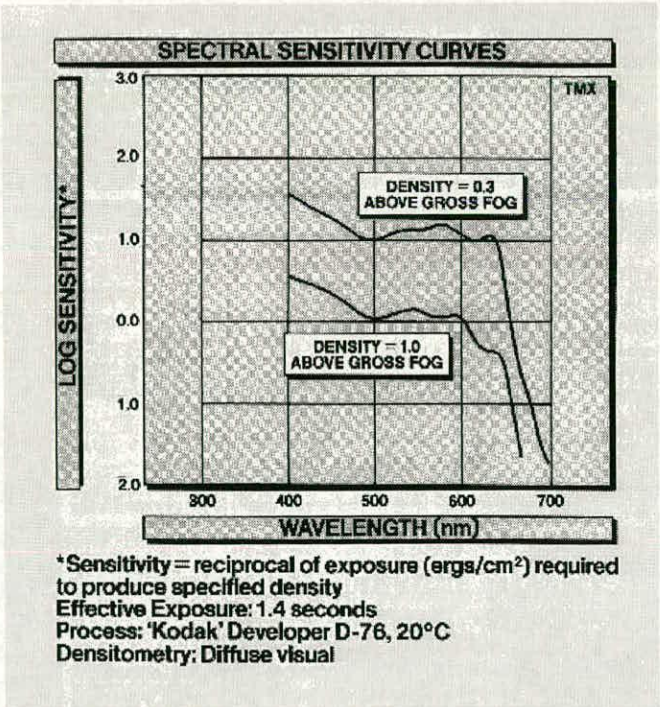


Figure 2.12: The spectral sensitivity curve for Kodak T-Max 100

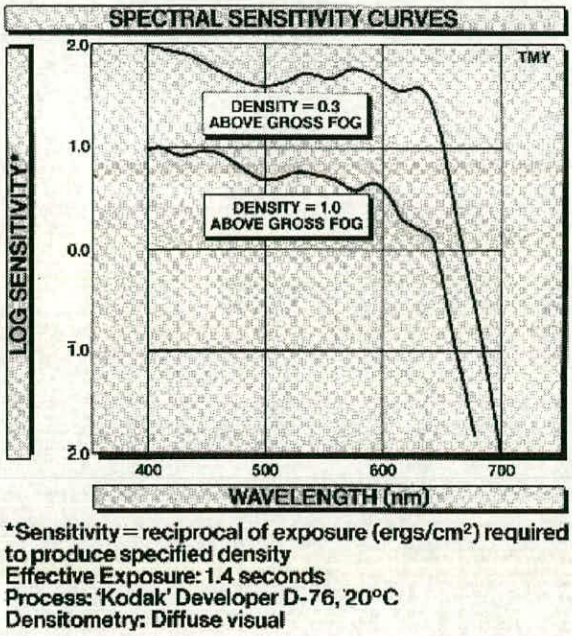


Figure 2.13: The spectral sensitivity curve for Kodak T-Max 400

CCD

Some PIV researchers have moved away from film recordings to use CCD cameras. This removes the time consuming photographic processing stages and can give "online" PIV data. CCD cameras with a resolution of 512 by 512 pixels are readily available and can achieve frame rates comparable with videos. Modest frame grabbers give an image resolution of 768 x 576 pixels with 8 bits per colour associated with each pixel. As the array size is increased the frame rate rapidly decreases. A modern CCD stills camera producing a 2000 x 3000 pixel image with 12 bits per colour can record around one frame per second[200]. CCD cameras are ideal for recording a series of single frames which can be analysed by cross-correlation, resolving the direction of motion of particles. For example, Westerweel *et al.*[201] described the use of a digital PIV system with a resolution of 1000 x 1000 pixels capable of recording 10 frames per second. Issues related to image digitisation are discussed later as they also apply to the digitisation of negatives, photographs, and the Young's fringe patterns produced by conventional analysis systems as well as to CCD based PIV recordings. Image intensifiers have also

been used to make PIV recordings with cheap, low intensity light sources[202].

2.2.7 The analysis of PIV recordings

Distribution of particles and images

It is useful to define several dimensionless groups that characterise PIV recordings and analysis, after Adrian[2]. The source density, N_s, as defined in equation(2.15), is the mean number of particles in a cylindrical volume defined by the illuminating light sheet and by projecting a particle image back to this plane from the recording plane. If two particles are contained within this volume their images must overlap on the recording, that is, large values of N_s will produce speckle-like PIV recordings. Small values of N_s imply that it is unlikely that images overlap and the probability of finding k particles within the volume is approximately $\frac{N_s^k}{k!}$.

$$N_s = C\ \Delta z_o\ \frac{\pi d_e^2}{4M^2} \tag{2.15}$$

where C is the mean number of particles per unit volume (particles/m^3), Δz_o is thickness of the light sheet (m), and the other terms are as previously defined.

It is also useful to define the number of particles, N_I, within the interrogation cell used for analysing the PIV image. If the interrogation cell has a diameter of d_I, then equation (2.16) defines N_I.

$$N_I = C\Delta z_o \frac{\pi d_I^2}{4M^2} \tag{2.16}$$

If $N_I \ll 1$ then the probability of finding more than one particle in an analysis area is small, corresponding to the low image density mode of PIV. When $N_I \gg 1$ the

interrogation spot will, on average, contain a large number of particle images and it is unlikely that any analysis area will contain no particle images.

Adrian[2] goes on to define the data density, N_λ, as the number of particles contained in a volume with a characteristic length based on the Taylor micro-scale, λ_T; see equation (2.17). Adrian estimates N_λ in the form of equation (2.18), and also defines the ratio of the mean spacing between samples of the flow field, $\overline{r}$, and the Taylor micro-scale, see equation (2.19). If $N_\lambda \gg 1$, implying high sampling rates, then turbulent structures will be spatially well resolved and the calculation of derived quantities from the velocity field is meaningful.

$$V_\lambda = C\lambda_T^3 \tag{2.17}$$

$$N_\lambda = \frac{4M^2\lambda_T^3}{\pi\Delta z_o d_I^2} N_I \tag{2.18}$$

$$\frac{\overline{r}}{\lambda_T} = \frac{0.55}{\sqrt[3]{N_\lambda}} \tag{2.19}$$

Optical/Digital - Digital/Digital analysis techniques

Fully digital processing of PIV recordings is the logical extension of the Young's fringe analysis technique. The initial optical transform of the image is equivalent to the discrete Fourier transform of the image multiplied by its complex conjugate. The result can be inverse transformed to give the auto-correlation function in the same way that the fringes may be captured via a video camera, digitised and transformed. A digital PIV image may be obtained by scanning a PIV negative, scanning a print made from a PIV negative, recording using a digital camera, or capturing and image from a CCD camera using a frame grabber.

According to the "Correlation theorem"[155], for real functions, the Fourier transform of the correlation between functions of the same variables is equivalent to the Fourier transform of one function multiplied by the complex conjugate of the Fourier trans-

form of the second function. In addition, the "Wiener-Khinchin theorem" states that the Fourier transform of the correlation of a function with itself, its autocorrelation, is equivalent to the square of the modulus of the Fourier transform of the function. Adopting the notation of Press *et al.*[155]:

$$g(k_1, k_2) \iff G(n_1, n_2) \tag{2.20}$$

$$h(k_1, k_2) \iff H(n_1, n_2) \tag{2.21}$$

$$Corr(g, h) \iff G(n_1, n_2)H(-n_1, -n_2) \tag{2.22}$$

$$Corr(g_{real}, h_{real}) \iff G(n_1, n_2)H^*(n_1, n_2) \tag{2.23}$$

$$Corr(g, g) \iff |G(n_1, n_2)|^2 \tag{2.24}$$

where g and h are complex functions and G and H their respective Fourier transforms; $\iff$ is used to indicate transform pairs; * is used to indicate the complex conjugate; and the subscript *real* used to indicate real functions. For real functions, $H(-n_1, -n_2) = [H(n_1, n_2)]^*$.

The correlation of two functions, g and h, denoted by $Corr(g, h)$ is defined by

$$Corr(g(k_1, k_2), h(k_1, k_2)) = \int_{-\infty}^{\infty} \int_{-\infty}^{\infty} g(k_1 + \tau_1, k_2 + \tau_2) h(\tau_1, \tau_2) d\tau_1 d\tau_2 \tag{2.25}$$

As the digitised PIV image represents discrete data the correlation of two discrete, real functions is given by

$$Corr(g(k_1, k_2), h(k_1, k_2)) = \sum_{m=-\infty}^{\infty} \sum_{n=-\infty}^{\infty} g(k_1 + m, k_2 + n) h(m, n) \tag{2.26}$$

$$Corr(g(k_1, k_2), h(k_1, k_2)) = DFT^{-1} \left(DFT\left(g(k_1, k_2)\right) DFT\left(h(k_1, k_2)\right)^* \right) \tag{2.27}$$

where DFT represents a Digital Fourier Transform and DFT^{-1} its inverse.

For an image of N pixels by M pixels, the direct calculation of the discrete correlation function requires a time proportional to N^2M^2. Whereas, the calculation of the correlation function using the properties of the discrete Fourier transform requires a time proportional to $3NM\log(NM)$ to determine the cross-correlation and a time proportional to $2NM\log(NM)$ to determine the auto-correlation, as discussed by Nussbaumer[203]. The transform method is usually used to calculate the correlation function to reduce the amount of computational time required. Improvements in computational speed can be obtained by calculating real Fourier transforms or using complex Fourier transforms to carry out two real transforms simultaneously. Alternatively, real transforms, such as the Hartley transform[204–214] can be used to calculate the correlation function using equivalent transform identities.

When using the auto-correlation technique, that is correlating an image with itself, the average displacement within an analysis area is found by locating the highest peak in the auto-correlation function, excluding the central self-correlation peak. The auto-correlation function has 2-fold rotational symmetry centred on the self-correlation peak which is the origin of the directional ambiguity associated with this technique. The cross-correlation function does not include a self-correlation signal and the correlation function is asymmetric. This implies that the direction of motion can be determined uniquely and that smaller displacements can be measured as the signal peak (now the highest peak) does not interact with a central self-correlation peak.

The signal peak is often initially located by finding the pixel with the highest value (excluding the central peak if present) in the correlation function. A sub-pixel estimate of the position is produced by calculating the centre of mass[215,216] as defined below.

$$E(\mathbf{X}) = \frac{\int_{A_1} \mathbf{x}R(\mathbf{x})\,d\mathbf{x}}{\int_{A_1} R(\mathbf{x})\,d\mathbf{x}} \tag{2.28}$$

where $E(\mathbf{X})$ is the expected value of the signal peak displacement, $\mathbf{x}$ is the location of a pixel element in the correlation function, $R(\mathbf{x})$ is the value of the correlation function at $\mathbf{x}$, and A_1 is an area defined in such a way as to include only the signal peak.

The area used for the estimate always contains some random fluctuations and the estimate of the peak location is inevitably contaminated. Determining the area to use is a non-trivial problem that has received little attention in the literature.

Alternatively, the position of the signal peak is estimated by the least squares fit of a function around the pixel used as the first estimate of the peak location. This is usually a parabolic or Gaussian[217] function. The signal peak is expected to be Gaussian[218] if the particle image has a Gaussian image profile on the recording media (as shown below for the one dimensional case for two Gaussian functions with the same e^{-1} width of 1, the same normalised intensity, and both centred at the origin). In practice, this result is approximate as a result of the non-linear response of the film and/or digitisation procedure. The correlation peak is broader than the signal peak by a factor of $\sqrt{2}$, ignoring any effects that may arise from the recording media.

$$\int_{-\infty}^{\infty} \frac{e^{-\frac{1}{2}x_1^2}}{\sqrt{2\,\pi}} \frac{e^{-\frac{1}{2}(x_1+x)^2}}{\sqrt{2\,\pi}} dx_1 = \frac{e^{-\frac{1}{2}\left(\frac{x}{\sqrt{2}}\right)^2}}{\sqrt{2}\sqrt{2\,\pi}} \tag{2.29}$$

All Optical Analysis

Optical correlators to interrogate PIV recordings have been proposed by Coupland and Halliwell[219], Wernet and Edwards[220], Kompenhans *et al.*[221], and Farrell and Goetsch[222,223]. All present similar optical methods to calculate the 2-D auto-correlation function directly.

A small section of the PIV negative is illuminated with a low powered laser, as in the Young's fringe technique. However, a hologram of the light amplitude in the Fourier plane of a transforming lens is recorded onto a Bismuth Silicon Oxide crystal using a

reference beam. When the reference beam is switched off the auto-correlation function is produced at the output plane of a second transform lens.

Farrell and Goetsch[223] were the first to apply the proposed technique to an experimental PIV recording. Their correlator had a dynamic range of 30:1; limited at small displacements by the size of the processor's focal spot and at large displacements by the speckle pattern. Coupland and Halliwell[224] applied a similar technique to recordings made of a 2D flow past a step. It was noted that the processing speed would be limited by the speed of the negative translation stage and the time required for the holographic exposure, although several interrogation areas can by processed at once using a system of parallel interrogation beams[225–228].

The performance of these optical correlators has been shown to be similar in cost, accuracy, and speed to the Young's fringe technique followed by digital processing of the fringes using discrete fast Fourier transforms[227,229,230]. The technique has been applied to analyse a range of experimental recordings[229,230]. The popularity of the technique seems to have declined in preference to all digital techniques with recent work limited to optimising the accuracy of the system[231–233].

2.2.8 Errors

Errors arising from experimental considerations

The optimisation of particle image velocimeters has been considered by Keane and Adrian[215,216,234]. A reduction in the number of particle pairs in the interrogation volume may be produced as the particles move out of the illumination plane or out of the interrogation area. For double pulse velocimeters[215], the movement of particles out of the light sheet reduces the signal-to-noise ratio but does not introduce any bias into the location of the signal peak s_D+. In contrast, loss of pairs from particle images tracks that extend outside the interrogation region introduces a velocity bias as the peak is shifted towards zero displacement, see equation (2.30). A similar relationship is found for multi-pulse velocimeters[216]. The error is negligible when $\frac{d_\tau}{d_I} \ll 1$.

$$\mathbf{s_D} + = \frac{M\mathbf{u_1}\Delta t}{1 + \frac{d_\tau^2}{d_I^2}} \tag{2.30}$$

Keane and Adrian showed that an optical Fourier transform from a Gaussian intensity beam profile and subsequent digitisation of the power spectrum followed by an inverse Fourier transform gave a signal peak with a diameter $\sqrt{2}$ times greater than that which would have been produced by direct calculation of the auto-correlation function. (The signal peak was located at the same position.)

Monte-Carlo simulation techniques were used to determine the effect of the relative displacement $\frac{|\Delta x|}{d_I}$, the particle image density, N_I, the detectability, D_o, and the relative out-of-plane motion, $\frac{w\Delta t}{\Delta z_o}$, on the valid detection probability. The detectability, D_o, is the ratio of the height of the signal peak to the height of self correlation peak in the autocorrelation function. (2.2.10). The conclusions are summarised in the recommendations below.

When strong velocity gradients are present in the analysis area the signal peak is broadened and its amplitude diminished[215,216]. For a simple shear flow the peak is broadened in the direction of shear. A local rotation, centred at the centre of the analysis area, gives equal broadening of the signal peak in all directions. In both cases the centroid of the signal peak is biased towards the lower velocities (gradient bias) and detection is less likely amongst the noise peaks as the signal peak intensity is reduced (detection bias). The dimensionless velocity gradient, $\frac{M|\Delta\mathbf{u}|\Delta t}{d_\tau}$, is related to the theoretical decrease in the signal peak amplitude by a factor of $\sqrt{1 + \left(\frac{M|\Delta\mathbf{u}|\Delta t}{d_\tau}\right)^2}$. The PIV simulations indicated that the dimensionless velocity gradient should be less than one. Care should be taken to avoid confusion over different definitions of the dimensionless velocity gradients, the denominator may be defined as d_τ, d_p, or $|\Delta\mathbf{x}|$.

For double pulsed velocimeters the following criteria were recommended:

1. the mean number of image pairs in the interrogation area, N_I, should be greater

than fifteen, ($N_I > 15$);

2. the magnitude of the maximum displacement should be less than or equal to a quarter of the characteristic length of the interrogation area ($\frac{|\Delta \mathbf{X}|}{d_I} \leq 0.25$) to give an RMS error in the measured displacement of less than 0.8% of the interrogation area diameter;

3. the maximum out of plane displacement should be less than one quarter of the width of the illuminating light sheet ($\frac{|w|\,\Delta t}{\Delta z_o} < 0.25$);

4. The magnitude of the maximum variation of the image displacement over the interrogation area should be less than one twentieth of the characteristic length of the interrogation area ($\frac{M\,|\Delta \mathbf{u}|\,\Delta t}{d_I} < 0.05$);

5. The detectability should be in the range 1.2 to 1.5 ($1.2 < D_o < 1.5$).

The performance of multi-pulsed velocimeters[216] was shown to be optimised using largely the same parameters except that N_I is replaced by N_p, the mean number of particle image pairs in the interrogation area, given by $N_I(n-1)$, where n is the number of pulses used to make the PIV recording. The detectability criterion may be relaxed for multi-pulsed systems and a value of $D_o = 1.2$ was recommended.

A more detailed assessment of the appropriate conditions can be made by referring to the results given by Keane and Adrian[215,216] with the characteristics of a particular flow field in mind. The optimisation of cross-correlation based velocimeters is also considered by the same authors[234]. Huang *et al.*[235,236] and Jambunathan *et al.*[237] present improved cross-correlation methods that take into account the presence of velocity gradients within the analysis area. This is done by deforming the second image to make the particle spacing constant across the analysis area.

Errors arising from digitisation and methods for locating the signal peak

Willert and Gharib[218] were the first to consider the effects of making digital PIV recordings and how these influenced the analysis procedure. They state that Nyquist

sampling criterion[155] (associated with the discrete Fourier transforms) implies that the maximum measurable displacement is half the characteristic size of the analysis area, and is normally found to be one third to one quarter of this value in practical applications[215,216,218,238]. Also, the spatial resolution of the technique can be no better than double the step size between analysis areas[218]. In addition, when the particle image size is less than about two pixels (measured as the e^{-2} diameter) the estimated particle separation is biased towards the values given by the nearest integer value to $\frac{\Delta X}{d_{pix}}$ due to under-sampling of the correlation function[239]. The accuracy of the method used to locate the position of the signal peak is obviously affected by the discrete sampling of the correlation function produced as a result of digitisation. In particular, the appropriate area of the correlation function to use for centre-of-mass based centroiding techniques is difficult to determine and the accuracy of curve fitting techniques depends on an appropriate choice of the fitted function: again it is stated that the signal peak is expected to have an approximately Gaussian shape[218].

Prasad *et al.*[239] considered the effect of the resolution to which PIV recordings are digitised on the speed and accuracy of the interrogation process. Test photographs were produced by translating and rotating black carbospheres glued onto a glass plate and then making the appropriate contact prints from the negatives. When the velocity gradient in the analysis area was negligible, parabolic and Gaussian curve fitting methods gave rms errors in the signal peak location half those found when using the centroiding technique. This is in contrast to the earlier work by Keane and Adrian[215,216] where centroiding was shown to be an appropriate estimator for peak location. However, this work conceded that the estimator would be affected by noise around the signal peak and did not assess the performance of other peak location methods. This confirms the advice offered by Willert and Gharib[218], that a Gaussian fit to the signal peak gives a better estimate of the signal peak location.

The high quality of the PIV recordings used by Prasad *et al.* is shown by the small percentage, 0.5%, of bad vectors. This, along with the absence of velocity gradients in the images, allows the authors to consider that noise in the digitised image arises only from the pixel resolution, the digitisation procedure, random errors from irregular

particles, film grain, and other sources discussed in the previous section. To compare different digitisation resolutions a 1 mm square from the PIV recording was captured using a CCD camera; depending on the magnifying optics, this area was captured at four resolutions: 256x256 pixels, 128x128 pixels, 64x64 pixels, and 32x32 pixels. The particle image size was $\approx 60\mu$m, implying that the ratio of the image size to the pixel resolution, $\frac{d_\tau}{d_{pix}}$, was equal to 15.4, 7.7, 3.8, and 1.9, respectively. The results from the translation images produced little variation with digitisation resolution. However, for the solid body rotation, when a top-hat distribution function would be expected for one component of the velocity, the measurement displacement histogram showed undulations with a period equal to the pixel separation, and the sides of the distribution were not as sharply defined as expected. The 256x256 and 128x128 analysis areas performed equally well.

The effect of inadequate pixel resolution was referred to as *mean bias error* and the effect of irregular particle sizes, electronic noise, etc, referred to as *random error*[239]. Random error was found to be independent of the pixel resolution but the bias error increased rapidly at the 32x32 digitisation resolution. In agreement with earlier predictions, the time required for the analysis of different sized analysis areas was proportional to $NM\log(NM)$. An experimental investigation of turbulent flow in a channel ($d_\tau = 35\mu$m, and again a 1 mm square analysis area) gave very similar velocity profiles when analysed using 256x256, 128x128, and 64x64 pixel areas. The rms error associated with the velocities determined by the smaller analysis size were approximately double those produced from the two larger sizes.

As discussed by Prasad *et al.*[239], bias error arises when the pixel resolution, $\frac{d_\tau}{d_{pix}}$, is inadequate: there is a discrepancy between the true image of a particle and the position calculated from the pixel information in the recording. In the limit, as $\frac{d_\tau}{d_{pix}}$ tends towards zero, the maximum possible bias error in locating the centroid of a particle is half the pixel spacing ($\pm\frac{d_{pix}}{2}$). A similar effect is produced when locating the signal peak in the correlation function; if the peak is poorly resolved its position will be biased towards the nearest grid point to $\frac{\Delta X}{d_{pix}}$. The bias error is sizeable when $\frac{d_\tau}{d_{pix}} \leq 2$. The bias errors reported here are for the centroid based peak location

method; the bias produced from curve fitting techniques would reflect the deviation of the signal peak from the expected Gaussian profile.

Prasad *et al.*[239] reported after Adrian[2], that the random error would be expected to be proportional to the image diameter, d_τ.

$$\text{Random error} = c\, d_\tau \tag{2.31}$$

where c is a constant of proportionality that depends on the interrogation method, the peak location technique, the irregularity of images, film grain noise, etc. It is reported in the range 0.05 to 0.07

Random errors are generally much larger than bias errors and a practical recommendation to minimise the overall error suggests that $\frac{d_\tau}{d_{pix}}$ should be approximately equal to 2. When $\frac{d_\tau}{d_{pix}} < 4$ the mean bias error is significant, but is negligible for higher resolution, and there is no advantage in using higher resolutions.

Meinhart *et al.*[240,241] describe an experimental application of a digital PIV system meeting the above requirements. A 1320 x 1035 pixel CCD camera was used to perform cross correlation on the images produced from a turbulent pipe flow. Typical image diameters on film recordings of the same flow were approximately 30 μm compared with the square 6.8 μm pixels in the camera. In this application $\frac{d_\tau}{d_{pix}} \approx 4$ and a 1 mm square analysis area with a resolution of 128x128 pixels was used to calculate the cross-correlation function. An adaptive windowing technique (ie one in which the size of the analysis area is altered in accordance with the local velocity to minimise the total error) was used to optimise the correlation area as the velocity varied over the PIV recording. Any remainder of the interrogation area was padded with zeros before calculating the Fourier transform. A parabolic curve fitting technique was used to estimate the location of the signal peak to sub-pixel accuracy. The parallel architecture used to analyse the images gave 100 128x128 pixel area analyses per second, compared with an estimated peak performance of 160 vectors/second.

Westerweel[242] presented a detailed consideration of the low resolution analysis of

digital PIV images. It was shown that the minimum required sampling rate of the image is of the order of a quarter of that produced by the matching imaging optics. This is of practical consideration as the minimum analysis size gives the minimum analysis time but does not necessarily imply a loss in accuracy of the vectors produced. Bias arising from the sampling of the correlation function and its interaction with the centre-of-mass and Gaussian fit estimators for the signal peak location were compared along with application of Gaussian and top-hat window functions to the analysis area. The Gaussian window function relates to processing using the Young's fringe approach and the second relates to digital analysis. It was stated that the image is under sampled if $\frac{d_\tau}{d_{pix}} < 1$ and over sampled if $\frac{d_\tau}{d_{pix}} > 1$. It was shown that the optimum sample rate is around $\frac{d_\tau}{d_{pix}} \approx 2$, in agreement with Prasad *et al.*[239]. The bias towards integer values of the displacement was also demonstrated, in agreement with earlier work. It was clear from the results and the conclusions that the Gaussian estimator of the signal peak position performed better than the centre-of-mass estimator and that the uniform window function performs better than the Gaussian variant. As an example, the bias in the location of the signal peak from a 32x32 analysis area given an image size $d_\tau = 5.6$ pixels was approximately 0.06 pixels. The estimated fractional displacement when the actual fractional displacement was zero is given below[242].

$$\mathrm{E}(\hat{\epsilon}) \approx -B(m_o, N) \begin{cases} \dfrac{\exp\left(\dfrac{-8}{d_R^2}\right)}{1 + 2\exp\left(\dfrac{-8}{d_R^2}\right)} & \text{for the centre-of-mass estimator} \\ \dfrac{2}{d_R^2} & \text{for the Gaussian estimator} \end{cases} \tag{2.32}$$

$$B(m_o, N) \approx \begin{cases} \dfrac{2}{1 - \dfrac{|m_o|}{N}} & \text{for the uniform window function} \\ \dfrac{16\,|m_o|}{N^2} & \text{for the Gaussian window function} \end{cases} \tag{2.33}$$

where m_o is the actual displacement rounded to the nearest integer, $\mathrm{E}(\hat{\epsilon})$ is the expected value of the measured fractional displacement, $\hat{\epsilon}$ (in this case the actual displacement $\epsilon = 0$), N is the characteristic size of the analysis area, and d_R is the width of the signal peak in the correlation given by $d_R \approx \sqrt{2d_\tau^2 + 4d_{pix}^2}$.

Westerweel[242] predicted the expected fractional displacement for fractional displacements other than zero by computation as the analytical approach is cumbersome. For non-zero fractional displacements the performance of the centre-of-mass estimator gives a discontinuity at $\epsilon = \pm\frac{1}{2}$ which becomes more marked as $\exp\left(\frac{-8}{d_R^2}\right)$ increases: as a result this estimator has a strong bias towards integer values of the displacement. The bias for the Gaussian estimator reduces to zero as the signal peak approaches a Gaussian shape. The Gaussian estimator for determining the location of the signal peak typically introduces a bias of 0.1 pixels as opposed to 0.5 pixels as given for the alternative technique. This is obviously important for low displacements and can have a significant effect on the values of derived quantities. For this reason, the authors recommend the use of the Gaussian fit estimator to determine the sub-pixel location of the signal peak in the correlation function. It was also recommended that the effects arising from any windowing function be corrected before analysis.

The analysis is applied by Westerweel *et al.*[243] to determine the appropriate recording parameters in the investigation of a fully developed turbulent pipe flow using a digital PIV system.

2.2.9 Directional Ambiguity

The auto-correlation analysis of PIV images gives velocity vectors that could be oriented in one of two, opposite directions. That is, the measured velocity is $\pm\mathbf{u}$ as opposed to the actual velocity $\mathbf{u}$. This ambiguity is clear when looking at any PIV recording. Early techniques for resolving directional ambiguity are discussed by Adrian[244]. Directional ambiguity can be resolved in a number of ways:

1. knowing the direction of flow beforehand;

2. recording a series of multiple or single exposure images and using cross-correlation analysis;

3. adding information to the recording to encode the direction of motion (this is referred to as image encoding);

4. imposing a known velocity onto the expected experimental range of velocities to ensure that they are all in one direction (this is referred to as image shifting).

Image encoding techniques

Several image encoding techniques have been proposed and used in PIV investigations. Colour encoding of images has been used by Stefanini *et al.*[245–247], Grant *et al.*[248], and Post *et al.*[192]. The coloured images from different time pulses can be separated and then used in cross-correlation. Reeves *et al.*[249] proposed an alternative technique for labelling the two images in a double pulsed recording. The two light pulses are orthogonally polarised and the images encoded using an "image labelling mask". This modulates the particle image with a series of fringes depending on the polarisation of the illuminating beam. The first and second particle images can be reconstructed and used in a cross-correlation analysis. Directional ambiguity has also been resolved by the introduction of intensity modulation, such as pulse tagging[250–252], and asymmetric time encoding[253]. However, the latter two techniques have been used successfully only in the low image density mode: the asymmetric coding introduces noise into the correlation function when using high image density analysis techniques. A holographic technique was proposed by Coupland *et al.*[254,255]. The images of particles from two illumination pulses are recorded onto a hologram using separate reference beams and can be independently reconstructed and again processed by cross-correlation techniques.

Image shifting techniques

Figure (2.14) shows the range of displacements that can be measured by an arbitrary auto-correlation technique and a range of displacements produced from an experimental

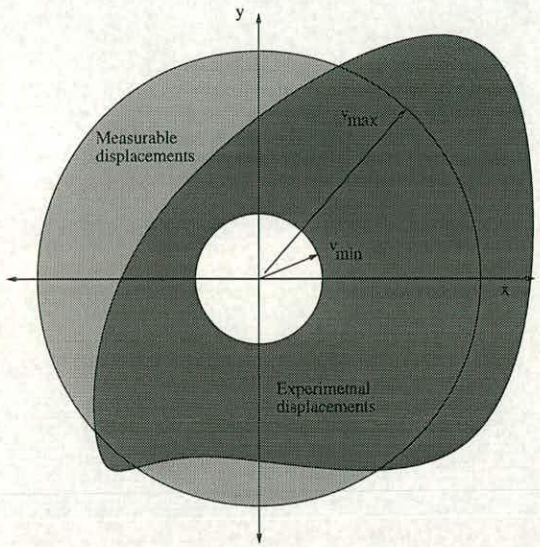


Figure 2.14: The range of displacements recorded and the range of measurable displacements.

investigation. It is clear that there are velocity magnitudes higher than those that can be measured and some below those that can be measured. The magnification and pulse separation can be used to scale the range of experimental displacements recorded but does not address the problem of directional ambiguity or the measurement of small displacements of the order of the recorded particle image size. Image shifting techniques add a known displacement onto the experimental displacements to give analysable displacements of known direction and above the threshold for detection. In combination with the scaling of the range of displacements, the displacements on the recording can be tailored to the analysis technique available, as shown in Figure (2.15).

Image shifting has been performed using a number of techniques including: a rotating mirror system[244,256–263], an electro-optical technique[264], and an optical technique[265,266]. There have been few attempts at image shifting by translating the camera or film (for example in a drum camera). In the first example, a rotating mirror is placed at a distance r from the illuminated plane and between the flow scene and the camera, as shown in Figure(2.16).

The superimposed displacement is given by

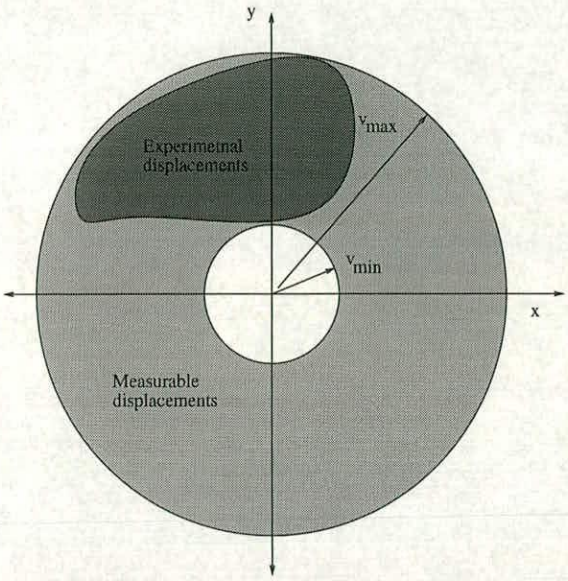


Figure 2.15: The range of measurable velocities and the range of displacements recorded after judicious use of image shifting and choice of recording parameters.

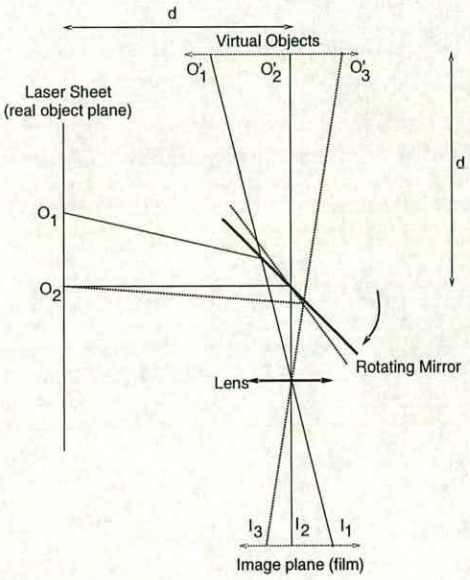


Figure 2.16: The rotating mirror image shifting system. $\overrightarrow{I_1I_2}$ represents the real displacement of the particle images, $\overrightarrow{I_2I_3}$ the superimposed displacement, and $\overrightarrow{I_1I_3}$ the measured displacement

$$\overrightarrow{I_2I_3} = 4\pi f d\Delta t \tag{2.34}$$

where f is the rotation frequency of the mirror (Hz), d is the distance between the mirror and the object plane (m), and Δt is the time between pulse recordings (s). The points and vectors are as defined in Figure(2.16).

However, it should be noted that the focal plane of the camera rotates as the mirror rotates leading to aberration in the images of the seeding particles[261]. Careful setup of the system can minimise the distortion[257] or attempts can be made to correct for the effective variation in superimposed displacement over the recorded image[260,261].

The electro-optical technique uses a birefringent crystal placed before the camera lens to produce differing angles of refraction and images for orthogonally polarised light pulses illuminating the same particle. For a double pulsed PIV recording this produces the required superimposed displacement. However, the shift depends on the thickness of the crystal, which is effectively fixed, and also relies on the light scattered from seeding particles retaining its polarisation, as is usually the case. Again, the imposed shift will change slightly over the recording plane as a result of the finite angle of view[266]. An alternative, purely optical method is reported by Lourenco[266] that produces a constant offset over the recording.

The encoding techniques that allow the separation of images associated with each illumination pulse should be preferred as the results can be analysed using the cross-correlation technique. However, the required recording parameters may not allow for this mode of operation and an alternative method for resolving directional ambiguity may be required. The methods discussed are also difficult to apply in multi-pulse recordings as the aberration increases or the technique relies on two pulses of orthogonally polarised light.

2.2.10 Post Processing

All PIV analysis schemes will produce a number of unrealistic vectors compared with those expected from a given flow field or those in the immediate neighbourhood[267]. The results of any PIV analysis requires some scheme to remove these invalid vectors and then a mechanism of interpolating or extrapolating to estimate the removed

vectors[268]. The resulting vector field is then often used to calculate derived quantities such as vorticity or components of the rate of strain tensor.

Vector validation

Vector validation can be carried out manually but is a laborious and time consuming task because of the number of vectors involved. As a result, several automated validation methods have been developed to minimise or remove any human involvement. Initially, properties of the auto-correlation function were used to validate vectors by recording the relative ratio of the signal peak to the next highest peak in the auto-correlation function. This is the detectability, D_o, as defined by Adrian[2] and given in equation (2.35).

$$D_o = \frac{Height\ of\ signal\ peak}{Height\ of\ next\ highest\ peak} \tag{2.35}$$

Keane and Adrian[215,216] recommend that $D_o > 1.35$ for double pulsed recordings and $D_o > 1.2$ for multi-pulsed recordings. It is also possible to specify that the signal peak be some minimum fraction of the self-correlation peak and to look for harmonic peaks in multi-pulsed recordings. The detectability of valid vectors may be comparable with that of erroneous vectors and implies that some acceptable vectors are deleted[269], for this reason various post-analysis tests and filtering techniques have increased in popularity.

Westerweel *et al.* [270] calculated the average of each component of the eight vectors in the surrounding neighbourhood of a particular vector. If the central vector differed by more than some predetermined value from the average, then the central vector was deleted. This is the same as the "dynamic mean" test discussed by Raffel *et al*[268]. Raffel *et al* also proposed that a global histogram operator be applied before using the dynamic mean test, essentially to reduce outlying vectors. The two components of each vector can be used to define a point on an $x - y$ plot to produce a 2D histogram.

Vectors outside an acceptable area are deleted. This combined method was shown to work better than validation methods based on image processing or on fluid mechanical operators such as the divergence or vorticity/circulation.

Westerweel[267] compared post-interrogation validation schemes based on the global-mean, the local-mean, and the local-median with conventional validation based on the detectability criterion. The conventional method was inefficient compared with the local-median test: the best of those considered. The median for each component of velocity was calculated for a 3x3 neighbourhood, and was shown to be the most robust estimate of the "average" velocity. The central vector is removed if it differs from the local, median vector by more than some predetermined value.

Meinhart *et al.*[269] report a two stage validation process similar to that described above. The initial step is termed "tolerance removal", the mean and standard deviation of each component of velocity are calculated over the whole velocity field and any vector more than 3.5-4.0 standard deviations way from the mean deleted. Poisson statistics indicate that any such vector has less than a 5% chance of being valid. The second stage is to calculate a magnitude difference, M_d, to compare the central vector with the median vector, as suggested by Westerweel[267]. M_d is defined in equation (2.36).

$$M_d = \sqrt{\frac{(u - u_{med})^2}{u_{rms}} + \frac{(v - v_{med})^2}{v_{rms}}} \tag{2.36}$$

where the subscript *med* refers to the median velocity component calculated from a 3x3 array of velocities in a rectangular grid and the subscript *rms* refers to the root-mean-square value of the velocity component considering all the vectors in the flowfield. The median velocity calculation should be modified at the edges of the data as suggested by Westerweel[267].

This is, in effect, the Euclidean or L_2 norm of the normalised velocity components. M_D is compared to two values: a low value below which the vector is reliable and a high value above which the vector is erroneous; between these values the vector is marked as questionable and human intervention is required to assess the validity of the vector.

Westerweel *et al.*[243] extend this process by adding a third stage of validation in which the local median of the fluctuating component of the velocity is also considered.

Hartmann *et al.*[271] use a similar vector median filtering technique, originally proposed by Astola *et al.*[272]; rather than using a test for validation the central vector in a 3x3 neighbourhood is replaced with the vector median of the array. The vector median filter has similar properties to the standard, scalar median filter: a step change is a root signal, edges remain sharp but may move - edge jitter, and values outside the sample can not be introduced into the data. Edge jitter arises when considering each component of the velocity independently and calculating the median for each, rather than selecting a median vector. This has a marked impact on filtering, and for example, may move the position of shock waves, but is unlikely to introduce any significant error into a validation scheme. The vector median is defined below using the L_2 norm, represented by $\|.\|_2$, and defined by $\|x\|_2 = \sqrt{x_1^2 + x_2^2}$.

The vector median, x_{VM}, must be one of the vectors $x_1 \ldots x_N$ and is chosen to minimise the sum of the L_2 norms of the vectors formed by subtracting the median vector from each vector. Formally stated below:

$$x_{VM} \in \{x_i | i = 1 \ldots N\} \tag{2.37}$$

such that for all $j = 1 \ldots N$

$$\sum_{i=1}^{N} \|x_i - x_{VM}\|_2 \leq \sum_{i=1}^{N} \|x_i - x_j\|_2 \tag{2.38}$$

In filtering applications an extended vector median filter may be defined to replace the central vector with the local average vector if the sum of the L_2 norms of the other vectors with the average vector subtracted is less than the sum of the L_2 norms of the other vectors with the median vector subtracted[271,272].

Interpolation

There are many interpolation and extrapolation schemes as demonstrated by those available in the NAG numerical libraries[273] and detailed by Press *et al.*[155]. A number of the techniques that have been popular in interpolating missing data in PIV vector fields have previously been used in interpolating the results from particle tracking and particle streak velocimetry onto a regular grid. For example, Imaichi and Ohmi[274] interpolated the data from streak investigations onto a regular grid by a local least squares fit of the velocity components to the equations below.

$$u_k = u + \frac{\partial u}{\partial x}\xi_k + \frac{\partial u}{\partial y}\eta_k \tag{2.39}$$

$$v_k = v + \frac{\partial v}{\partial x}\xi_k + \frac{\partial v}{\partial y}\eta_k \tag{2.40}$$

where u, $\frac{\partial u}{\partial x}$, $\frac{\partial u}{\partial y}$, v, $\frac{\partial v}{\partial x}$, and $\frac{\partial v}{\partial y}$ are determined by a least squares fit over an appropriate neighbourhood of data points.

Jiménez and Agüí[275] considered a similar reconstruction of randomly sampled data, again important for presenting the results of fluid mechanical measurements on regular grids, and in particular to ease the calculation of derived quantities. Low order polynomial interpolation gave comparable or better performance with respect to non-adaptive convolution methods using a smoothing window.

Spedding and Rignot[276] compared two interpolation techniques: adaptive Gaussian windows (AGW) and thin shell Splines (STS). In particular, the effect of the interpolation method on the value of vorticity calculated using a finite difference scheme was considered. STS gave errors approximately half those for the AGW technique. This was explained as the difference between a simple, implicit *ad hoc* smoothing applied by the AGW technique, and the smoothing akin to viscous effects associated with the STS technique. STS performed better in reducing the mean and local error in both velocity and vorticity.

However, weighted spatial averages, such as that used by Meinhart *et al.*[269] are commonly quoted as interpolation methods or smoothing filters. Wang *et al.*[277] have shown that weight function interpolation schemes may be better suited to the interpolation of real PIV data compared with other techniques. Real PIV images were processed and validated, a varying number of vectors deleted at random, and the performance of two point linear interpolation, higher order polynomial interpolation, spline based interpolation, Newton's bivariate interpolation, least squares interpolation, and weight function interpolation compared.

For scattered data Wang *et al.*[277] quote a common form for the interpolation function $F(x, y)$, given by

$$F(x,y) = \frac{\sum_{h=1}^{m} W_h(x,y) f_h}{\sum_{h=1}^{m} W_h(x,y)} \tag{2.41}$$

where $W_h(x, y)$ is the weight function evaluated at one of the data points, (x, y) the location of individual data points f_h compared to the position of the point at which interpolation is required, and m is the number of data points.

The weight function is normally defined in terms of a distance between the interpolation point and each data point, D, such that

$$D = \sqrt{(x - x_h)^2 + (y - y_h)^2} \tag{2.42}$$

where (x_h, y_y) is the location of an individual data point.

The weight function can take many forms, but in general gives a greater weighting to local data, such as the inverse square form, $W_h(x, y) = D_h^{-2}$ or the exponential (or

Gaussian) form, $W_h(x,y) = \exp\left(-\frac{D^2}{4E}\right)$, where E is an experimental constant. Both methods were found to perform well by Wang *et al.*[277], although the effect of the interpolation scheme on the estimation of derived quantities was not considered.

It remains to be demonstrated which of STS and weight function interpolation is more appropriate for interpolating experimental PIV data and to quantify the effect the interpolation schemes have on the calculation of derived quantities.

Filtering and smoothing

The vector median filter described previously can be used to replace erroneous vectors with the local median or local mean vector. It is common to smooth the validated vector field with a Gaussian kernel, for example that used by Hartmann *et al.*[271] is given below. The effect is that of a low pass spatial filter that smoothes out noise arising from the peak location method, film grain, etc. Westerweel *et al.*[270] used a Gaussian function with a width at the half maximum height equal to half the size of the interrogation region in a similar smoothing process.

$$\frac{1}{16}\begin{pmatrix} 1 & 2 & 1 \\ 2 & 4 & 2 \\ 1 & 2 & 1 \end{pmatrix} \tag{2.43}$$

Derived quantities

It is common to calculate vorticity using either finite difference schemes[18,217,218,270,274] or by numerically estimating the local circulation and making use of Stoke's theorem to estimate the vorticity[17,258,278,279]. For normal PIV recordings only the out of plane vorticity, ω_z can be calculated, or ω_θ in axisymmetric situations. Both are defined below.

$$\omega_z = \frac{\partial v}{\partial x} - \frac{\partial u}{\partial y} \tag{2.44}$$

$$\omega_\theta = \frac{\partial u_r}{\partial z} - \frac{\partial u_z}{\partial r} \tag{2.45}$$

The first is typically calculated using a second order central differencing scheme as reported by Lourenco and Krothapalli[217], as shown below.

$$\left(\frac{\partial v}{\partial x} - \frac{\partial u}{\partial y}\right)_{x,y} = \left(\frac{v^*_{j+1} - v^*_{j-1}}{2\Delta x} + \Delta x^2 \Re + \frac{\varepsilon}{\Delta x}\right) - \left(\frac{u^*_{i+1} - u^*_{i-1}}{2\Delta y} + \Delta y^2 \Re + \frac{\varepsilon}{\Delta y}\right) \tag{2.46}$$

where the in-plane velocity components, $\mathbf{u}(u, v)$ are measured as u^* and v^* with ε equal to the absolute error in the velocity measurement, and $\Re$ representing higher order terms. $u^* = u + \varepsilon$ and $v^* = v + \varepsilon$

This formulation emphasises the two sources of error: the truncation of the finite differencing scheme, of order $(\Delta x^2, \Delta y^2)$; and the absolute error in the velocity, ε, of order $(\frac{1}{\Delta x}, \frac{1}{\Delta y})$. Lourenco and Krothapalli[217] observed that this implies the existence of an optimum grid spacing that minimises the total error. It is also only possible to obtain meaningful estimates of the vorticity if ε remains small. An iterative scheme based on Richardson's extrapolation method[217,280], was demonstrated. Initially a coarse grid is used for the calculation of vorticity so that the truncation error is much greater than the error associated with the PIV measurements. The grid is refined until the errors arising from the two sources are comparable. The performance of this scheme showed a significant improvement over a simple differencing scheme, with further improvements observed by using a least squares second order polynomial fit to the velocity data in order to estimate the spatial derivatives of the velocity. This method could be applied to any derived quantity calculated using a finite difference scheme.

The alternative method for estimating the vorticity at a point requires that the circu-

lation, Γ, be evaluated around a closed contour surrounding that point, as presented by Landreth *et al.*[17].

$$\Gamma = \oint \mathbf{u}\, d\mathbf{l} \tag{2.47}$$

Stokes' theorem is then used to relate the circulation per unit area to the out-of-plane component of the vorticity at the required point.

$$\omega_z = \lim_{A \to 0} \frac{\Gamma}{A} \tag{2.48}$$

The closed contour is usually defined by the eight points surrounding the point where the local vorticity is required. After Landreth *et al.*[17] for a grid equally spaced in the x and y directions,

$$\begin{aligned} \omega_z(i,j) = \frac{\Delta l}{(2\Delta l)^2} \Bigg\{ & u_{(i,j-1)} + \frac{1}{2}\left(u_{(i+1,j-1)} + v_{(i+1,j-1)}\right) \\ & + v_{(i+1,j)} - \frac{1}{2}\left(u_{(i+1,j+1)} - v_{(i+1,j+1)}\right) \\ & - u_{(i,j+1)} + \frac{1}{2}\left(u_{(i-1,j+1)} + v_{(i-1,j+1)}\right) \\ & - v_{(i-1,j)} + \frac{1}{2}\left(u_{(i-1,j-1)} - v_{(i-1,j-1)}\right) \Bigg\} \end{aligned} \tag{2.49}$$

where Δl is the spacing between grid points, and the subscript (i,j) refers to the grid location of a node.

Abrahamson and Lonnes[281] fitted a local model velocity field using a least squares technique. The model field included components to represent uniform translation, rigid rotation, plane shear, and a point source. This was then used to estimate the vorticity.

A vector field produced from a direct numerical simulation was used to compare this method with the method based on calculating the circulation. Both methods were found to spatially filter the vorticity field. Overall, the circulation method performed better than the least squares method and they produced the greatest error under the same conditions - where the vorticity is a minimum or maximum. It should be noted that application of a smoothing algorithm will tend to reduce the maximum velocity gradient and hence lead to an underestimate of the maximum vorticity.

It is also possible to calculate components of the rate-of-strain tensor, e_{kl} using finite difference techniques as shown below for e_{11}, after Landreth *et al.*[17].

$$e_{11(i,j)} = \frac{1}{2\Delta l}(u_{(i+1,j)} - u_{(i-1,j)}) \tag{2.50}$$

Utami and Ueno[18] also calculated turbulence statistics, Reynolds stress, and divergence ($e_{11}+e_{22}$). Westerweel *et al*[270] also used a finite difference technique to estimate e_{33}. Imaichi and Ohmi[274] used numerical schemes to estimate the relative pressure and the stream function.

The correlation of fringe visibility with turbulence has already been mentioned[134,166–169,282]. Liu *et al.*[283] used a line averaging technique to determine turbulent statistics in a channel flow and compared the results with LDV measurements and numerical simulations. Westerweel *et al.*[270] concluded from PIV simulations that PIV analysis can only be expected to resolve large scale turbulent motions, those at least double the size of the spatial resolution of the PIV analysis area. However, the application of a low pass filter gave reasonable results at smaller scales. Large scale structures have been measured by Utami *at al.*[18], McCluskey *et al.*[284], and Liu *et al.*[283], amongst others.

Hinsch *et al.*[285] suggest that peak deformation observed in the auto-correlation function could be used for turbulence estimation; comparing the width of the central peak, $2\sigma_0$, with the width of the signal peak, $2\sigma_1$ (both measured at e^{-1} of the peak height),

to give an estimate of the RMS variation in the measured displacement across the interrogation area, σ_d. The expected relationship is given by equation (2.51).

$$\sigma_d^2 = \sigma_1^2 - \sigma_0^2 \tag{2.51}$$

This approach should be used with caution as peak broadening may also occur from loss of pairs as particles move out of the analysis area and as a result of velocity gradients within the analysis area[215,216]. It may be more appropriate to fit Gaussian profiles to the central and signal peaks and compare the results to estimate turbulence or to confirm that the time between illumination pulses is small enough to resolve time dependent flow features.

2.2.11 Related techniques

Particle Tracking - Summary

Particle tracking is an alternative technique for analysing flow visualisation recordings made with low seeding densities. Particle images may be a series of individual images held on consecutive recordings[4,286–292], a series of images held on a single recording[4,293–296], or a pattern of dots and streaks held on a single recording[275,297–301]. The methods used for determining the velocities in the last case are often application dependent, but the analysis of the of the first two recording methods can be summarised as follows:

1. if the recording was not made digitally, transfer the the image to a digital format;
2. thresholding and gradient techniques are used to identify individual particles;
3. the centroids of the identified particles are located;
4. an algorithm is used to determine particle trajectories.

For example, Hassan and others [4,286–292] use a predictor corrector method. A particle in the first frame is identified, a search area is identified in the second frame considering the likely velocities in the flow. Particles within this region form potential tracks. Each potential track is used to predict the particle position in the third frame, the track is valid if a particle is found within certain tolerances of the predicted point, see Figure (2.17). This can be continued for a large number of frames[302].

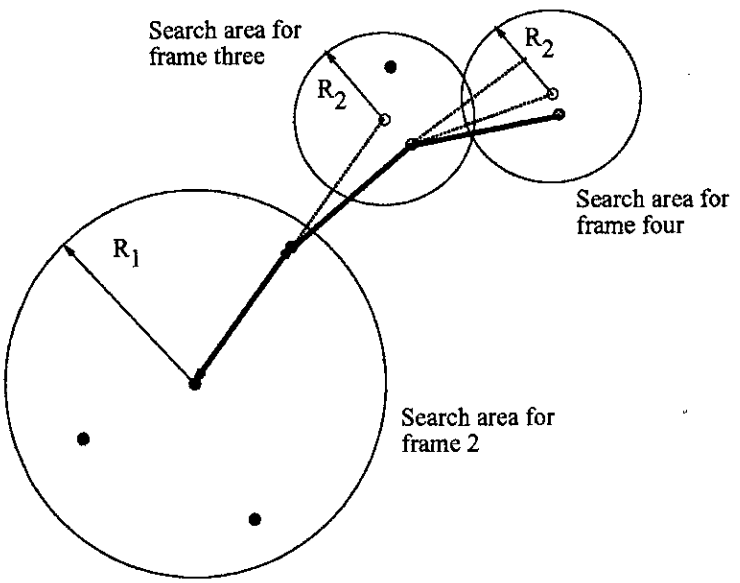


Figure 2.17: Particle tracking: black images are in the first frame, red in the second, blue in the third and purple in the fourth.

The accuracy of the technique is discussed by Agüí and Jeménez[3], Wernet[288], and Wernet and Pline[291]. The error in the measured velocity arises from the errors in locating the particle positions and the time interval between recording frames. In particular, Wernet and Pline[291] compare the merits of particle tracking and cross-correlation. The errors of individual velocities produced from PTV are higher than those for the cross-correlation technique, but if the individual tracks are averaged over the interrogation area a better average velocity is obtained. PTV can show features smaller than the interrogation area and will work well in the presence of velocity gradients or where particle image intensities vary. Cross-correlation analysis will perform better when there are high noise levels in recordings. It will also be more efficient when the seeding density makes particle identification and tracking difficult because of overlapping images, the number of particle images to process, and an increasing

number of possible tracks that become more difficult to verify. Advances in the cross-correlation technique now give a much better performance in the presence of velocity gradients[235–237]. Dalziel[303] used an alternative particle tracking algorithm . An objective function with a cost associated with potential matchings is minimised to follow all the seeding particles between images. If two or more differing views of particle tracks are recorded then the technique can be extended to three dimensions[304–315]. The particle locations are found by matching particle images in the recordings. The use of particle tracks, rather than individual images can make this matching procedure more reliable.

The application of neural networks to analysing PIV and PTV images has been investigated be Cedenese and Romano[316], Grant *et al.*[251], Derou and Herault[317], and Grant and Pan[252]. In each case a relatively low seeding density was used giving a small number of seeding particles to consider in each interrogation area: these methods present an alternative to the more popular predictor-corrector approach outlined above. The analysis system presented by Grant and Pan[252] was able to determine the direction of motion from tagged PIV images, and for the recording made, performed better than the statistical analysis in simulated turbulent and rotating flows.

Stereoscopic PIV

Stereoscopic PIV has been proposed by a number of authors[248,311,318–321]. The work of Arroyo and Greated[318] may be considered typical and will be considered here for simplicity. It is customary to use two cameras with their optical axes normal to a laser light sheet and the film in each camera aligned in the same plane, although other configurations can be used. The two cameras record the motion of the same seeding particle slightly differently, as a result of their different positions, from which it is possible to determine the third component of the velocity. The error in the out-of-plane displacement is found to be approximately three times that typical for the in-plane displacements. The accuracy of the out of plane velocity component increases with the distance between the two cameras, this is limited by the aperture of the lens: lens aberrations limit the angle of view. This often leads to a requirement to

use low apertures, and as a result, high power illumination sources. In this case[318], the stereoscopic images were recorded on the same negative using a series of mirrors, once setup the correlation between the two images is straight forward. The technique, although proven, has seen little experimental application.

Holographic PIV

Several schemes for making holographic PIV-like recordings have been proposed[135,269,319,322–331]. In each case a holographic recording of the seeding material was made to obtain a velocity field from a probe volume and to determine all three components of the velocity vector.

Hinsch *et al*[331] recorded information in several illumination planes with separate reference beams. Moritatis and Buchhave[330] present an optical method for processing double exposure seeded flowfield holograms. Grant *et al.*[319] compare stereoscopic PIV and stereo-holographic techniques. Bryanston-Cross *et al.*[323] used a holographic technique to measure all three velocity components within a 2 mm illuminated sheet of a flow.

Of particular note, Coupland and Halliwell[324,325] demonstrated that 3D velocity data could be extracted from double exposure PIV holograms and observed that the use of different reference beams would allow analysis using the cross-correlation method. A photographic technique was used to demonstrate the real time optical correlator proposed for analysing the holographic recordings. Barnhart *et al.*[322] and Meinhart *et al.*[269] presented a holographic technique that allows the reconstruction of 2 images in each of two directions that can be analysed using cross-correlation techniques and the results used to infer all three components of velocity. This method was applied to the flow in a channel to produce the first measurements of all three velocity vectors over an illuminated volume. An alternative approach is demonstrated by Gray and Greated[328] who use a CCD camera on a translation stage to scan interrogation volumes reconstructed at two different time intervals using two reference beams. Cross-correlation techniques were then used to process the data.

2.3 Discussion

Much of the work required to establish PIV as a powerful quantitative flow visualisation technique has been completed. However, there are some applications for which the PIV recordings require analysis using the auto-correlation approach and these recordings may contain analysis areas within which there are appreciable velocity gradients. It would be useful to have a technique to correct for such velocity gradients, along the lines of that used to correct for similar effects in cross-correlation analysis. This is likely to be of particular importance in applying the PIV technique to study the flows around artificial heart valves where the presence of significant velocity gradients is to be expected. As yet, the problem of deforming the analysis area to correct for velocity gradients in the analysis of multi-pulse PIV recordings has not been addressed.

One approach to allow for the presence of significant velocity gradients might be to perform particle tracking within conventional PIV analysis areas, after conventional PIV analysis, to improve the spatial resolution. The results of conventional analysis are used to reduce the search area for a second particle image compared with the usual approach for particle tracking. This allows particle tracking to be used to analyse recordings with a higher seeding density than is normally practical. Keane and Adrian[332] show that this can give an improvement in the spatial resolution of no more than the square-root of the effective number of particle pairs, $\sqrt{(N_P)}$. In the example presented in their work the spatial resolution was improved by a factor of 2.5 for recordings in which $N_P = 10$. It was proposed that the sub-interrogation spot particle tracking technique only be carried out where estimates of the velocity gradient indicate that the resolution and accuracy of conventional PIV analysis may not be sufficient. As such, this procedure is only practical for the digital analysis of PIV recordings and bears some relation to the mesh refining techniques common in CFD applications.

It is also unclear how validation schemes, interpolation and extrapolation schemes, smoothing and spatial filtering, and the calculation of derived quantities interact. To assess some of these interactions and to validate the performance of an analysis system a method to simulate a range of PIV recordings would be useful.

A major role of PIV, and other techniques, is to provide the supporting experimental evidence to validate the results from numerical simulations, which is already in evidence in the investigation and understanding of turbulent channel flow.

The potential application of the PIV technique to study the flows around prosthetic heart valves and in validating CFD simulations of such flows is obvious. In particular, a quantitative flow visualisation technique such as PIV, allows the assessment of the cycle-to-cycle variation of the flow; and the estimation of derived quantities such as the wall shear stress, the vorticity, the local deformation rate and some components of the rate-of-strain tensor, and consequently viscous dissipation. It is the near instantaneous nature of the technique that could make it so useful in such an application. It may be possible to record sequential PIV images to improve the calculation of the RBDI, discussed in the first section of this literature review. Of particular interest in optimising the fluid dynamic performance of prosthetic valves, areas of recirculation are easy to identify, as are the locations of separation and reattachment points. It may even be possible to make crude residence time measurements with particles on the same scale as blood components to asses their convective mass transport as the concentration of light scattering particles should be related to the self-correlation peak in the auto-correlation function.

It seems that PIV may play a significant role in addressing some of the fluid mechanical factors of heart valve design as discussed by Woo and Yoganathan[99]: tissue overgrowth, material failure, damage to the endothelial lining, haemolysis, leakage, and the opening and closing behaviour of the valve; as all are influenced by the fluid mechanical performance of the artificial valve.

The prerequisites and mechanism of thrombus deposition, from a fluid mechanical view, are still unclear. The work of Christy and various co-workers[1, 26, 64] attempted to link flow structures with clot formation. The application of PIV to characterise the simple flows around bluff bodies appears to be an attractive step to determine any such relationship because of the simplicity of the geometry. Future developments of the PIV technique to produce a variant capable of resolving all three components of velocity

over an illumination volume seem likely. Such a technique would be of greater use in this and other applications both to make experimental measurements and validate CFD predictions.

Chapter 3

Analysis, simulation and developments of the PIV technique

3.1 Introduction

A digital PIV system has been used throughout this study. In this chapter, a range of developments to the PIV technique are discussed along with the errors associated with the particular analysis system used. In order to assess many of the errors and test the reliability and operation of the analysis program, simulated PIV images have been generated. The method for producing these images is also discussed.

Initial PIV investigations of the flow around artificial heart valves indicated the presence of regions containing significant velocity gradients. It was not possible to reduce the bias arising from these velocity gradients or increase the signal-to-noise ratio by manipulating the recording parameters as these were limited by seeding and illumination considerations. To overcome this problem, an iterative approach was developed to deform individual interrogation regions. This reduces the velocity gradient in an analysis area making the particle spacing more uniform thus improving the shape of the signal peak and the signal-to-noise ratio. An integral part of this approach is the automated orientation and validation of the vector fields produced after each analysis

step, which is another topic of discussion in this chapter.

Another development, of importance in the investigation of two-phase flows, concerns the analysis of PIV recordings containing two distinct series of particle images, each associated with a different phase in the flow. This was prompted by the work of D. R. McCluskey *et al.*[333] on particle roping and by Rix *et al.*[334] in studying the free-board region of conventional fluidised beds. There are, however, many other potential applications of methods, similar to those discussed here, in multi-phase flows.

All the algorithms have been implemented in ANSI standard C and have been run under a range of UNIX based operating systems. The raw portable grey map image file format was chosen as the base file format. It is a simple format for which there are many inter-conversion and manipulation routines in existence. For example, see the PBM plus toolkit by Jef Posansker, and the XV display and manipulation program, both available in the "contrib" section of the MIT X distribution that can be obtained from most major FTP sites.

The algorithms for orienting velocity vectors and for correcting the analysis of multi-pulse PIV images containing velocity gradients have been tested both through the use of simulated data, CFD results, and experimental results.

3.2 Simulating PIV recordings

3.2.1 Introduction

PIV recordings were simulated to test the analysis program and the algorithm to correct for velocity gradients within PIV recordings. Simulation was also used to test the algorithm to separate the individual phase information for two-phase flows,

3.2.2 Flows simulated

The simulation program can produce pseudo PIV images for flows with a constant velocity or containing a free, forced or Oseen vortex. This allows a range of simulations' to made including simple steady flows with no velocity gradients and flows containing large velocity gradients. Other flows can be generated by adding a constant velocity to the vortical flow. This feature can alternatively be used as an ideal image shifting system, as in section 3.3. Two-phase flows can be simulated be producing two PIV recordings and combining them together. For example, two PIV images with seeding particles of different sizes may be simulated and then simply added together.

3.2.3 Method

The simulation program allows the selection of the diameter of the particle images, their intensity (in the range 0-255), the number of illumination pulses, and the time between illumination pulses. Particle images are simulated with a Gaussian intensity profile as would be expected from particle images the size of which is determined by the point response function of the recording optics. The seeding density and the number of illumination pulses fixes the number of effective particle image pairs. Over-lapping images are treated by summing the intensity contribution from each particle for a given image pixel. If the resulting intensity is over the maximum it is rounded down to the maximum. This results in behaviour similar to that observed when saturation is reached on photographic film. The simulated particles are modelled as ideal; that is, they are perfectly spherical, neutrally buoyant, and show no slip relative to the flow.

An initial, randomly located, seeding particle image is generated. The position of the seeding particle is then calculated at the next illumination pulse, given the flow field to be simulated. An image of the seeding particle is then generated at this new position in the flowfield. This process is repeated for the required number of illumination pulses and the chosen number of seeding particles to give recordings characteristic of particular seeding densities in real PIV recordings.

The effect of turbulence can be introduced assuming the same Gaussian distribution for the fluctuating part of both components of the velocity by selecting a turbulence intensity to apply across the simulated image. In practice, the location of the seeding particle is adjusted relative to the calculated particle's position according to a normal distribution determined by the turbulence parameters. Two phase flows can be modelled by simulating each phase independently and combining the resultant PIV images.

The radial component of velocity, u_r, is zero for all the simulated vortical flows. The azimuthal velocity, u_θ, is defined as follows for no vortex, a forced vortex, a free vortex, and an Oseen vortex:

$$u_\theta = 0 \tag{3.1}$$

$$u_\theta = \Omega r \tag{3.2}$$

$$u_\theta = \frac{\Gamma}{2\pi r} \tag{3.3}$$

$$u_\theta = \frac{\Gamma}{2\pi r}\left(1 - e^{-(\frac{r^2}{4vt})}\right) \tag{3.4}$$

where u_θ is the axial velocity in pixels/s, Ω is the angular velocity associated with the forced vortex in rad/s, r is the distance from the centre of the vortex in pixels, Γ is the circulation associated with a free or Oseen vortex in pixels^2/s, v is the kinematic viscosity of the fluid in pixels^2/s, and t is the time in seconds.

For particle images with a Gaussian intensity distribution, pixels within the simulated particle image are assigned an intensity equal to the average over the pixel as given below. This is similar to the integrating effect of a single pixel in a CCD element.

$$I = I_{max} \int_{x-\frac{1}{2}}^{x+\frac{1}{2}} \int_{y-\frac{1}{2}}^{y+\frac{1}{2}} e^{-\frac{(x_c-x)^2}{s^2} - \frac{(y_c-y)^2}{x^2}} dydx \tag{3.5}$$

or

$$
\begin{aligned}
I \;=\; & +\frac{\pi}{4}s^2\mathrm{erf}\left(\frac{y_c-\frac{1}{2}-y}{s}\right)\mathrm{erf}\left(\frac{x_c-\frac{1}{2}-x}{s}\right)I_{max} \\
& -\frac{\pi}{4}s^2\mathrm{erf}\left(\frac{y_c-\frac{1}{2}-y}{s}\right)\mathrm{erf}\left(\frac{x_c+\frac{1}{2}-x}{s}\right)I_{max} \\
& -\frac{\pi}{4}s^2\mathrm{erf}\left(\frac{y_c+\frac{1}{2}-y}{s}\right)\mathrm{erf}\left(\frac{x_c-\frac{1}{2}-x}{s}\right)I_{max} \\
& +\frac{\pi}{4}s^2\mathrm{erf}\left(\frac{y_c+\frac{1}{2}-y}{s}\right)\mathrm{erf}\left(\frac{x_c+\frac{1}{2}-x}{s}\right)I_{max}
\end{aligned}
\tag{3.6}
$$

Particles with an approximately constant intensity profile can be produced by setting the maximum intensity to a value much greater than 255, effectively generating saturated images. The simulation does not include noise arising from the out-of-plane motion of seeding particles although this could be included along with a Gaussian profile for the illuminating beam.

Sample simulations are shown in Figures (3.4,3.15, and 3.25).

3.3 Analysis system

3.3.1 Introduction

The digitisation of PIV images has been carried out using two methods. Initially, A4 photographic prints were made from PIV negatives and transformed into digital format using an HP Scanjet Plus flatbed scanner. The scanner has an optical resolution of 300 dots-per-inch. This gives a maximum image size of approximately 3500 by 2500 pixels for a maximum negative size of 35 by 24 mm. This allows particle images recorded on the film with an image diameter of 20 μm be digitised with $\frac{d_\tau}{d_{pix}} \approx 2$, meeting the criteria given by Prasad *et al.*[239] and consistent with the image sampling rate as discussed by Westerweel[242]. In later work, a Nikon Coolscan colour negative scanner

was used to digitise PIV recordings direct from the photographic negative. As before, the 2700 dpi resolution of this scanner allows particle images on the negative with a diameter of 20 μm to be adequately resolved according to the same criteria. For both digitisation systems, the scanner was attached to a networked PC to allow the images to be transferred onto a network of SUN workstations, where the images are converted to the appropriate image format and analysed.

3.3.2 The analysis of digital PIV images

The analysis program has undergone continual development over the duration of the project. Initially, the digital images from the flatbed scanner were transformed to a binary image using a simple thresholding technique and then analysed using a binary algorithm to calculate the autocorrelation function[20]. This approach allows the centre of the correlation peak to be located to within one quarter of a pixel (Lourenco - private comment and discussion at Euromech Colloquium 279, Delft, Holland). The increasing power of the workstations available to perform the analysis has made this approach unnecessary. The autocorrelation function can now be calculated using single or double precision real fast-Fourier transforms; and the cross-correlation function by using double precision complex Fourier transforms. The direct calculation of the correlation function is also possible but computationally inefficient. The transform routines are adapted from the two dimensional transform given by Press *et al.*[155]. All 256 grey scale levels are retained for the calculation. The size and spacing of the analysis areas can be selected; the size is rounded up to the nearest integer power of two for computational convenience, any additional space is padded with zeros, as is conventional[155,240,241]. The relative size of the padded area to the analysis area may also be selected. This removes so called "wrap around pollution" as the convolution theorem and transform calculations assumes that the input data is periodic and infinitely repeating. The minimum amount of padding in pixels should be equal to the position of the displacement peak plus the peak width. If the analysis area dimensions are typically three to four times the maximum displacement expected in the PIV recording then this suggests that the data should be zero padded along 30-40% of the

characteristic length of the analysis area. More conveniently, the analysis size should be chosen as 60-70% of an integer power of two.

There are several alternative methods available in the analysis program for determining the location of the correlation peak: selection of the highest pixel, a linear least squares fit to the signal peak in the correlation function, a quadratic least squares fit, a Gaussian least squares fit[217], determination of the volume moment[215–217], or using Whittaker's interpolation method[217]. The properties of the autocorrelation function may be used in validating the velocity vector. This can be done according to the double and multi-pulsed criteria presented by Keane and Adrian[215,216]. In addition, the validation method for multi-pulsed recordings has been extended to include the detection of the first harmonic of the signal peak within a two pixel radius of the expected position in the correlation function.

The algorithm to deform individual analysis areas, described in section 3.5, has also been implemented to allow the iterative analysis of PIV recordings to reduce the error introduced by velocity gradients.

The analysis program produces a MATLAB (Mathworks' mathematical laboratory) data file. MATLAB can then be used to produce vector plots, manually validate data, interpolate values for invalid vectors using the method of Renka and Cline[273], or produce plots of derived quantities such as vorticity. Derived quantities may be calculated using differencing schemes in MATLAB or by using routines written in C that in turn use NAG interpolation routines[273]. In particular, several NAG routines include stages to estimate the spatial derivatives of the velocity. It is simple to apply smoothing kernels to the velocity field in MATLAB.

The analysis system was chosen for adequate digitisation resolution, ease and flexibility of analysis, and cost. The digital system also allows cautious manipulation of the PIV image before analysis. For example, enhancing the images using sharpening algorithms, removing background noise by selecting a grey scale level below which pixels are ignored, or the removal of artifacts such as wall glare from the image. Any manipulation of the image should be carried out with caution: information is likely to be lost and

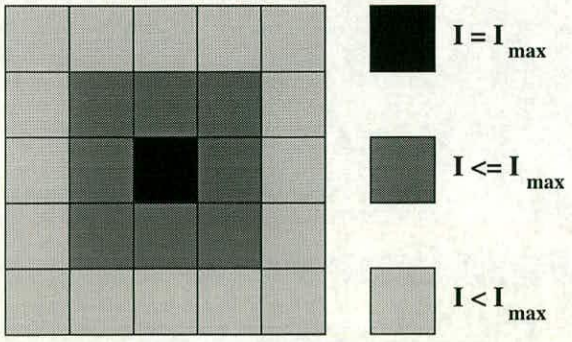


Figure 3.1: Peak location criteria

deforming the intensity profile of the recorded images will adversely affect the Gaussian fit estimator to determine the location of the signal peak.

3.3.3 Peak location

The first step in estimating the position of the central peak is to determine the location of the pixel corresponding to the maximum of the signal peak. Peaks are determined in the correlation function by considering a five by five array of pixels. If the central pixel value is higher than the outermost sixteen pixels and is greater than or equal to the values of the eight pixels surrounding it a peak has been located. Each pixel of the correlation function is considered in sequence with a record maintained of the four highest peaks located. The highest peak in the auto-correlation function is the self correlation peak: the signal peak is the second highest peak. It should be noted that there is a bias associated with the method used to determine the location of the signal peak[320], as discussed previously.

The volume moment based method for peak location uses the position of the highest pixel in the correlation function as a starting point. The area over which the volume moment is calculated is then determined by moving out horizontally and vertically in the correlation function until the value of the correlation function falls to below 50% of the maximum value or the correlation function starts to increase. If the correlation peak is Gaussian with a diameter roughly $\sqrt{2}d_p$ then this method of signal peak location can only be expected to give sub-pixel accuracy when more than one pixel contributes

H_1	H_4	H_7
H_2	H_5	H_8
H_3	H_6	H_9

Figure 3.2: Definition of points for Gaussian fit to correlation peak

to the volume moment.

The Gaussian fit estimator of the signal peak location involves the calculation of a least-squares fit for the function given by equation (3.7)[217] using the highest pixel in the correlation peak and the eight points surrounding it.

$$H(x,y) = C\exp\left(-\frac{(x_0-x)^2}{\sigma^2} - \frac{(y_0-y)^2}{\sigma^2}\right) \tag{3.7}$$

where $H(x,y)$ is the value of the correlation function at (x,y), x_0 and y_0 define the centre of the Gaussian distribution, and are determined by a least squares fit-along with σ and C.

If the natural logs of the values of the autocorrelation function of the eight pixels surrounding the highest value in the signal peak are $h_1 \ldots$, corresponding to $\log(H_1)\ldots$ (with the central peak having the subscript 5, as shown in Figure (3.2) then the least squares estimates of x_0 and y_0 are given by equations (3.8) and (3.9). These expressions were determined using MAPLE, a symbolic mathematics package.

$$x_0 = \frac{2\,h_1\,x_5 - h_2\,x_5 + 2\,h_3\,x_5 - x_5 h_6 - h_8\,x_5 + 2\,h_7\,x_5 - 4\,x_5 h_5 + 2\,h_9\,x_5 - x_5 h_4 + h_1 + h_2 + h_3 - h_8 - h_7 - h_9}{2\,h_1 - h_2 + 2\,h_3 - h_6 - h_8 + 2\,h_7 - 4\,h_5 + 2\,h_9 - h_4} \tag{3.8}$$

$$y_0 = \frac{2\,h_1\,y_5 - y_5 h_2 + 2\,h_3\,y_5 - h_6\,y_5 - y_5 h_8 + 2\,h_7\,y_5 - 4\,y_5 h_5 + 2\,h_9\,y_5 - h_4\,y_5 + h_1 - h_3 - h_6 + h_7 - h_9 + h_4}{2\,h_1 - h_2 + 2\,h_3 - h_6 - h_8 + 2\,h_7 - 4\,h_5 + 2\,h_9 - h_4} \tag{3.9}$$

To avoid the calculation of $\log(0)$, if the autocorrelation function at any point is equal to zero it is assumed to be 1.

Whittaker's reconstruction or Cardinal interpolation, as defined by Lourenco and Krothapalli[217] and given by equation (3.10), is an interpolation technique that is applied recursively to determine the location of the signal peak.

$$H(x,y) = \sum_{k=i-2}^{i_2} \sum_{l=j-2}^{j_2} H(k\lambda_x, l\lambda_y) \frac{\sin\left(\frac{\pi}{\lambda_x}(x-k\lambda_x)\right)}{\frac{\pi}{\lambda_x}(x-k\lambda_x)} \frac{\sin\left(\frac{\pi}{\lambda_y}(y-l\lambda_y)\right)}{\frac{\pi}{\lambda_y}(y-l\lambda_y)} \quad (3.10)$$

where λ_x and λ_y are the sampling intervals in the x and y directions and i and j are the indices of the point in the discrete correlation function estimated in the first stage of peak location.

The autocorrelation function is interpolated on a new grid with half the spacing of the original, giving eight extra points about the initial estimate of the maximum point. The maximum is selected from the initial estimate of the maximum and the eight new points. The interpolation procedure is repeated until the peak location is interpolated on a grid of $\frac{1}{64}^{th}$ of the original spacing.

3.3.4 Performance

Appendices A and B present the results from a number of simulated PIV recordings. The simulations give an estimate of the "best case" as there are no effects from background noise or out-of-plane particle motion. These would be useful features to add to the simulation program.

Bias from loss of image pairs

The results in Appendix A show that for particle images with an e^{-2} diameter of two pixels or greater the error and the bias are both lowest for Whittaker's method of determining the position of the signal peak. Correspondingly, the error and bias is greatest for the volume moment method. The Gaussian fit gives an intermediate

performance. The percentage error in the measured velocity and the bias are both seen to increase, as expected[215,216], with the particle image size. No correction for the bias has been carried out for the results given in Appendix A. If the number of effective particle image pairs is constant then the percentage error and the bias in the velocity vectors are both reduced in multi-pulse recordings, with little improvement beyond three illumination pulses. Again, this is in agreement with the work of Keane and Adrian[215,216]. The overall percentage error and bias in the measurement velocity below the actual velocity are also seen to decrease with the effective number of particle pairs, as demonstrated in the same work.

The results in Appendix A show that the error appears to be minimised when $\frac{d_p}{d_{pix}} \approx 2$, in agreement with Prasad *et al.*[239] and Westerweel[242]. It should be noted that the Gaussian fit performs very badly for particle image sizes of one pixel and well for particle images of a diameter of two pixels. This arises from an effective under-sampling of the data used to define the correlation peak that gives a signal peak with a non-Gaussian shape and a loss as a nine point neighbourhood is used in determining the least squares fit.

This assessment of the analysis program validates its performance and suggests optimum recording parameters broadly in agreement with those reported before[215,216,239,242], with the additional suggestion that the Gaussian estimator or Whittaker's method be used for peak location. Figures (A.59) and (A.60) show that relative errors in the measured velocity of less than 1% can be obtained for displacements in the range $2d_p < \frac{\Delta x}{d_I} < \frac{1}{3}$. The relative error falls with increasing displacement to a minimum value of around 0.1%. The underestimate of the displacement magnitude is a maximum for smaller displacements where the measured velocity is underestimated by 0.3%. This falls to 0.1% for higher displacements and agrees with the correction factor given by Keane and Adrian[215,216] of $\left(1 + \frac{d_p^2}{d_I^2}\right)$. This implies that the measured displacement for particles of e^{-2} diameter 2 pixels analysed using a 64 by 64 pixel analysis area is expected to be 99.9% of the actual value. The correction factor has been explicitly applied in the results presented in Appendix B where there are a few uncorrected results for contrast. The error is small and the correction is not usually

required.

The effect of the validation algorithm described in the following section can also be seen on the spread of expected results. It is also evident that validation becomes a more significant problem as the effective number of particle pairs decreases.

Appendix A only considers displacements of an integer multiple of the pixel size. Bias in the estimated velocity will arise from the loss of image pairs (partial images at the edges of the interrogation region leading to a distorted signal peak and an underestimate of the velocity) and sampling of the correlation function. However, for displacements between these integer values bias is introduced by the method used to determine the centre of the correlation peak due to sampling and the background value for the correlation function. this bias is expected to be zero for integer and half-integer displacements[320].

Bias associated with fractional displacements

Appendix B, section B.1 shows the error in the determined velocity as a function of the fractional displacement between 10 and 11 pixels in the x-direction. The vectors are validated by excluding any vectors with an x component less than 9.5 pixels/s or greater than 11.5 pixels/s. Again it should be noted that the Gaussian fit method performs badly for image sizes of one pixel and well for image sizes of two pixels. The volume moment method for peak location appears to give anomalous results and over-estimates the image displacement[239,242]. This was investigated further by considering a greater range of effective particle pairs in an analysis area; the results presented in section B.1. The anomalous behaviour occurs when there are 10, 16, or 24 image pairs and not when there are only 1 or 2 effective image pairs per interrogation area. This suggests that this unexpected bias arises as particle images overlap and lead to an additional mechanism for the deformation of the signal peak. In obtaining these results different criteria to determine the area over which to calculate the volume moment were used, as opposed to those described earlier, to illustrate those normally used by other workers. As a result of these observations a smaller area than conventional is used to calculate the volume moment is a compromise between under-sampling and this effect: the method outlined

earlier. The effect is seen to be reduced when the results are compared. The effect is also reduced for the same effective number of particle image pairs as the number of illumination pulses is increased as the signal-to-noise ratio is increased[216]. More work is required to characterise this source of bias in more detail.

Padding the Fourier transform to reduce wrap around pollution seems to have little effect on the performance of the Gaussian fit and Whittaker's interpolation method to determine the signal peak location. The maximum bias is reduced slightly, and becomes more significant with increasing $\frac{d_\tau}{d_{pix}}$. The reduction in bias for the volume moment technique is less marked than reported elsewhere[217] and may be due to the lack of background noise in the simulated images. It is arguable that the data should be padded with the mean intensity value to avoid introducing additional noise, especially when only a small area of the analysis region is filled with zeros.

The bias resulting from the Gaussian interpolation method is generally about half that produced using Whittaker's interpolation method. Both show that this source of bias is little affected by the number of effective particle pairs. This is readily explained as the signal peak is roughly Gaussian and the fit will be less good as the peak is distorted. This is emphasised comparing the results for different numbers of illumination pulses, where the bias remains roughly constant for Whittaker's method but decreases with the number of illumination pulses for the Gaussian fit. Again this can be explained as the signal peak is expected to be more Gaussian in character as the signal-to-noise ratio is increased. In any case the effects are small for images with particle diameters of two pixels and recorded with three illumination pulses, giving a bias of less than 0.2%. The work of Lourenco and Krothapalli[217] broadly reflects these results although the effects they observe are more pronounced. This is likely to be due to the noise free PIV recordings produced by the simulation program.

Section B.1 illustrates the combined effect of bias from fractional displacements and from loss of image pairs.

The results show that the volume momenting technique is sensitive to peak distortion and how the area over which to calculate the moment is determined. The interpola-

tion and fitting methods perform better for a range of different recording parameters although the Gaussian fit produces bias in the opposite sense to that expected for recordings where the particle images have a diameter of one pixel. In practice, a scatter plot of the fractional part of the x and y components of the velocities in a vector field can be used to visualise this bias. For many applications, the Gaussian estimator is the most robust.

3.4 Validating and orienting velocity vectors

3.4.1 Introduction

Any PIV analysis system will produce spurious velocity vectors that differ significantly, in both magnitude and orientation, from their neighbours and from values that might be expected in the flow under study. Typically, 5% of velocity vectors may be erroneous, resulting from fluctuations in seeding density, out of plane motion, and other noise [2,267]. This percentage is increased when the flow field contains appreciable velocity gradients[215,216,234] resulting from flow features such as areas of stasis. Approaches to correct for these velocity gradients in cross-correlation analysis have been discussed in the literature[235–237]. An essential step in applying a similar technique to auto-correlation analysis is the development of a reliable post analysis step to validate and orient vectors between the successive stages of the iterative procedure required. In the work by Huang *et al.*[235,236] and Jambunathan *et al.*[237], the results from previous analyses are used to distort the second analysis area to reduce the effect of velocity gradients on the cross-correlation analysis. The process is repeated until the velocity field and the velocity gradients are consistent between two steps. The validation of vectors between steps is required but the orientation of vectors is known. The correction for velocity gradients in auto-correlation analysis is more complicated: this section discusses one possible approach to solve the intervening post-processing problem that must be addressed at the same time as developing the algorithm for distorting the analysis area.

Directional ambiguity has been resolved in a number of ways by other authors, for example, using image tagging[250–253], image encoding[192,245–249], and image shifting[244,256–261,264,266] techniques. Image tagging does not address the problem of velocity gradients within flow fields and uses the additional information recorded to determine the direction of the velocity vector. The image shifting technique, with an appropriate choice of the imposed velocity and time interval between illuminating pulses, resolves directional ambiguity and goes some way to addressing the problems of velocity gradients within the flow.

A novel computational approach to resolve directional ambiguity has been investigated which makes use of the expected similarity between neighbouring velocity vectors. This approach appears attractive given the usual criteria for making good PIV recordings[215,216,234]: these imply that the velocity differences between neighbouring analysis areas are small in comparison with the actual velocity. Indeed, similar approaches are taken in validating velocity fields[267].

The recommendations of Keane and Adrian[215,216,234] for making good PIV recordings have already been discussed. In particular the two constraints $\frac{M\Delta u\Delta t}{d_\tau} < 1$ and $\frac{|\Delta X|}{d_I} < 0.25$ imply that

$$\frac{\Delta u}{u_I} < 4\frac{d_\tau}{d_I}$$

Considering normal and image shifted recordings of the same flow, the right hand side of the inequality is likely to be of similar magnitude; u_I will depend in both cases on the time interval between illumination pulses, and in the case of the image shifting technique, on the imposed velocity. An image shifting technique gives greater freedom to choose the time interval between illumination pulses: this interval can be reduced making it easier to satisfy the constraint $\frac{M\Delta u\Delta t}{d_\tau} < 1$. This, however, decreases the accuracy to which the displacement can be determined[215,216]. The main advantages of all image shifting techniques are to remove directional ambiguity and, when considering a single recording where the range of velocities is known beforehand,

to allow the range of recorded displacements to be optimised for the analysis system used. In particular, this allows small displacements to be measured where particle images would overlap in unshifted recordings making analysis, at best, unreliable. In addition, the displacement produced by the largest velocity can be scaled by altering the illumination frequency and adjusted to the maximum that can be measured by a particular analysis system.

Image shifting techniques have disadvantages when studying the flows around artificial heart valves or other pulsatile flows. The shift is applied to any surface in the flow, which may make some areas of interest, particularly those close to these surfaces, unanalysable as a result of the multiple surface images. This problem is reduced if the time interval between illumination pulses is shortened or fewer illumination pulses recorded. The pulsatile nature of the flow makes it difficult to select an optimal image shift that applies over the whole pulse cycle when recording a series of PIV images. The range of velocities within the flow field must be known prior to making a PIV recording in order to choose the appropriate image shift. The image shifting techniques themselves have a number of potential problems. With some techniques the number of pulses that can be recorded on any PIV image may be limited[249,264,266]. The scanning mirror technique[244,256–261], without careful consideration of the experimental setup, introduces systematic errors, including additional velocity gradients, into the recording. This is exacerbated when making multi-pulse recordings and/or making a series of PIV recordings between which the mirror can not be reset.

A post-interrogation procedure for validating and orienting the velocity vector maps produced from digital, auto-correlation analyses of PIV recordings may avoid the need for image shifting. The procedure is presented below and applied to a specimen flow field. Spurious vectors are removed by successive applications of the global-mean-velocity and local-median-velocity tests described by Westerweel[267], modified to allow for the directional ambiguity of vectors. If velocity vectors can be oriented in relation to their neighbours there remains ambiguity only in the orientation of the whole flow field, which can be resolved given the gross nature of the flow. An algorithm is presented that achieves this for flows where a high proportion of velocity vectors are valid.

Conventionally, the validity of vectors is determined using criteria related to the correlation function, for example, D_o , the ratio of the tallest peak to the second tallest peak in the auto-correlation function, as adopted by Landreth and Adrian[17]. This method may remove valid vectors and leave some erroneous vectors, requiring a further post-processing validation step. The new algorithm has been developed to minimise the errors introduced by the validation step, whilst at the same time leaving all plausible vectors.

3.4.2 Method

Post-interrogation detection of spurious vectors

The interrogation region used in the digital analysis of PIV images is normally rectangular. The orthogonal components of the velocity vector referred to subsequently would normally be aligned with the base and sides of such an interrogation region, although some advantage would be gained by using axes where one direction is aligned with the direction of the local median velocity. The average and standard deviations of the magnitudes of the chosen two, orthogonal components of velocity within the measurement plane are calculated for the vector field. All vectors with a velocity component of magnitude greater than three standard deviations (or other factor depending on the flow field) from the mean of that component over the flow field are marked as spurious. The magnitudes of the velocity vector components are used to avoid problems with directional ambiguity. In addition, range checks on the magnitudes of the two velocity components could be applied to mark unrealistic velocity vectors. The marked vectors are then removed: velocity vectors are not deleted as the algorithm sweeps through the data but in a step at the end so that the starting point and the direction of sweep do not affect the result of the validation process. This is similar to the process described by Meinhart *et al.*[269].

The local median velocities for groups of nine vectors in a 3x3 arrangement are calculated after Westerweel [267] who showed the local median velocity to be the most robust estimate of the local mean velocity. The calculation of this mean velocity is

modified, as suggested, at the edges of the velocity map.

The local median test is modified to allow for directional ambiguity. This requires an additional initial stage in which the group of nine velocity vectors are aligned relative to each other. Assuming that the mean magnitude of one orthogonal component of the nine velocity vectors is larger than the others, it is likely that the nine velocity vectors are oriented so that this component of velocity is in the same sense for each of the vectors. This fixes the relative orientation of the nine vectors. In order to determine which component should be fixed the mean of the magnitude of each velocity component (u_{mean} and v_{mean}) is determined. If i and j are the unit vectors in the two orthogonal directions then $\mathbf{u_i} = i * u_i + j * v_i$ and u_{mean} and v_{mean} are defined below.

$$u_{mean} = \frac{\sum_{i=1}^{9} |u_i|}{9} \tag{3.11}$$

$$v_{mean} = \frac{\sum_{i=1}^{9} |v_i|}{9} \tag{3.12}$$

$$\tag{3.13}$$

If $u_{mean} > v_{mean}$ the nine velocity vectors are oriented so that the component of velocity in the i direction is in the same direction. Conversely, if $u_{mean} < v_{mean}$ the nine velocity vectors are oriented so that the component of velocity in the j direction is in the same direction. The oriented vectors are identified as u_i'. The median vector, with components u_{med} and v_{med}, can now be determined as described by Westerweel[267] using the nine oriented vectors. The central vector, identified by the subscript c is marked for deletion if it fails a relative or absolute test based on the L_2 norm shown below.

$$C_1 > \sqrt{(u'_c - u'_{med})^2 + (v'_c - v'_{med})^2} \tag{3.14}$$

$$C_2 > \frac{\sqrt{(u'_c - u'_{med})^2 + (v'_c - v'_{med})^2}}{\sqrt{(u'_{med})^2 + (v'_{med})^2}} \tag{3.15}$$

where C_1 and C_2 are constants to be determined by trial.

It is possible that some vectors may pass these tests but still be oriented dubiously. To overcome this problem the smaller of the two angles between the lines defined by the median velocity vector and the central velocity vector is determined and the central vector marked as spurious if this is greater than some arbitrary angle, again dependent on the flow field. This procedure is outlined in Figure(3.3). After all the vectors in the field have been considered the marked vectors are deleted.

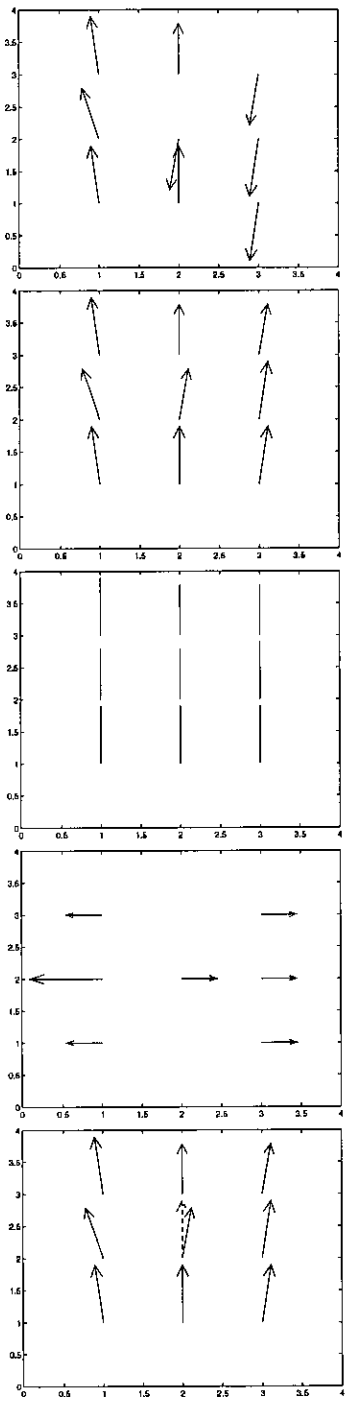
These two validation steps are repeated until no further deletions are required giving a velocity field consistent with the applied criteria.

The rough estimate of the standard deviation from the mean velocity has been used in an attempt to give a post-processing step that adapts to the local variation in the flow field. As the validation process repeats the tolerances decrease as erroneous vectors are deleted with the intention of giving a progressively more reliable data set. As originally suggested by Westerweel, a constant could have been used in comparing the local-median velocity to the central velocity in a single validation step.

Resolution of directional ambiguity

The approach adopted here attempts to include the same factors that would influence an experimenter manually orienting the velocity vectors produced from a PIV analysis.

For each group of four velocity vectors forming a square, one of the velocity vectors is considered to be fixed in orientation, the mean and variance of the velocity components



A group of nine velocity vectors.

Velocity vectors are oriented so that each has one component that lies in the same sense. This component is chosen to be the one with the largest mean magnitude over the nine vectors.

Each component of the median velocity is determined from the oriented vectors.

A test based on then L_2 norm is applied to the central vector.

The direction of the median velocity vector is compared with that of the central velocity vector. The central vector is marked for deletion if the angle is greater than a predetermined value.

Figure 3.3: The validation procedure

are then calculated for the eight possible combinations of orientations of the other three vectors. A record of the orientation giving the lowest sum of the variances of the velocity components is kept along with this value. No change has yet been made to

the orientation of any of the velocity vectors.

The square with the lowest total for the velocity variances (and non-zero velocities) is then set with the vectors in the recorded orientation. The vectors forming the square are noted as an oriented region in the flow field. The process is repeated for the square with the next lowest variance in velocity. The record of oriented regions is updated: where orienting the current square adds to a region, the orientation is matched with the region; where orienting the square joins regions the square and regions are oriented with the largest region. This process is repeated until the whole flow field is oriented.

This approach attempts to orient regions where velocity changes are small and then to connect these oriented regions by the route along which the velocity varies least. This produces a vector field effectively determined by fixing the local orientation of velocities to minimise the L_2 norm of the local velocities after the mean local velocity is subtracted. That is, for a set of four neighbouring points where the velocities are $\mathbf{u}_1$, $\mathbf{u}_2$, $\mathbf{u}_3$, and $\mathbf{u}_4$, and the mean velocity computed using the mean of each component is $\bar{\mathbf{u}}$ then the locally correct orientation is found when $\mathbf{v}_i$ are chosen such that $\sum_{i=1}^{4} \|\mathbf{v}_i - \bar{\mathbf{u}}\|$ is a minimum. Where $\mathbf{v}_1 \in \{+\mathbf{u}_1\}$, $\mathbf{v}_2 \in \{+\mathbf{u}_2, -\mathbf{u}_2\}$, $\mathbf{v}_3 \in \{+\mathbf{u}_3, -\mathbf{u}_3\}$, and $\mathbf{v}_4 \in \{+\mathbf{u}_4, -\mathbf{u}_4\}$.

Conventional validation of vectors

The criteria based on the auto-correlation function used to validate vectors are listed below:

- The highest non-central peak has to be at least 20% of the height of the central peak;
- $D_0 = 1.2$ for four pulse PIV images and 1.35 for double pulsed PIV images [215,216];
- For multi-pulsed recordings, a harmonic peak must be detected within a definable radius of its expected position, given the location of the first peak.

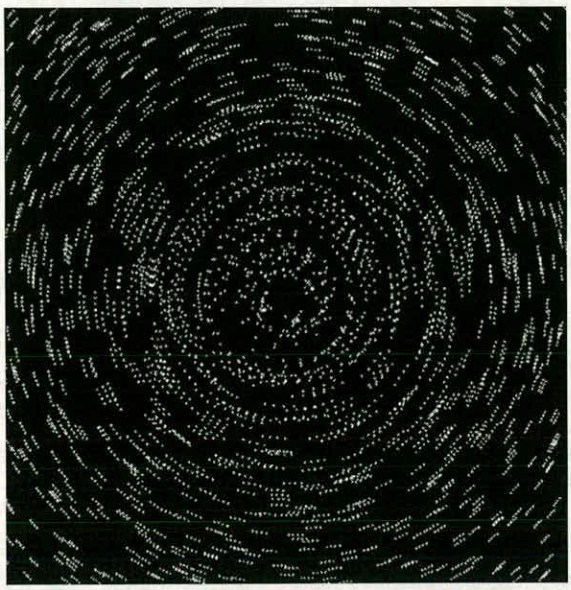


Figure 3.4: Simulated velocity field.

3.4.3 Results

Results from a sample flow field are presented. Figure (3.4) shows the results from a Monte-Carlo simulation of a four pulsed PIV recording from seeding particles in a free vortex; Figure (3.5) shows the vector map produced with no validation criteria applied, Figure (3.6) shows the vector map produced with conventional PIV validation, Figure (3.7) shows the vector map produced using the proposed validation procedure, and Figure (3.8) shows the vector map produced from Figure (3.7) after the application of the algorithm to remove directional ambiguity. The vortex is centred at the centre of the velocity map, N_I, the number of particle image series as defined by Keane and Adrain [216] is 10, and the total area of particle images is around 10% of the analysis area. The circulation of the vortex was 10,000 pixel^2 s^{-1} and Gaussian images generated at 1 second intervals. The image generated was 693 by 693 pixels, the analysis area was 63 by 63 pixels and the spacing between analysis areas 21 pixels in each direction. This gives an appreciable velocity gradient in many analysis areas. This particular example was chosen after Huang *et al*[235,236] who used a similar test flow field (an Oseen vortex) to demonstrate their improvements to PIV by correcting for velocity gradients in cross-correlation.

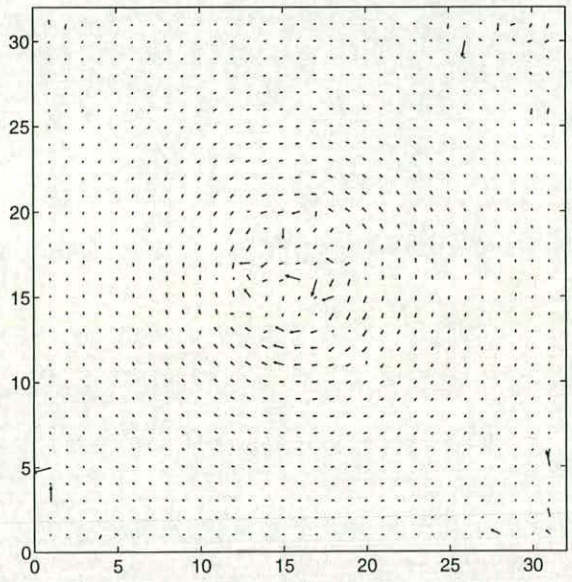


Figure 3.5: The velocity vectors produced after the analysis of Figure (3.4), with no validation of the results.

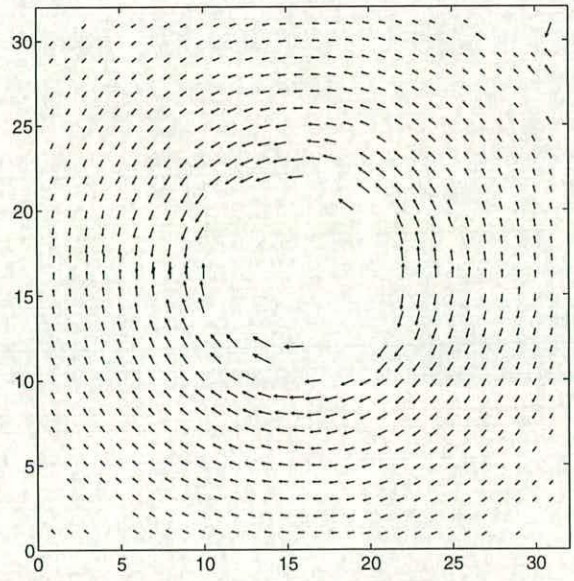


Figure 3.6: As Figure (3.5), after applying conventional multi-pulse validation criteria.

Figures (3.9 and 3.10) show how the measured velocity vectors compare with those expected at the centre of the interrogation areas for the conventional validation method. Figures (3.11 and 3.12) show the same information for the proposed validation method. Figures (3.13 and 3.14) show u_θ with the expected value for u_θ subtracted to give a clearer indication of the scatter about the expected values. For the old method, the

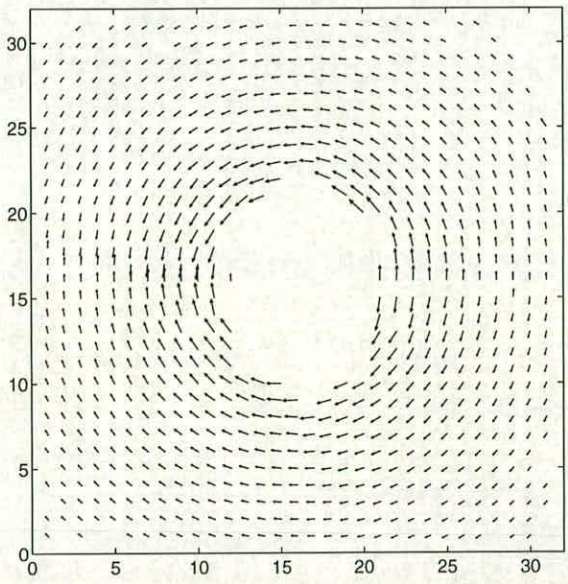


Figure 3.7: As Figure (3.5), after applying the new validation algorithm.

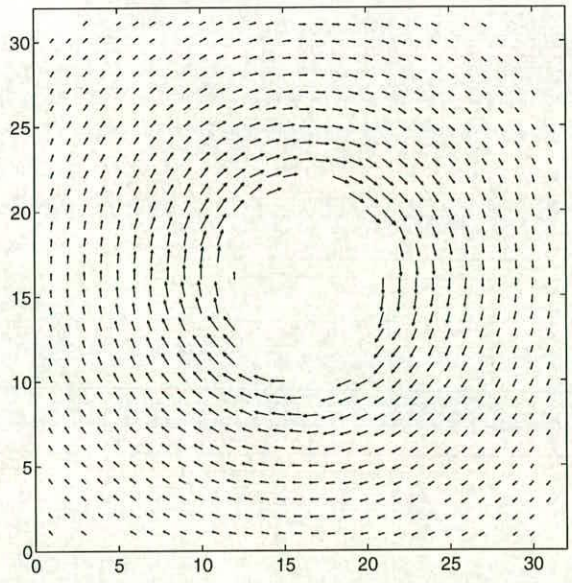


Figure 3.8: As Figure (3.7), after applying the algorithm to resolve directional ambiguity.

standard deviation in u_r is 0.42 pixels/s and in u_θ is 0.48 pixels/s compared with the new method where the standard deviation in u_r is 0.31 pixels/s and u_θ 0.73 pixels/s. (Zero velocities were ignored when calculating the standard deviations.) Applying the double pulse criteria ($D_0 = 1.35$) gave only one valid vector.

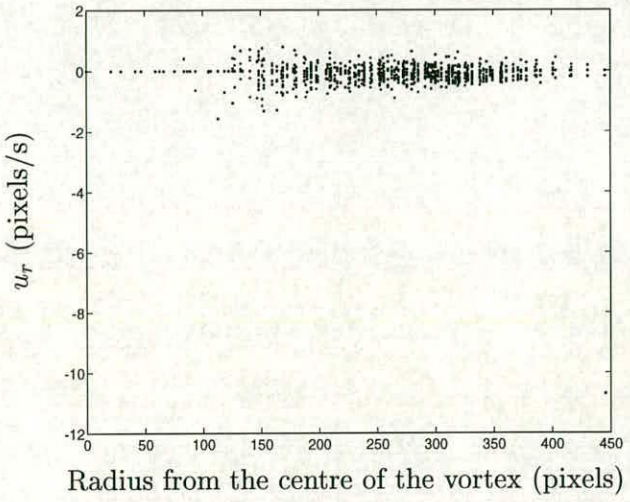


Figure 3.9: u_r as a function of distance from the centre of the vortex for the conventional validation method.

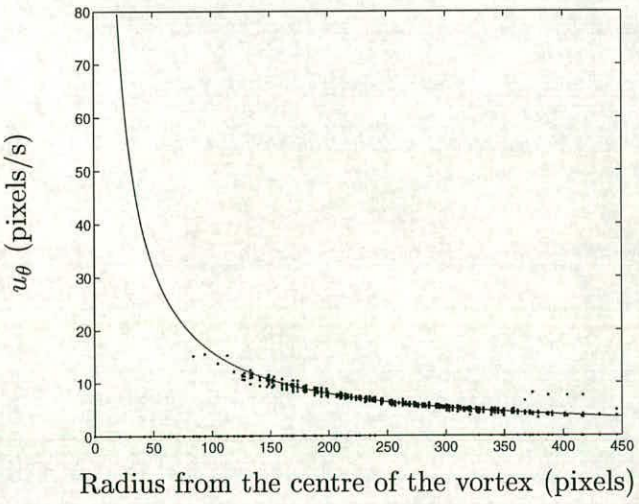


Figure 3.10: u_θ as a function of distance from the centre of the vortex for the conventional validation method (compared with the expected value).

Figure (3.15) shows the simulated PIV recording of the same flow as depicted in Figure (3.4) but with an imposed velocity of 40 pixels/s to the right and with the time interval between illumination pulses reduced to 0.3 seconds. All other simulation parameters are the same for the two flow fields. The image shift is not ideally optimised for the flow under study; a trial and error approach was used to find a suitable combination of the shift velocity and the time interval between pulses to give sensible image displacements so that the image shifted recording could be analysed with the same analysis parameters

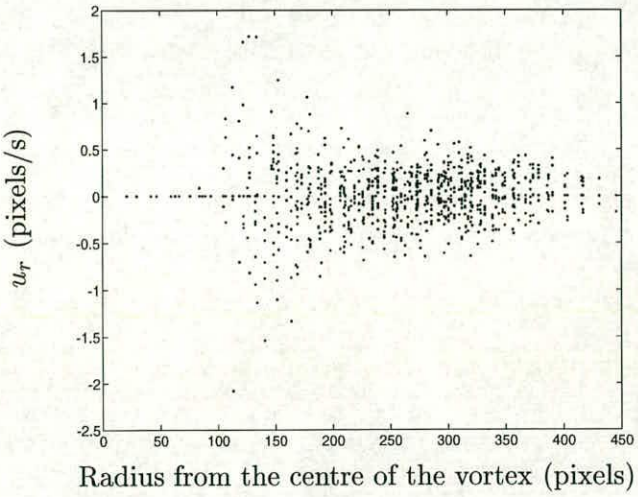


Figure 3.11: u_r as a function of distance from the centre of the vortex for the proposed validation method.

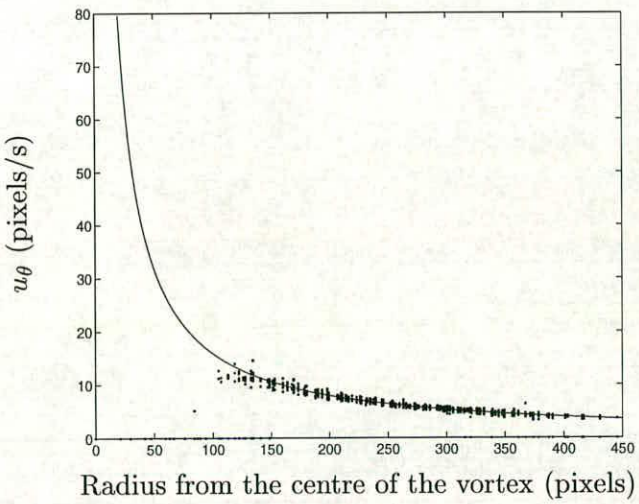


Figure 3.12: u_θ as a function of distance from the centre of the vortex for the proposed validation method (compared with the expected value).

as used for the unshifted recording. The discontinuity in the velocity field at the centre of the free vortex is still unanalysable. The raw velocity field produced is shown in Figure (3.16) and with the imposed velocity subtracted in Figure (3.17). Figure (3.18) shows the variation of u_r with distance from the centre of the vortex; Figure (3.19) the variation of u_θ as a function of distance from the centre of the vortex; and Figure (3.20) the difference between u_θ and the expected value of u_θ as a function of distance from the centre of the vortex. The standard deviation of u_r for the unvalidated vector

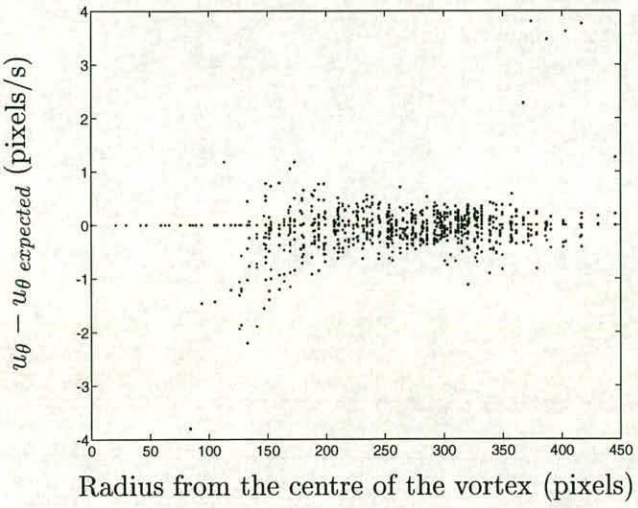


Figure 3.13: $u_\theta - u_{\theta\ expected}$ as a function of distance from the centre of the vortex for the conventional validation method.

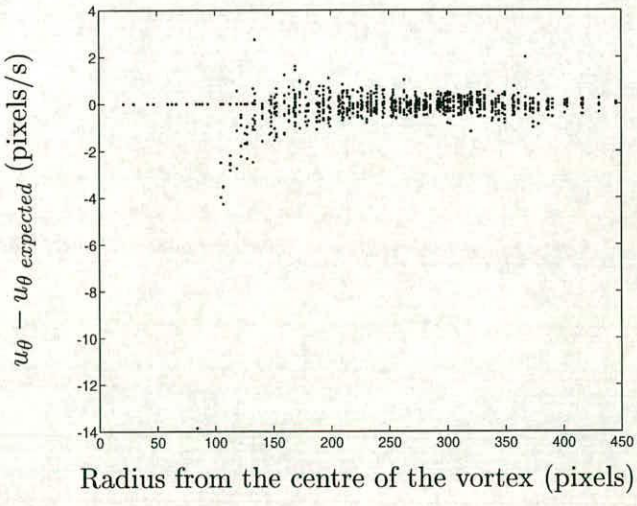


Figure 3.14: $u_\theta - u_{\theta\ expected}$ as a function of distance from the centre of the vortex for the proposed validation method.

map was 1.7 pixels/s.

3.4.4 Discussion

From the validated velocity maps it is clear that the old validation method (section 2.3) tends to remove a small number of reasonable vectors and to leave some vectors that are erroneous. The new validation method gives a more convincing velocity field; fewer

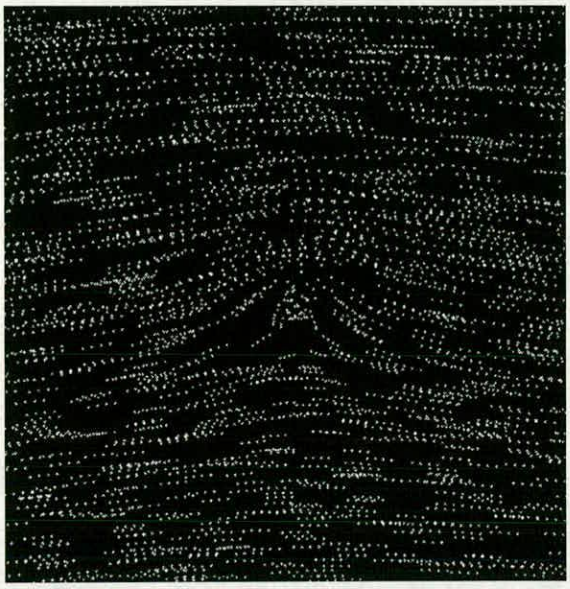


Figure 3.15: Simulated PIV recording using an 'ideal' image shifting technique.

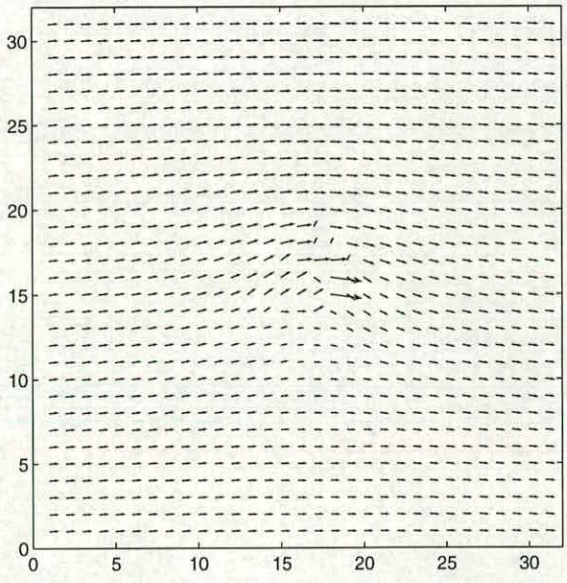


Figure 3.16: The velocity vectors produced from analysis of the image shifted recording shown in Figure(3.4)

velocity vectors are wrongly deleted and no obviously erroneous vectors remain. The errors in the measured velocities are similar, although where there are high velocity gradients in the flow the new validation method yields more reasonable vectors with greater scatter about the expected value compared with the old method that gives fewer vectors with less scatter. The new method works well where there is a high

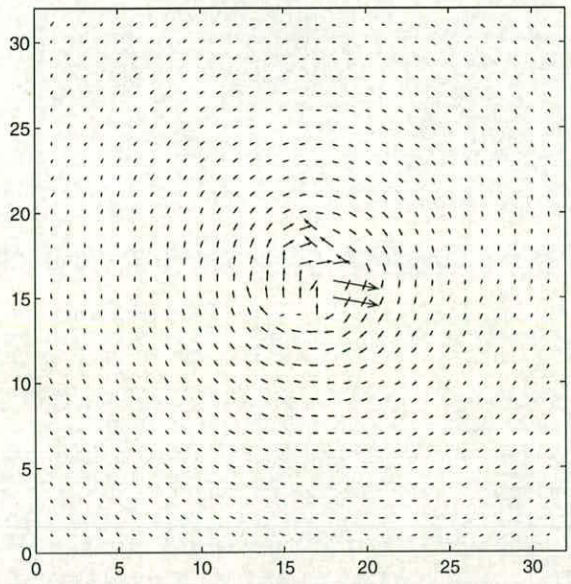


Figure 3.17: The velocity vectors produced from analysis of the image shifted recording shown in Figure(3.4) with the shift velocity subtracted

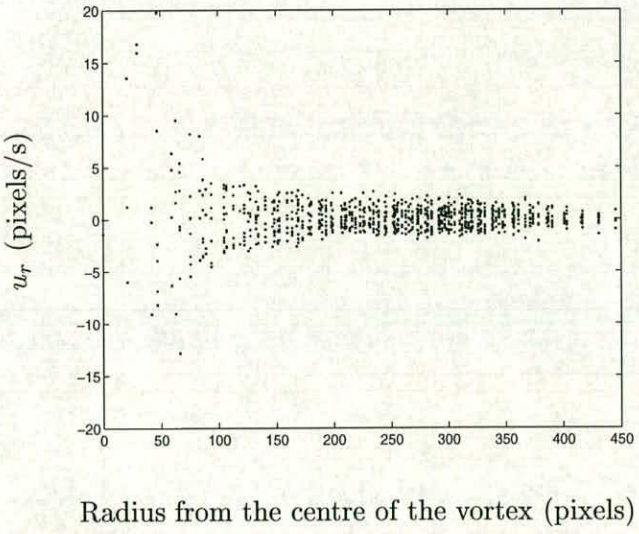


Figure 3.18: u_r as a function of distance from the centre of the vortex for the image shifting technique.

density of valid vectors. Where valid vectors are interspersed with random vectors the new method will tend to delete them after comparison with the neighbouring erroneous vectors and post-processing methods based on the auto-correlation function would be expected to work better. The new method also works well at lower velocities. The

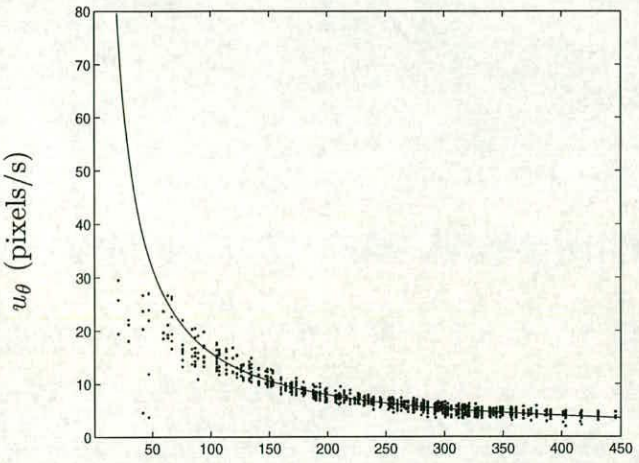


Figure 3.19: u_θ as a function of distance from the centre of the vortex for the image shifting technique (compared with the expected value).

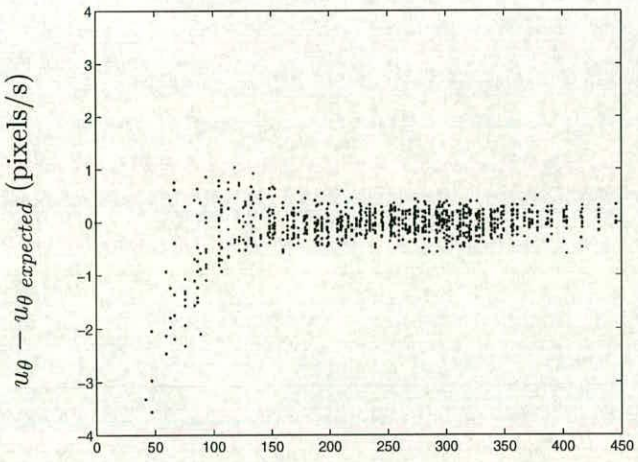


Figure 3.20: $u_\theta - u_{\theta\ expected}$ as a function of distance from the centre of the vortex for the image shifting technique.

errors in velocity due to noise and the accuracy of peak location method remain the same.

Figures (3.13) and (3.14) clearly show the value of u_θ underestimated as the velocity gradient in the analysis area increases, as anticipated from the work of Keane and Adrian [215,216]. As would also be expected, the validation method based on the

properties of the auto-correlation plane performs badly where the velocity gradient is high and the signal peak is broadened and reduced in amplitude.

The arbitrary number of standard deviations used when comparing vectors to the global-mean and local-median, and the arbitrary angle that vectors can deviate from the local-median, should be chosen for particular flow fields from experience and trial-and-error. Once fixed, a large number of flow fields from similar PIV recordings can be validated.

The algorithm used to resolve directional ambiguity clearly works for this example. For flow fields where analysable regions are not contiguous each area will be oriented consistently but not relative to other areas. The orientation of each region depends on the first square fixed. The validation and orienting algorithms work well for the same types of flow fields, those that produce one connected region of valid vectors. These two post-processing steps could form a reliable link in an iterative analysis scheme that deforms interrogation areas in auto-correlation analyses.

Comparing Figures (3.12) and (3.19), the image shifting technique produces more plausible vectors than the unshifted recording as the time interval between illumination pulses can be reduced; as would be expected from Keane and Adrian's[215,216] investigation of the effect of velocity gradients on the analysis of PIV images. Again, in agreement with these results, Figures (3.18, 3.19 and 3.20) show an increase in the scatter of the measured velocity values about those expected as the absolute error in peak location remains roughly constant and the magnitude of the displacement decreases as the time interval between illumination pulses is decreased. In particular, the scatter in u_r for the different techniques at the same distance from the centre of the vortex gives a good estimate of the error associated with peak location. Again, it should be noted that the image shifting velocity field is unvalidated although comparisons between the techniques away from the centre of the vortex are straight-forward. The ideal image shifting process used here allows any number of illumination pulses to be recorded and is not affected by the experimental realisation of an image shifting technique.

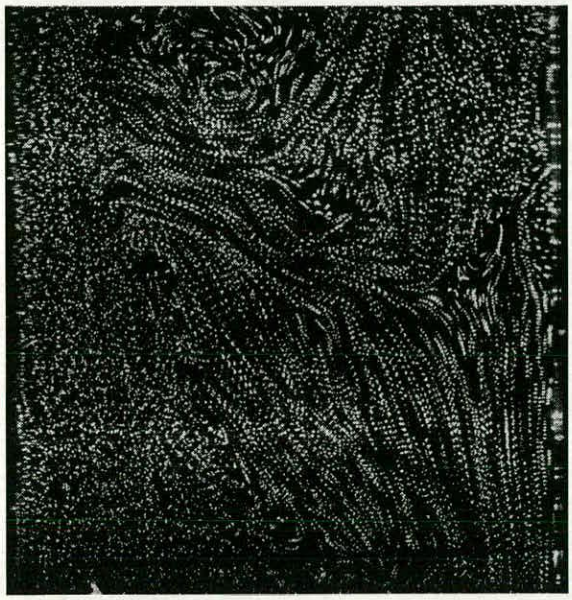


Figure 3.21: A PIV image of the flow downstream of an artificial heart valve.

3.4.5 Experimental Application

The post-processing method described has been applied to the flow downstream of an artificial heart valve where large velocity gradients would be expected and correction for the errors associated with these velocity gradients would be useful. Figure (3.21) shows a PIV recording of the flow downstream from a Björk-Shiley valve. The water flow through the valve is seeded with 50 μm, neutrally buoyant pollen grains to give high contrast images that can be digitised from A4 photographs using a flat bed scanner with ample resolution according to accepted criteria [215,216,218,239]. Figure (3.22) shows a schematic diagram of the flow field imaged in Figure (3.21). There is a fast moving jet to the left of the image that expands downstream from the major opening of the valve. A smaller jet of fluid is produced at the minor opening of the valve, this meets the recirculating flow produced by the large jet giving complex, transient, three dimensional structures in the region imaged.

Figure (3.23) show a series of vector maps produced during the iterative analysis of this flow to correct for velocity gradients. (This correction procedure will be presented later.) Figure (3.23a) shows the raw velocity field and Figure (3.23b) the velocity field

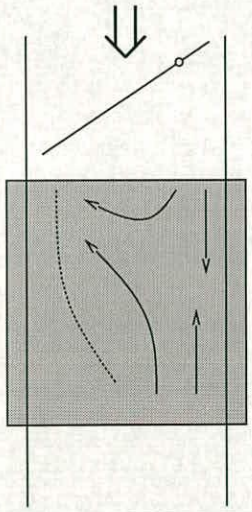


Figure 3.22: A schematic diagram of the flow shown in Figure (3.21)

after validation, Figures (3.23c) and (3.23d) show the same velocity maps after three iterations of the velocity gradient correction algorithm and Figures (3.23e) and (3.23f) after six iterations. Figure (3.23) shows that with careful adjustment of the validation criteria, appropriate to the velocity field under study, a reliable validation of vectors can be produced, after which the most likely orientation of vectors can be determined.

Figure (3.23d) and (3.23f) show the two areas of vectors in Figure (3.23b) correctly oriented with respect to each other after the two areas have been connected by valid vectors as a result of an iterative procedure to correct for velocity gradients. After orientation, only the direction of the whole flow field is unknown which is trivial to correct manually. This stage could be automated by integrating the velocity over an appropriate section of the flow to give a mean flow and then using this to orient the overall flow.

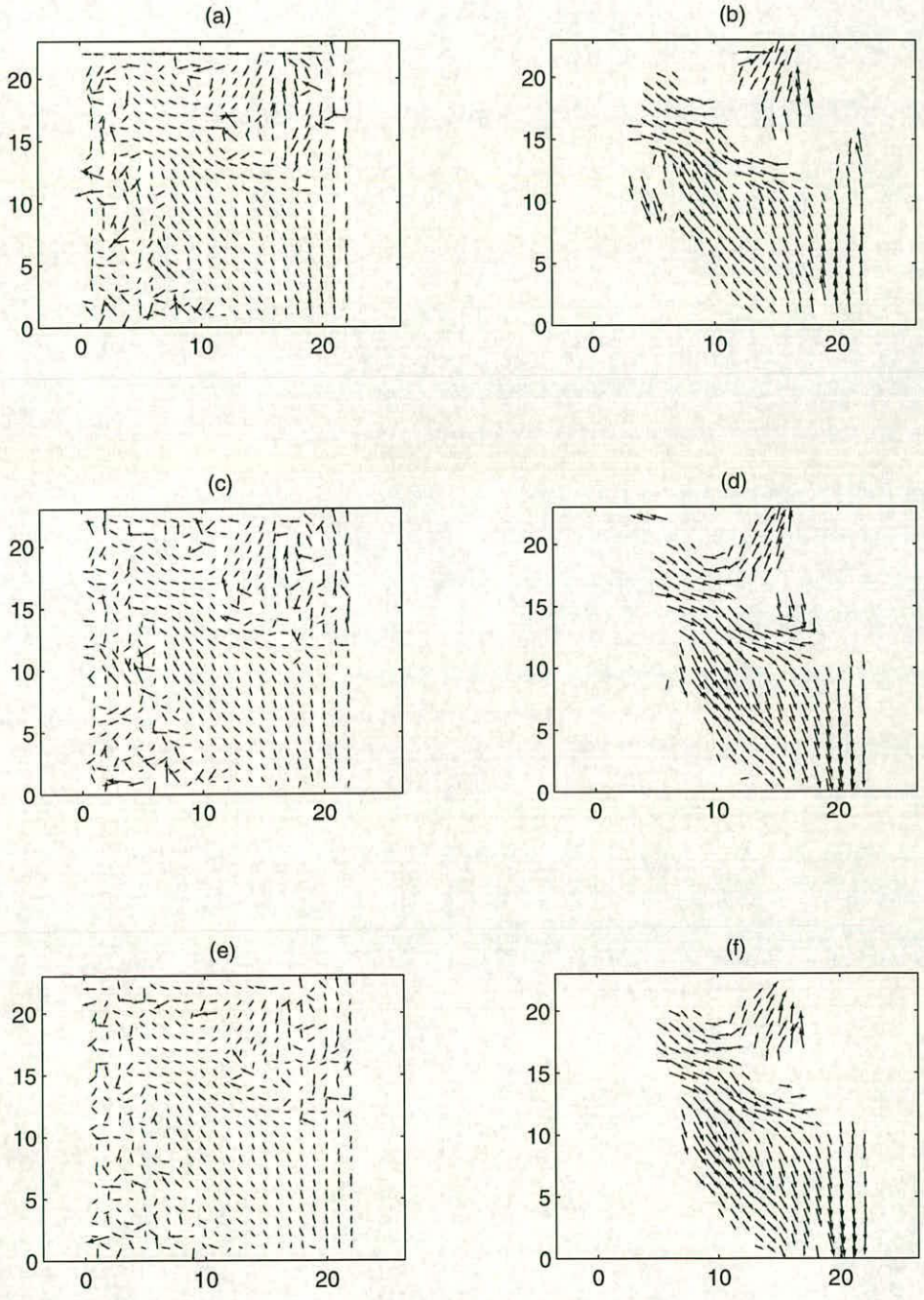


Figure 3.23: The new validation and orientation algorithm applied to a series of velocity fields produced in analysing (3.21).

After successive applications of an algorithm to correct for velocity gradients within the flow the validation and orienting algorithm finds more plausible vectors and connects correctly, originally unconnected areas. The flow chosen here contains large velocity gradients, regions of stasis and a wide range of velocities, although the faster velocities are not analysable from this recording. It is important to record images at various times within a single cycle as the flow varies significantly both during the pulse cycle and between cycles. This requirement, the problems already discussed regarding individual image shifting techniques, and the need for a suitable validation step in the iterative correction of velocity gradients were the reasons for developing the orienting and validation algorithms.

In this example, the regions of the flow are connected by a few vectors. In practice, the technique would be expected to be more reliable in the presence of smaller velocity gradients or where velocity gradients have been corrected, as the percentage of valid vectors increases. The algorithm performs optimally by connecting the most similar regions first. The validated vector field can be used to estimate the velocities and velocity gradients in unanalysable regions of the flow. Where this region is initially unanalysable, due to the presence of velocity gradients, the iterative correction for velocity gradients will increase the likelihood of obtaining a valid vector and in turn make the connection of analysable regions more reliable. This is seen to a limited extent in this experimental application.

3.4.6 Conclusions

The post-processing validation method proposed by Westerweel [267] for cross-correlation analysis has been adapted for auto-correlation analysis and compares well with validation techniques based on properties of the auto-correlation function. Directional ambiguity can be resolved by a simple algorithm that mimics, to some extent, the manual process of vector validation. The post-processing algorithm was successfully applied to simulated and experimental velocity fields. The orientation algorithm performs worse than an image shifting technique with regard to optimising the range of displacements recorded for the analysis technique but orients velocity vectors reliably when there is a

high density of valid vectors. This validation scheme forms an important stage between iterative corrections for velocity gradients recorded on multi-pulsed images. If the PIV recording is made using image shifting then only vector validation would be required between iterations.

3.5 Reducing the error from velocity gradients in the auto-correlation analysis of PIV images

3.5.1 Introduction

Errors associated with the velocities produced by the PIV technique have already been discussed in section (2.2.8). In summary velocity gradients place a fundamental limit on the measurements that can be made using PIV, along with the limit to the size of seeding particles that can be recorded and the smallest scales of motion that can be resolved.

These constraints are expressed by Keane and Adrian[215,216] in recommending:

$$\frac{\Delta u}{u} < 4\frac{d_\tau}{d_I} \tag{3.16}$$

Meeting this inequality limits the bias arising from velocity gradients to around 6% and gives a detection probability of 92% or greater. There will always be flows of interest which give recordings that can not be analysed without appreciable velocity gradients in some analysis areas. In these areas the above inequality is difficult to achieve and is in conflict with other recommendations. It is suggested that the appropriate way to reduce bias arising from velocity gradients is to find an appropriate compromise between reducing the interval between illumination pulses and the increasing error associated with measuring small displacements. Correcting for velocity gradients using a simple formula was also suggested. Alternatively the size of the interrogation area can be reduced but this will reduce the number of effective image pairs. Detection

bias can be reduced by using a multi-pulsed system although gradient bias remains the same [216].

Correction of these errors by formula, as suggested by Keane and Adrian [215], does not improve the signal-to-noise ratio in the auto-correlation function but tries to correct the measured displacement. It is proposed here that a correction technique based on deforming the analysis area from a multi-pulse recording will improve the signal-to-noise ratio and correct for both detection bias and gradient bias. A technique for correcting the same errors in cross-correlation analysis methods has been presented by Huang *et al.*[235,236] and Jambunathan *et al.*[237]. The analysis image from the second recording is deformed according to the velocity gradients detected after an initial conventional PIV analysis stage. An iterative procedure is then employed to minimise errors from velocity gradients. Missing velocity vectors are interpolated in order to estimate the velocity gradients in unanalysable areas of the flow. With this information, initially unanalysable areas yield PIV data after the iterative analysis stages. Unfortunately, the approach adopted in the cross-correlation case is not readily extended to auto-correlation analysis and an alternative method is required.

3.5.2 Method

Principle

An ideal PIV image would be divisible into small analysis areas in which particle images are separated by the same displacement. The aim of this section is to develop an algorithm that will take a PIV analysis area meeting all the usual recording and analysis recommendations[215], but containing velocity gradients, and transform this image to give something closer to the ideal. Such an ideal image is essentially of a one dimensional flow and would have equally spaced parallel streamlines. In contrast, the image requiring correction may have apparent variations in velocity across the analysis area arising from spatial velocity gradients, accelerating motion, compressible flow, a three dimensional component to the flow, and noise. Correcting for the apparent velocity gradients redresses all these factors to some extent.

For a two dimensional flow, the stream function [335] is defined as follows:

$$\frac{\partial \psi}{\partial y} = u \tag{3.17}$$

$$= \frac{\partial u}{\partial x}x + \frac{\partial u}{\partial y}y + u_0 \tag{3.18}$$

$$-\frac{\partial \psi}{\partial x} = v \tag{3.19}$$

$$= \frac{\partial v}{\partial x}x + \frac{\partial v}{\partial y}y + v_0 \tag{3.20}$$

where u and v are the x and y components of the velocity vector which can be expressed as functions relative to the velocities at the centre of the analysis area (u_0 and v_0) assuming a linear velocity gradient. The stream function defined in this way represents in incompressible flow that obeys continuity. On integration equations (3.18) and (3.20) give:

$$\psi = \frac{\partial u}{\partial x}xy + \frac{\partial u}{\partial y}\frac{y^2}{2} + u_0 y + 0 \tag{3.21}$$

$$\psi = -\frac{\partial v}{\partial x}\frac{x^2}{2} - \frac{\partial v}{\partial y}xy + v_0 x - 0 \tag{3.22}$$

if $\psi = 0$ at (0,0). Clearly these equations are only compatible for incompressible flows, where $\frac{\partial u}{\partial x} = -\frac{\partial v}{\partial y}$. However, if the velocity gradients affecting the u component of velocity were corrected then equation (3.21) represents streamlines equally spaced in the x direction and the appropriate expression for the stream function can be used to correct for velocity gradients involving v.

Deforming the analysis area

Consider an arbitrary point (x, y) in the analysis area: the spacing between particle images in the x direction at this point is proportional to the x component of velocity, u, at this point. If this velocity is compared with the velocity at the centre of the analysis area, u_0, then this point should be moved to x_{un} in a scaling process that equalises the separation of particles in the x direction. That is:

$$\frac{x}{x_{un}} = \frac{\frac{\partial u}{\partial x}x + \frac{\partial u}{\partial y}y + u_0}{u_0} \tag{3.23}$$

or

$$x_{un} = \frac{u_0 x}{\frac{\partial u}{\partial x}x + \frac{\partial u}{\partial y}y + u_0} \tag{3.24}$$

This is presented as an intuitive result; the result can be derived rigorously and is presented in Appendix C.

Problems with division by zero can be avoided by an initial rotation of axes and re-calculation of the velocity gradients in the new coordinate frame. If the x axis is aligned with the velocity vector there is least likelihood that the x component of velocity will change sign in the analysis area. $\frac{\partial v}{\partial x_{un}}$ is now a function of x_{un}. If all the points were transformed at once this would give an intermediate image where $\frac{\partial u}{\partial x_{un}}$ and $\frac{\partial u}{\partial y}$ are both zero. The stream function in this intermediate analysis area is now defined by:

$$\frac{\partial \psi}{\partial y} = u_0 \tag{3.25}$$

$$-\frac{\partial \psi}{\partial x_{un}} = \int_0^{x_{un}} \frac{\partial v}{\partial x_{un}} \partial x_{un} + \frac{\partial v}{\partial y}y \tag{3.26}$$

$$\psi = u_0 y - \int_0^{x_{un}} \int_0^{x_{un}} \frac{\partial v}{\partial x_{un}} \partial x_{un} \partial x_{un} - \frac{\partial v}{\partial y} x_{un} y \tag{3.27}$$

Noting that as a result of the change of axes v_0 will be zero and that $\int_0^{x_{un}} \frac{\partial v}{\partial x_{un}} \partial x_{un}$ must be $\frac{\partial v}{\partial x} x$ then

$$\psi = u_0 y - \int_0^{x_{un}} \frac{\partial v}{\partial x} x \partial x_{un} - \frac{\partial v}{\partial y} x_{un} y \tag{3.28}$$

and substitution for x in terms of x_{un} allows an analytic solution or in a numerical estimate of the integral. It should be noted that if the flow were incompressible then the last term in equation (3.27) would be zero and differentiation with respect to y would give the expected answer. Here this term is retained as the flow may be compressible and equation (3.27) used to give a function that can be used for correcting velocity gradients arising from density changes in the flow. In this work MAPLE, a symbolic mathematical package, was used to carry out the integration and generate suitable code to calculate the exact value of the integral.

The stream function at the point in the transformed area (x_{un}, y) is calculated using equation (3.28), this must then be equal to the stream function in the analysis area when $\frac{\partial v}{\partial x_{un}}$ and $\frac{\partial v}{\partial y}$ are zero. That is:

$$u_0 y_{un} = \psi = u_0 y - \int_0^{x_{un}} \frac{\partial v}{\partial x} x \partial x_{un} - \frac{\partial v}{\partial y} x_{un} y \tag{3.29}$$

The point (x_{un}, y_{un}) has now been deformed from the point (x, y) and can be transformed back to the original coordinate frame. The coordinates for the point in the deformed analysis area in the original coordinate frame (x', y') will generally not correspond to an exact pixel location and the intensity is conventionally divided between four neighbouring pixels as adopted by Huang *et al.* [236]. Supposing

$$x' = x_0 + \delta x \tag{3.30}$$

$$y' = y_0 + \delta y \tag{3.31}$$

where x_0 and y_0 are the integer parts of x' and y', and δx and δy are the real remainders, then if the intensity of the point is $I(x', y')$ then

$$I(x_0, y_0) = I(x', y')(1 - \delta x)(1 - \delta y) \tag{3.32}$$

$$I(x_0, y_0 + 1) = I(x', y')(1 - \delta x)\delta y \tag{3.33}$$

$$I(x_0 + 1, y_0) = I(x', y')\delta x(1 - \delta y) \tag{3.34}$$

$$I(x_0 + 1, y_0 + 1) = I(x', y')\delta x \delta y \tag{3.35}$$

Particle images may overlap in the distorted image as the deformation effectively broadens particle images. The intensity at a point in the deformed analysis area must be the sum of all contributing intensities calculated using the above method considering all points in the original area. Points that are deformed to positions outside the original analysis area are ignored.

This procedure should give an interrogation area with no velocity gradients that can be processed by conventional analysis methods.

Determination of velocity gradients

Velocity gradients were calculated using the NAG interpolation routine E01SAF that implements the method of Renka and Cline for interpolation given a set of randomly located data points. This routine calculates and uses the velocity gradients at each data point. The routine was also used to extrapolate velocities in unanalysable regions and thus estimate the velocity gradients in these areas.

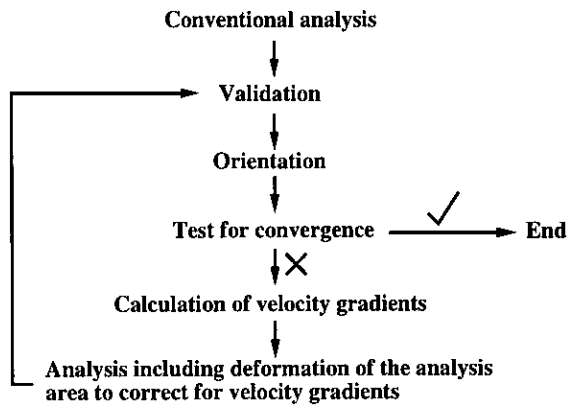


Figure 3.24: The iterative procedure used to correct the velocity fields produced from multi-pulse PIV recordings that include significant velocity gradients.

Iteration

A reliable method for validating and orienting velocity vectors is required after each analysis stage: the method described in the previous section was used. Iteration should give progressively better estimates of the velocity field with convergence assumed when successive velocity measurements differ by less than a given threshold. Here, the post processing algorithm for orienting and validating velocity vectors described in section 3.4 has been used. The iteration procedure is shown in Figure (3.24).

3.5.3 Applying the technique to a simulated Oseen vortex

A similar example flow field has been chosen to that used by Huang *et al.*[236]. The velocity distribution for an Oseen vortex located at the origin of a polar coordinate system is given by:

$$u_\theta = \frac{\Gamma}{2\pi r}\left(1 - e^{\frac{-r^2}{4\nu t}}\right) \tag{3.36}$$

$$u_r = 0 \tag{3.37}$$

and the vorticity is

$$\Omega = \frac{\Gamma}{4\pi vt} e^{\frac{-r^2}{4vt}} \tag{3.38}$$

where Γ is the circulation, v the flow kinematic viscosity, and t the time in appropriate units.

The only non-zero derivative of velocity is given by

$$\frac{\partial u_\theta}{\partial r} = -\frac{\Gamma\left(1 - e^{-\frac{r^2}{4vt}}\right)}{2\pi r^2} + \frac{\Gamma e^{-\frac{r^2}{4vt}}}{4\pi vt} \tag{3.39}$$

A PIV image 693 by 693 pixels was generated using a Monte-Carlo technique with the centre of the vortex at the centre of the recording, a circulation, $\Gamma = 5000[pixel]^2/s$, and $vt = 2000[pixel]^2$. 1200 particles were recorded as a series of four images of e^{-2} diameter four pixels, with four simulated illumination pulses 4 seconds apart, and with a Gaussian intensity profile, with a maximum intensity of 256 (out of a realisable range of 256). The simulated image is shown in Figure(3.25).

Figure (3.26a) shows a typical analysis area containing velocity gradients and Figure (3.26b) the resulting analysis area after correcting for velocity gradients. Figures (3.27a) and (3.27b) show the respective auto-correlation functions.

The results of a conventional PIV analysis are shown in Figure (3.28). Figure (3.28a) shows the unvalidated vector map. Figure (3.28b) shows this velocity map after removing vectors 3 standard deviations away from the global mean velocity or 1.4 standard deviations away from the local median velocity, and vectors which are oriented at an angle greater than $\frac{\pi}{8}$ from the local median velocity. Figure (3.28c) shows the variation in u_r as a function of distance from the centre of the vortex, r. Figure (3.28d) shows the variation of u_θ with r. Analysis was carried out using standard digital techniques [218] with an analysis area of 63 by 63 pixels with a 21 pixel spacing between areas. It is clear from Figure (3.35) that inequalities discussed in the introduction are not always met.

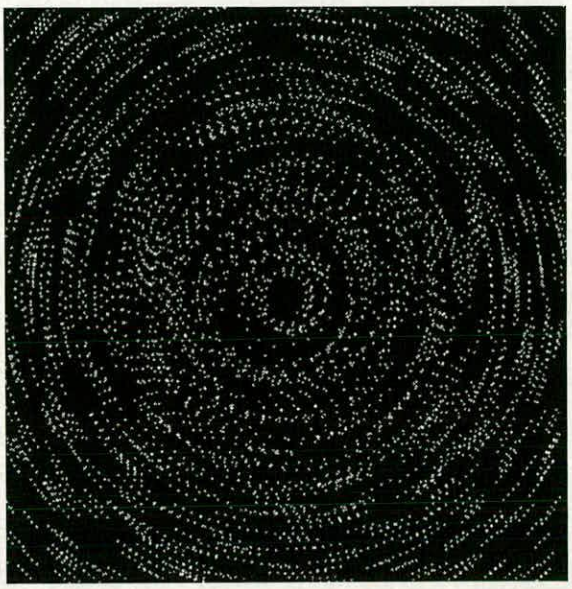
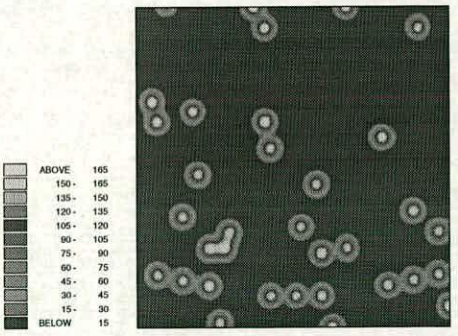
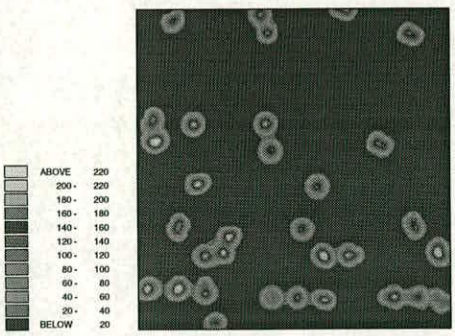


Figure 3.25: A simulated PIV image of an Oseen vortex - see text for details

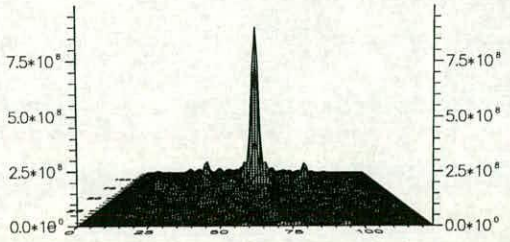


a)

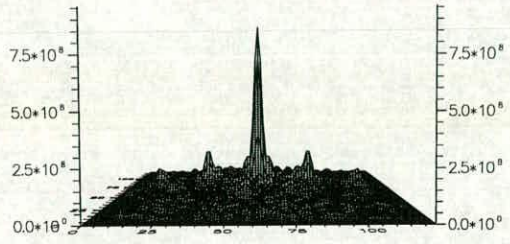


b)

Figure 3.26: **a)** A PIV analysis area before correction for velocity gradients and **b)** the analysis area after correction



a)



b)

Figure 3.27: **a)** The auto-correlation function from the PIV analysis area before correction for velocity gradients and **b)** the auto-correlation function after correction

Figure (3.29) shows the same set of information after one iteration using the deformation analysis. Figures (3.30) and (3.31) show the results after five and ten iteration steps respectively. The results of smoothing the velocity map after the tenth iteration are shown in Figure (3.32): Figure (3.32a) shows the smoothed velocity map, Figure (3.32b) the variation in u_r as a function of distance from the centre of the vortex r, and Figure (3.32c) the variation of u_θ with r. The velocity map was smoothed using a simple nine point mean. The number of invalid vectors detected and the standard deviation of non-zero values for u_r after each iteration step are shown in Figure (3.33).

3.5.4 Discussion

The auto-correlation functions for analysis areas before and after correction for velocity gradients show that when velocity gradients have been removed from the area the peaks

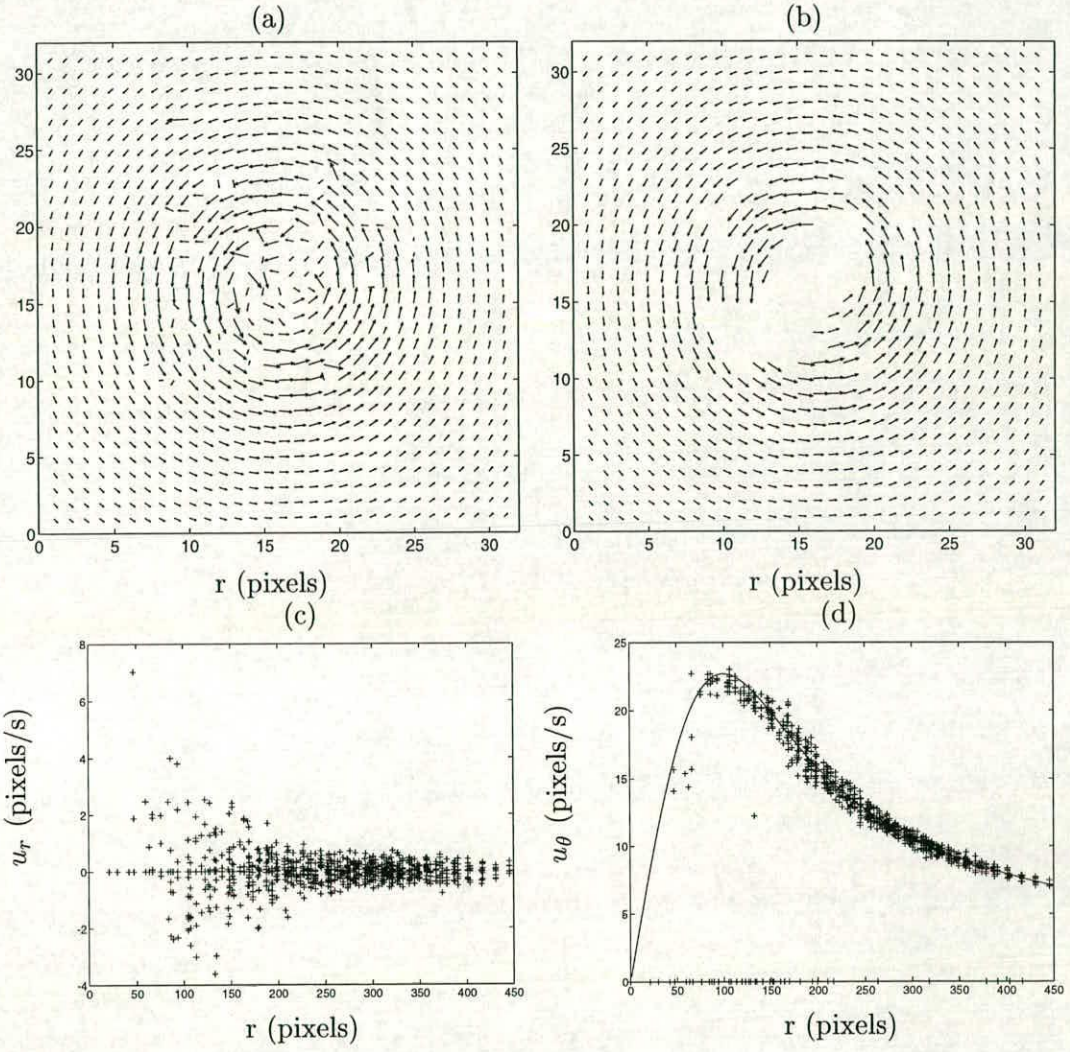


Figure 3.28: The result of conventional PIV analysis: **a)** the raw velocity field, **b)** the velocity field after validation, **c)** the variation of u_r with r, and **d)** the variation of u_θ with r.

are clearer. The signal peak is slightly larger after correction and the second harmonic peak is much larger. The deformed analysis area shows that the particle tracks have been aligned with the mean velocity at the centre (along the horizontal) and the spacing between particle images is more uniform.

The sequence of Figures (3.28-3.31) shows that even with one iteration where the analysis area is deformed there was a significant increase in the number of valid vectors detected and a decrease in the spread of results. The effect was more pronounced for five iterations of the deformation analysis algorithm and ten iterations gave little further

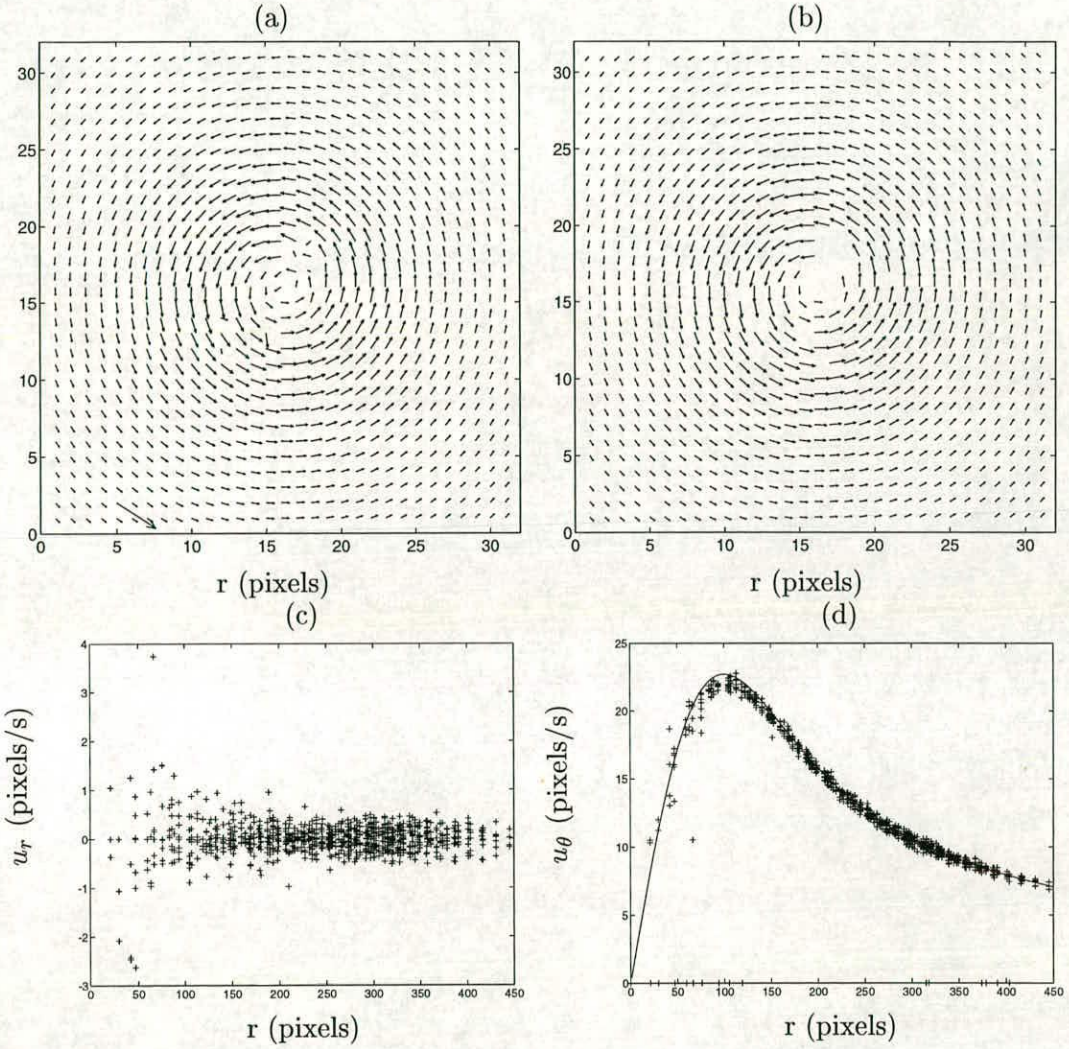


Figure 3.29: The results after one iteration of the analysis method including deformation: **a)** the raw velocity field, **b)** the velocity field after validation, **c)** the variation of u_r with r, and **d)** the variation of u_θ with r.

improvement. This is seen in Figure (3.33) where the percentage of invalid vectors and the standard deviation in u_r decreases little after the first four or five iterations. This gives an indication that the centroid of the signal peak is determined with an accuracy of ± 0.35 pixels. These results agree well with those produced by Huang *et al.*[236] for their correction to the cross-correlation analysis technique for a similar simulated flow. The twelfth iteration gave an increase in the number of invalid vectors detected at the centre and edge of the vorticity field. This iteration step gave a vector field for which the validation criteria were probably too stringent.

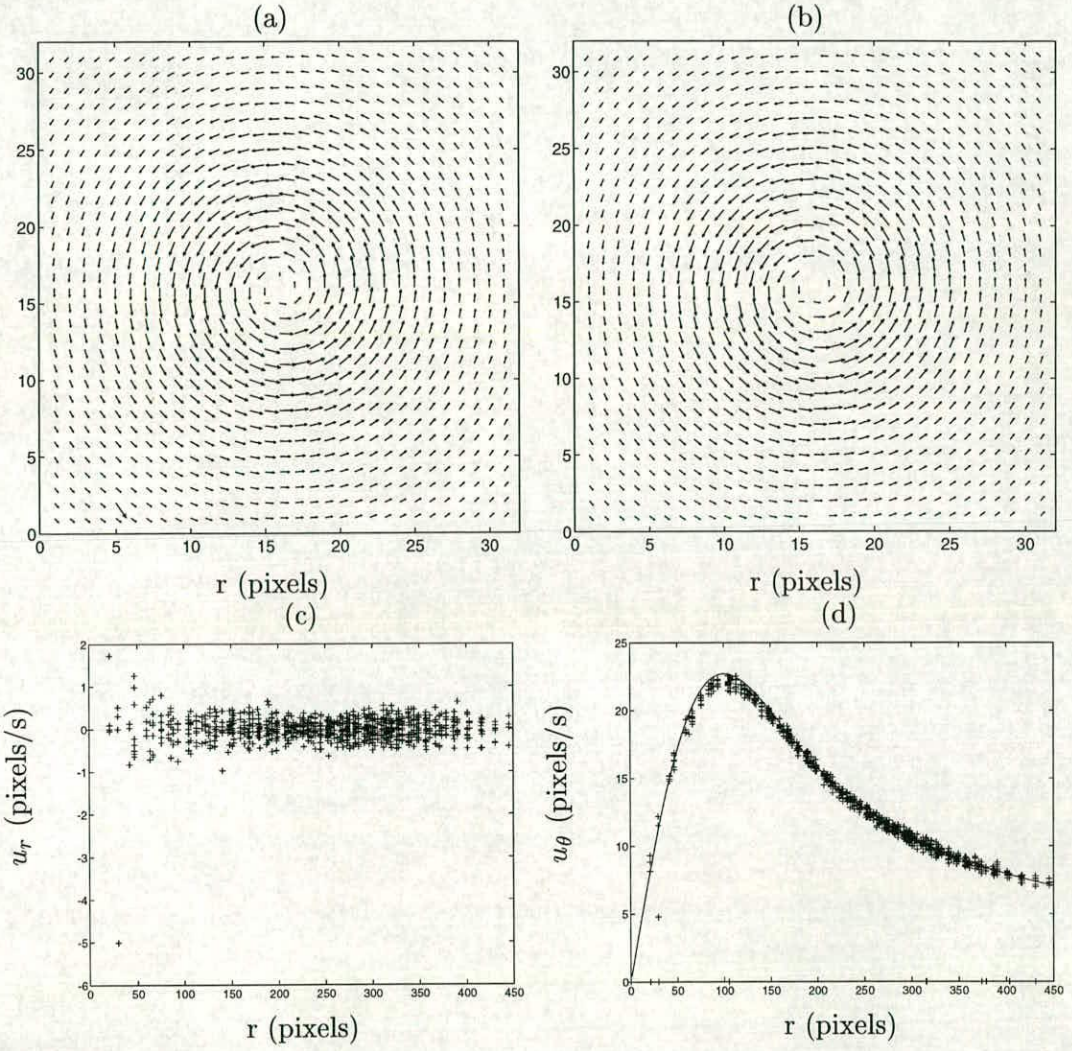


Figure 3.30: The results after five iterations of the analysis method including deformation: **a)** the raw velocity field, **b)** the velocity field after validation, **c)** the variation of u_r with r, and **d)** the variation of u_θ with r.

The assumption of a linear velocity gradient is obviously incorrect in some analysis areas although the algorithm still produces reasonable correction. More complicated expressions could be incorporated into the deformation algorithm. The overhead in performing the deformation of the analysis area is about nine times the time required to calculate the auto-correlation function for a 63 by 63 area. So five iterations of the analysis including deformation would increase the total time for analysis six fold. In this case each analysis iteration with deformation required about 1 minute on a SUN SPARC station 20 with four processors. This estimate will obviously depend on the nature of the flow. An improvement in speed may be achieved by direct calculation of

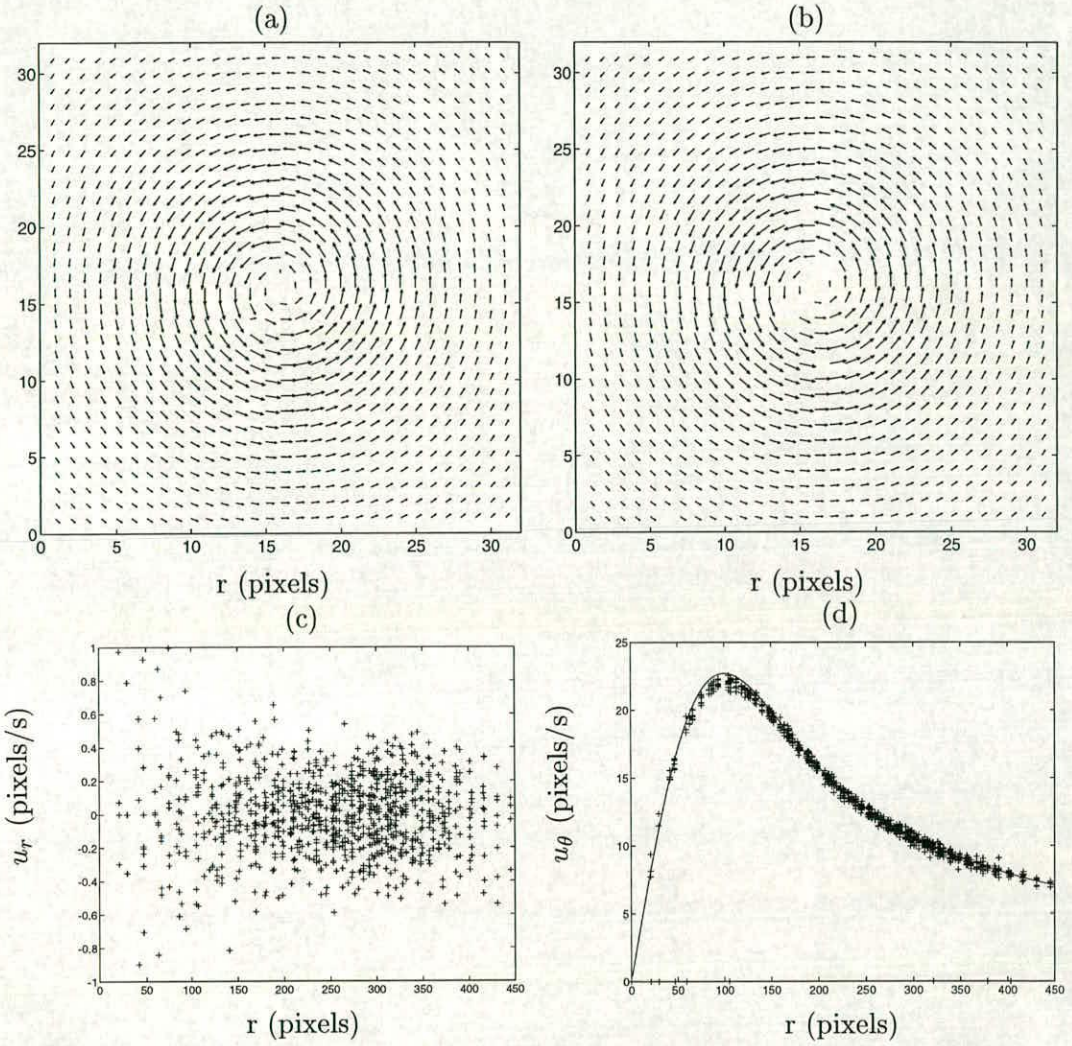


Figure 3.31: The results after ten iterations of the analysis method including deformation: **a)** the raw velocity field, **b)** the velocity field after validation, **c)** the variation of u_r with r, and **d)** the variation of u_θ with r.

the auto-correlation function around the area where a valid signal peak was found in the previous analysis step.

A reliable computational method for validating velocity vectors is required between analysis steps that should err on the side of caution to avoid any invalid vectors. Such erroneous vectors would introduce incorrect velocity gradients and lead to a much reduced signal peak. The number of iterations required for the vector field to converge will be increased if incorrect vectors are not removed and they may inhibit convergence.

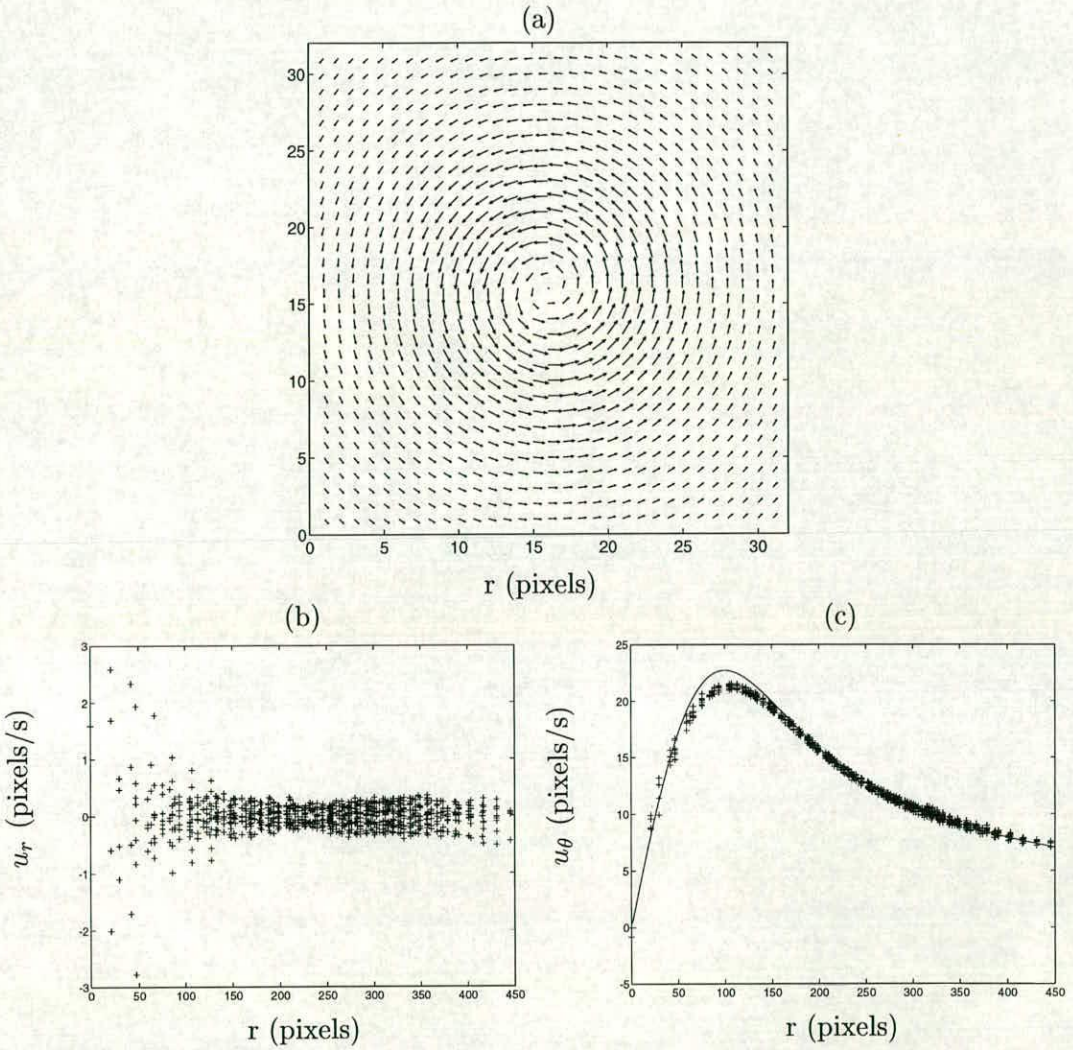


Figure 3.32: The results after ten iterations of the analysis method including deformation: **a)** the velocity field after validation and smoothing, **b)** the variation of u_r with r, and **c)** the variation of u_θ with r.

After correcting for velocity gradients there is still bias in the measured results as can be seen in Figure (3.31) that is greatest for high velocities. The use of a simple smoothing scheme, Figure (3.32) is also seen to introduce bias into measurements in areas where the velocity gradient is high, to some extent negating the improvement produced by deforming the analysis area. A plot of the ratio of $u_{\theta,measured}$ to $u_{\theta,expected}$ as a function of the dimensionless velocity gradient, Figure (3.36) shows that the measurement bias remains within 6% up to values of the dimensionless velocity gradient of 0.4. This is a significant improvement over the results obtained by Keane and Adrian[215] where it is recommended that this dimensionless velocity gradient is less than 0.05 to limit

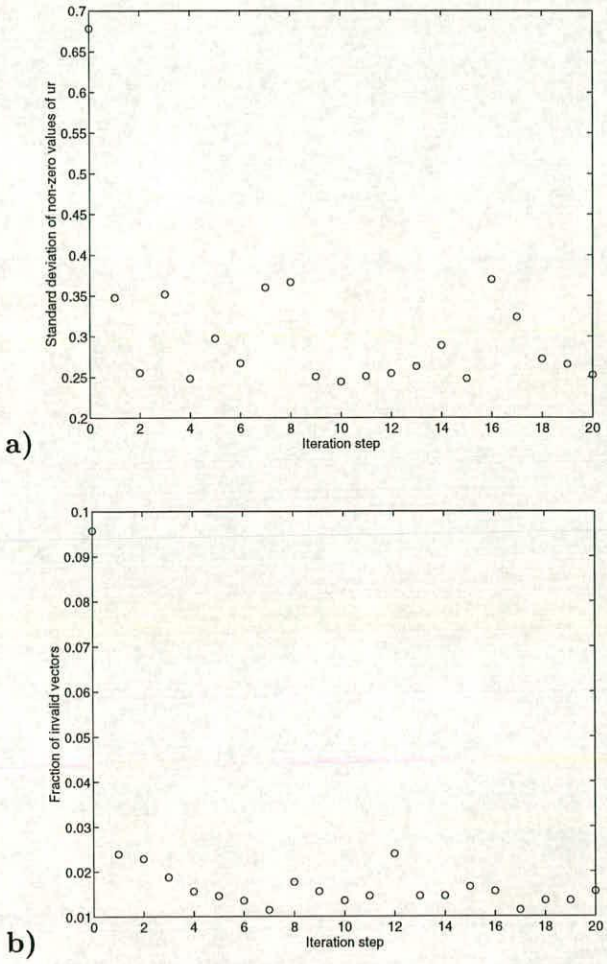


Figure 3.33: **a)** The variation in the standard deviation of u_r and **b)** the fraction of invalid vectors detected after each iteration step.

the bias to 6%. After normal PIV analysis the mean value of $\frac{u_\theta\, measured}{u_\theta\, expected}$ is 0.99 with a standard deviation of 0.41. After ten iteration steps this value remains 0.99 with a standard deviation of 0.024. This compares well with the accuracy expected from typical PIV recordings of about 2.5% [215]. Application of the deformation algorithm gives measurements in flows containing appreciable velocity gradients with almost the same accuracy as investigations where the flow contains velocity gradients meeting previous criteria.

Quantities derived from vector maps are of importance in visualisation and determining flow structures and features. Figure (3.37) shows the variation in measured vorticity compared with the expected value. The measurements of vorticity agree with the

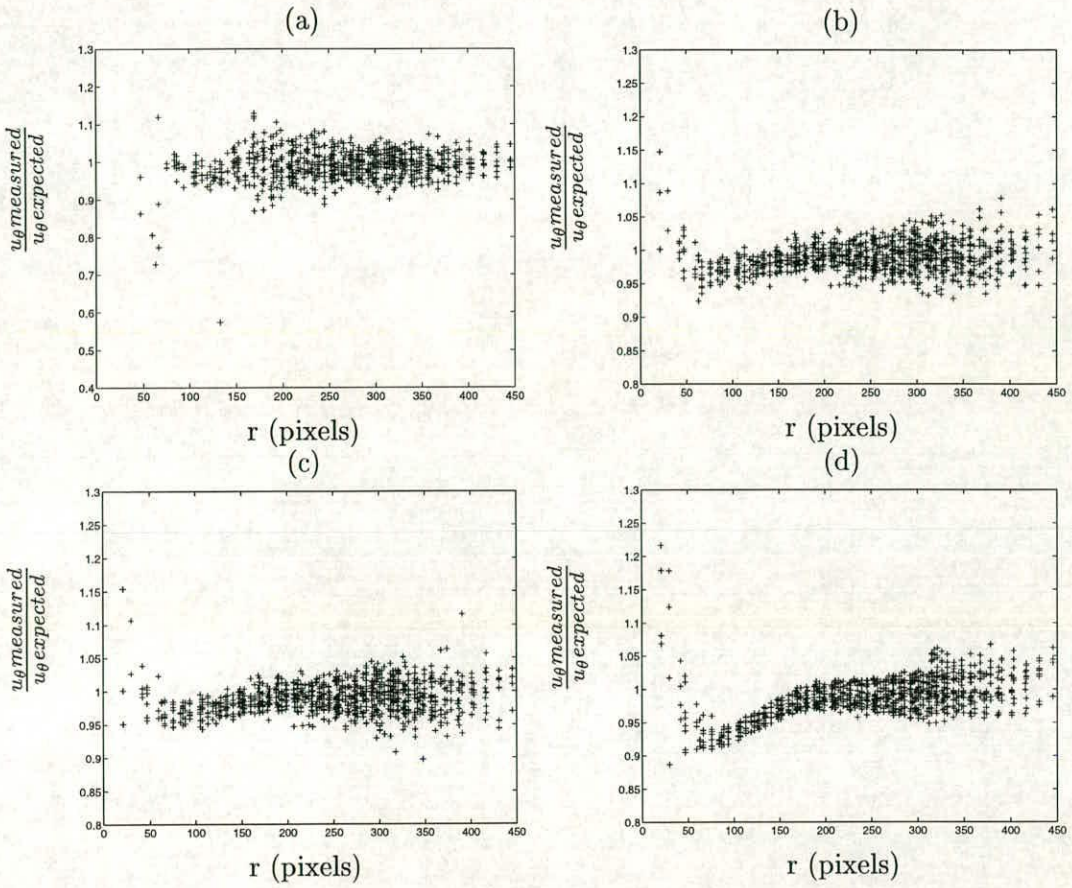


Figure 3.34: The ratio of the measured value for u_θ divided by that expected as a function of r, Figures a), b), c), and d) show the results after normal analysis, five iterations, ten iterations, and ten iterations with smoothing.

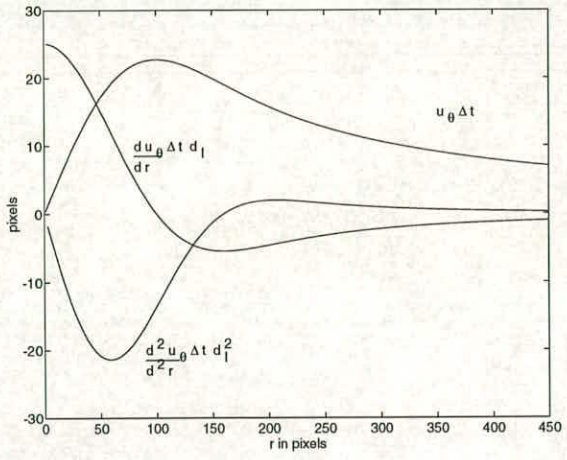


Figure 3.35: The variation of u_θ and its first and second derivative with respect to r as a function of r.

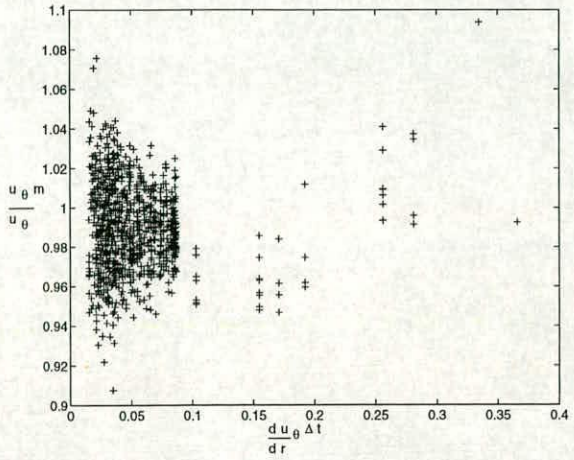


Figure 3.36: The variation in the detected value for u_θ divided by the expected value as a function of the dimensionless velocity gradient.

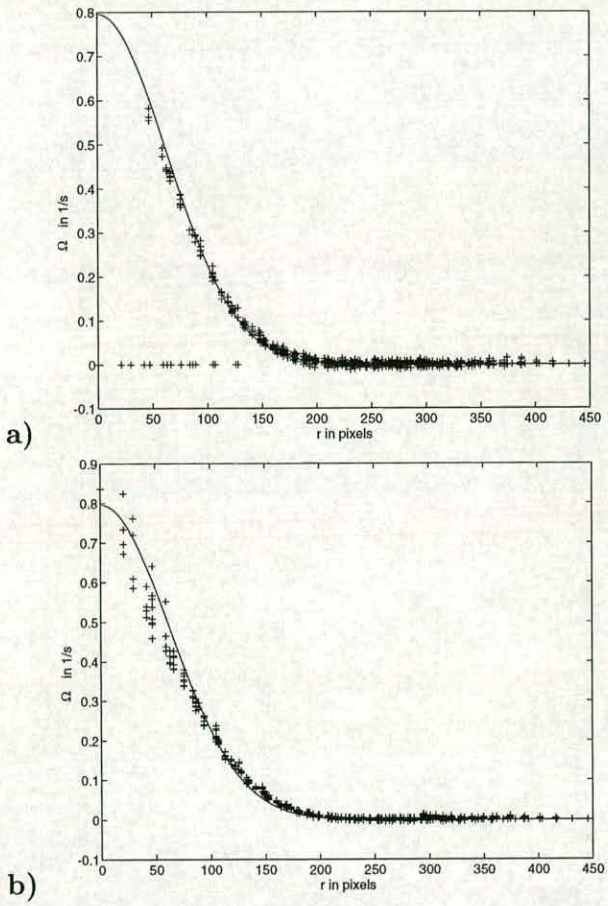


Figure 3.37: **a)** the variation of vorticity with r calculated after ten iterations, **b)** the variation in vorticity calculated after ten iterations and smoothing. The expected value for vorticity is shown for comparison.

expected values for the unsmoothed data but giving a slight underestimate at the higher vorticities. The smoothed results give a greater under estimate at higher values of vorticity. This under estimate is associated with positive values of $\frac{\partial u_\theta}{\partial r}$. Where this velocity gradient is negative the vorticity tends to be over estimated.

3.5.5 Conclusions

An algorithm has been presented that deforms analysis areas used in the auto-correlation analysis of PIV images to remove velocity gradients from the analysis area. This is an iterative procedure using the results from previous analysis stages and requires a reliable validation and orientation step between iterations. Correction for velocity gradients improves the signal quality and yields velocity data from previously unanalysable areas. The bias in velocity measurement is also reduced. PIV recordings of flows that can not be made and analysed without including velocity gradients can be more reliably analysed relaxing the recommendations made by Keane and Adrian [215]. Analysis areas with $\frac{M \mid \Delta u \mid \Delta t}{d_I} < 0.4$ gave results within 6 % of those expected as opposed to $\frac{M \mid \Delta u \mid \Delta t}{d_I} < 0.05$ as recommended for conventional analysis[215]. The use of a simple smoothing algorithm can increase the errors in regions where there are appreciable velocity gradients.

3.6 Analysing two-phase flow data

In separate flow studies in collaboration with Dr. D. McCluskey, the above techniques were applied to the analysis of two-phase PIV images. The section is concerned with the separation of the images associated with the seeding of each phase.

The investigation of two phase flows arose out of the work of McCluskey *et al.*[22] in studying particle roping effects, but is of interest in other areas as demonstrated by Hassan *et al*[336] who studies the induced flow of a liquid caused by rising bubbles. In the latter work, the bubble image was subtracted from a sequence of digital images by fitting both Gaussian and $\frac{1}{r^2}$ intensity profiles to the bubble image. The $\frac{1}{r^2}$ intensity

profile was found to give the best match. The fitted profile was subtracted from the image to leave the images of particles used to seed the fluid in and around the region of the bubble.

A similar approach could have been adopted to separate the images of the air seeding and transported particle images in the analysis of particle roping PIV recordings. However, the difference in radii of the two types of particle image is less than in the previous study and there is little to be gained from attempting to separate particles out in this way. There is no advantage in trying to resolve air phase seeding within the transported particle image. Instead, particles in the images above a selected diameter, with an eccentricity below a chosen value, and with an intensity exceeding a given threshold are identified and copied into a separate digital image. The air phase seeding PIV image is obtained by subtracting this image from the original.

3.6.1 Method

Particles are identified by considering a horizontal line within the image and locating the leading and trailing edges using the intensity and the intensity gradient. At the mid point between two detected edges, a vertical line in the image is considered and the leading and trailing edges of the particle are detected using the same criteria. If the eccentricity of the two radii calculated using this method is below a given value and the radius is above a given value then the estimate radii are used to approximate the limits of a particle image. The position and orthogonal estimates of the radius are calculated using volume moments. The location and radius are added to a list of discovered particles and the procedure repeated throughout the remainder of the image. When all the image has been considered the particles are deleted.

The radius of the deleted area is larger (by a chosen factor) than the particle detected. This ensures that all of a large particles image will be removed from the smaller phase seeding information in an attempt to minimise the noise in this phase. The separated recording containing the seeding particle images from the larger phase will contain some additional noise from the smaller seeding phase but should have little effect on

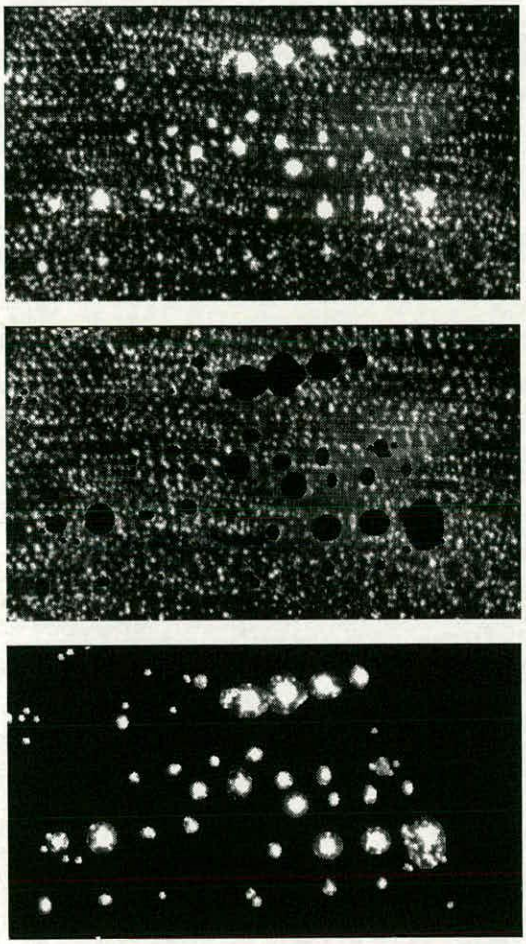


Figure 3.38: A simulated two phase recording and the separated seeding phases

the results for this phase. It is inevitable that in digitising the recording the information from one phase will be over sampled, this may be scaled down to speed analysis. An example of the combined and two separated images is shown in Figure 3.38.

3.6.2 Discussion

The technique is described by Hind *et al.*[21] and McCluskey *et al.*[22] and used by Jakobsen *et al.*[233] to study particle conveying in a pipe bend.

The initial application of the technique gives reasonable separation of the two image phases although some cross-talk between the images was observed[233]. However, it is

clear that the direct measurement of slip velocity is possible.

The image separation may be improved by fitting Gaussian profiles to detected particles or identifying particles using methods similar to those used in particle tracking. The method used here was chosen to allow for the separation of overlapping particle images, a phenomenon that has presented some problems in particle tracking applications.

The preliminary work is encouraging but further work is required in optimising the method to separate particle images, in considering how they should be deleted and the intensity with which they should be replaced, to assess the cross-talk between the separated images and how this affects the error associated with the determined velocity vector.

Chapter 4

Experimental Equipment

The flow system used in this work was relatively simple. It was designed to duplicate the flow conditions used by Christy[1] who investigated the clotting behaviour of a blood analogue fluid about a range of bluff bodies and mechanical heart valve prostheses. The purpose of the experimental equipment described here was to correlate flow features, determined using the PIV technique, to the clotting behaviour observed in the earlier work.

4.1 Flow system

In steady flow applications approximately 25 litres of water was stored in a 120 litre tank, open to atmosphere, and seeded with one of a range of seeding materials discussed later. The tank contained a partition to separate the returning flow from the exit situated near the bottom of the tank. The tank was elevated relative to the pump to avoid cavitation and air ingress as bubbles in the flow would obscure particle images in the PIV recording. From the tank the water flowed to the suction side of a Stewart & Turner 10H single-stage, centrifugal pump. There was a valve on the suction side of the pump to prevent leakage of the tank contents when not in use. The output from the pump flowed into a PVC flow-straightening section of pipe before entering a Perspex™ test section. The flow was regulated using a globe valve and measured using a metric, size 14, rotameter; both placed before the flow-straightening section.

From the test section, the flow passed through another short section of PVC pipe and was then returned to the tank via a 13 mm internal diameter plastic tube with a wall thickness of 0.2 mm. The same specification plastic pipe was used for all other connections. Connections between PVC and Perspex™ pipe sections were secured by flanges and sealed using rubber gaskets. All hose connections were fixed using hose-clips. A schematic of the flow system is shown in Figure (4.1).

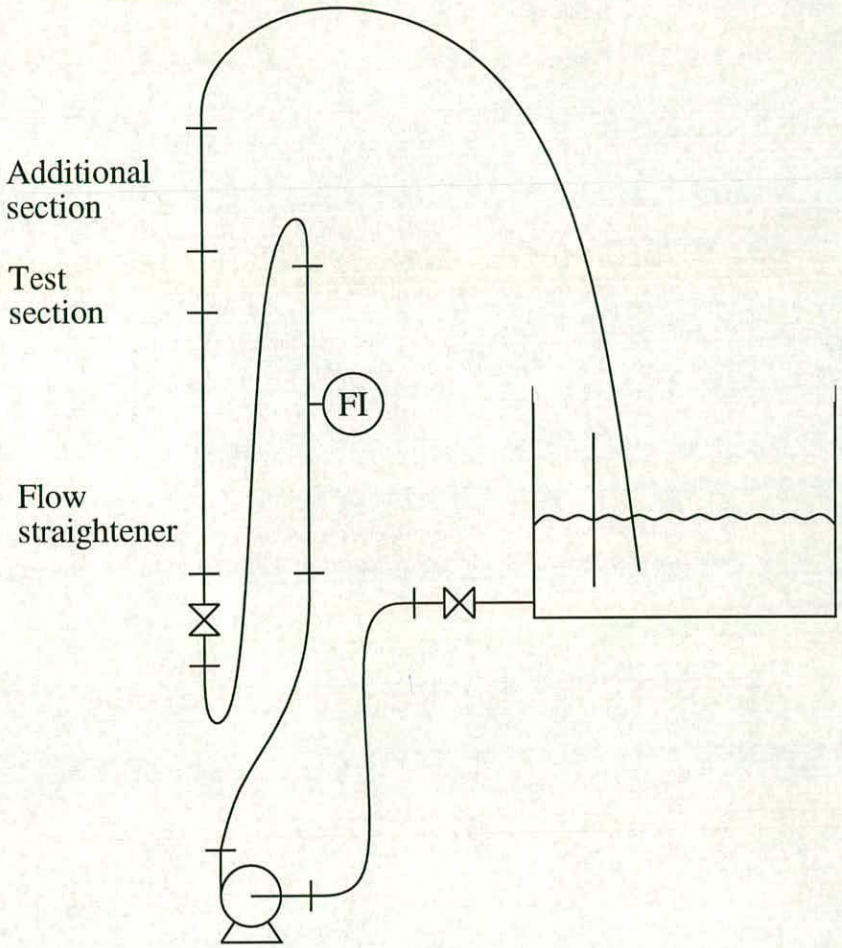


Figure 4.1: Steady flow arrangement of the test rig.

The flow-straightener was constructed from a length of PVC tube with an internal diameter of 32 mm and a length of 625 mm to the ends of which were fixed two 9 mm thick flanges. A 50 mm cylindrical block of PVC with a series of 43, 3 mm holes, arranged symmetrically, was fixed 30 mm in from the upstream end of this section. This effectively removed gross swirl from the flow and allowed 545 mm for the flow

profile to develop. A typical flowrate in the steady flow experiments was about 2×10^{-5} m^3/s; this gave a Reynolds number, based on the pipe diameter and water as the test fluid, of about 800. The entry length required for laminar flow to develop, x_e, is given by Kay and Nedderman[335] as $\frac{2x_e}{d} = 0.0575\ Re$. For this case a length of 740 mm would be required to give a fully developed flow.

Two test sections have been used, differing only in length. In each case, the test section was made up of a length of Perspex™ tube with an internal diameter of 32 mm. Surrounding this tube a square duct with an outer side of 51 mm was constructed from 2.8 mm thick Perspex™ sheet. The cavity between the pipe and the square duct was filled with water to minimise refractive distortion when viewing or illuminating the flow. The construction of the test section is shown in Figure (4.2). The short test section has an overall length of 90 mm and the long test section an overall length of 500 mm. Again, the section was connected to the flow straightener and other sections using flanges and sealed using rubber gaskets 1.44 mm thick. An additional PVC tube section with an internal diameter of 32 mm and length 160 mm was also available to maintain the flow conditions downstream from the test section.

In pulsatile flow investigations, the centrifugal pump was replaced by a positive displacement pump. The downstream globe valve and rotameter were not included in the flow loop. The flowrate was measured by noting the time required to fill a 2 litre measuring cylinder placed in the water tank. A 300 mm section of 13 mm rubber tube was added to the flow loop to introduce some compressibility and avoid air ingress and bubble formation arising from rapid acceleration of the test fluid and the resultant pressure transients. The pump, Figure (4.3) was designed and built within the Department of Chemical Engineering. A 200 W stepper motor drives a piston mounted on a helical thrust bearing: the brass piston has a maximum distance of travel of 50 mm, a diameter of 40 mm, and a length of 120 mm. The position of the piston can be computer-controlled to allow a range of time varying flows to be produced. Alternatively, the pump can be driven by a sine wave generated within the pump power supply. The non-return valves at the inlet and outlet are made from a circular section of plastic sheet that sits over six holes, giving an operation similar to so called "Jellyfish" valves.

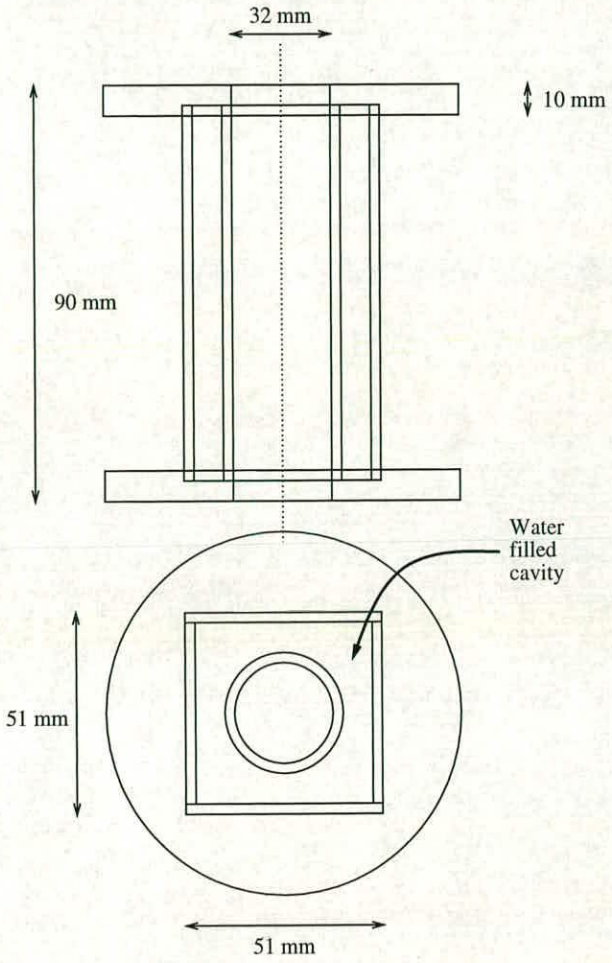


Figure 4.2: Construction of the test section.

Operating with a sinusoidal driving function of 1 Hz and with the maximum piston travel gives a theoretical flowrate of around 6×10^{-5} m^3/s. The maximum frequency of the sine wave that can be generated is restricted by the power of the motor. The piston position can be expressed as a function of time and frequency using the maximum displacement and assuming a sinusoidal motion. This allows the velocity and acceleration of the piston to be determined. The instantaneous force required can then be estimated as the mass of the water within the flow loop is roughly constant and the mean acceleration of the piston and hence the fluid is known. The product of the instantaneous required force and velocity gives the instantaneous power. The maximum instantaneous power requirement, neglecting frictional losses in the pipes and motor drive along with inertial effects of the drive shaft, is given by

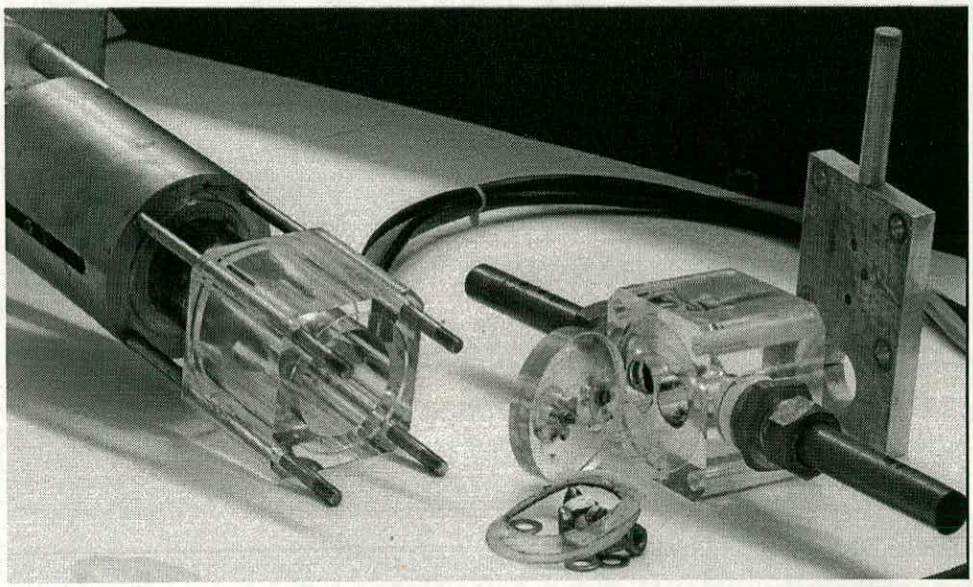


Figure 4.3: The dismantled head of the positive displacement pump used to generate pulsatile flows.

$$P_{max} = \frac{m x_{max}^2}{2} (2\pi\omega)^3 \tag{4.1}$$

where P_{max} is the maximum value of the instantaneous power, m is the mass of water moved plus the mass of the piston (kg), x_{max} is the amplitude of the piston oscillations relative to the centre position (m), and ω is the pulsation frequency (Hz).

Estimating the mass of water held in the system to be no more than 1.2 kg and the mass of the brass piston as 1.3 kg, the maximum signal frequency to which the pump could be expected to respond is about 10 Hz. A pump of similar construction, but with double the piston area, is also available in the department that would give approximately double the flowrate at any given frequency but would only respond to waveforms requiring a lower instantaneous acceleration.

A section that allowed the injection of dye or seeding material from a syringe was also used. Material was introduced along the direction of flow and the position of injection manipulated across the area of the pipe. This section was only 300 mm long and did not contain any flow straightening device after the initial expansion from the 13 mm

diameter pipe connecting the pump to the 32 mm diameter PVC injection section.

All the flow sections were securely fixed to the end of the table holding the laser and optical train to maintain the optical alignment of the system, although this was checked at the start of each experiment.

Water was used as the test fluid in all experiments. This was justified as Newtonian or near-Newtonian behaviour would be expected from blood and milk in ducts of the size used here. The Reynolds number is the key indicator of flow similarity required to obtain results that can be compared with the milk clotting experiments carried out by Christy[1] in steady flows. In unsteady flows around the test bodies the pulsatile Reynolds number $\mathrm{Re}_{pulse} = \frac{\rho d(u_{max} - u_{mean})}{\mu}$ and the Strouhal number, $\mathrm{Str} = \frac{u_{mean}}{dt}$ must also be considered. Alternatively, Christy[1,64] used the mean flow Reynolds number, the nature of the driving pulse and a frequency parameter α to define the nature of pulsatile flows. Christy's definition of α is given below.

$$\alpha = \tau\sqrt{\frac{2\pi f}{v}} \tag{4.2}$$

where f is the pulse frequency, τ the pipe radius, and v the kinematic viscosity.

In comparing the flows of milk and water it should be noted that the kinematic viscosity of milk is approximately three times that of water. As the experimental equipment is essentially that used by Christy the pulse frequency should be reduced by a factor of three. A pulse frequency of 0.4 Hz should be used with water as the test fluid to compare with the pulse rate of 1.17 Hz used by Christy[64], giving $\alpha \approx 25$. Christy also notes that doubling the value of α had little effect on the flow patterns observed behind the test bodies in dye tracer studies. For a pulse rate of 1 Hz, used in some later experiments, $\alpha \approx 40$.

4.2 Illumination System

Three methods have been used to produce a pulsed light sheet to illuminate the flow. In the first method, the beam from a 35 mW HeNe laser passed through an optical chopper, shown in Figure (4.4) and then was expanded in one direction using a plano-concave cylindrical lens with a focal length of 6 mm. The light sheet was then roughly collimated and focused using a pair of plano-convex cylindrical lenses each with a focal length of 300 mm. In the second method, a scanning beam illumination system was developed using a rotating octagonal mirror and a collimating parabolic mirror. The parabolic mirror was manufactured by machining a section of aluminium to shape and securing a front mirrored strip of polycarbonate to the aluminium using double-sided tape. This produced a marked improvement in the quality of the photographic images obtained compared with the beam expansion system. The third light sheet generation method used the multi-line output of a 4 W Argon ion laser as the light source and the same scanning beam system. This gave a one hundred-fold increase in the light available to expose each particle. In the scanning beam system the output beam from the Argon ion laser was focused using a spherical lens with a focal length of 1 m positioned approximately 1 m from the centre of the test section (measured along the beam path). The front head of the laser was approximately 0.28 m from this lens. The rotating mirror was mounted 0.65 m from the focusing lens with the beam incident on the rotating mirror approximately at the focus of the parabolic mirror. The mirror surface was roughly 0.35 m from the front of the test section. The laser head and light sheet generating optics were all enclosed. The rotation rate of the octagonal mirror is governed by a stepped voltage provided by the mirror power supply. The rotation rate can be fixed by an internal oscillator or an external frequency generator.

Figure (4.5) shows the components of the scanning mirror system. Figure (4.6) shows the overall experimental setup including the position of the optical components and the test chamber.

The rotating mirror comprises a polygon-mirror/motor assembly (model M-660-010-LVWOB from the Lincoln Laser Company) driven using a power supply based around

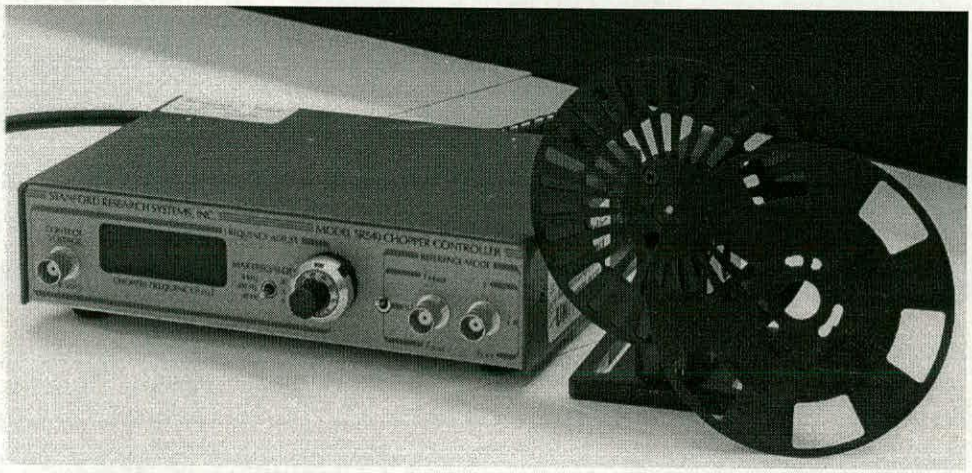


Figure 4.4: The mechanical chopper used in the initial experiments.

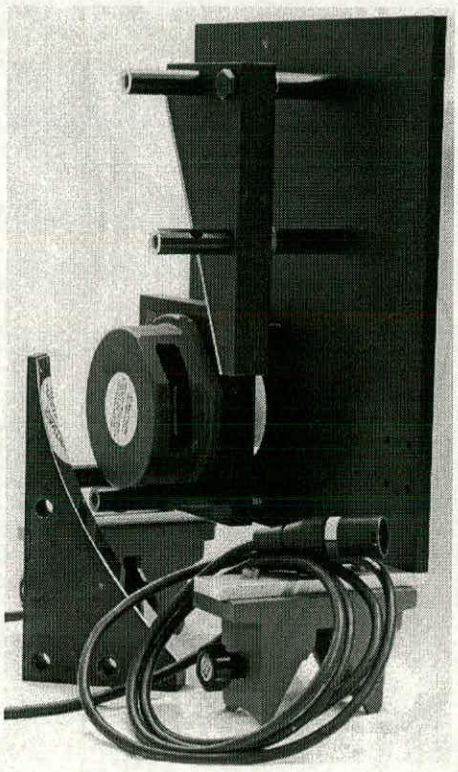


Figure 4.5: The scanning mirror system with the parabolic mirror to the left hand side.

the DC-2C driver card with drive frequency display (from the same suppliers) and developed within the department. The driver card was modified by the supplier to give rotation rates between 600-15000 rpm giving pulse frequencies in the range 80-2000 Hz. At a scanning rate equivalent to a pulse frequency of 400 Hz, as determined by the

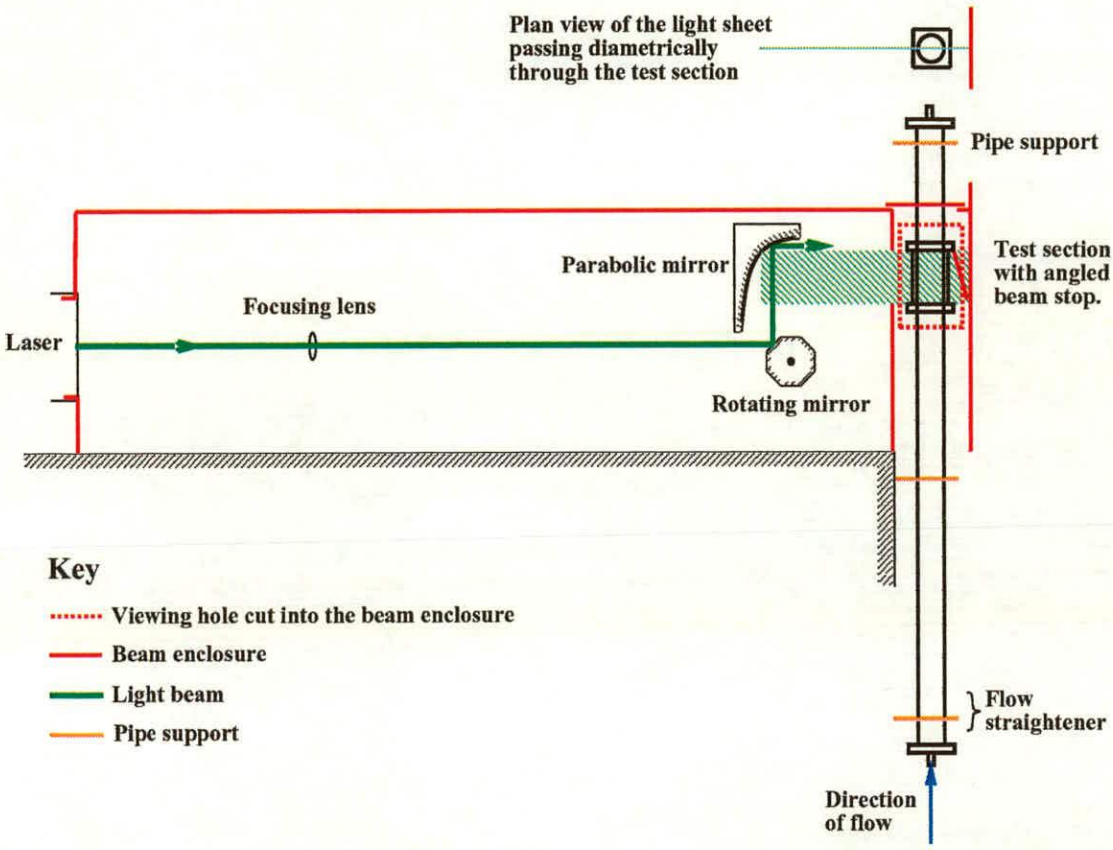


Figure 4.6: A schematic diagram of the experimental equipment, approximately to scale.

signal to the motor, the manufacturer's tests showed that 5 seconds were required for the motor to synchronise with the driving signal and a speed stability of 0.0116% was observed. Similarly, at a scanning rate equivalent to a pulse frequency of 2000 Hz the same tests showed that 29 seconds were required for the motor to synchronise with the driving signal and that the rotation rate was stable to within 0.0056%. This indicates that an error of less than 0.1% would be expected over the range of pulsation frequencies used in the experiments described in the next chapter. It is therefore reasonable to set the rotation rate of the mirror using the frequency of the signal to the drive circuit. The estimated inaccuracy compares favourably with the minimum error expected from the PIV analysis technique.

In addition to observing the local laser rules agreed with the University Laser Safety Officer the power supply for the laser was always well away from any water and poten-

tial spills. Care was taken to ensure that the rotating mirror was operational before powering up the laser to avoid damaging the mirror surface.

4.3 Seeding particles

A wide range of seeding materials have been used during the period of this study, the properties of the important ones are listed in Table (4.1). The range of Scotchlite™ Glass Bubbles manufactured by 3M proved to be too buoyant and are not included in the table. Irodin® 120 Lustre Satin - a pearl lustre pigment - comprised largely non-spherical particles that produced varying intensity images as a result of a tumbling motion as the particles followed the flow.

	Seeding					
Material	Spheriglass		Sphericel™	Al_2O_3		Conifer Pollen
Grade	3000	5000	110PS	CK	MA65	
Density (kg/m^3)	2450-2550		1100	3950		$\approx$ 1000
Refractive Index	1.51-1.52		—	1.5-1.7		—
Mean diameter (μm)	20	5	8	60	6	50
D(v,0.1) (μm) ❶	—	—	0.41	20.07	0.36	38.83
D(v,0.5) (μm) ❶	—	—	8.66	60.38	6.16	51.41
D(v,0.9) (μm) ❶	—	—	18.6	119.24	13.99	70.53
Slip velocity (m/s) ①	3×10^{-4}	3×10^{-5}	4×10^{-6}	6×10^{-3}	6×10^{-5}	0
Slip velocity (m/s) ②	3×10^{-8}	2×10^{-9}	2×10^{-9}	4×10^{-7}	4×10^{-9}	7×10^{-8}
Slip velocity (m/s) ③	1×10^{-4}	3×10^{-5}	3×10^{-6}	6×10^{-4}	6×10^{-6}	0
Λ (μm) ④	28	11	17	52	11	58

Table 4.1: Seeding particle data: ❶ determined using a Malvern Instrument's Mastersizer S (long bed), ① the terminal velocity calculated using Stokes' Law given by equation (2.5), ② The slip velocity calculated using Adrian's method[2] given by equation (2.7) and estimating the maximum acceleration to be of the order of 1 m/s^2 , ③ the slip velocity calculated according to the method of Agüí and Jiménez[3] given by equation (2.11) and estimating the lowest turnover rate of the largest structures to be of the order of the pulsation frequency (1 Hz), ④ the macro scale of turbulence expected to be resolved by the seeding particles according to the method of Lim *et al.*[4] given by equation (2.10).

For low flows, around 2×10^{-5} m^3/s, the mean fluid velocity in the pipe work was about 2.5×10^{-2} m/s. The terminal velocities for the various seeding particles calculated using Stokes' law (① in the table) and using equation (2.7) (③ in the table) are below 0.2% of the mean velocity for Spheriglass particles of grade 5000, Sphericel™ particles, the finer Al_2O_3 grade, and conifer pollen. In particular, the slip velocity of the Sphericel™ particles is expected to be below 0.02% of the mean velocity. The light scattering properties of the Sphericel™ particles, enhanced by both water-glass and glass-air interfaces, results in brighter particle images compared with the other seeding materials and considering the difference in size. Sphericel™ particles, the finer grade Al_2O_3, and conifer pollen were used in a number of investigations. In all cases, the estimated slip velocity was small or comparable to the minimum error associated with the PIV analysis technique. The scales of motion that should be resolved, as predicted by equation (2.10), seem overly optimistic: particles must affect motions of the same order of magnitude. In addition, the predicted scales do not correlate well with the sampling rate of the flow field, as discussed previously, and this method seems flawed although stated to apply in PTV investigations of flows around heart valves. There seems little to choose between seeding particles with reference to the refractive index. The most likely way to improve the light scattering response of the available seeding materials would be a silver coating process for the Sphericel™ particles. Centrifuging Sphericel™ particles made little difference to the particle size distribution except to remove the very top end of the size range. In this case the particles were left to settle for 15 minutes to remove any particles with an unexpectedly high terminal velocity.

The seeding particle concentration was adjusted from experience and the images seen while focusing the camera. The residence time of fluid within the tank was such that particles with a settling velocity greater than 8×10^{-4} m/s would be expected to deposit on the floor of the tank. When injecting particles into the flow during boundary layer visualisation experiments care was taken to match the momentum of the injected flow to that of the flow so as to produce as little disturbance as possible. This was achieved by repeated practice to produce a steady stream of seeded material flowing down the axis if the test chamber onto the centre of the upstream surface of the test body. The seeding material was injected using a bent hypodermic needle mounted into the pipe

before the test section. Both the axial and radial position of the injection point could be manipulated. In residence time investigations a pulse of seeding material was injected into the suction side of the pump.

4.4 Recording system

PIV images were recorded onto film using a Nikon F3 camera body fitted with an AF Micro-Nikkor, 105 mm, f/2.8 lens. This particular system was chosen for its rugged construction and the lens for its flat focal field and low distortion. The camera was fitted with a MD-4 motor drive capable of taking 5.6 frames per second at a shutter speed of $\frac{1}{125}$ s, 5.3 frames per second at a shutter speed of $\frac{1}{60}$ s, 5.1 frames per second at a shutter speed of $\frac{1}{30}$ s, and 4.2 frames per second at a shutter speed of $\frac{1}{15}$ s. The camera was mounted on a Manfrotto™ Art 132 Professional Tripod fitted with a cross-arm and head with three orthogonal axes of adjustment.

PIV images were typically recorded at a magnification of 0.4 onto ASA 400 film (either Kodak Tri-X Pan or Ilford HP5 *plus*, both producing similar results). The film was developed according to the manufacturers' instructions for normal or push-processing. For HeNe illumination, relatively low f numbers of f/2.8 and f/4 had to be used to provide enough light to adequately expose particle images on the film which was push-processed by $\frac{2}{3}$ to 1 stop. When using the Argon Ion laser the aperture could be reduced to f/8 or lower to give an improved depth of field and a development process that did not require push processing (reducing the noise associated with the film grain). It was then possible to use faster rotation speeds of the polygon mirror to get comparable exposures to those obtained using the HeNe laser system. Printing of PIV negatives requires high contrast and slight over exposure to produce acceptable prints. The scanning systems used for translating the prints or negatives into digital format have already been described.

The camera was synchronised with the pulsation cycle of the pump using the same control program and interface board that was used to drive the pump. Time was

Depth of field for HeNe illumination (mm)					
Magnification (M)	f number				
	2.8	4	5.6	8	11
1	0.08	0.16	0.32	0.64	1.27
0.6	0.14	0.28	0.56	1.13	2.26
0.4	0.24	0.48	0.97	1.94	3.89
0.2	0.71	1.43	2.86	5.72	11.43
0.1	2.40	4.80	9.61	19.22	38.43

Table 4.2: The depth of field as calculated from equation(2.14) for HeNe illumination at 633 nm. The depth of field would be expected to be around 80% of these value for Argon ion illumination with a wavelength of 500 nm.

d_τ (μm) when $d_p = 8$ μm with Argon ion illumination					
Magnification (M)	f number				
	2.8	4	5.6	8	11
1	11.3	13.2	16.3	21.3	28.8
0.6	8.3	9.9	12.6	16.7	22.7
0.4	7.0	8.5	10.9	14.5	19.8
0.2	5.9	7.2	9.3	12.4	17.0
0.1	5.5	6.7	8.6	11.4	15.6

Table 4.3: The particle image size as a function of the recording magnification and aperture for 8 μm seeding particles illuminated with an Argon ion laser. Recorded image sizes indicated in type face will be under-sampled using the digitisation system, those in type face are approaching the required digitisation resolution.

allowed for the flow to develop in laminar applications and for the pulsation cycle to become established in unsteady application before taking PIV recordings. In the latter case, there was usually a period of at least ten minutes while the flowrate was determined.

The depth of field and expected image size for a selected range of seeding particles and illumination conditions are given in the following tables. The depth of field is in broad agreement with that given in the data sheet for the lens.

There is obviously a balance to be struck in obtaining an appropriate depth of field, appropriate sampling of the particle image, adequate exposure, seeding particle diameter, laser power, and the rotation rate of the octagonal mirror. In practice, the required settings were determined using a series of trial investigations. Focusing was carried out

d_τ (μm) when $d_p = 50$ μm with Argon ion illumination					
Magnification (M)	f number				
	2.8	4	5.6	8	11
1	50.6	51.1	52.0	53.8	57.1
0.6	30.8	31.2	32.2	34.0	37.3
0.4	20.9	21.5	22.5	24.5	28.0
0.2	11.5	12.2	13.5	15.8	19.6
0.1	7.4	9.1	9.9	12.4	16.3

Table 4.4: The particle image size as a function of the recording magnification and aperture for 50 μm seeding particles illuminated with an Argon ion laser. Recorded image sizes indicated in type face will be under-sampled using the digitisation system, those in type face are approaching the required digitisation resolution.

d_τ (μm) when $d_p = 8$ μm with HeNe illumination					
Magnification (M)	f number				
	2.8	4	5.6	8	11
1	12.4	15.2	19.5	26.0	35.7
0.6	9.3	11.6	15.2	20.5	28.4
0.4	7.9	10.0	13.1	17.9	24.8
0.2	6.7	8.5	11.2	15.3	21.2
0.1	6.3	7.9	10.4	14.1	19.5

Table 4.5: The particle image size as a function of the recording magnification and aperture for 8 μm seeding particles illuminated with a HeNe laser. Recorded image sizes indicated in type face will be under-sampled using the digitisation system, those in type face are approaching the required digitisation resolution.

d_τ (μm) when $d_p = 50$ μm with HeNe illumination					
Magnification (M)	f number				
	2.8	4	5.6	8	11
1	50.9	51.6	53.0	55.8	60.9
0.6	31.0	31.8	33.3	36.0	41.0
0.4	21.3	22.1	23.7	26.6	31.7
0.2	12.0	13.0	15.0	18.2	23.4
0.1	8.0	9.3	11.5	14.9	20.1

Table 4.6: The particle image size as a function of the recording magnification and aperture for 50 μm seeding particles illuminated with a HeNe laser. Recorded image sizes indicated in type face will be under-sampled using the digitisation system, those in type face are approaching the required digitisation resolution.

under normal conditions using the HeNe based illumination system or at just above the minimum setting using the Argon ion laser, to give images of the actual seeding particles to determine the focus and assess the depth of field. The beam stop after the test section was angled to minimise reflections back into the test section and produced better quality PIV images.

4.5 Description of test bodies and valves

Bodies of revolution

Steady and pulsatile flow investigations were made in the vicinity of the same test bodies as used by Christy[1] but painted black to minimise glare from the light sheet. This introduced a small change in the surface roughness of the test bodies but this was not expected to play a dominant role in the flows investigated experimentally. The test bodies are shown in Figure (4.7). The test bodies were mounted along the axis of the flow on a 1.3 mm diameter sting fixed to a mounting flange. The downstream end of the test bodies were thus held at a position 50.6 mm upstream from the centre of the flange. The downstream apex tear-drop, on the left of the figure, is 10.7 mm at the widest point and measures 23.5 cm in length. Similarly, the ball-shaped body has a diameter of 10 mm, the oblate a diameter of 10 mm and depth of 3.4 mm, the upstream apex cone a projected diameter of 10 mm and length 10.3 mm, the downstream apex cone a projected diameter of 10 mm and a length of 8.8 mm, the smaller upstream apex tear-drop a projected diameter of 10.3 mm and length of 18.5 mm, and the longer upstream apex tear-drop a projected diameter of 10 mm and a length of 22.9 mm. All lengths are measured along the axis of the test body to the join with the sting. The smaller downstream apex tear-drop and the test body to the far right on the diagram were not used. Figure (4.8) shows a schematic of the mounting and illuminating of the tear drop shaped body in the test chamber. The Reynolds number, based on the diameter of the test bodies, was approximately 250 in a flow of 2×10^{-5} m^3/s.

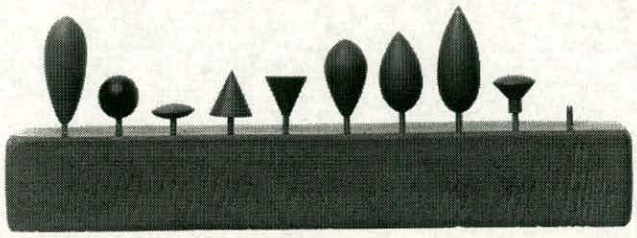


Figure 4.7: The test bodies used (excluding the one on the far right). Reproduced from Christy[1].

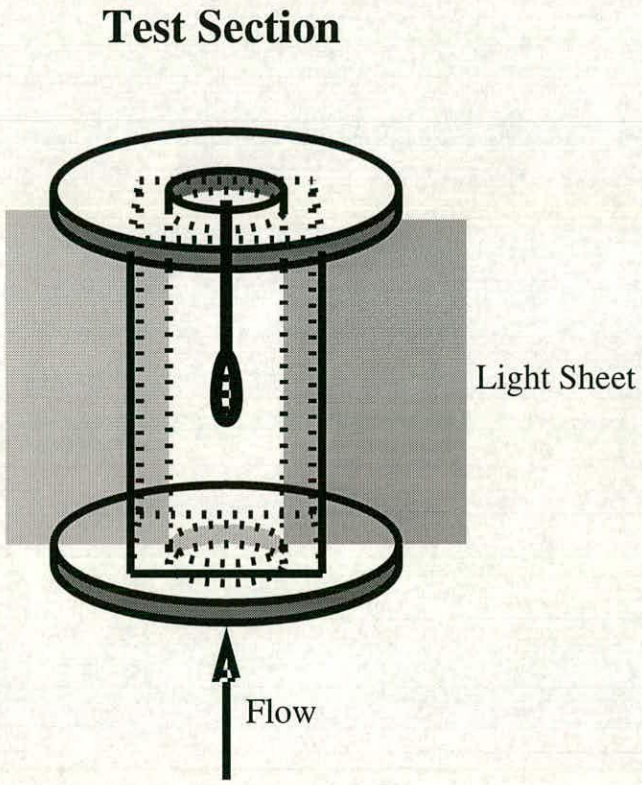


Figure 4.8: A schematic of the long downstream apex tear-drop mounted in the test section.

Test valves

The valves tested in both steady and pulsatile flow were: a valve designed by Dr. Norman Macleod with an orifice of internal diameter 23.90 mm and an aerofoil shaped occluder, a Björk-Shiley valve with an orifice of internal diameter 23.96 mm shown in Figure (4.9a), and a Starr-Edwards valve, shown in Figure (4.9b), with four enclosing

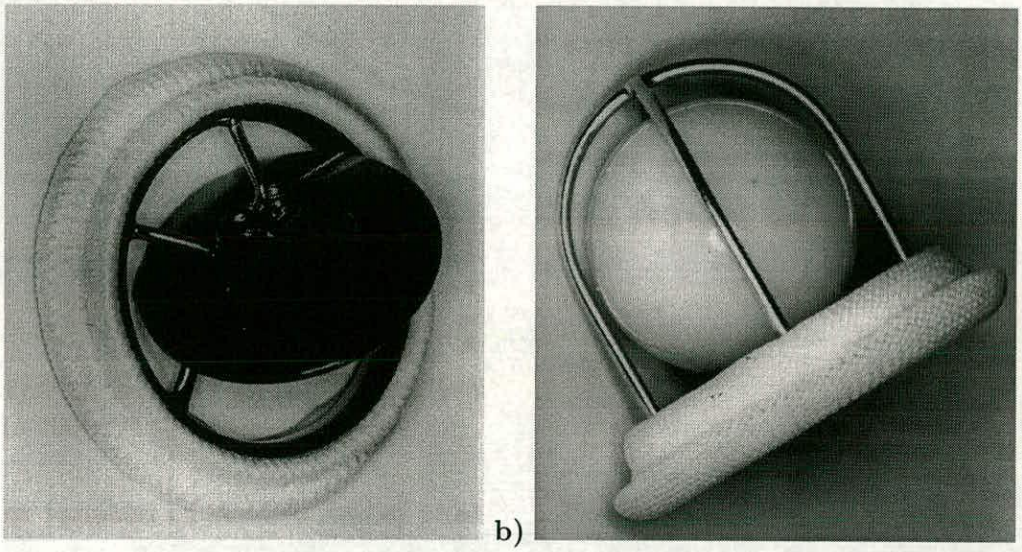


Figure 4.9: A selection of heart valve prostheses investigated: **a)** a Björk-Shiley mechanical valve and **b)** a Starr-Edwards mechanical valve.

wires of diameter 1.2 mm used to form a cage extending 26 mm from the front of the sewing ring and containing a plastic ball of diameter 22.6 mm. In each case, the sewing ring of the valve was encased within a plastic mount around 7 mm in depth and fixed before the observation section. The construction of the valve mount and test section made it impractical to record PIV images immediately around the valve. The Reynolds number based on the diameter of the sewing ring was between 500 and 600. Figure (4.10) shows a schematic of a heart valve mounted before the test section.

4.5.1 Experimental procedure

The experimental procedure falls into six distinct parts.

1. Assembly of the flow system and fixing it to the optical bench.

   The axial position of the test bodies and heart valve prostheses was set in the test chamber by adjusting their position after viewing from above, along the axis of the flow system.

2. Alignment of the scanning mirror system and laser.

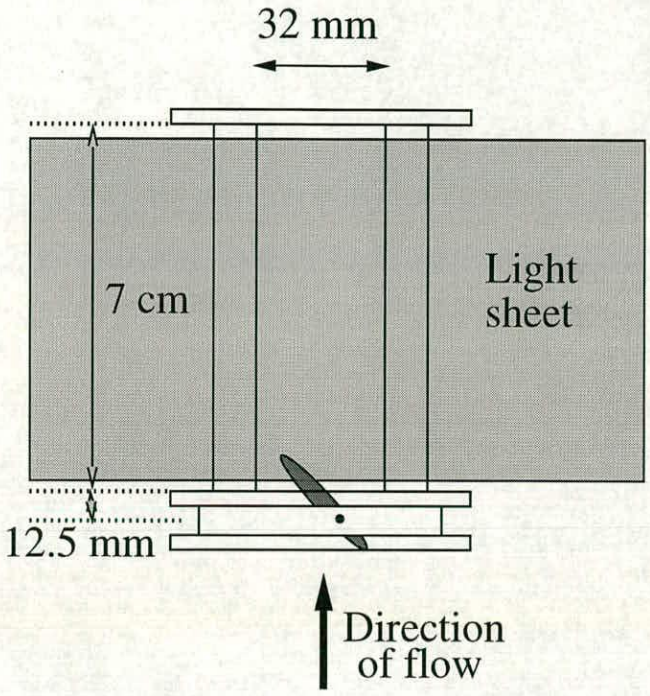


Figure 4.10: A schematic of a valve mounted before the test section.

Alignment of the scanning mirror system was carried out at a power setting of around 60 mW. To avoid damaging the surface of the scanning mirror it should always be rotating when the laser is on. The reflected beam from the surface of the lens and mirror was aligned with the incident beam. Laser goggles were worn during all alignment stages.

3. Checking and fine adjustment of the position of the test section with respect to the illuminating light sheet.

   This was carried out at a low power setting. The initial location of the light sheet and test section were set by measurement. Practically it is easiest to align individual items by ensuring that reflected light is in the same vertical plane as the incident light. The diametrical positioning of the light sheet through the test section was confirmed by observing the light reflected from the surfaces within the test section normal to the illuminating light sheet.

4. Establishing the required seeded flow through the test chamber.

The flow through the flow system was allowed to develop. In particular, any air bubbles were allowed to escape from the system. For steady flows the volumetric flowrate was measured using a rotameter. In pulsatile flows it was determined using a 2 litre measuring cylinder. The seeding particles were allowed to settle for 15 minutes to remove any clumped material. When investigating the behaviour of heart valve prostheses in pulsatile flows the outlet non-return valve in the head of the positive displacement pump must be removed. This ensures that the valve acts as expected.

5. The positioning and focusing of the camera.

   The restricted depth of field that can be obtained makes this stage crucial. The power output of the laser is increased slightly to provided clear images of the seeding particles upon which to focus. The limited depth of field allowed the camera to be aligned normal to the test section and illuminating light sheet by considering the relative image clarity at the four corners of the view-finder. An extended surface, such as ruler, was fixed horizontally against the outside of the test chamber using a spirit level. The camera was set in a horizontal plane using the spirit level on the tripod. The extended surface could then be aligned with the markings on the camera indicating the image plane. In pulsatile flows the computer driving the pump was used to syncronise the camera shutter with the pulse cycle.

6. Dismantling and cleaning the apparatus.

   The equipment was cleaned after use to reduce the number of light scattering particles other than the seeding material.

Chapter 5

Experimental Results

5.1 Laminar Flow

5.1.1 Test section

Figures (5.1) and (5.2) show PIV recordings of the developing laminar flow profile in the short test section, in each case made with the same PIV recording parameters given below. The flow was seeded with 50 μm conifer pollen and illuminated using the HeNe laser and the optical beam expansion arrangement. One hole was left open on the five hole disk of the chopper and the light sheet pulsed at 50 Hz. This gave an illumination time of 2 ms with 20 ms between each light pulse. The camera shutter was open for one eighth of a second giving six images of each seeding particle. An aperture of f/2.8 was required to provide adequate exposure of the film to the detriment of the depth of field. Figure (5.1) shows the results obtained for a flow of 8.3×10^{-6} m^3/s ($Re = 330$) and Figure (5.2) the results for a flow of 2×10^{-5} m^3/s ($Re = 800$). Figure (5.1) was made with a higher concentration of seeding particles.

Both pictures clearly show a variation in the illumination intensity across the recording. This arises from three sources: the Gaussian profile of the beam, reflections from the mounting for the small diverging lens, and reflections and refraction arising from the test section itself. Figure (5.1) shows a 2453 by 2289 pixel PIV recording containing

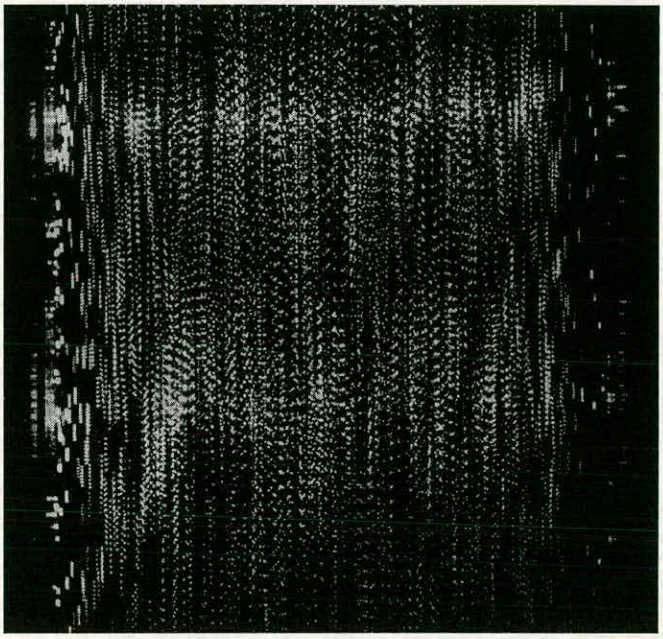


Figure 5.1: A PIV recording of laminar flow through the short test section, Re = 300.

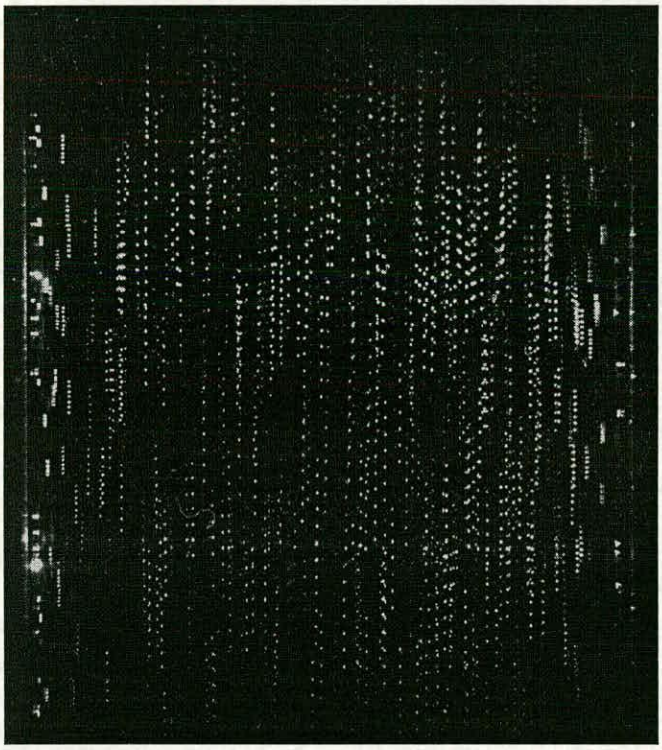


Figure 5.2: A PIV recording of developing laminar flow through the short test section, Re=800.

particle images with a diameter between 3 and 10 pixels. This image was analysed using a 1023 deep by 129 pixel wide analysis area spaced every 64 pixels in the horizontal direction and 512 pixels in the vertical direction. The velocity profile averaged over the test section is shown in Figure (5.3). The position of the centre line of the test section was determined using the location of the maximum in the velocity profile after correction for velocity gradients and also from the photographic print: agreement was found between the two approaches. Figure (5.3) clearly shows a developed laminar profile with good correlation between the expected velocity profile and that obtained experimentally. The entry length required for this flow to develop is approximately 300 cm, significantly less than the length of pipe between the flow straightener and the test section. The rms error in the readings was about 2% of the expected values and the error in the maximum velocity was 0.4%. These are of the same order as the error associated with the rotameter reading. This shows that the error introduced from the slip velocity between the conifer pollen and water is negligible or at worst comparable to the errors inherent in the PIV technique. Correction for velocity gradients reduced the rms error from 2.2% to 2.0%; a very modest improvement.

Figure (5.4) shows a developing flow profile obtained by analysing Figure (5.2). The image shown in Figure (5.2) is 1181 pixels across and 2265 pixels high and contains individual particle images with a diameter between two and six pixels. The analysis was performed using the same parameters as for the previous image. The profile observed appears consistent with a developing laminar profile[335] except that the expected flat section in the centre of the profile is distorted. The flow is developing in the sense that entrance effects are still significant. This is likely to arise as a result of the initial flow through the flow straightening section in which the superficial velocity is 2.4 times greater than that in the unobstructed pipe.

The spatial resolution that could be obtained from these recordings was limited by the large size of the seeding particles. The particle size also imposes a lower limit on the magnitude of the velocities that can be resolved as the signal peak and self correlation peak start to interact in the auto-correlation function. For this reason a range of smaller seeding particles were compared under the same flow conditions. Six

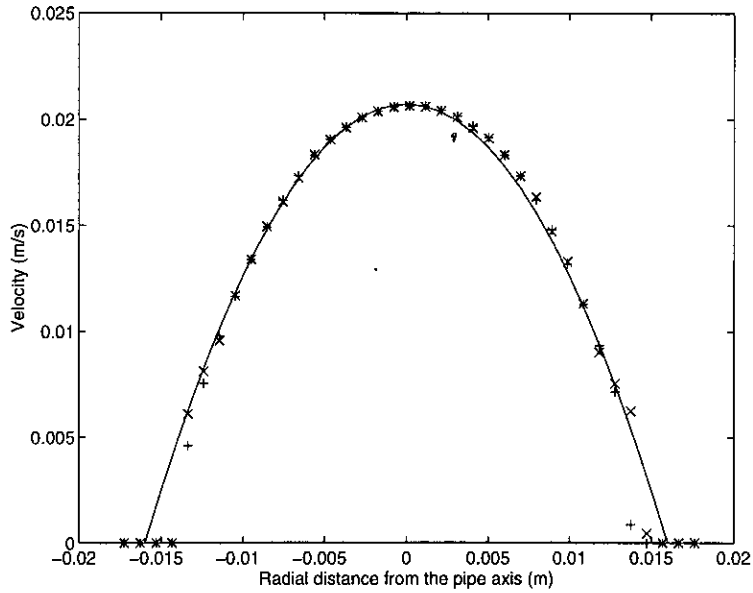


Figure 5.3: The mean velocity profile over the test section determined at a Reynolds number of 330 from the image shown in Figure (5.1). The points marked with an 'x' are from the initial analysis and those marked with an '+' after 10 iterations of the procedure to correct for velocity gradients. The solid line represents the expected fully-developed laminar for the measured flowrate of 8.3×10^{-6} m^3/s.

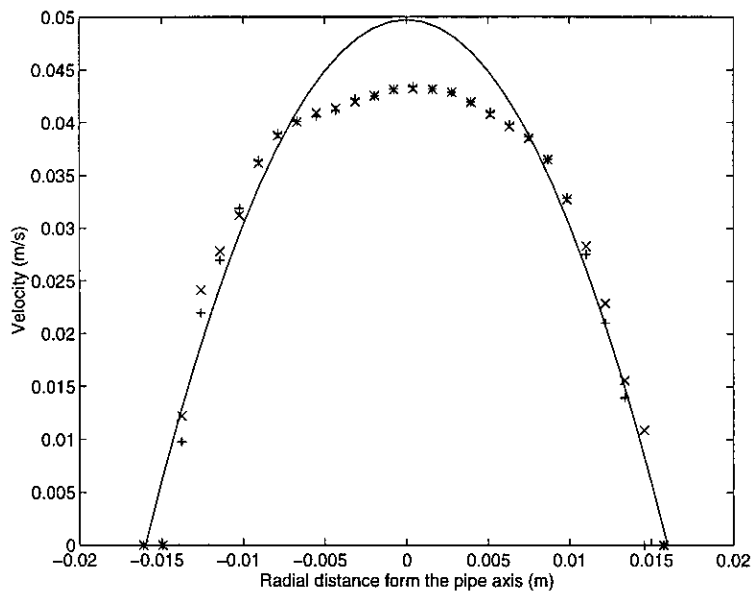


Figure 5.4: The mean developing velocity profile over the test section determined at a Reynolds number of 800 from the image shown in Figure (5.2). The points marked with an 'x' are from the initial analysis and those marked with an '+' after 10 iterations of the procedure to correct for velocity gradients. The solid line represents the expected fully-developed laminar for the measured flowrate of 2×10^{-5} m^3/s.

micron aluminium oxide particles and eight micron hollow glass spheres were found to give a similar performance and a modest improvement in the spatial resolution was achieved in later recordings.

5.1.2 Bluff bodies

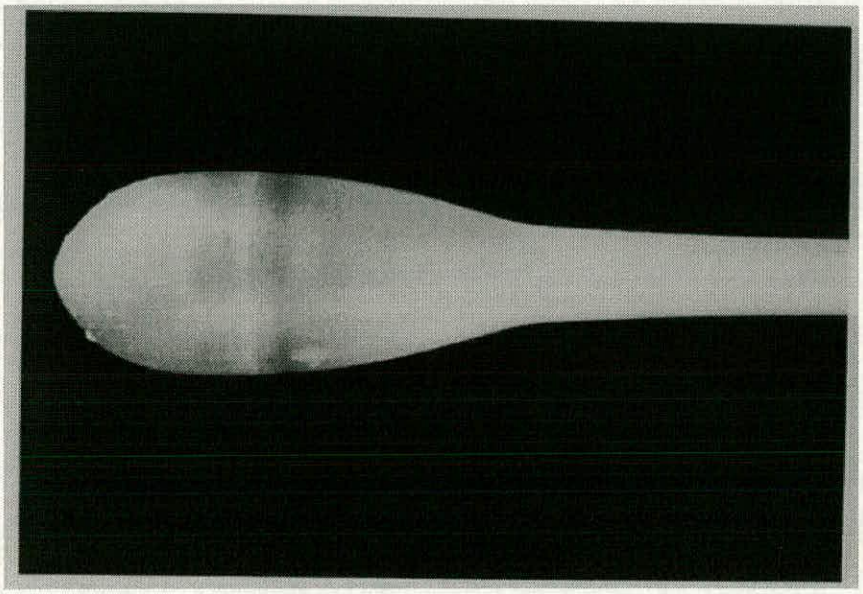
Downstream-apex large tear-drop

The clot formed about the downstream-apex large tear drop is shown in Figure (5.5) reproduced from the work of Christy[1]. This is compared with the boundary layer visualised by slowly injecting seeding particles along the centreline of the flow at comparable flow conditions. The locus of the edge of the boundary layer together with the shape of the test body were used to estimate the volume of the recirculation zone as 0.17 cm^3, assuming axial symmetry. The similarity between the shape of the boundary layer and the shape of the clot is immediately striking.

Figure (5.6) shows a PIV recording and the resulting velocity vector field super-imposed on the vorticity map for the same test body under the same flow conditions. The flow was seeded with 8 μm aluminium oxide particles and illuminated using the HeNe illumination system using optical beam expansion. The pulsation frequency of the illuminated light was 75 Hz, as registered by the optical chopper. A shutter speed of $\frac{1}{8}$ of a second and an aperture of f/2.8 were used to make the recordings. The section near the test body is shown in more detail in Figure (5.7). The velocity field was interpolated using the NAG routines E01SAF and E01SBF[273], which implement the interpolation method of Renka and Cline. Manually digitised points on the flow boundaries and beyond were introduced into the data used for interpolation to incorporate a no-slip criterion upon the resulting vector field.

The flow around the test body was also modelled using FLUENT (version 4.3) - a CFD package which uses a non-staggered control volume technique to discretise the differential conservation equations. Sixteen points defining the shape of the test object were determined from a digitised photograph showing the test objects side-on. The simula-

a)



b)

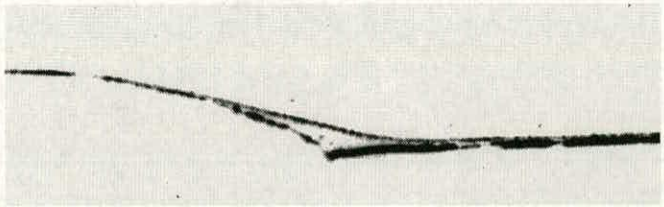


Figure 5.5: **a)** the clot formed about the downstream-apex large tear-drop -see Christy[1] for experimental details. **b)** The boundary layer to the same scale.

tion was performed at the same flow conditions in a 32 mm internal diameter pipe. The flow was assumed to be uniform 500 mm upstream from the test body and allowed to develop over this length. A 100 mm portion of a supporting sting was included downstream of the test body. The region was discretised on a structured grid 450 nodes in the axial direction and 30 nodes in the radial direction, assuming axial symmetry. The test fluid used was water. The highest order discretisation scheme available was used (QUICK) and the most robust pressure correction method (SIMPLEC). The line Gauss-Seidel linear equation solver was used for both components of the velocity and the multi-grid technique to solve for pressure. To aid propagation of the boundary conditions alternate sweep directions of the solver were used along with block correction methods when appropriate. Under-relaxation parameters were chosen according

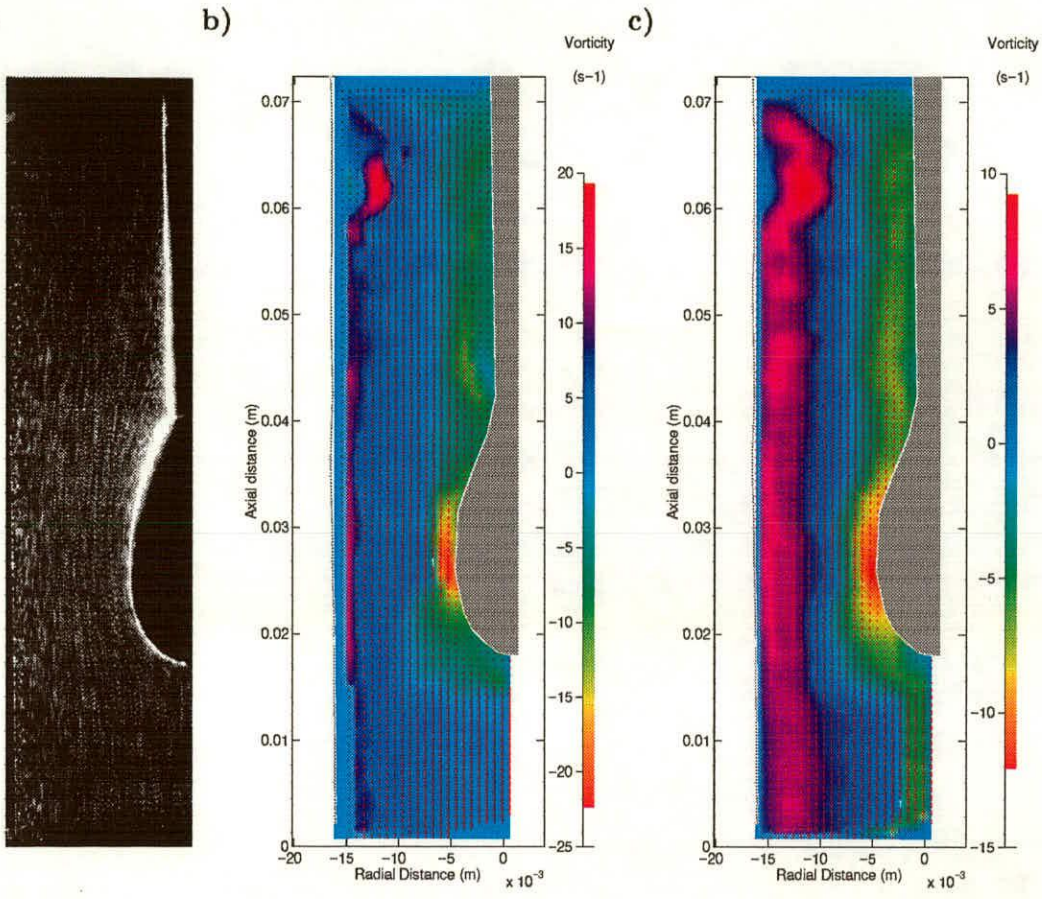


Figure 5.6: **a)** A PIV recording of the flow round the downstream-apex test body at a Reynolds number of 250, based on the projected diameter of the test body. **b)** The vorticity map and velocity field produced after one iteration of the procedure to correct for velocity gradients. The maximum velocity is indicated by a white vector which represents 0.0473 m/s. **c)** as b) but after the velocity field was smoothed with a low pass filter. Again, the maximum vector is indicated in white and represents 0.0444 m/s.

to good practice[280] and modified by trial-and-error. No significant problems arose in either the grid generation or solution stages. The results of the simulation are shown in Figure (5.8) and the results of using a grid with half the resolution in each direction in Figure (5.9). The correlation between the two indicates that a near grid-independent solution to the problem was obtained: there are no significant differences in the flow features resolved using the different discretisation resolutions.

Figure (5.10) shows the change of particle concentration in the recirculation zone. Photographs are taken at one second intervals; the first at the top right hand corner

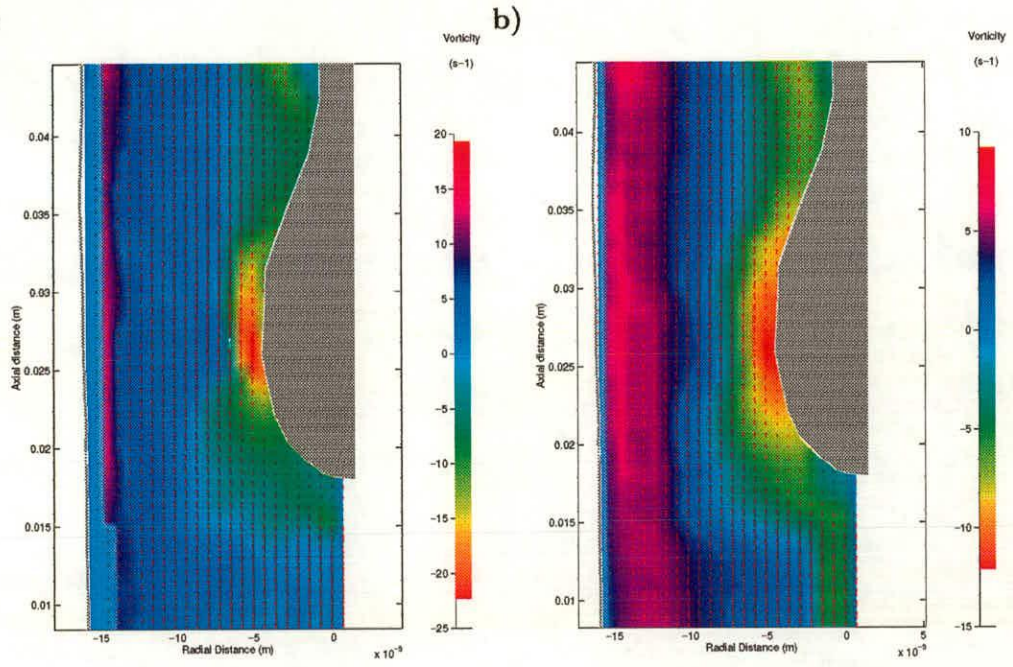


Figure 5.7: An enlarged view of the section around the test body **a)** from Figure (5.6:b) and **b)** from Figure (5.6:c).

and then reading left to right. The negatives from the residence time distribution investigation were processed and manipulated in exactly the same way. The percentage of white points after dithering the image to black and white was used to estimate the particle concentration. The axisymmetric nature of the flow was taken into account by weighting the intensity proportional to radius and then finding the percentage of white points after dithering. This assumed that the scattered light intensity was proportional to the number of scattering particles. A more complicated approach would be to locate all the centres of the image points and weight them by radius to give concentration. This would rely on clear individual particle images being resolved in the recirculation zone. It is doubtful whether the images were clear enough for this approach.

A plot of the light intensity weighted by radius (normalised to the first photograph) against time is shown in Figure (5.11). A continuously stirred reactor (CSTR) into which a single injection of particles is made at time zero gives a particle concentration that decays as:

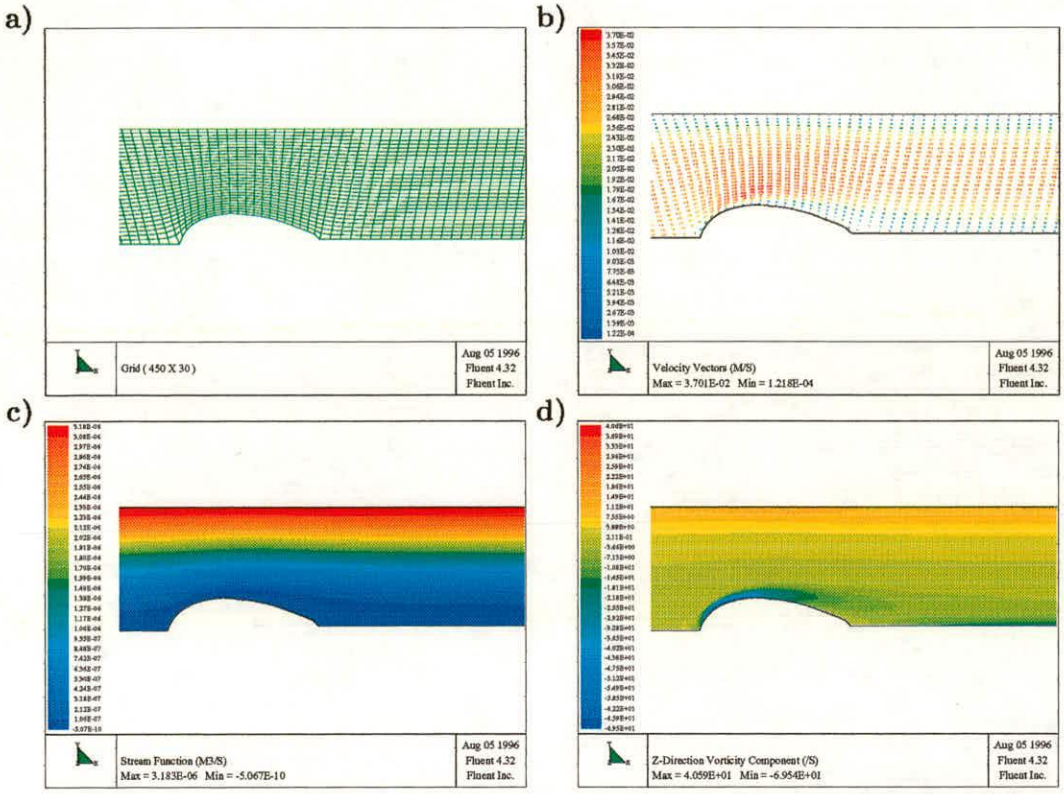


Figure 5.8: Predictions of the flow around the tear-drop shaped test body made using FLUENT v4.3 at a Reynolds number of 250 based on the diameter of the test body: **a)** the computational grid, **b)** the velocity vectors, **c)** contours of the stream-function, **d)** the out of plane, or z-component, of vorticity.

$$c = c_o e^{-\frac{1}{\tau}t} \tag{5.1}$$

where c is the particle concentration at time t, c_0 the particle concentration at some initial time $t = 0$, and τ is the mean residence time for the reactor[8].

The data presented here for the recirculation zone behaves in the same way as CSTR with a mean residence time of around 20 seconds. This result was then used to estimate the amount of clot formed as a function of time and correlated with the observations of Christy(1). Assuming that all the clot forms in the recirculation zone, and that any material that enters the recirculation and remains there for 30 seconds forms some clot - as observed by Christy(1) in his modified Lee-White clotting test - the following equation would govern clot growth:

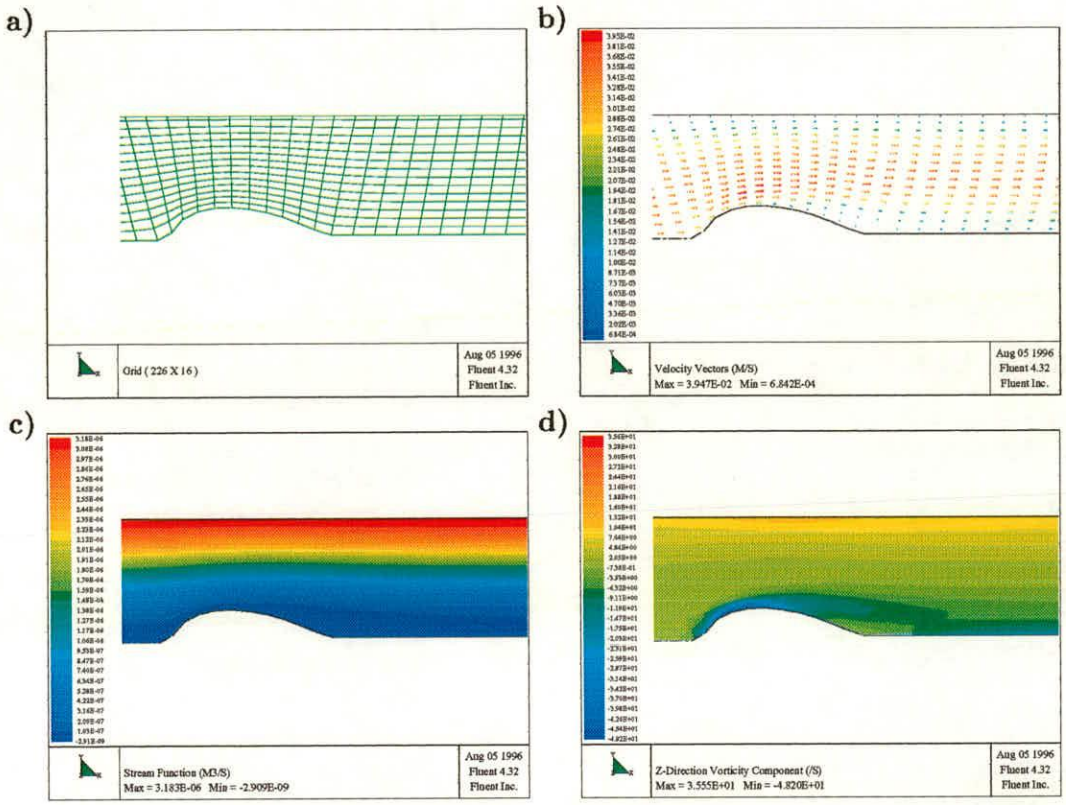


Figure 5.9: As Figure (5.8) but with the number of grid points halved in each direction: **a)** the computational grid, **b)** the velocity vectors, **c)** contours of the stream-function, **d)** the out of plane, or z-component, of vorticity.

$$-\frac{dV}{dt} = \frac{V}{\tau} e^{-\frac{1}{\tau}30} \tag{5.2}$$

where V is the volume of the recirculation zone.

Upon integration, using the values for constants determined above, equation (5.2) can be used to predict the time for a particular amount of clot formation.

Percentage of recirculation zone filled with clot	Predicted time (minutes)
50	1.0
90	3.3
95	4.3
99	6.7
99.9	10

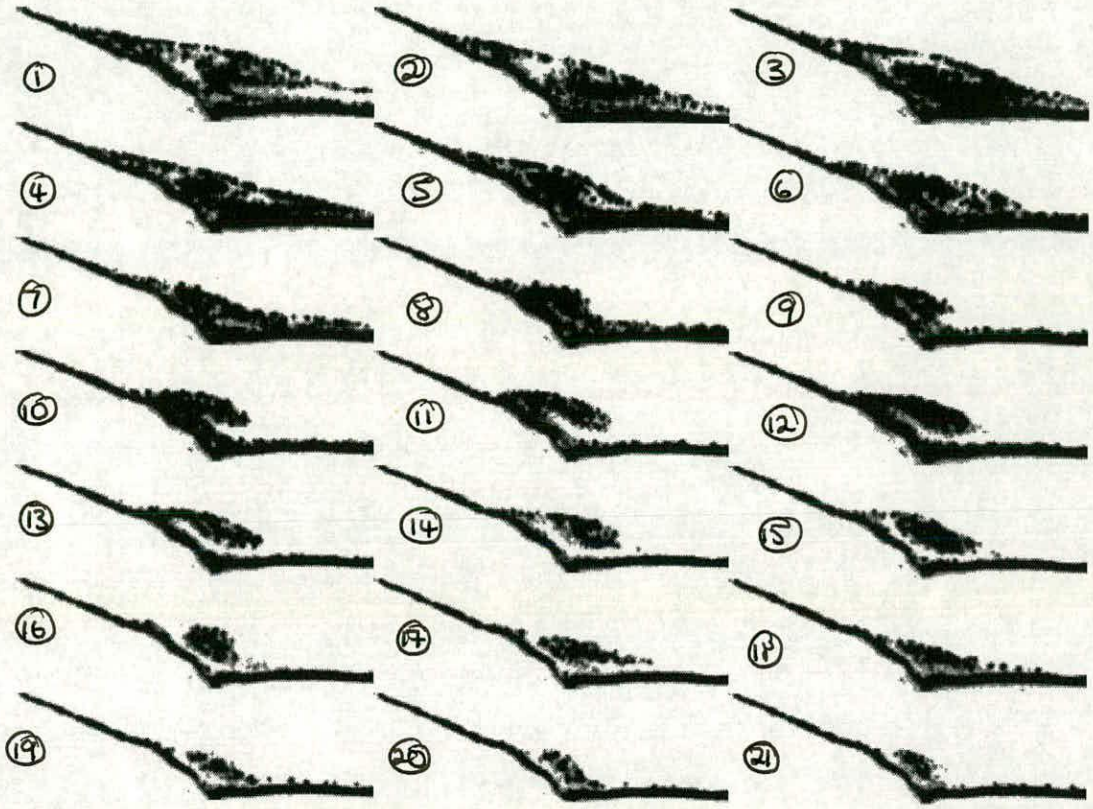


Figure 5.10: Recordings of seeding particles in the recirculation region distal to the tear-drop shaped test body at a Reynolds number of 800 based on the pipe diameter. The images are recorded at one second intervals and follow a sequence as numbered.

The ultrasound observations made by Marosek[337] are in qualitative agreement with the predictions made above. It has been observed that a period of about 5 minutes is required for the clot to reach full formation.

The PIV analysis allows the distribution of shear-stress to be calculated within the flow. The maximum value was 0.021 Nm^{-2}, where the test object reaches its maximum width. The value for blood will be slightly higher as the relative viscosity is about 3, complicated further by slight non-Newtonian behaviour. These values are well below those reported to produce damage to platelets and red blood cells, 50-500 Nm^{-2} depending on the time of exposure to the shear. This suggests that the initiation for the reactions leading to clot formation occurs elsewhere. It should, however, be noted that the measured shear stress is an underestimate as values near to the object surface are difficult to resolve.

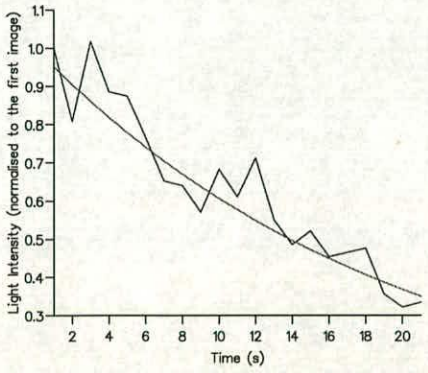


Figure 5.11: Estimated particle concentration from the scattered light intensity weighted with radius and normalised to the first recording.

Comparing the shape of the clot formed with the shape of the boundary layer and the measured velocity field there appears to be a correlation between clot formation and the recirculation zone behind the test body. This supports the hypothesis put forward by Christy and Macleod[64], that stasis is an important factor in clot formation. Here it appears that the boundary layer around the test object and the recirculation zone give the reaction time to reach completion, with clot then being deposited on the test body. Flow around the boundary layer must also allow the reaction phase to reach completion and deposition to occur. The presence of clot around the front of the test body may result as the clotting reaction proceeds in the boundary layer or from the transport of particles of clotted material by the flow. Since the flow pattern will evolve as the clot develops, this growth will be difficult to model. Here it has been assumed that the major changes to the flow will act to remove areas conducive to deposition as the clot grows, reducing recirculation and creating streamline flow. This could be tested by making a series of bodies in the shape of the developing clot. This has been investigated recently by Marosek[6] using an ultrasound technique but the image resolution was inadequate to observe clot growth on the test bodies. The limit to thrombus deposition may occur when the shear stress at the surface of the clot is sufficient to carry away any further clot deposited.

The residence time distribution results give only a rough estimate of the mean residence, τ, based on the assumption that the recirculation zone is behaving as a continuously

stirred reactor. The apparent flow structures shown in Figure (5.10) do not confirm this behaviour and the need for a more complex model is indicated. The fluctuations seen in Figure (5.11) in concentration may arise from several sources; particle overlap, concentration variations within the recirculation zone, inaccuracy in aligning the images. Indeed, structures can be observed clearly within the recirculation zone as the seeding particles clump and move around as seen in Figure (5.10). This large scale investigation of the flow could not resolve the detail in the recirculation area.

Sphere

Figure (5.12) shows a PIV recording and the resulting velocity field about the spherical test object in a steady flow of 2 $\times 10^{-5}$ m^3/s. The maximum velocity determined from the PIV investigation was 0.050 m/s compared with the predicted maximum velocity of 0.0436 m/s from the CFD simulation. In both cases, the maximum velocity occurs, as expected, just downstream of the widest point of the test body. Comparing the clot shape observed by Christy as shown in Figure (5.13) with the experimental and predicted flow fields, Figures (5.12, 5.14, and 5.15), the relationship between the location of clot formation and the recirculation zone is less clear than for the downstream apex tear-drop. This may be explained as the wake region is unsteady, as would be expected for a less streamline test body. Unsteady wake regions are also exhibited in the residence time experiments made behind the other, less streamlined, bodies presented in the following sections. However, residence time measurements were not made for this test body and are required to confirm this conjecture. The maximum value for the shear-stress, determined using the properties of water, was 0.02 N/m^2, well below the values thought to cause damage to blood cells or the arterial wall. The CFD predictions made with a computational grid of half the original resolution shows that a near grid independent solution to the problem was obtained. The distribution of the shear-stress about the test body, determined by experiment, did not yield information in the recirculation zone. This was due to reflection from the sting and the low velocities observed in this region. Such results would be useful in relating the limits of clot formation to the shear-stress and perhaps to determine the critical shear level above which forming clot is disrupted. Interpolation of velocities in the region is of little value as there are no actual measurements of any of the velocities within this region. The wake region would be better resolved using a cross-correlation technique or by making use of image shifting.

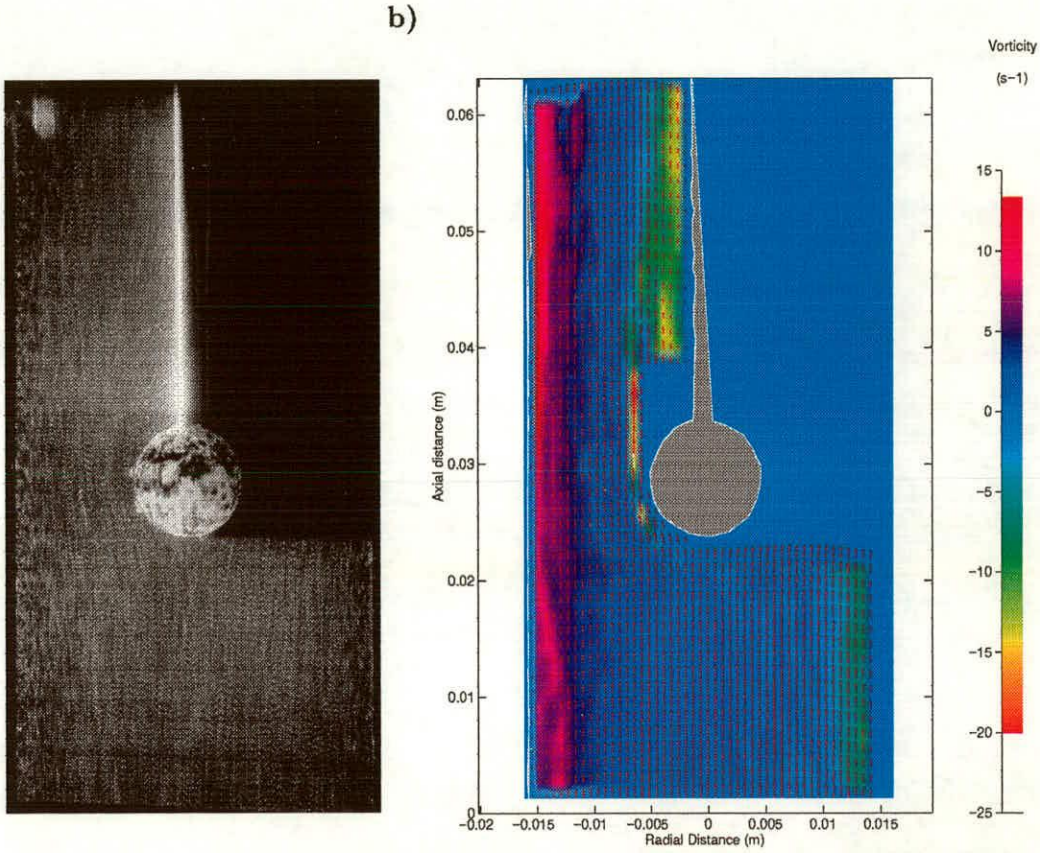


Figure 5.12: **a)** A PIV recording of the flow round the spherical test body at a Reynolds number of 250 based on the projected diameter of the test body. **b)** The vorticity map and velocity field produced after normal PIV analysis and interpolation. The maximum velocity is indicated by a white vector which represents 0.050 m/s.

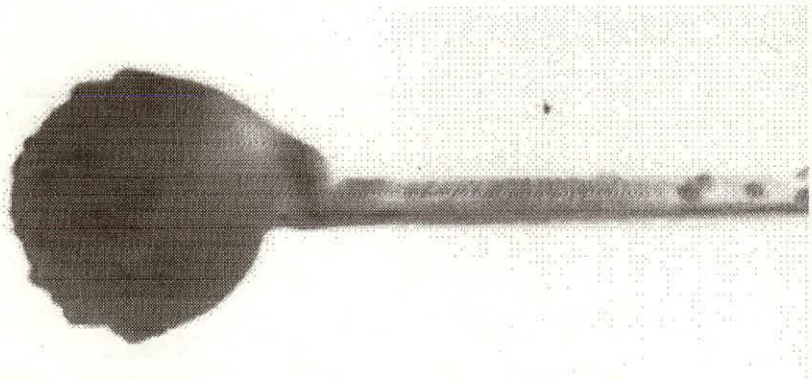


Figure 5.13: The clot formed around the sphere in steady flow as reported by Christy[1].

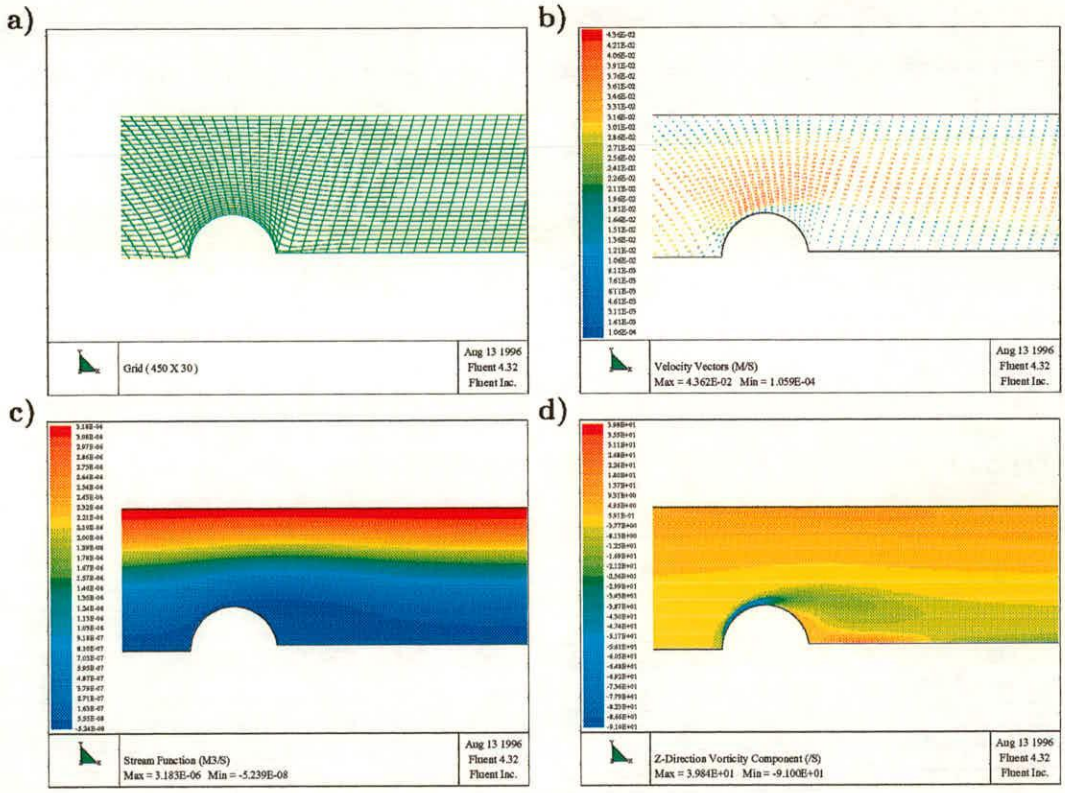


Figure 5.14: Predictions of the flow around the sphere made using FLUENT v4.3 at a Reynolds number of 250 based on the diameter of the test body: **a)** the computational grid, **b)** the velocity vectors, **c)** contours of the stream-function, **d)** the out of plane, or z-component, of vorticity.

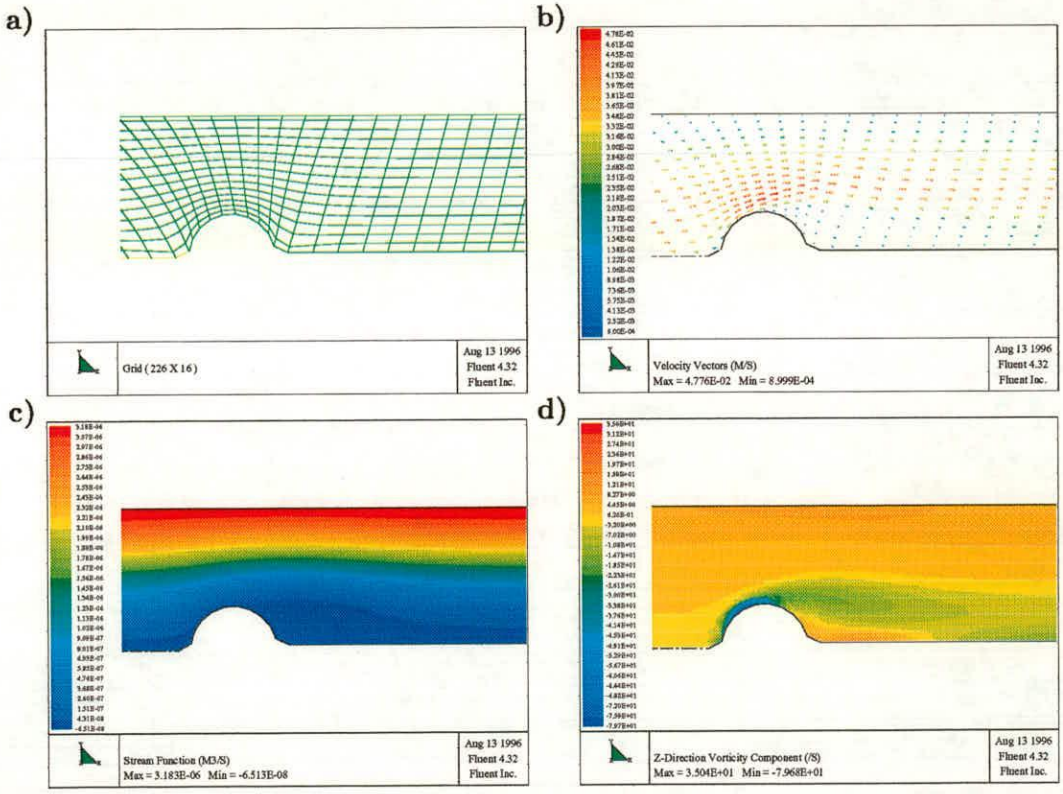


Figure 5.15: Predictions of the flow around the sphere made using FLUENT v4.3 at half the grid resolution used in Figure (5.14): **a)** the computational grid, **b)** the velocity vectors, **c)** contours of the stream-function, **d)** the out of plane, or z-component, of vorticity.

Oblate

Figure (5.16) shows the results of the residence time distribution measurements made about the disk shaped test object. The images are separated by one second and read from top to bottom and then from left to right. It is clear that over 28 seconds the majority of seeding particles are swept out of the recirculating zone behind the test object. The images clearly show that this region contains significant structure and material is ejected from this zone approximately every 2 seconds. This is most likely to be related to vortices being shed from the test object. The clot observed about this test body by Christy[1] is not readily explained by these structures although clot seems to be most likely to form in the areas of stagnation where there would appear to be the longest residence times and at the front of the test body where clotting material is likely to be carried onto the test body by its momentum.

The PIV recording of the flow around the disk produced a few vectors in the recirculation region making interpolation in this area sensible. The PIV recording and resulting velocity and vorticity maps are shown in Figure (5.18). Again, the maximum measured shear stress of 0.026 N/m^2, calculated for water as the test fluid, was well below that expected to damage blood components and endothelial cells. There is also reasonable correlation between the simulated and experimental results. The maximum measured velocity was 0.0508 m/s and that determined by simulation was 0.0511 m/s. The values of vorticity in the vicinity of the separated boundary layer are also of similar magnitudes and the predicted position of the centre of maximum vorticity distal to the body shows some agreement with the experimental results although this region is not well resolved. Flare from the test body was minimised by repainting the test bodies and sting with matt black paint.

In this case, the attainment of a grid independent solution to the CFD simulation was tested by doubling the grid density in the radial direction. This results in some refinement of the stream function and vorticity maps and a slight increase in the maximum velocity. The version of FLUENT available has a maximum number of 500 nodes in any direction, preventing refinement in the axial direction.

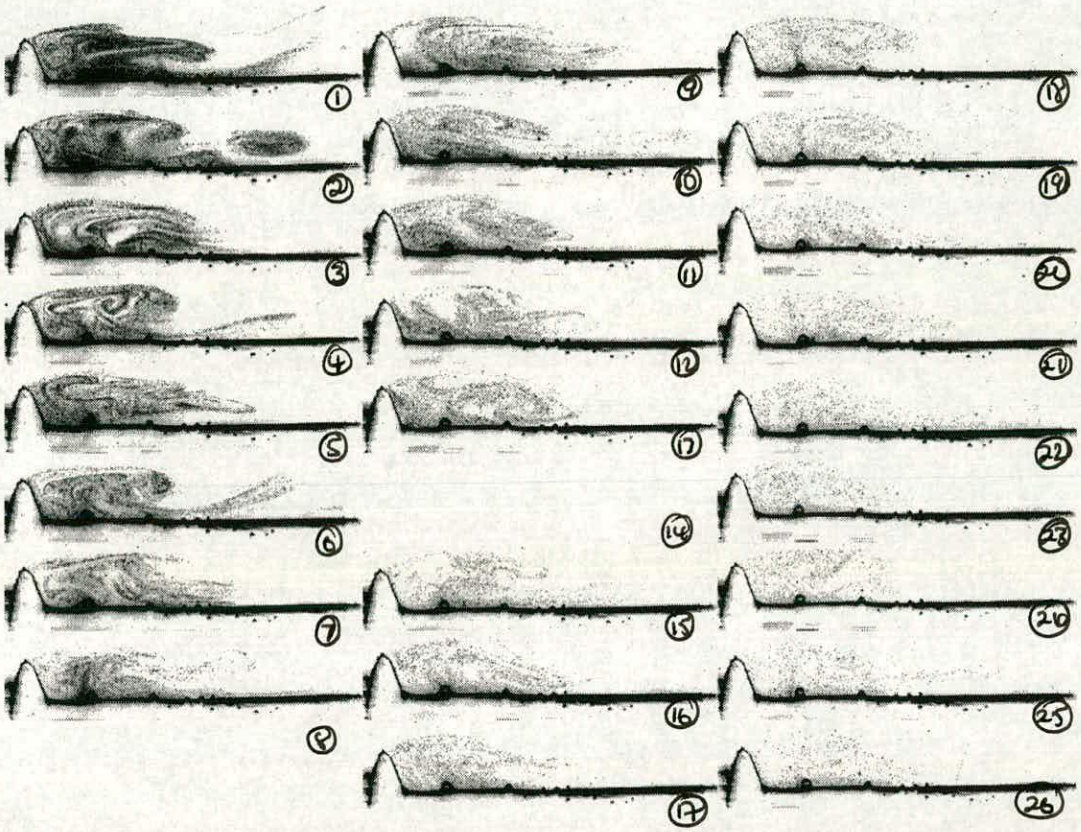


Figure 5.16: Recordings of seeding particles in the recirculation region distal to the oblate shaped test body at a Reynolds number of 800 based on the pipe diameter. The blanks represent partially illuminated recordings that have been omitted. The images are recorded at one second intervals and follow a sequence as numbered.



Figure 5.17: The clot formed around the disk shaped test body in steady flow as reported by Christy[1].

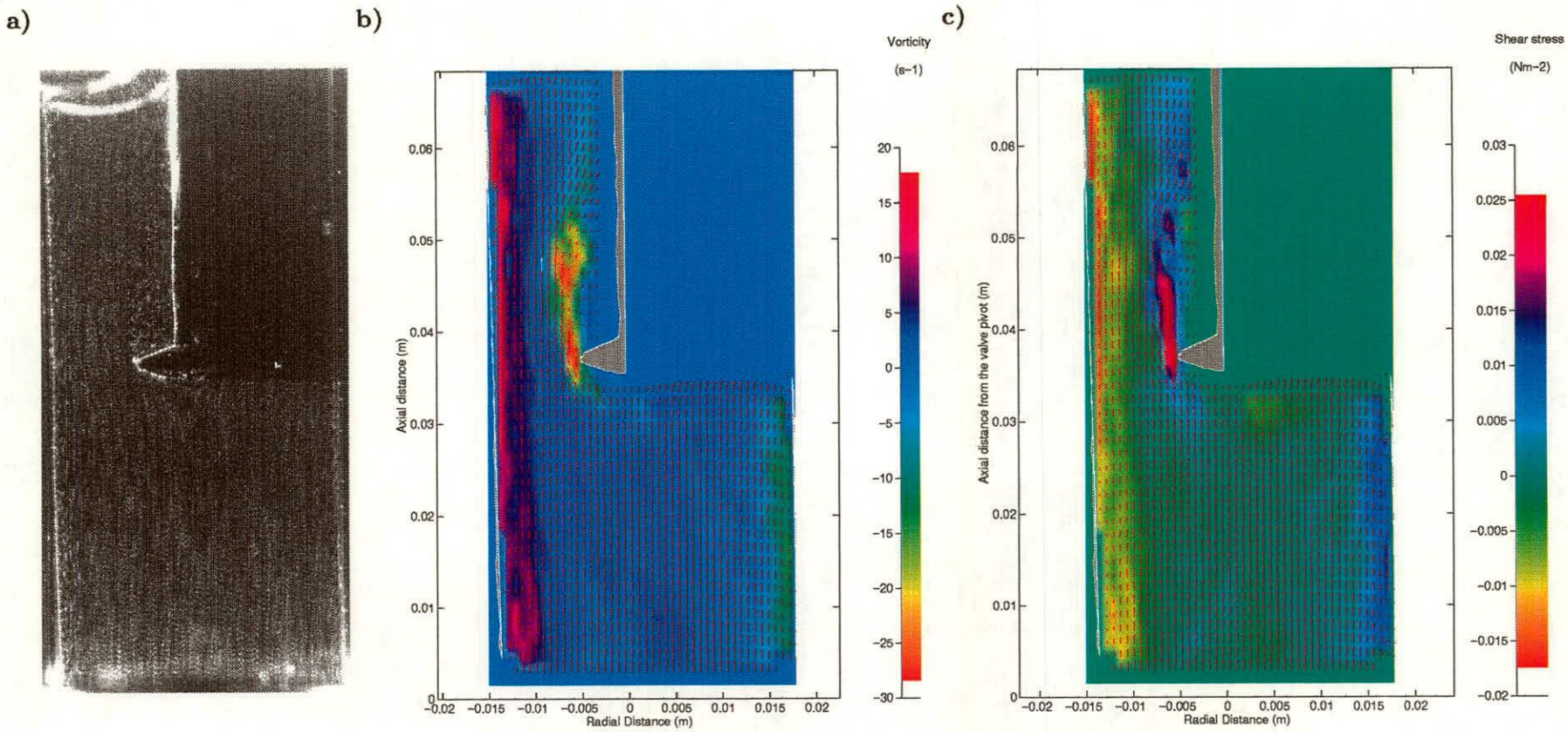


Figure 5.18: **a)** A PIV recording of the flow round the disk at a Reynolds number of 250 based on the projected diameter of the test body. **b)** The vorticity map and velocity field produced after normal PIV analysis and interpolation. The maximum velocity is indicated by a white vector which represents 0.0508 m/s. **c)** The shear stress map and velocity field produced after normal PIV analysis.

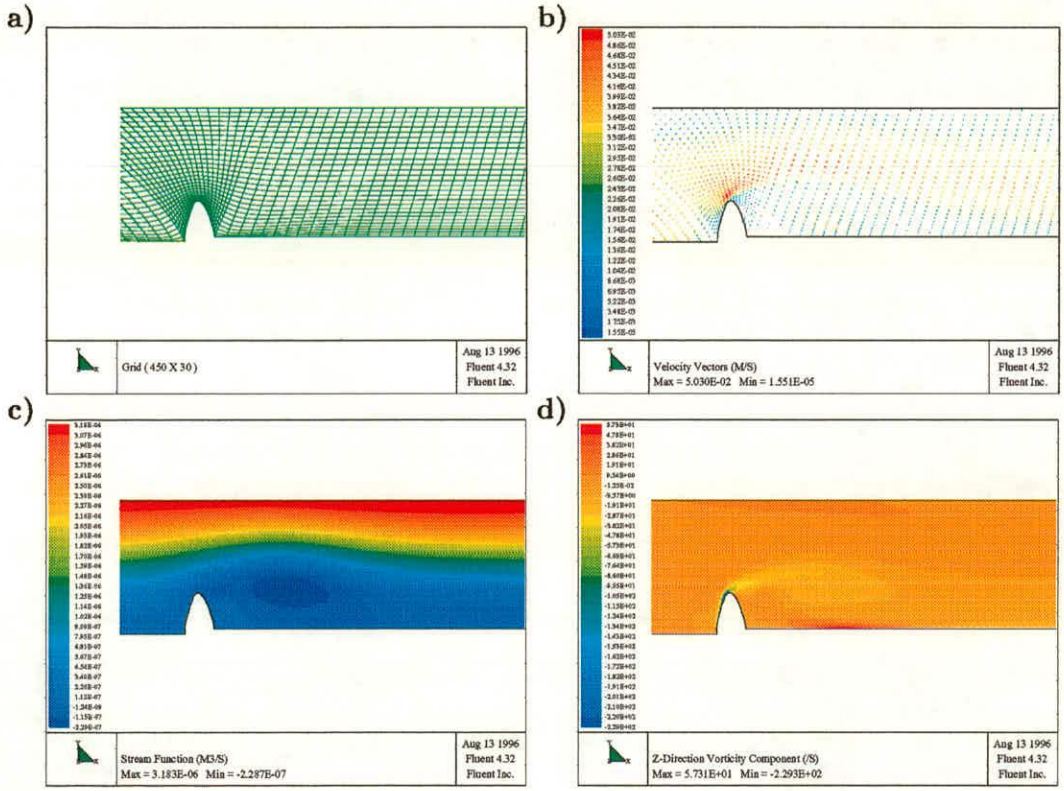


Figure 5.19: Predictions of the flow around the oblate shaped test body made using FLUENT v4.3 at a Reynolds number of 250 based on the diameter of the test body: **a)** the computational grid, **b)** the velocity vectors, **c)** contours of the stream-function, **d)** the out of plane, or z-component, of vorticity.

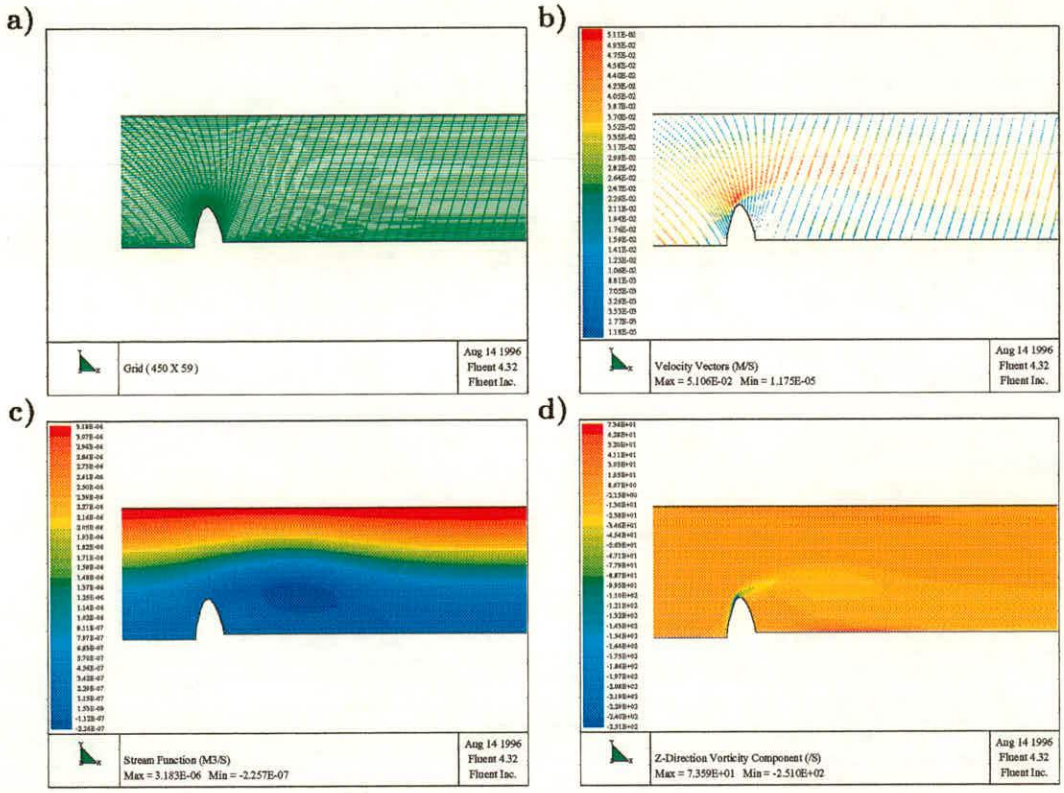


Figure 5.20: Predictions of the flow around the oblate shaped test body made using FLUENT v4.3, with the grid density doubled in the radial direction compared with Figure (5.19): **a)** the computational grid, **b)** the velocity vectors, **c)** contours of the stream-function, **d)** the out of plane, or z-component, of vorticity.

Upstream-apex cone

Figure (5.21) shows a series of residence time measurements made around the upstream apex cone in a flow of 2 $\times 10^{-5}$ m^3/s of water. Like the disk shaped test object, the concentration of seeding particles diminished rapidly over the 28 seconds spanning the recordings. The images also indicate the varying nature and volume of the recirculation zone showing significant structure. The periodic ejection of material is also evident but the temporal resolution of the recordings is not adequate to determine the frequency of this effect.

The PIV recording shown in Figure (5.23) is of a better quality than those presented so far and represents the result of repeated efforts to determine the structure within the recirculation zone, which should be most pronounced and easily analysed for this particular test object. As a result the shear stress and vorticity distributions distal to the object are better resolved and the interpolation of velocities within the recirculation zone is more reliable but should still be considered with some scepticism. After interpolation of missing vectors the vector field was smoothed with the low pass filter used by Westerweel *et al.*[270]. This may explain the curious position of the maximum velocity vector which would be expected just downstream of the maximum projected diameter of the test body, as produced in the CFD experiments. Obviously, where the velocity gradients are highest the smoothing effect is greatest and the velocities in this region would be expected to be reduced relative to their initial values. In fact, in the unsmoothed and uninterpolated velocity field the maximum velocity vector is located in the expected region and is 21% greater in magnitude. The maximum shear stress determined as 0.021 N/m^2 is again well below the threshold values thought to be required to induce damage to erythrocytes. There appears to be some correlation between the shear-field and the clot formed around this particular test body.

The CFD predictions at two different grid resolution are in good agreement as are the values of vorticity found distal to the test object. The discrepancy between the maximum velocity found in the CFD predictions of 0.0475/ms and the velocity of 0.0540 m/s obtained in the validated vector field can be explained by what appears to be a

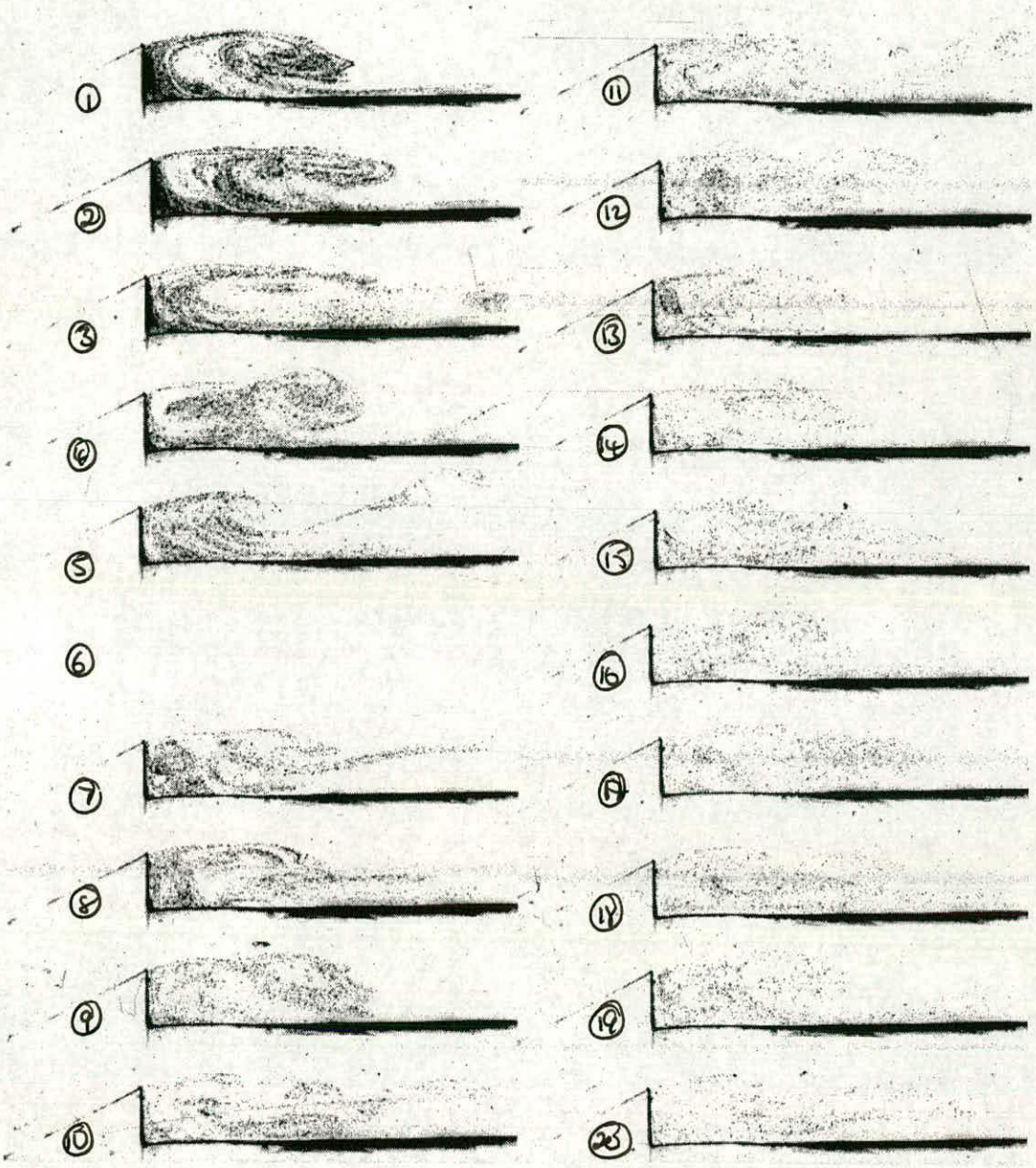


Figure 5.21: Recordings of seeding particles in the recirculation region distal to the upstream-apex cone at a Reynolds number of 800 based on the pipe diameter. The images are recorded at one second intervals and follow a sequence as numbered.

slightly skew mounting of the test body on the sting.

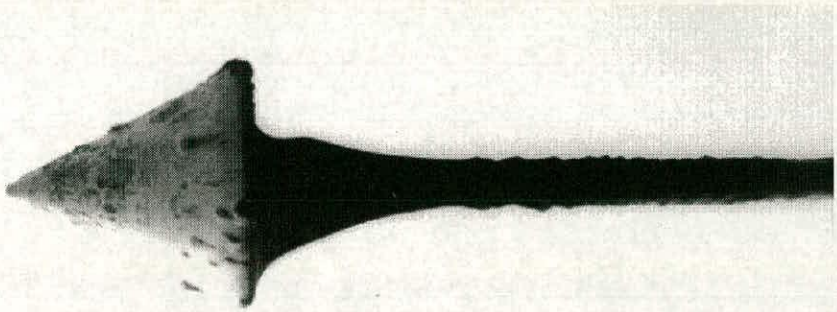


Figure 5.22: The clot formed around the upstream apex cone in steady flow as reported by Christy[1].

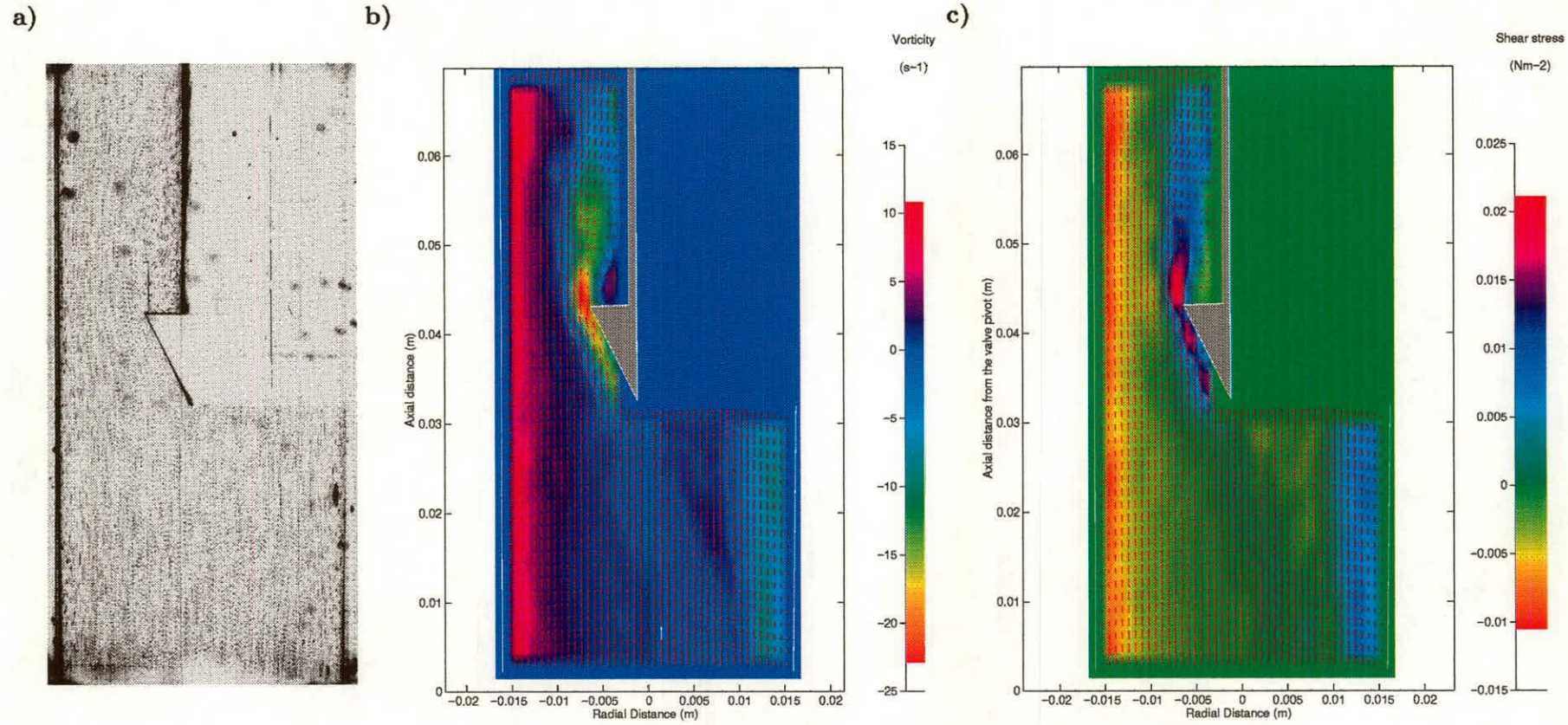


Figure 5.23: **a)** A PIV recording of the flow round the upstream apex cone at a Reynolds number of 250 based on the projected diameter of the test body. **b)** The vorticity map and velocity field produced after normal PIV analysis, interpolation and the application of a low pass filter. The maximum velocity is indicated by a white vector which represents 0.0445 m/s. **c)** The shear stress map and velocity field produced after normal PIV analysis.

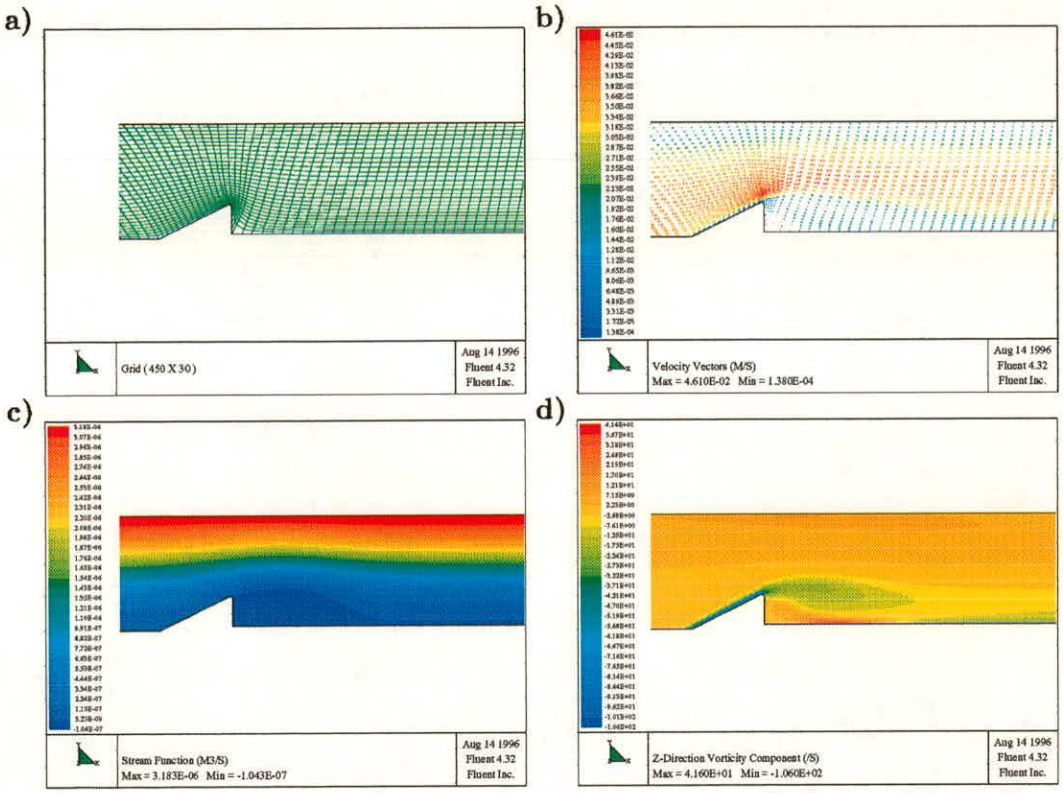


Figure 5.24: Predictions of the flow around the upstream apex cone made using FLUENT v4.3 at a Reynolds number of 250 based on the projected diameter of the test body: **a)** the computational grid, **b)** the velocity vectors, **c)** contours of the stream-function, **d)** the out of plane, or z-component, of vorticity.

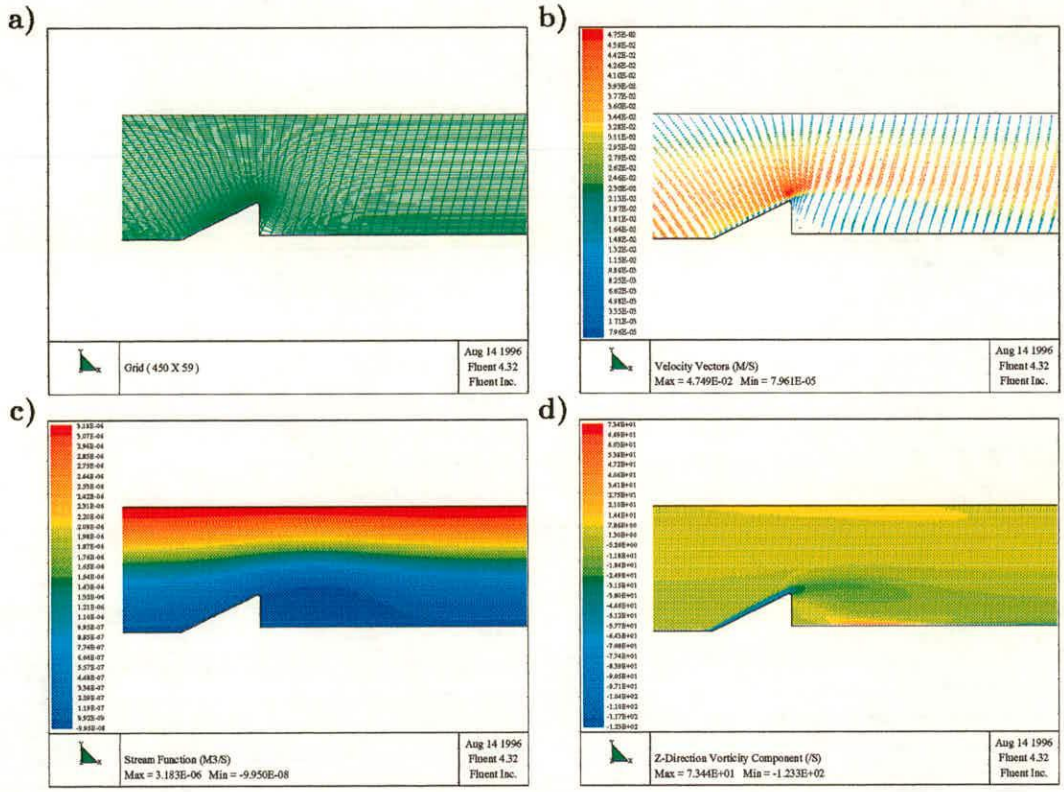


Figure 5.25: Predictions of the flow around the upstream apex cone made using FLUENT v4.3, with the grid density doubled in the axial direction compared with Figure (5.24): **a)** the computational grid, **b)** the velocity vectors, **c)** contours of the stream-function, **d)** the out of plane, or z-component, of vorticity.

Downstream-apex cone

The residence time measurements behind the down-stream apex cone, Figure (5.26) show considerable structure and, again, a periodic ejection of material from the re-circulation zone with a frequency of the order of 0.5 Hz. This test body also shows the greatest variation in the size and location of the recirculation zone. Unfortunately, Christy[1] gives no record of the clot formed about this particular test body.

The PIV recording of the flow under the same flow conditions, shown in Figure (5.27), show significantly more structure in the recirculation region of the flow than produced by the steady state CFD results. The region within the recirculation zone beside the sting immediately downstream of the test body gave velocity vectors after analysis and validation. This allowed the flow in this region to be interpolated with some confidence. The PIV recording also indicates that the test body and sting were slightly skewed to the left. A maximum experimental shear stress of 0.0211 N/m^2 is unlikely to lead to any damage of blood components. The PIV analysis also shows that it is relatively insensitive to the presence of small air bubbles on the test chamber wall if they do not significantly reduce the number of particle pairs in any given analysis region.

The differences in the location and magnitude of the maximum velocity vector are explained in the previous section. Again, the CFD results display near grid independence and the experimental and calculated vorticity maps show similar features and values of the same order of magnitude in the region of the detached boundary layer.

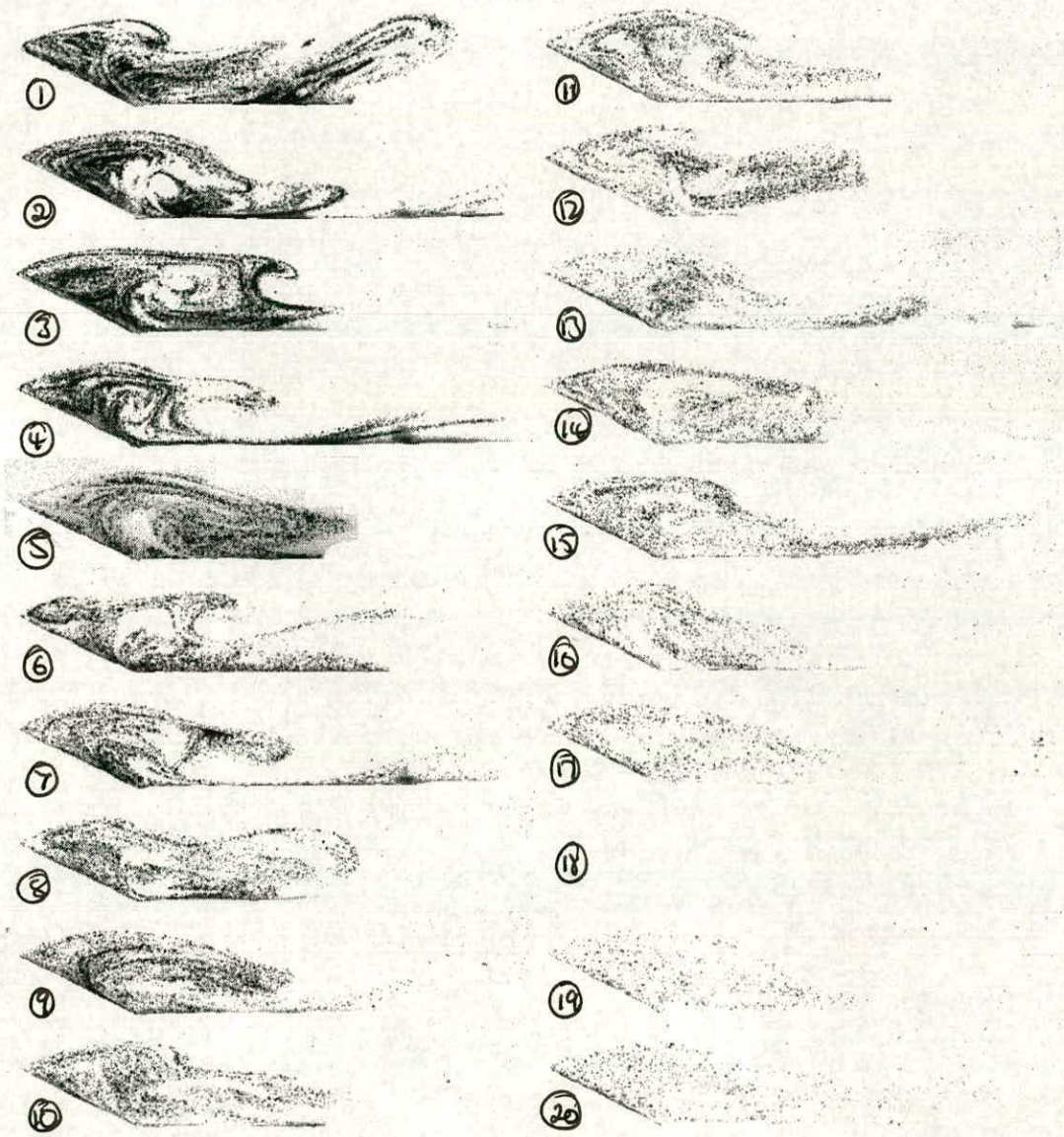


Figure 5.26: Recordings of seeding particles in the recirculation region distal to the downstream-apex cone at a Reynolds number of 800 based on the pipe diameter. The images are recorded at one second intervals and follow a sequence as numbered.

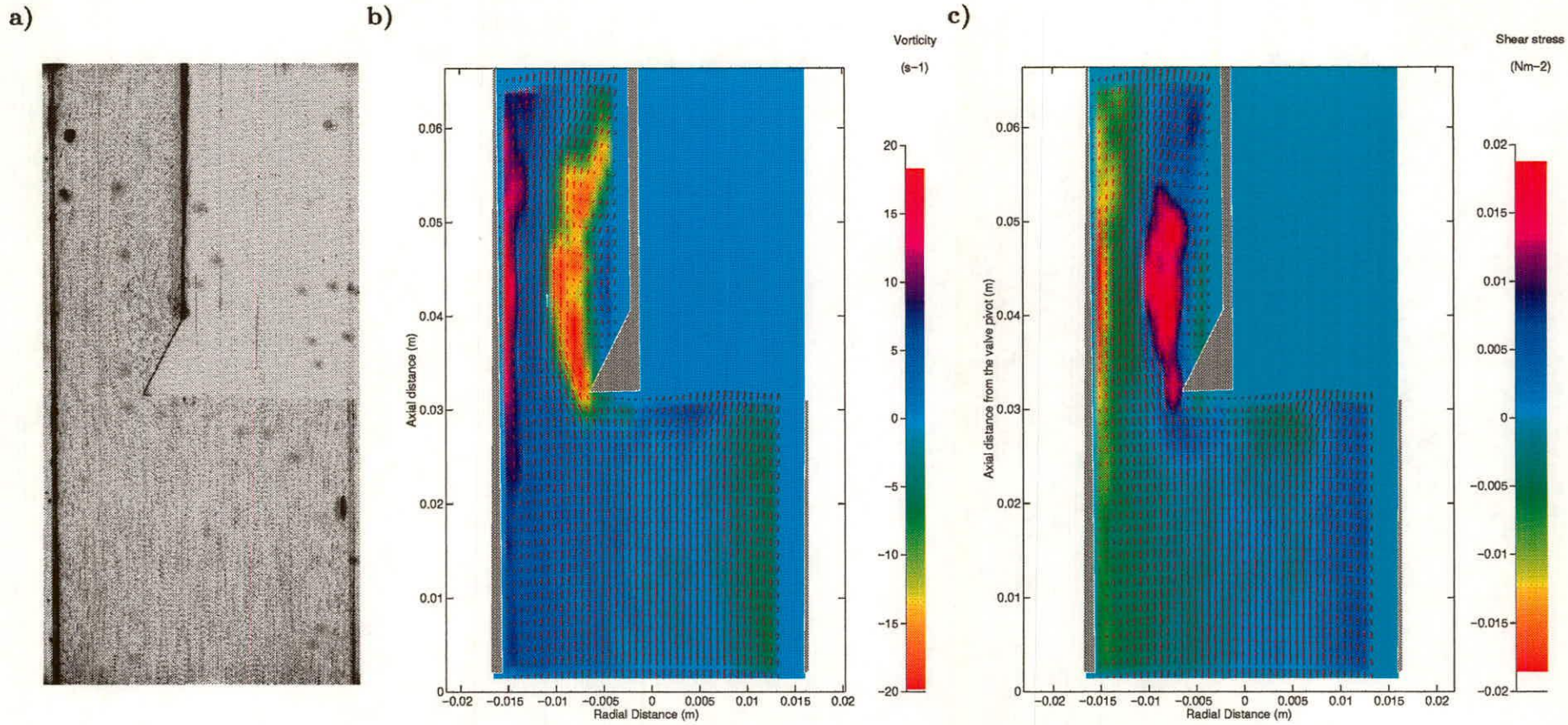


Figure 5.27: **a)** A PIV recording of the flow round the downstream apex cone at a Reynolds number of 250 based on the projected diameter of the test body. **b)** The vorticity map and velocity field produced after normal PIV analysis, interpolation and the application of a low pass filter. The maximum velocity is indicated by a white vector which represents 0.0468 m/s. **c)** The shear stress map and velocity field produced after normal PIV analysis.

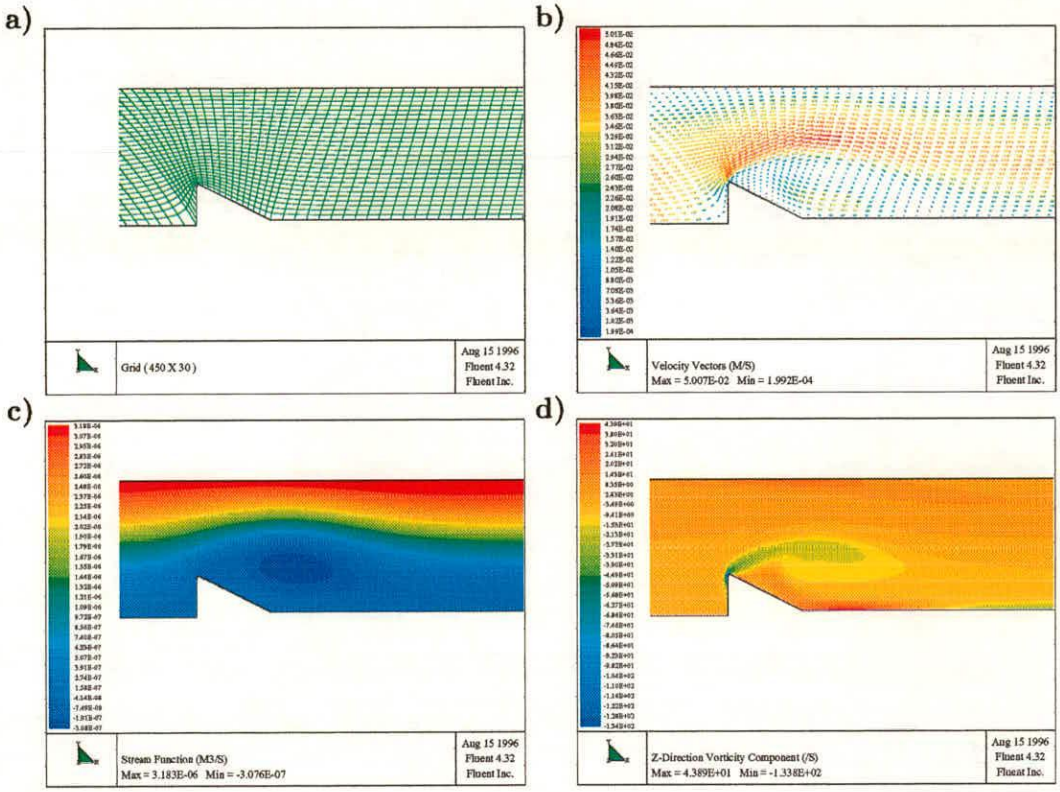


Figure 5.28: Predictions of the flow around the down-stream apex cone made using FLUENT v4.3 at a Reynolds number of 250 based on the projected diameter of the test body: **a)** the computational grid, **b)** the velocity vectors, **c)** contours of the stream-function, **d)** the out of plane, or z-component, of vorticity.

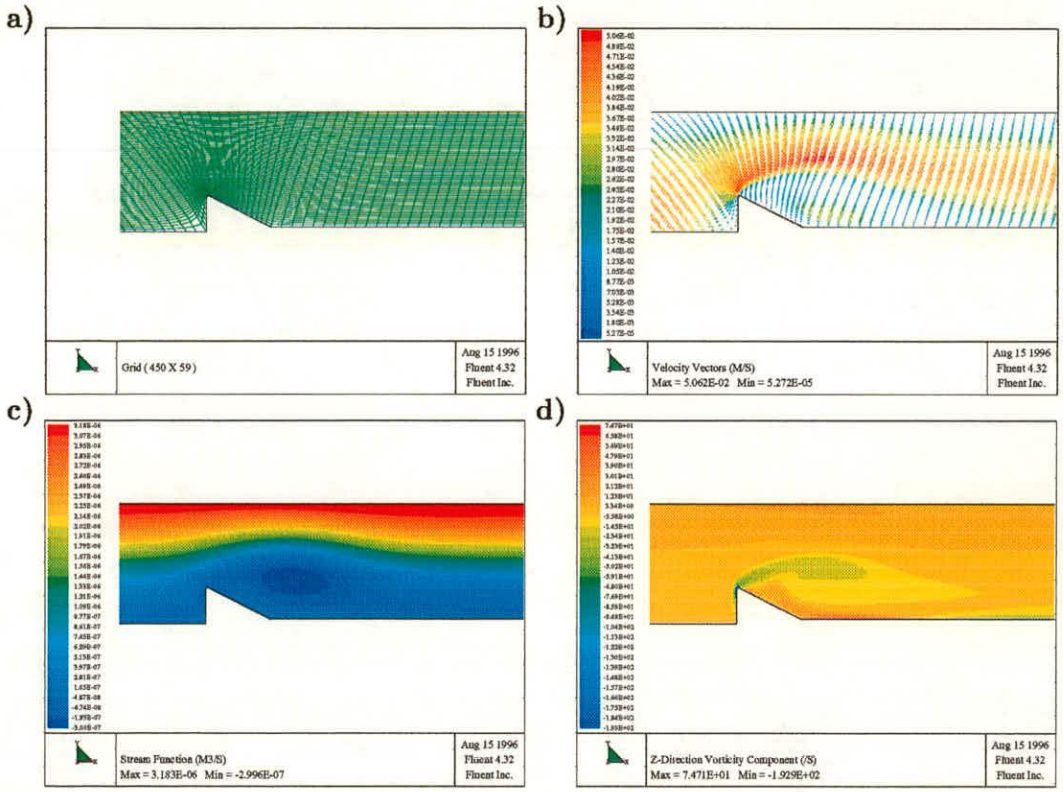


Figure 5.29: Predictions of the flow around the down-steam apex cone made using FLUENT v4.3, with the grid density doubled in the axial direction compared with Figure (5.28): **a)** the computational grid, **b)** the velocity vectors, **c)** contours of the stream-function, **d)** the out of plane, or z-component, of vorticity.

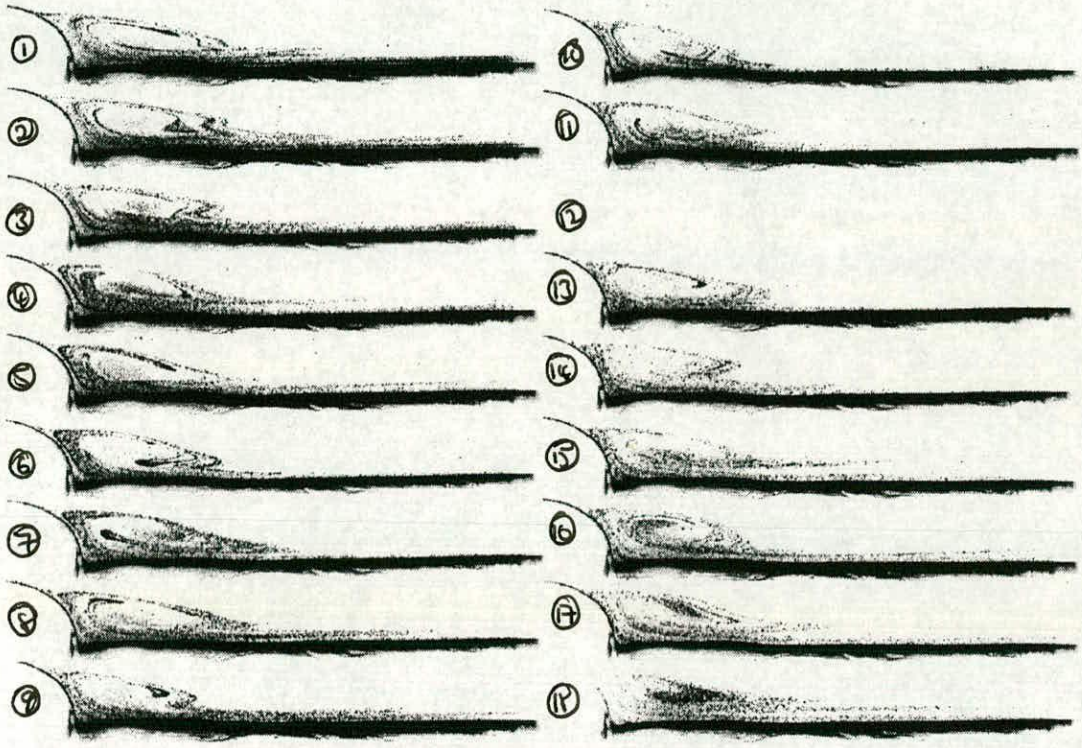


Figure 5.30: Recordings of seeding particles in the recirculation region distal to the upstream apex small tear-drop at a Reynolds number of 800 based on the pipe diameter. The images are recorded at one second intervals and follow a sequence as numbered.

Upstream-apex small tear-drop and Upstream-apex large tear-drop

The residence time measurements about the upstream-apex, small tear-drop and the upstream-apex large tear-drop are presented for completeness. Again, both sets of results show significant structure and the periodic discharge of material from the recirculation zone.

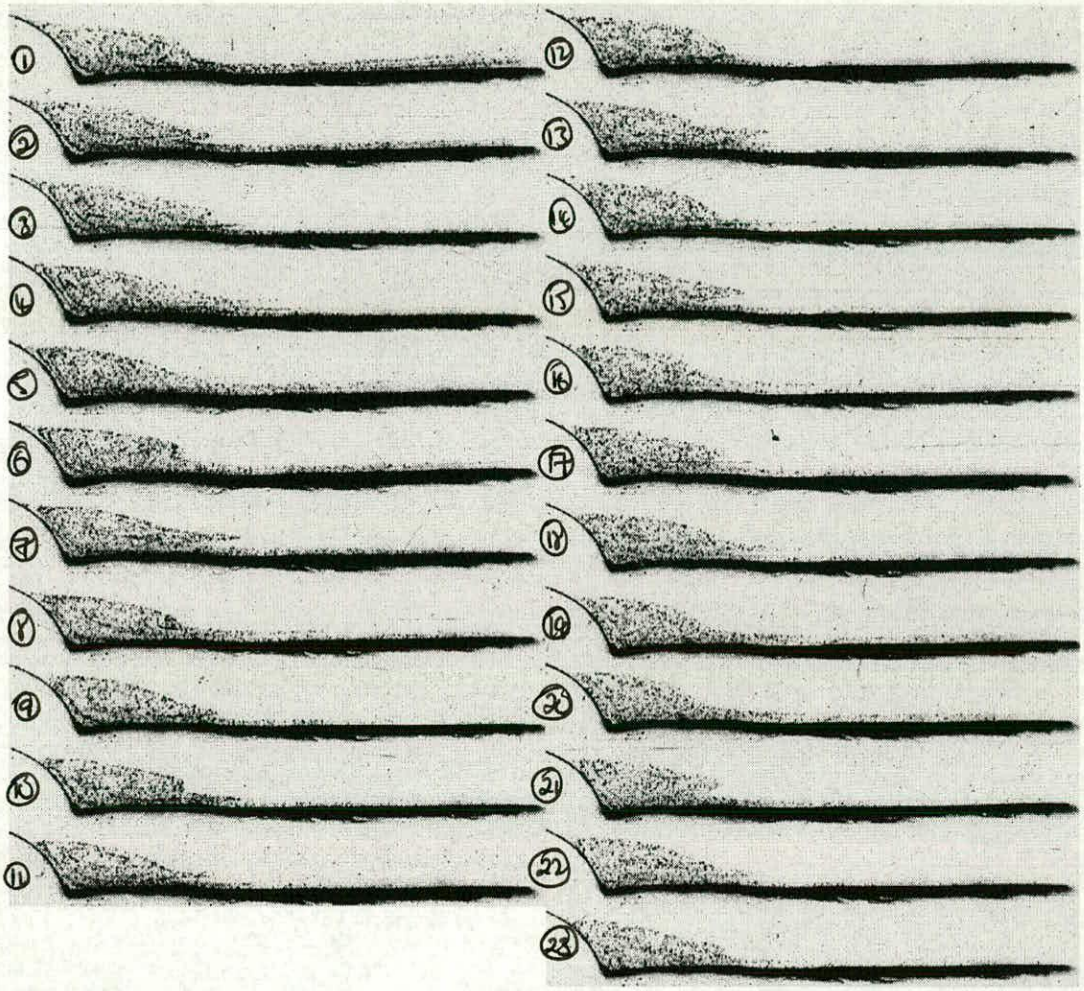


Figure 5.31: Recordings of seeding particles in the recirculation region distal to the upstream-apex large tear drop at a Reynolds number of 800 based on the pipe diameter. The images are recorded at one second intervals and follow a sequence as numbered.

5.1.3 Heart Valves

Björk-Shiley Valve

The results of the steady flow investigations downstream of the Björk-Shiley Valve are presented in Appendix D. The variation between PIV recordings made at one second intervals is striking and they show considerable three dimensional structure. The time between the recordings was not short enough to unambiguously resolve the development of flow structures. The presence of such high frequency variations in steady flow suggests that in pulsatile flow the pattern of flow at a particular phase of the cycle is unlikely to be constant from cycle-to-cycle. This implies that averaging data from successive cycles particularly in LDA investigations may well include cycle-to-cycle variations that have been assumed to be unimportant.

It was not possible with the current experimental setup to obtain PIV recordings in the immediate proximity of the valve.

Starr-Edward's Valve

The Starr-Edward's valve gave complex flow patterns that proved difficult to resolve using conventional PIV techniques and are not presented here.

5.2 Pulsatile flow

In light of the quality of PIV images obtained and in the interests of brevity, only results at low frequencies and low flowrates will be presented for flow in the empty test chamber. Simulated results for the pulsatile flow in the empty test chamber are also included for comparison. PIV recordings made around the downstream apex tear drop and the upstream apex short teardrop captured a series of structures that correlate well with the observed clot deposition under similar circumstances. Results at low and physiologically relevant flow rates and pulse frequencies are presented for the valve

designed by Dr. Norman Macleod. Considerable difficulty was found in optimising the PIV parameters required to resolve and analyse these time varying flows. In particular, the velocity gradients present in the recordings gave rise to a significant error when using conventional analysis techniques and the approach described earlier was adopted in an attempt to overcome these problems. The data resolution was low compared with that expected from the technique and the most important information about shear stress could be more readily estimated from manual tracking of particles in the required regions.

5.2.1 Test section

Figure (5.32) shows the velocity profiles obtained from the empty test section with a mean flow of 1.3×10^{-5} m^3/s with a rectified sinusoidal driving frequency of 0.4 Hz for the pump. The profiles were taken at eight equally spaced times over a single cycle, after allowing several minutes to ensure that at any initial effects were not included in the measurements. The PIV recordings used to determine these profiles were made using 6 μm aluminium oxide seeding particles illuminated with the light from the 35 mW HeNe laser using the scanning mirror method of beam expansion. The frequency of the illumination was 40 Hz. The images were recorded onto Kodak Tri-X film using an aperture of f/2.8 a shutter speed of 1/8 second and a recording frequency of 3.2 Hz. The frequency of taking PIV recordings was near the maximum attainable at this particular shutter speed leading to a missed recording on occasion.

The results in Figure (5.32) are presented in terms of a dimensionless time defined as the time from the first recording made at the peak flowrate divided by the pulse cycle time. The most notable phenomenon shown by Figure (5.32) is the unexpected velocity profile obtained in the decelerating flow period shown at dimensionless times of 1/8, 2/8 and 3/8 after the peak flow. During this phase the momentum of the fluid within the circulation system draws more fluid through the non-return valves in the pump until conditions are such that these valves seal. At a dimensionless time of 1/8 approximately 71% of the initial volumetric flowrate would be expected for a rectified sinusoidal flowrate. The effect is more prominent at a dimensionless time of 2/8 when

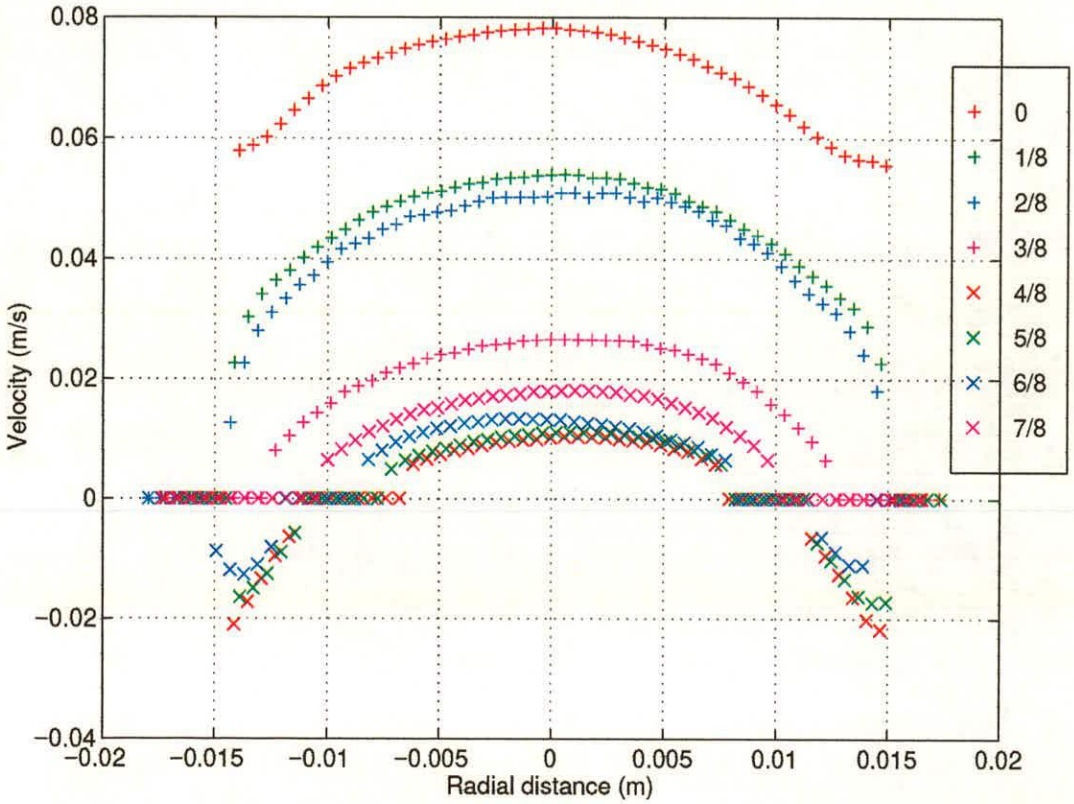


Figure 5.32: The velocity profiles produced at eight equally spaced intervals in the cycle of pulsatile pipe flow. The first profile was obtained at the peak flowrate. The legend indicates the dimensionless time at which the profile is obtained by taking the recording time (relative to the peak volumetric flowrate) and dividing by the period of the pulse.

the expected flowrate is zero; there is still a significant forward flow and the developed nature of the profile is evident. At dimensionless times of 4/8, 5/8 and 6/8 the expected profile in the zero flow portion of the pulse cycle develops. At a dimensionless time of 7/8 a forward volumetric flow equal to that at a dimensionless time of 1/8 would be expected. This is clearly not produced as a result of backflow through the suction side valve of the pump and large difference in the momentum of the fluid moving at these two points in the cycle.

A CFD simulation of the flow was performed under the same conditions. As a result of the periodic nature of the flow the boundary condition at the inlet was expressed as a Fourier series. The first 24 terms of the series approximating a rectified sine wave

were used as given in equation (5.3).

$$u(t) = \frac{A}{\pi} + \frac{A}{2}\sin(2\pi\omega t) - \frac{2A}{\pi}\sum_{\substack{n=2,\,4,\,6\,\ldots \\ n\ even}}^{\infty} \frac{\cos(2\pi n\omega t)}{n^2 - 1} \tag{5.3}$$

The time step used was 1/800 of the period of the pulse with the resulting velocities saved every 100 time steps to give comparable predictions with the experimental results. Conservative under-relaxation parameters were selected. At the start of the simulation the first step did not converge after 100 iterations. Subsequently convergence was achieved in between four and twenty iterations, dependent on the inlet velocity boundary condition. Five pulses were simulated to give a developed time dependent solution to the problem. The differences between the simulated and experimental velocity profiles are evident and arise for the reasons presented in the previous paragraph.

Test bodies

The clot deposits reported by Christy[1] in pulsatile flow, Figure (5.34), show a distinct band in which there is a thicker deposit of clot for the sphere and downstream-apex teardrop. It was suggested that this arose due to the recirculation zone behind the test body rolling up the test body producing extended contact times of hyper-coagulable material in the appropriate area of the test body. A sequence of 8 PIV images taken around the short upstream apex teardrop is shown in Figure (5.35). During the period when there is no forward flow two vortical structures develop in the region of the test body. It appears that the recirculating fluid in the wake of test body does indeed move forward and out into the bulk flow adjacent to the test body. In addition, a region of reverse flow along the wall develops, as shown in the simulations and experiments for the empty test section but the presence of the test body divides the pipe into two recirculating regions. As a result, a feature develops downstream from the test body where the flow reverses. These two structures interact to produce a jet of fluid that impinges upon the surface of the test body carrying material from the wall and also material that would previously have been trapped in the wake during forward flow.

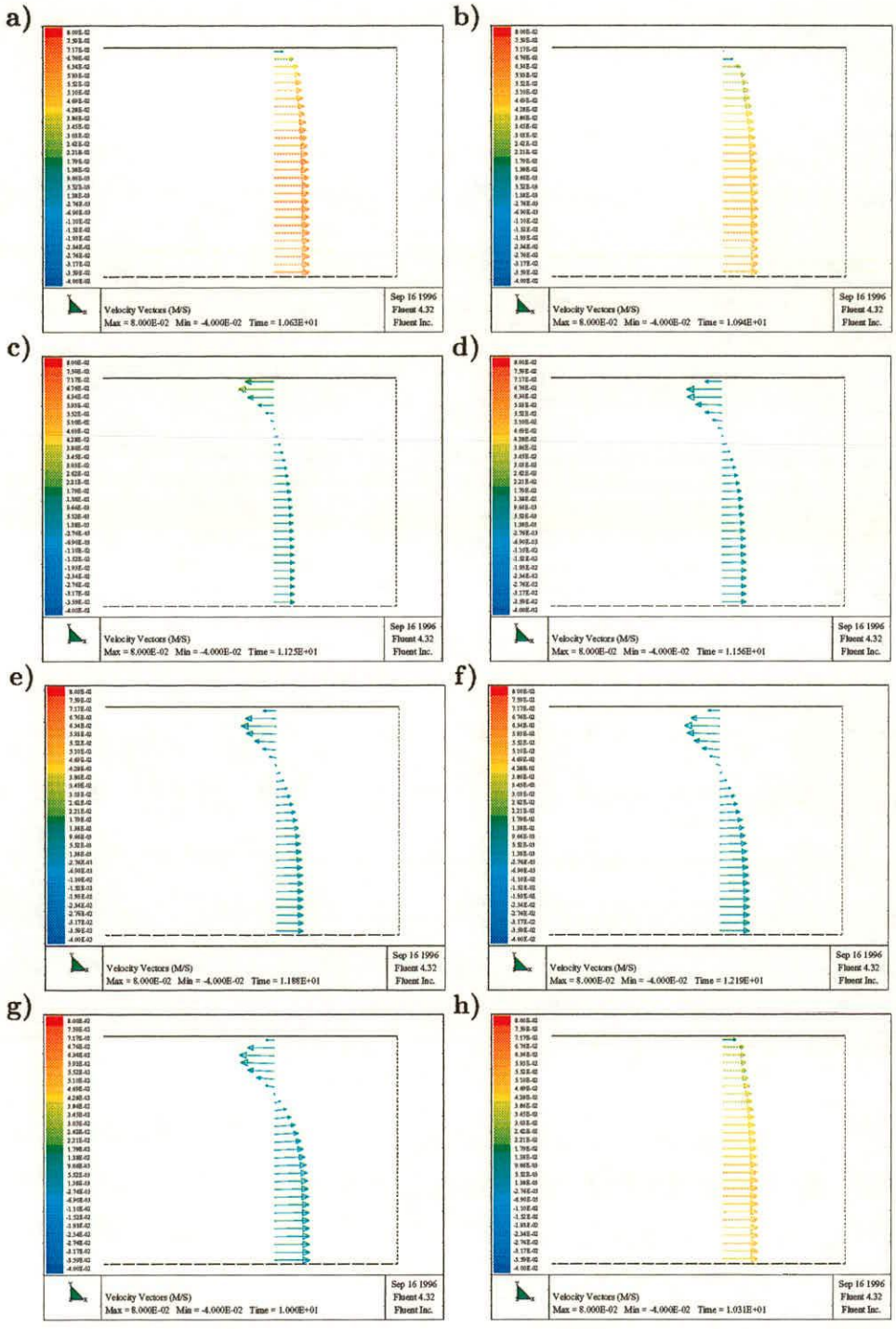


Figure 5.33: Predictions of the flow in the empty test section for an ideal rectified sinusoidal volumetric flowrate. Re = 530, α=25. The images a) through h) are at the respective dimensionless times of 0, 0.125, 0.25, 0.375, 0.5, 0.625, 0.75 and 0.875. These results are taken from the fifth cycle in the simulation.

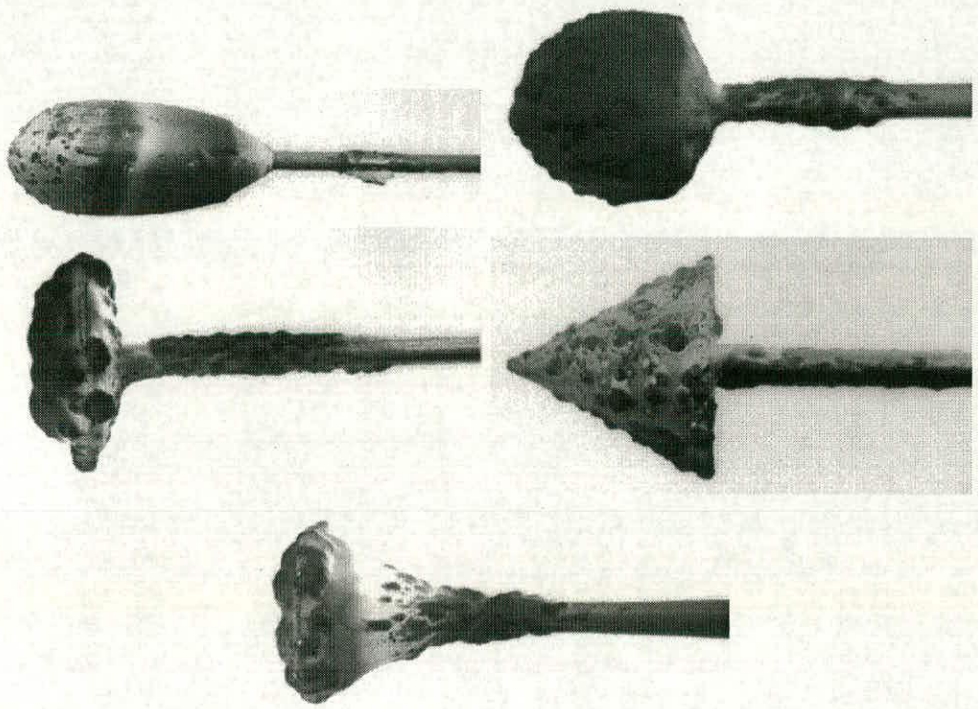


Figure 5.34: The clots observed by Christy[1] in pulsatile flow. The mean flowrate was 2×10^{-5} m^3/s and the pulse frequency 1.167 Hz.

The recordings do not resolve the origin of the fluid trapped in the recirculation zone as forward flow develops. It might be expected that the sphere would show much the same behaviour, although this was not investigated. The region of thicker clot formation observed by Christy[1] for the spherical test body may also be explained by the formation of the same type of impinging flow onto the surface of the test body.

Pulsatile flow around the upstream apex teardrop was investigated but the primary aim of these investigations was to determine the appropriate parameters to use in using the scanning beam illumination system and optimise its setup. Figure 5.36) shows example results from recordings made at random points in the pulse cycle. Again, there is clear evidence of material being transported both from near the wall and the recirculating region in the wake of the test body to the areas which exhibit the most clot deposition. Similarly, flows that are directed onto the body's surface in this region are produced and may well be the underlying factor leading to the enhanced clot deposition observed in pulsatile flow[1].

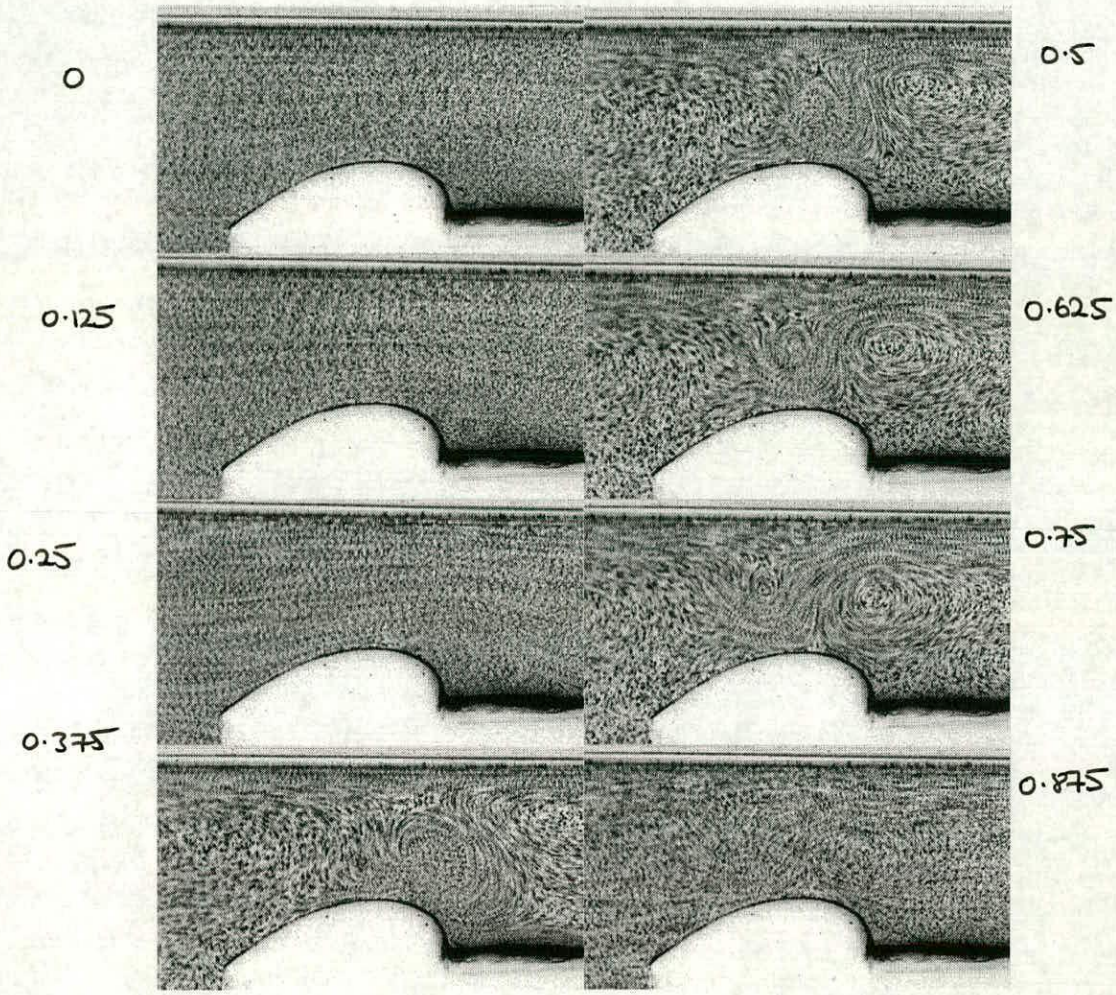


Figure 5.35: A series of 8 PIV recordings made around the short, upstream-apex teardrop in a pulsatile flow of 1.3×10^{-5} m^3/s with a frequency of 0.4 Hz. The images reading from top to bottom and then left to right were made at dimensionless times of 0, 0.125, 0.25, 0.375, 0.5 0.625. 0.75 and 0.875. The flow was seeded with 6 μm aluminium oxide particles and illuminated using the HeNe laser with the scanning beam system. The light sheet was pulsed at 40 Hz.

5.2.2 The valve designed by Dr. Norman Macleod

The low flowrate results are presented in Appendix E. The recordings show considerable variation between the same points within the pulsation cycle for consecutive pulses. This supports the evidence in steady flow suggesting significant variation in the structures found downstream of artificial valves in pulsatile flows.

PIV recordings were made at a pulse frequency of 1 Hz and at a mean volumetric

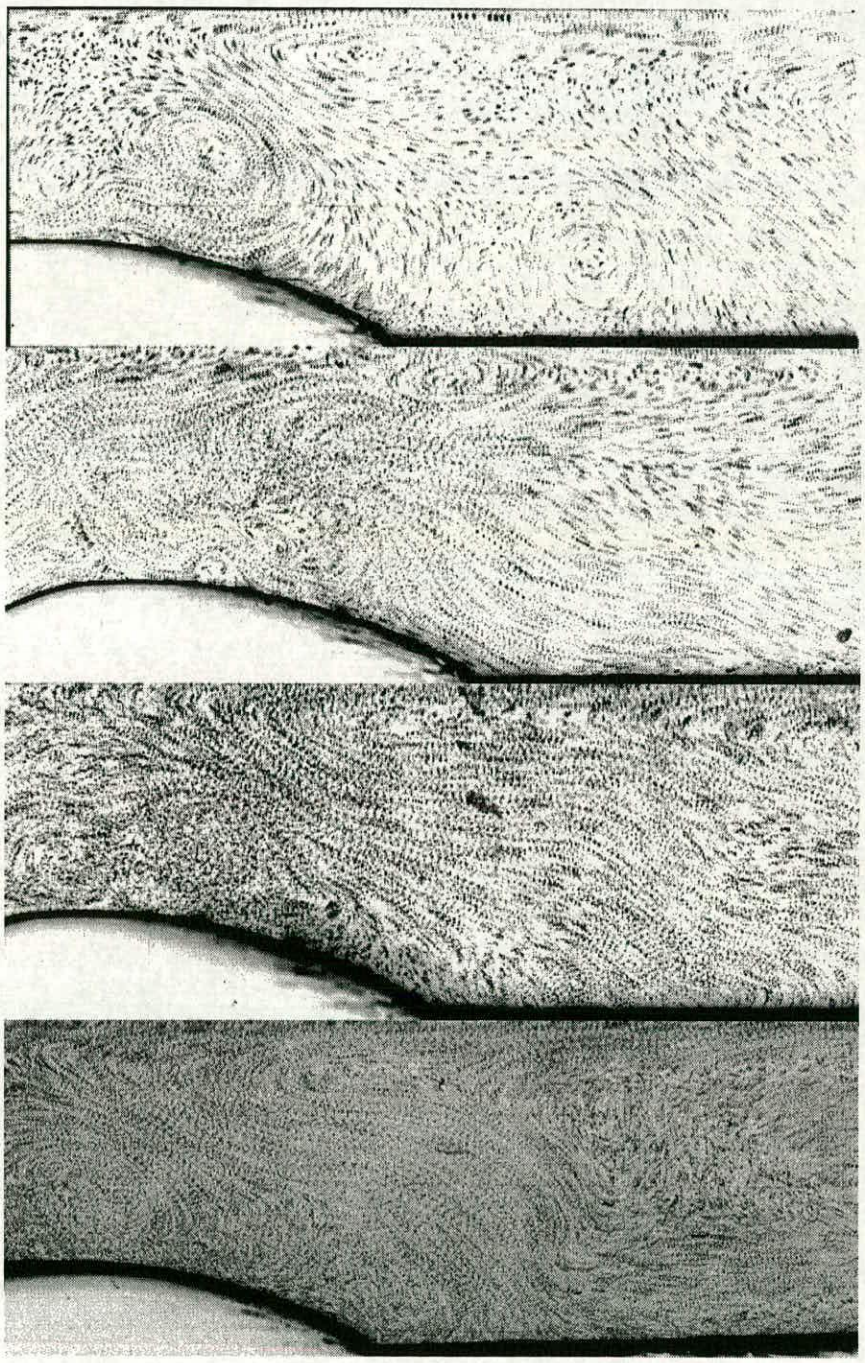


Figure 5.36: A series of 4 PIV recordings made around the downstream-apex teardrop in a pulsatile flow of 2×10^{-5} m^3/s with a frequency of 1.0 Hz. Images were recorded at random times, these represent those at various points in the stagnant phase. The illumination frequency was 75 Hz.

flowrate of 6.7 $\times 10^{-5}$ m^3/s using the Argon ion laser operating at 3W and the scanning beam illumination system. However, multiple reflections and a low signal to noise ratio arising from the use of ASA 400 film gave poor quality PIV images. The additional energy from the illuminating beam was used to increase the depth of field and allow the use of higher illumination frequencies. An aperture of approximately f/9.4 and an illuminating beam with a frequency of 300 Hz was used. This should have produced the same recording conditions as those obtained with the HeNe laser, an aperture of f/2.8, and an illumination frequency of 75Hz. The resulting images were over exposed and with larger grain than obtained before. The recordings should have been made on 100 ASA film.

However, the recordings around the peak flowrate contain images near the valve surface and wall surface that allow the minimum value of the maximum shear stress to be estimated. Figure (5.37a) shows the area around the valve at the peak flowrate (zero dimensionless time) and Figures (5.37b) and (5.37c) a similar region at a dimensionless time of 0.05. Figure (5.37d) shows a section near the wall at a dimensionless time of 0.05. All recordings were made with an illumination frequency of 300 Hz. Thus the shear stress can be estimated by taking the nearest series of particle images to the valve surface, estimating the distance to the surface, dividing the image spacing by this distance and multiplying by the frequency and the viscosity.

The figures allow the minimum values of the maximum wall and bulk shear shear to be estimated at between 0.5 and 2 N/m^2. Well below the values expected to cause to damage to erythrocytes but where structural changes to endothelial cells might be expected.

Björk-Shiley Valve

The PIV recordings produced were of better quality than those for the valve designed by Dr. Norman Macleod. This was due to the use of ASA 100 film. However, The smaller opening angle of the valve prevented measurements from being obtained in the region of the trailing edge of the moving disk. The results at a dimensionless time of

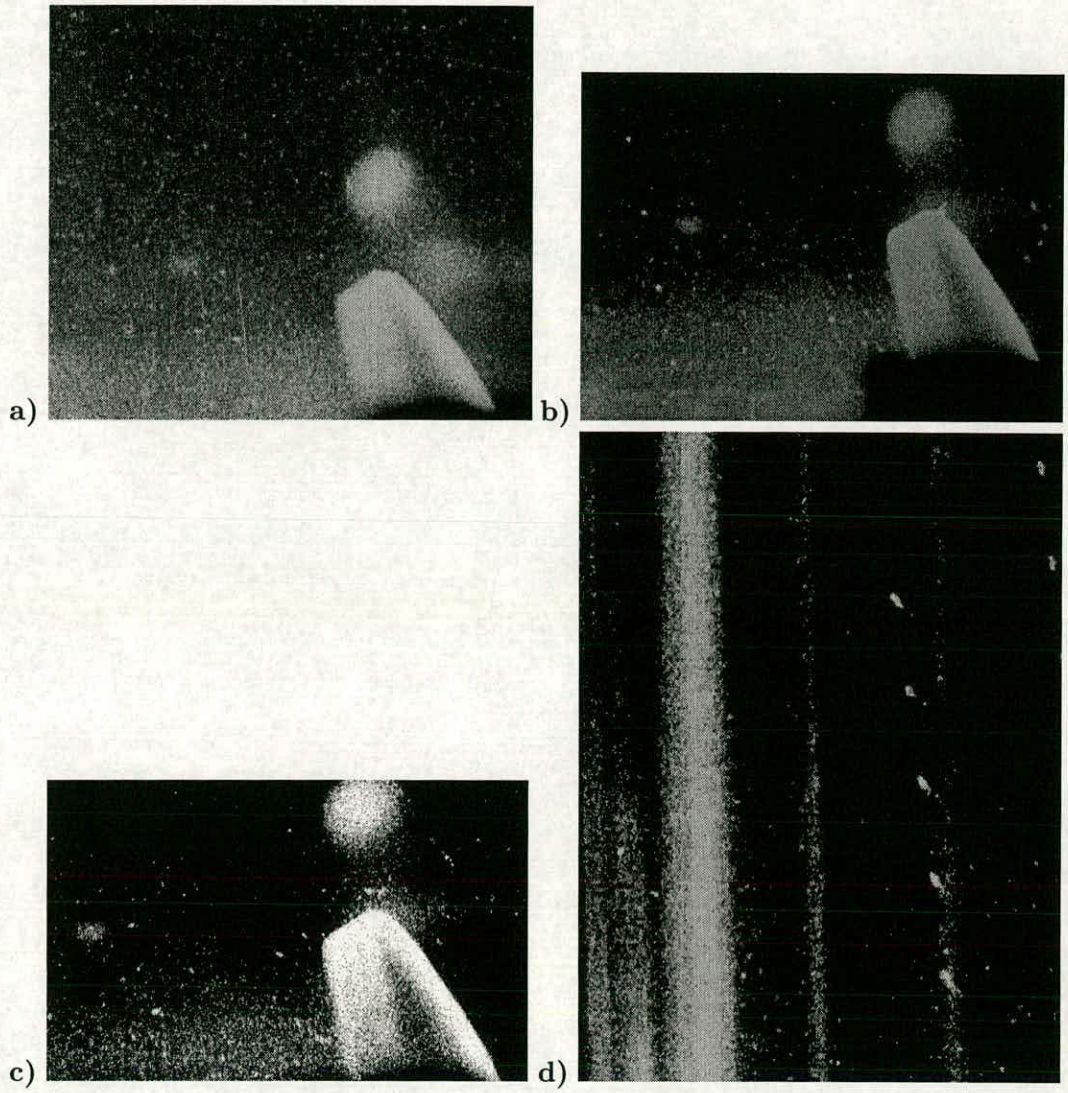
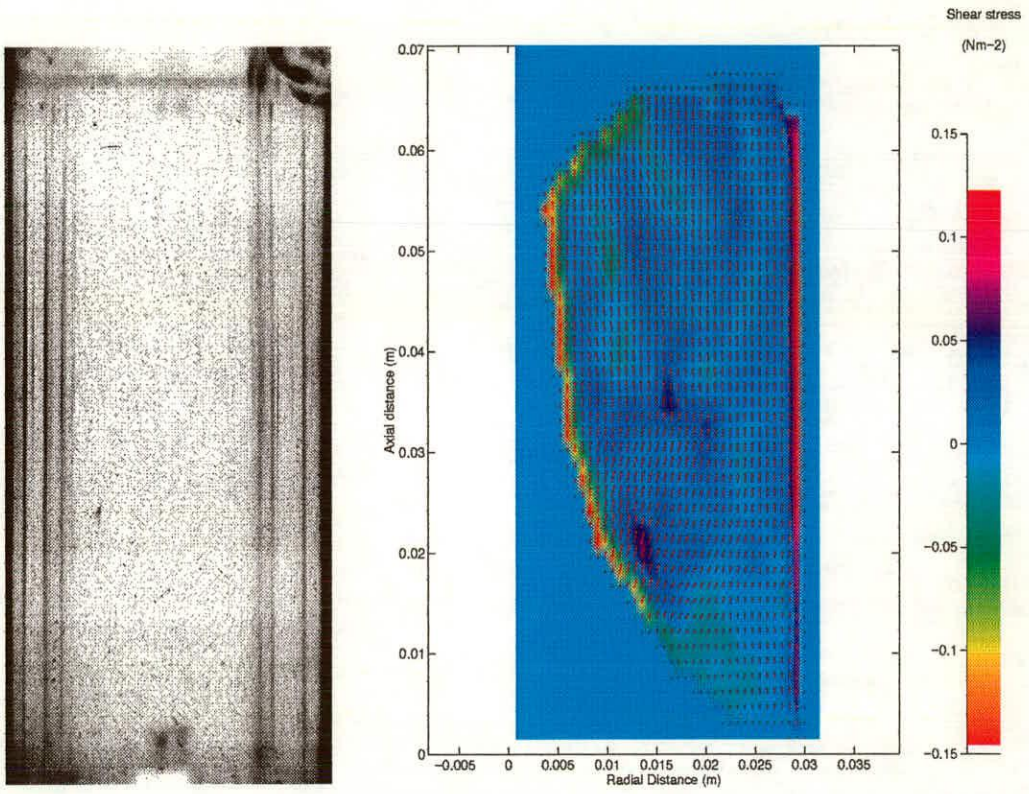


Figure 5.37: Close up sections of the PIV recordings around Dr. Norman Macleod's valve.

1/8 are presented as an example in Figure (5.38). The image was analysed using a 255 pixel deep by 127 pixel wide analysis area spaced every 32 pixels in the horizontal direction and every 64 pixels in the vertical direction.

The smoothing kernel applied to the velocities produced after analysis introduces invalid vectors at the edges of the interpolated velocity field. This produces regions of artificially high shear stress. The shear stress at the wall has a maximum of the same order of magnitude as for the valve designed by Dr. Norman Macleod. Damage to erythrocytes in this region of the flow seems unlikely.



a) b)

Figure 5.38: **a)** PIV recording made downstream of the Björk-Shiley Valve in a rectified sinusoidal pulsatile flow of 6.7 $\times 10^{-5}$ m^3/s and a pulsation frequency of 1 Hz. Re (based on the tube diameter) = 2700 and $\alpha = 40$. The flow was seeded with 6 μm aluminium oxide particles and illuminated using the scanning beam system with the light sheet pulsed at 300Hz. The recording was made at a dimensionless time of 1/8. **b)** The resulting velocity field. The maximum velocity is 0.371 m/s.

Chapter 6

Discussion

6.1 The PIV technique

6.1.1 Steady Flow

Good quality PIV images were obtained about the same bluff bodies as were used by Christy[1] and Marosek[6]in their investigations of the clotting behaviour of a blood analogue fluid. However, the range of velocities present in these flows, often referred to as the dynamic range, was such that it proved difficult to resolve the entire flow field and, in particular, the low velocities in the wake regions observed behind the test bodies. Initially, it was also found that reflections arising from the surfaces of both the test body and its supporting sting swamped the light scattered from seeding particles within the recirculation zone. The wake regions distal to the upstream and downstream apex cones were clearly recorded after repainting the test bodies matt black. The agreement observed between steady-state simulation and the experimental results was encouraging; in particular there was a strong correlation between the predicted and estimated values of the vorticity. This implies that the steady state CFD results might reasonably be used to infer information about the mean flow in the recirculation zone, where PIV measurements are difficult to obtain, and to relate areas of stasis and flow features with clot deposition.

The velocimetry results obtained in a water flow of 2 $\times 10^{-5}$ m^3/s downstream of the Björk-Shiley valve indicated the presence of significant three dimensional structures in the flow and that these structures were subject to substantial variation with time. The structures recorded proved difficult to analyse using the conventional PIV technique due to the presence of velocity gradients of sufficient magnitude to cause excessive variation in the particle image spacing over some interrogation areas. For this reason an approach was sought to deform an analysis area according to the velocity gradients within it, producing a uniform inter-image spacing. This correction procedure was assessed by applying it to simulated PIV recordings. The results suggest that in actual recordings within regions that yield a large percentage of valid vectors the deformation technique will reduce the error in the measured velocities. Applying the analysis technique to actual PIV recordings produced velocity fields that varied more evenly, particularly in areas that produced a high percentage of valid vectors, and gave valid vectors that were previously not obtained. At the periphery of structures associated with stagnation points, three dimensional flow and rotational flow, less improvement was observed; and within these features almost no improvement. The extension of the range of valid vectors into regions where the velocity gradients are relatively high was found to depend critically on the validation method used between analysis steps and on the interpolation method employed to estimate the velocities within these areas.

6.1.2 Pulsatile flow

For pulsatile flow investigations it is anticipated that a wide range of velocities will be encountered. This presents a significant challenge, particularly to make several PIV recordings within the same pulse cycle. Ideally, the illumination frequency, the shutter speed of the camera, and the laser power should be set to the optimal values for each part of the flow. The first may only be achieved using a pulsed laser system as the angular momentum of the rotating mirror (or chopper) and the power of the drive motor limit the rate of change of the pulsation frequency. In practice, these problems were resolved by the use of two techniques: firstly, by selecting reasonable recording parameters for all points during the flow pulse and making measurements at

low frequencies; and secondly, by taking a series of recordings at the same point in the cycle over a number of cycles and setting the recording parameters appropriately.

For the two test bodies investigated, slightly out of focus and blurred images were obtained; however, they served their intended purpose largely as flow visualisation experiments. Practical difficulty was experienced in focusing on the illumination plane and in aligning the camera axis normal to the light sheet. This arose as a result of the limited depth of field that could be obtained using the HeNe illumination system.

The results of the investigation of the pulsatile flow downstream of the valve designed by Dr Norman Macleod, characterised by a pulse frequency of 0.4 Hz and a mean volumetric flow rate of 1.3 $\times 10^{-5}$ m^3/s, were presented in the previous chapter. The results from different pulse cycles clearly indicate significant cycle-to-cycle variation. This is unlikely to arise solely as a result of the pump and flow system and is most readily explained by flow variations between cycles. This conclusion has significant implications for the measurement of turbulence statistics in the region of artificial valves using techniques such as LDA. Typically, estimates of Reynolds stresses are made using data gathered over the same small time interval at the same phase of a number of cycles. The typical number of cycles over which such results are averaged and the inherent variation that is likely between two successive cycles suggests that such measurements should be treated with caution. Flow structures that would not be regarded as truly turbulent may have been included in measurements of Reynolds stresses. This conjecture is supported by the evidence of Baldwin *et al.*[105] who showed that a significant decrease in the estimated values of the Reynolds stresses were obtained by applying a simple filtering technique.

The flow structures observed in the PIV recordings downstream of valve prostheses, particularly in the stagnant phase of the flow, are more complex than those observed in steady flow investigations. The presence of apparent sinks and sources indicates a complex three dimensional structure that is not possible to elucidate from a measurement of two components of the velocity in a single plane of the flow.

The example PIV recording made using the Argon ion laser at a mean flowrate of

6.7 $\times 10^{-5}$ m^3/s around the Björk-Shiley valve represents a significant improvement in the signal-to-noise ratio obtained compared with previous investigations, also using the same 6 μm aluminium oxide seeding particles. This was due to the increased power of the laser and the use of ASA 100 film. However, the recordings made using the Argon ion laser produced significantly greater refraction from the Perspex/air and Perspex/water interfaces than was found with the HeNe laser: although every effort was made to align the beam down the centre of the test section and to ensure that the beam was at its minimum width as it passed through the test section. Despite this uncertainty in the location and width of the illuminating beam, a relatively large analysis area still produced acceptable results, even in areas where there was significant reflection, demonstrating that good quality PIV images can be obtained in pulsatile flows of physiological significance. The typical cardiac output under resting conditions is approximately 70 beats per minute and results in a flow of 8.3 $\times 10^{-5}$ m^3/s [6]. The results at other parts of the cycle, not presented for the sake of brevity, again showed considerable variation in the PIV recordings obtained at the same points in different cycles. A problem with air ingress was observed at this higher pulsatile flowrate and from time-to-time bubbles were observed in the flow. The problem was reduced, but not eliminated, by raising the water tank to increase the static head in the flow system. These bubbles could have provided a mechanism by which cycle-to-cycle variations may have arisen, but this was not thought to be the dominant factor as significant variation was also seen in recordings made at the peak flowrate and at lower flowrates.

6.1.3 Damage to erythrocytes and endothelial cells

The experimental values of the bulk viscous shear stress and the stress at the walls do not exceed the threshold values required to damage erythrocytes. However, the maximum wall shear stress, estimated to be of the order of 0.5 N/m^2, does approach the value shown to introduce cell alignment and shape alteration of endothelial cells[61]. These wall shear levels may also affect the way in which damaged cells regenerate and may enhance the adhesion between endothelial cells and platelets[61]. Investigations are required in the immediate region of the valve to determine the maximum bulk

shear stress and wall shear stress that occur in the flow. Measured values of the bulk shear stress at the tip of the valve designed by Norman Macleod, of the order of 0.5 N/m^2, are again too low to cause erythrocyte damage. Other factors that may be responsible for red blood cell damage should be given equal or greater consideration. For example, cavitation, the flow through gaps around the valve when shut, and the viscous dissipation of turbulent kinetic energy.

6.1.4 Developments of the PIV technique

The developments to correct for velocity gradients clearly improve the results for simulated flow fields when there are significant velocity gradients[27]. However, in applying the method to real PIV recordings it was found difficult to set the appropriate validation parameters. A cautious approach was found to give improvements in the areas of the PIV recording already analysable and containing a large proportion of valid vectors. However, errors arise from the prediction of the velocity gradients between separated, analysable regions, the relative orientation of which can not easily be determined. It is likely that regions in the velocity field are, or become, disconnected as a result of stringent validation. These areas will then be oriented at random. For n separated regions the probability that they are all aligned correctly relative to each other is $\frac{1}{2^{(n-1)}}$. Two close regions of maloriented vectors will obviously lead to incorrect predictions of the velocities in the area between them, resulting in an erroneous correction procedure and in fact making analysis worse. A less rigorous test of the raw velocity field would leave some invalid vectors that have a similar detrimental effect on subsequent iterations of the analysis procedure. The optimal choice of validation parameters is thus critical in the algorithm's performance.

The algorithm should be compared with the alternative approach of sub-interrogation region particle tracking[332] that gives a similar improvement in measured velocities as well as an optimal spatial resolution. In fact, applying the interpolation method to corrected PIV analysis results should produce a spatial resolution comparable to that obtained using a sub-interrogation region particle tracking method, provided that the velocity variation over the interrogation region is indeed linear. A more detailed

analysis is required to determine which of the two approaches is more favourable in areas containing high velocity gradients. The particle tracking approach will always improve the results from already analysable areas. It will not yield information where conventional PIV analysis is not successful unless an interpolation scheme is used to predict velocities and then particle tracking is carried out in these areas.

The interpolation scheme used in the iterative analysis method was not optimal. A scheme better suited to interpolation in a vector field would be a thin shell spline technique as the smoothing effect of the interpolation scheme is similar to a viscous smoothing effect[276].

The procedure for orienting velocity fields was found to work well for all the PIV vector fields produced. This represents a robust method for orienting the velocity vectors produced from auto-correlation analysis methods making use of the expected smooth variation between neighbouring vectors in validated vector fields to orient vectors relative to each other.

6.1.5 Improved PIV recordings about artificial heart valves

An imaging shifting technique, as discussed in section (2.2.9) could be used to impose a known velocity upon the measured velocity field to resolve the direction of motion of the fluid and to produce measurements in the near stagnant regions of the flow. Unfortunately, any such shift velocity will be imposed on the surfaces also imaged with the technique, thus increasing the problems with flare and obscuring potential measurements close to the test bodies, wall, or valve. These regions may have proved difficult to analyse in any case without using particle tracking but even this option will then be removed. A cross-correlation approach, perhaps using two coloured pulses generated from the multi-mode output from the Argon ion laser, could be used to make two successive images of each particle image on one recording and still allow a series of photographs to be recorded, resolving the flow at several points in one pulse cycle or at the same point in successive cycles. Specialised cross-correlation cameras and digital still cameras do not allow individual frames to be captured at an appropriate rate or for

an extended period of time. As commented earlier, recent attempts at cross-correlation downstream of artificial heart valve prostheses have suffered from a low data yield and poor spatial resolution. The work of Hirt *et al.*[76] is a notable exception.

The two colour approach to resolve the third component of the velocity[193] would also be attractive in obtaining information critical in determining the three dimensional nature of the flow in the vicinity of artificial valve prostheses.

6.1.6 Potential developments of the PIV technique

The two phase PIV technique merits further attention as there are many potential applications in the chemical engineering field. In particular, the effect of replacing the removed phase with zero intensity or the mean intensity over the analysis area requires consideration. Cross-talk between the two images as a function of the separation algorithm also needs careful consideration to select the best approach. A programme of simulation and experimentation would be required to resolve these issues, which is beyond the scope of this work.

A novel development that has been used in a few simple flow situations[189,338–341] is to use encapsulated liquid crystals as seeding material and illuminate the flow with a pulsed white light source. This allows the simultaneous measurement of temperature and velocity: a useful augmentation to the techniques currently available for measuring heat transfer phenomena. The calibration between hue and temperature[342,343] requires careful attention, particularly to determine how this relationship varies with the angle between the illumination plane, the direction of observation, and how the calibration varies over the field of view. Potential hue variation over the recorded images of encapsulated liquid crystal particles must also be addressed. The use of a shear sensitive seeding material, such as encapsulated liquid crystals, may provide an alternative method to assess the fluid-mechanical damage to erythrocytes.

Problems with reflected and refracted light obscuring areas of the PIV recording may be overcome by using fluorescent particles. A significant proportion of the incident

light must be absorbed by the seeding particles and then emitted at a wavelength significantly different from that of the illuminating beam. Seeding particle images may then be separated from reflected light using a narrow band-pass filter or by selecting pixels of a particular hue range from a digital image. This technique may be more appropriate for making two phase investigations than the method described above. In particular, the scattered light from bubble surfaces in liquid/vapour flows may be illuminated.

6.2 The experimental flow system

The experiments described in the previous chapter were deliberately carried out under conditions similar to those used by Christy[1]. Similar experiments should be carried out in mock circulatory loops to predict the *in vivo* performance of prosthetic valves, for example the apparatus used by Yoganathan *et al.*[11] and Nygaard *et al.*[13]. Further improvements to the flow chamber incorporating the valve could be made by using a model sinus region. Results in the immediate vicinity of the valve could also be captured with an instantaneous technique such as PIV with an appropriately designed transparent test section. This may require that the refractive index of the fluid used to model blood be matched to the refractive index of the material of construction of the test chamber to minimise refractive distortion. It may be also be possible to make a transparent valve to get simultaneous information from all parts of the flow. The use of a test fluid with non-Newtonian behaviour similar to blood, for example xantham gum[60], would be appropriate, particularly to investigate cavitation behaviour at the same time as determining the flow field.

The relation of clot formation to fluid mechanical structures requires information about the location and volume of clot formed as a function of time. The structures that are present at particular times in the clotting process may then be determined. The ultrasound based investigations of Marosek[6] were not clear enough to determine the shape of the developing milk clot using the same blood analogue fluid and flow system as Christy[1].

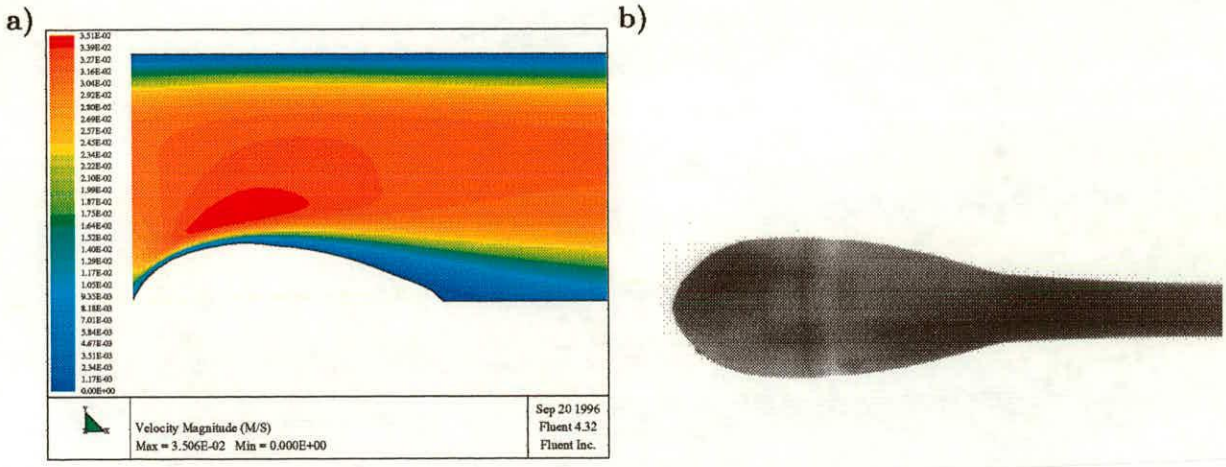


Figure 6.1: A comparison of the simulated velocity magnitude with the location of clot formation for the downstream apex teardrop in steady flow. The Reynolds number based on the test body diameter is 250. The two images are shown to the same scale.

6.3 Relating flow features to clot deposition

The discussion will be limited to the test bodies investigated by Christy[1] in his medium length test chamber. Figures (6.1), (6.2), (6.3), and (6.4) show the velocity magnitude determined using FLUENT with the highest grid resolution, as previously described, and the clot deposition observed by Christy[1]. The correlation between areas of clot deposition and stasis and indeed the surface of the clot and the lowest value contours of the velocity magnitude is immediately striking and supports the hypothesis that stasis is a necessary condition for clot deposition to occur.

6.3.1 Steady Flow

Figure (6.1) shows correlation between the formation of clot and the small region of stagnation at the point where the test body meets the supporting sting. The clot formed on the sting in this case is significant, in contrast to the clot formed on the sting downstream of the other test bodies. This may be explained by the stability of the recirculation zone: no periodic ejection of material was evident in the residence time investigations although there was significant structure within the recirculation zone. This supports the assumptions made in predicting the clot growth for this particular

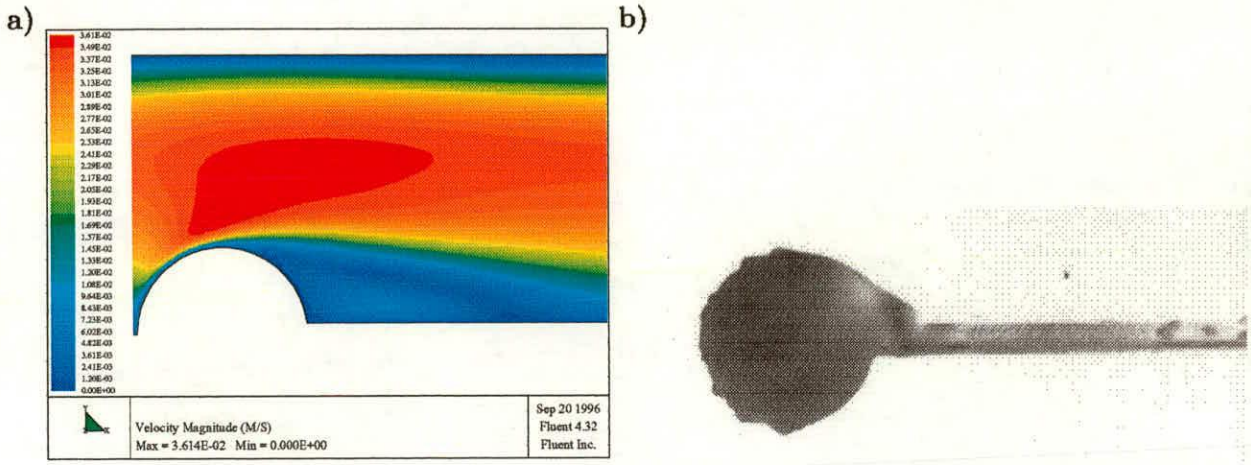


Figure 6.2: A comparison of the simulated velocity magnitude with the location of clot formation for the sphere. The Reynolds number based on the test body diameter is 250. The two images are shown to the same scale.

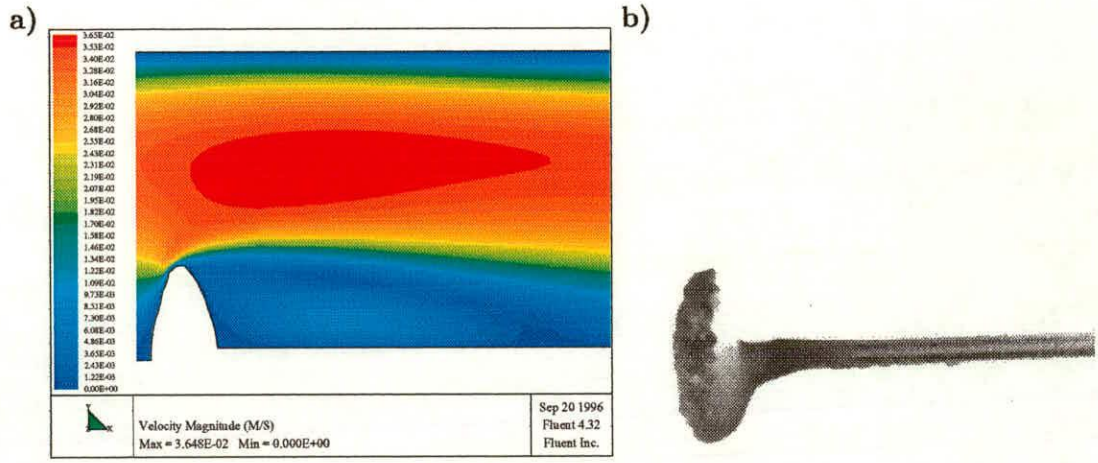


Figure 6.3: A comparison of the simulated velocity magnitude with the location of clot formation for the oblate. The Reynolds number based on the test body diameter is 250. The two images are shown to the same scale.

body as the clot does appear to form in the entire wake region of the body. This would appear reasonable given the stability of the recirculation zone. Further clot may be deposited at the clot surface as the reaction reaches completion in these areas of comparatively low velocity. This seems a reasonable explanation for the observed behaviour and supports similar arguments put forward by Christy[1], and Christy and Macleod[64]. It would be useful to have information about the clot shape as a function of time to confirm this hypothesis. An alternative might be to simulate the clotting

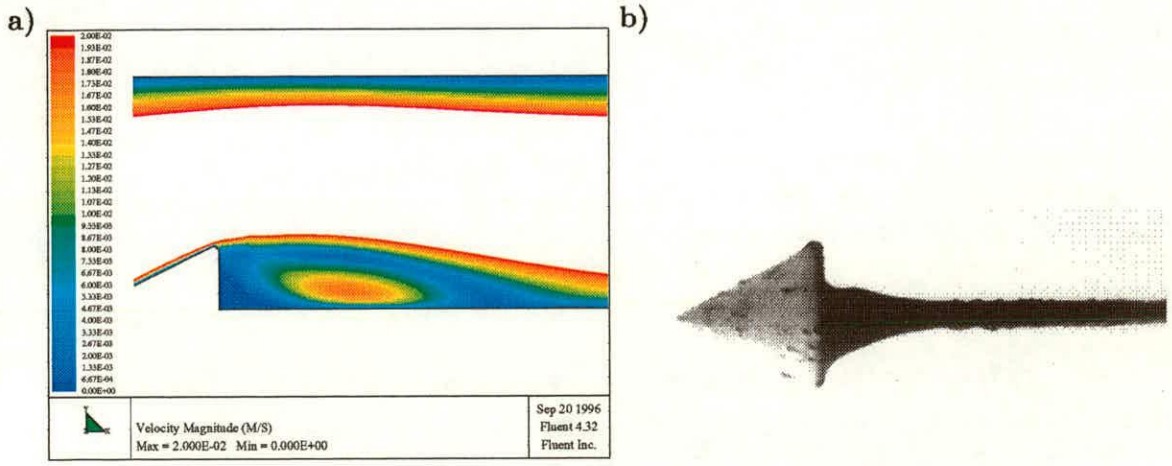


Figure 6.4: A comparison of the simulated velocity magnitude with the location of clot formation for the upstream apex cone. The Reynolds number based on the test body diameter is 250. The two images are shown to the same scale.

reaction in FLUENT by approximating the reaction kinetics and making a product with high viscosity and/or non-Newtonian behaviour.

Figures (6.2), (6.3), and (6.4) show the significantly different clotting behaviour observed around the sphere, disk, and upstream-apex cone. In the residence time investigations reported in the previous chapter the recirculation zone behind these test bodies was shown to be less stable than that observed behind the teardrop. For these three obstacles a periodic ejection of material was observed from the recirculation region with a period of about two seconds, which was presumed to be associated with vortex shedding. The wake regions behind these test bodies also exhibited a lower mean residence time, evident from the decay of the seeding particle concentration, although this could not be estimated in the same way as for the teardrop. The results are broadly in agreement with Christy's[1] observations from dye tracer experiments. As would be expected, the steady state CFD predictions do not predict the vortex shedding shown in the PIV recordings. However, there is a striking correlation between the shape and location of clot deposition and the iso-velocity-magnitude contours within the regions of stasis. It seems likely that clot is deposited where there is almost no fluid movement. Compared with the teardrop shaped test body, the structure within the wake region and a lower residence time tends to reduce the rate at which clot is formed within the

remainder of the recirculation region and in particular on the surface of the sting.

The clot deposition observed by Marosek[6], again using milk as a blood analogue fluid, is difficult to compare with the observations made by Christy[1] as a result of numerous differences in experimental conditions. In general, the investigations reported by Marosek[6] produced greater clot deposition. The clot reported about the teardrop shaped test body resembled that given by Christy[1] in the short test section. The clot deposition reported by Marosek[6] for the disk and upstream apex cone was much more pronounced within the recirculation region, to the extent that the clot about the disk resembles a downstream apex cone. For this reason, Marosek concludes that clot is preferentially formed in the wake region of the test bodies where the mean residence time near the test body is increased compared with the bulk flow. Ultrasound imaging, although unable to determine the changing shape of the clot, did capture images of air bubbles within the recirculation region. The motion of these bubbles indicated that the wake region decreased in volume and elongated over time as clot was deposited[6]. A marked variation in the deposition of clot around the same shape of test body constructed from a range of materials was observed in steady flow by Marosek[6]. The clots reported in the wake region of the the disk and upstream apex cone show some agreement with the simulated and experimentally determined recirculation zone, although there are differences arising as a result of the more extensive clot deposition.

Marosek[6] also observed thinning of the clot formed on the test section wall in the region of the test body. Comparison with the predicted and experimentally determined flows shows that this correlates well with the shape of streamlines deformed by the presence of the the test surface in roughly the same shape as the observed clot. The reduced deposition may arise as a result of either increased shear disrupting forming clot or a decrease in the mean residence time in this region of the flow.

6.3.2 Pulsatile Flow

The PIV recordings made about the test bodies in pulsatile flow essentially served their purpose by providing an accurate visualisation of the flow. The presence of the test

body produced a marked change in the flow structures seen during the stagnant part of the pulse cycle compared with those observed without the test body. In both cases, a region of reversed flow is expected at the wall of the test chamber and is evident in the PIV recordings. In the stagnant phase of the flow, the recirculating region behind the test body appears to move towards the outer wall and slightly upstream producing a flow feature to the side of the test body. Downstream of the test body the momentum of the fluid maintains forward flow at the same time as reversing flow is developing at the walls, producing a vortical structure. These two features then interact to direct material on to the surface of the test body. The material is directed from the reverse flow region near the wall and also from within the recirculating region. In forward flow these are regions of lower velocity and therefore the clotting reaction is likely to be more advanced in the fluid originating from these locations. It seems probable that hyper-coagulable material is thus directed on to the surface of the test body in regions that correlate with the formation of thicker layers of clot[1]. This proposed mechanism must be regarded with some scepticism until it can be shown that the developing clot structure and its interaction with the flow produces similar structures. However, given the streamlines shown by particle tracks this seems plausible. This behaviour was shown for the upstream apex short teardrop and the downstream apex teardrop and, although similar features would be expected for the other test bodies, these have yet to be investigated. The development of structures during the onset of forward flow were too rapid to be resolved.

In pulsatile flow the clot observed by Marosek[6] shows better agreement with that observed by Christy[1], However, a conical deposition of clot was observed adhering to the supporting sting downstream of each of the test bodies. It is possible that this is related to the oscillating nature of the flow near the sting surface producing an increased contact time between the surface and coagulable material. More pronounced thinning of the wall clot adjacent to the test section was observed in pulsatile flow situations[6]. This may reflect the combined effect of the structures observed in the pulsatile flow investigation tending to direct material from the wall towards the pipe centreline, enhancing mass transfer.

The preliminary investigations of the flow fields around artificial heart valves clearly indicate the potential of the PIV technique in this particular application. There is scope to resolve turbulent structures within the flow with a size an order of magnitude greater than that of the seeding particles. Further, the size of the seeding particles is the same order of magnitude as red blood cells and so they should produce a similar interaction with the energy dissipating structures within the flow. In areas further downstream from the valve, the line of flight method[18,270] might be used to estimate turbulent statistics and allow direct comparison with previous LDA measurements. After correction for velocity gradients, the shape of the self-correlation and signal peaks can be compared to determine whether the structures with the fastest turnover rate have been resolved. This would be indicated if there was broadening of the signal peak arising from velocity fluctuations within an analysis area. In addition, it should be possible to make a better assessment of the interaction of jets with arterial surfaces, to determine locations of stasis, and possibly to record and quantify the effects of cavitation.

Chapter 7

Conclusion and recommendations for future work

7.1 Conclusions

① The PIV technique has been applied with some success in steady and pulsatile flows around a series of axisymmetric test bodies and heart valve prostheses. The complex nature of the structures observed required that the PIV technique be extended to cope with analysis areas over which there is a significant change in the inter-image spacing. Preliminary results have been obtained under pulsatile flow conditions representative of the normal cardiac output.

② The maximum viscous shear stress determined downstream of the prostheses under investigation was of the order of 0.5 N/m^2, well below the value thought to produce damage to erythrocytes and platelets. However, such viscous shear levels at the arterial wall may induce behavioural changes to endothelial cells and promote the adhesion of platelets to endothelial cells. Typical values of the bulk viscous shear stress were an order of magnitude lower than those found near surfaces.

③ Steady flow investigations and their comparison with clotting observations clearly support the hypothesis that stasis plays a dominant role in governing the location of deposition. A crude prediction of clot growth within the stable recirculation

region found in the wake of the teardrop shaped test body gave a reasonable estimate of the time required experimentally for the clot to develop.

④ Pulsatile flow investigation around the test bodies, although not as extensive as the investigations in steady flow, indicate a relationship between the formation of thicker layers of clot on the test body and the structures developed in the stagnant part of the flow cycle. These structures essentially direct material that has been trapped in the wake region and also from the wall of the test section on to the surface of the test body. The location of this impingement coincides with the position of thicker clot deposits.

⑤ An automated procedure for the validation and orientation of velocity vectors has been used through out this work. The orientation algorithm has been shown to be robust for a considerable range of recordings. The validation algorithm is a simple extension of those based on the global mean and local median tests, adapted to take into account the ambiguity in the velocity vectors obtained from auto-correlation analysis. Some difficulty in selecting the appropriate tolerances for the tests was encountered, particularly when used to validate the vector fields between stages of the iterative procedure to compensate for velocity gradients.

⑥ A comprehensive assessment of the errors associated with a PIV analysis program has been carried out leading to the following recommendations (in addition to those accepted by convention): the digitisation procedure should resolve particles with an e^{-2} diameter of two pixels; the Gaussian peak location method should be used; padding should be included to avoid wrap around noise at the largest displacements expected; and post analysis validation procedures are more reliable than those based on properties of the auto-correlation function.

⑦ The flows downstream of the tilting disk artificial heart valve showed considerable three dimensional structure and this structure varied significantly over time.

⑧ Investigations of the flows observed in the wake regions of tilting disk valves in pulsatile flows indicate that there was significant cycle-to-cycle variation of flow structure. This has direct implications on the use of averaging techniques, such as commonly used with LDA, to estimate turbulence statistics. It seems likely

that structures that would not be regarded as turbulent in nature and inherent variations in the flow will artificially increase the estimated degree of turbulence and estimates of the Reynolds stresses.

⑨ A deformation algorithm has been developed to correct for the variation in inter-image spacing over a PIV analysis area that arises from the presence of velocity gradients. This was shown to give a significant improvement in both the accuracy and percentage of valid vectors produced when analysing a simulated PIV recording of an Oseen vortex. The application of the algorithm to real PIV images suffered because of the lower data yield and unrealistic flows generated by the interpolation/extrapolation schemes employed.

7.2 Further Work

① Residence time experiments, similar to those carried out in steady flow, should be made for the range of test bodies in pulsatile flows. Residence time experiments in the wake region of the sphere would also be useful.

② Further PIV investigations of the flow structures around the test bodies should be carried out in the appropriate pulsatile flow regimes. This is required to confirm the link between the surface impingement of material from the wake and wall regions and the location of enhanced clot deposition.

③ Experimental equipment should be constructed to simulate the flow resistance and compliance of the circulatory system. PIV investigations of the flows around heart valves in sections modelling the flows in the mitral and aortic valve locations could then be made. The flow features likely to promote haemolysis and thrombosis can then be ameliorated by modifications in valve design.

④ PIV results should be used to validate CFD predictions of the flows around heart valve prostheses. Once the code modelling the fluid behaviour in pulsatile flows has been validated an attempt might be made to include the kinetics of the clotting reaction and simulate deposition.

⑤ The performance of other valves not included in the this study could be assessed to develop a systematic approach for their comparison, perhaps based on evaluating the red blood damage index proposed by Giersiepen *et al.*[7].

⑥ Directional ambiguity and the near zero velocities in the wake regions of the test bodies could be resolved using a cross-correlation technique. Bearing in mind the nature of the flow and the information sought, this may best be achieved using a two colour technique. Green and blue illumination pulses of comparable intensity of around 1 W could be obtained by splitting the multi-mode output of the 4 W Argon ion laser and directing each beam onto the rotating mirror system. Alternatively, two coloured beams could be produced slightly offset in the illumination plane. This would give a hue change as particles passed through the illumination plane that would be related to the third component of the velocity.

⑦ The method used to interpolate velocity vectors between stages of the algorithm that corrects for velocity gradients requires further evaluation. A thin shell spline technique appears attractive as it incorporates an effect similar to viscous smoothing.

⑧ The next step in relating flow structures to clot growth requires that the shape and location of the growing coagulum be determined as a function of time. At the moment the investigations are limited to studying the flows in the initial stages of thrombus formation.

⑨ The construction of the test section requires refinement to minimise the refracted and reflected light recorded in the PIV negatives. Alternatively, the use of fluorescent seeding particles may allow the light emitted from the seeding material and scattered from surfaces within the test chamber to be separated. The use of such particles may have wider application in the investigation of two-phase flows. A further augmentation to the PIV technique, appropriate for studying heat transfer phenomena, may be made by using a white light source and encapsulated liquid crystal seeding material.

Appendix A

A.1 The performance of the analysis algorithm for ideal PIV recordings

This appendix presents the results from generating a large number of PIV recordings using the simulation algorithm. All the simulated images were 2048 by 2048 pixels containing Gaussian particle images with a maximum intensity of 255 (the maximum value for the PGM file format). Images were simulated for two, three, and four pulse recordings with a velocity in the x direction in the range 1 to 40 pixels/s and zero velocity in the y direction. The time interval between illumination pulses was one second. The number of effective image pairs was also investigated, values of N_P equal to 1, 4, 8, 10, 16, and 24 were used. This gave a total of 2916 simulated PIV recordings. Image sizes with e^{-2} diameters of 1, 2, 4, 6, 10, an 16 pixels were simulated.

The images were analysed by performing real, fully padded fast Fourier transforms of 64 by 64 pixels (128 by 128 when padded). The signal peak location was calculated using (a) the volume moment technique, (b) Gaussian interpolation over the nine points surrounding the maximum value, and (c) Whittaker's interpolation technique. Each set of results was validated by removing vectors six standard deviations away from the global mean velocity, six standard deviations away from the local median velocity, and velocity vectors over an angle $\frac{\pi}{4}$ rotated from the local median velocity. These values were chosen to take account of the uniform flowfield expected from the simulation.

For each simulated PIV recording the mean velocity over the recording is determined both before and after applying the validation procedure. Each point on the following plots represents an average from 1024 PIV analysis areas. For each combination of peak location method, image size, and image particle intensity a series of PIV recordings were simulated with varying inter-particle image spacings and particle image densities. The results are summarised in a series of four plots. Plot a) represents the ratio of the measured displacement to the actual displacement in the simulated image. This ratio is ploted as a function of the actual displacement with the particle image density as a parameter. The average velocity is determined from each vectior map before validation. Plot b) repreents the same information as plot a) but the velocity filed was validated

before calculating the mean velocity. Plot c) shows how the percentage error in the measurement of the displacment varies as a function of the actual displacement with the particle image sensity as a parameter. The percentage error is determined from the unvalidated vector field for each point. Plot d) represents the same information as plot c) but after validating each vector field. Some plots are repeated on a magnified scale to reveal greater detail in the plots. The caption indicates only the number of illumination pulses and the diameter of the image particles of the simulations used in producing the information reported.

A.2 Volume moment peak location method

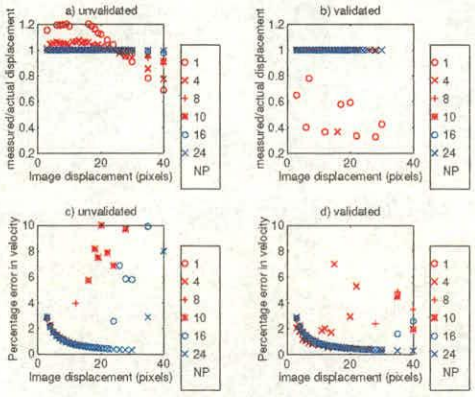


Figure A.1: Results for two pulses and an image diameter of 1 pixel.

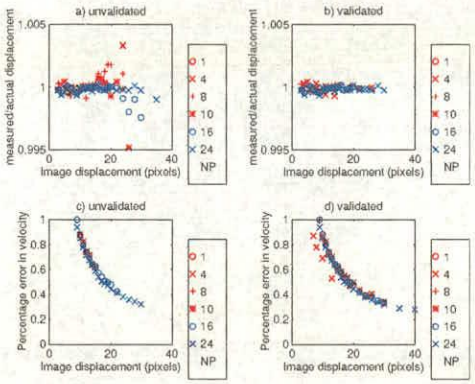


Figure A.2: Results for two pulses and an image diameter of 1 pixel. (Magnified view)

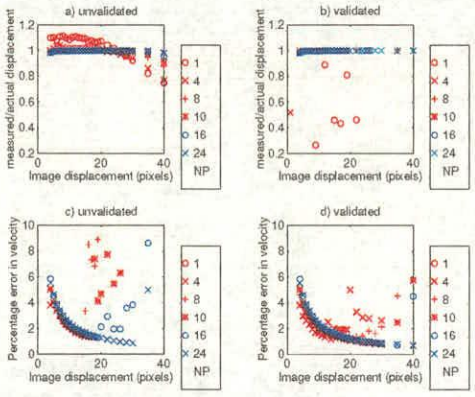


Figure A.3: Results for two pulses and an image diameter of 2 pixels.

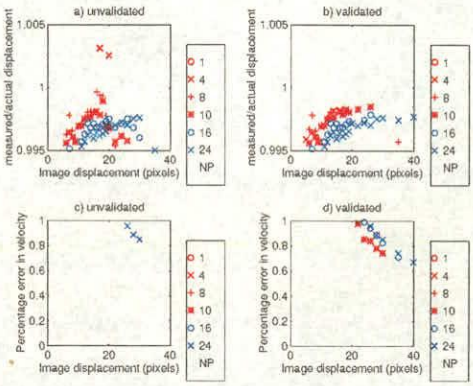


Figure A.4: Results for two pulses and an image diameter of 2 pixels. (Magnified view)

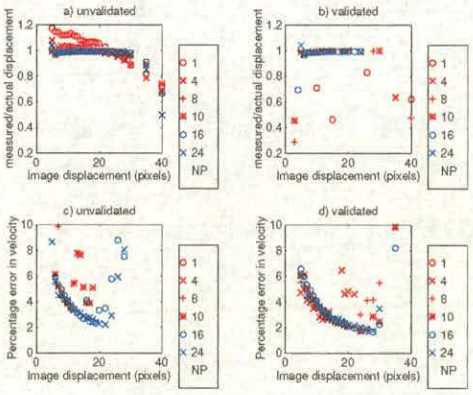


Figure A.5: Results for two pulses and an image diameter of 4 pixels.

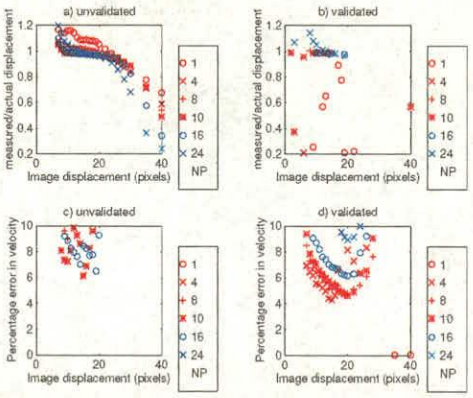


Figure A.6: Results for two pulses and an image diameter of 6 pixels.

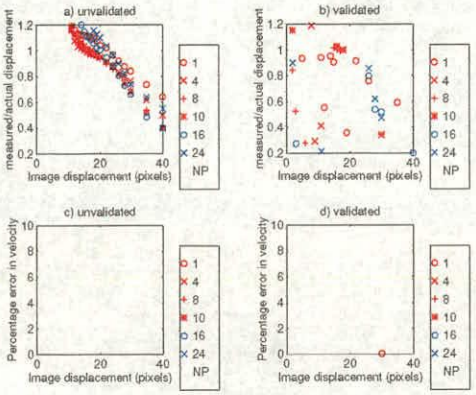


Figure A.7: Results for two pulses and an image diameter of 10 pixels.

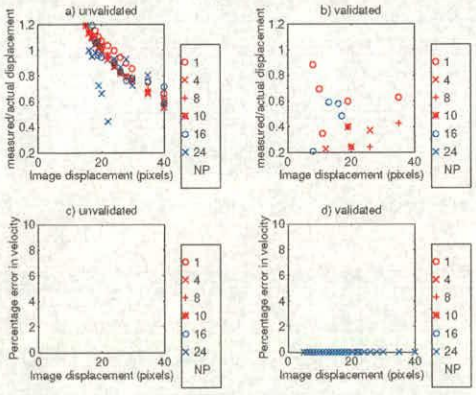


Figure A.8: Results for two pulses and an image diameter of 16 pixels.

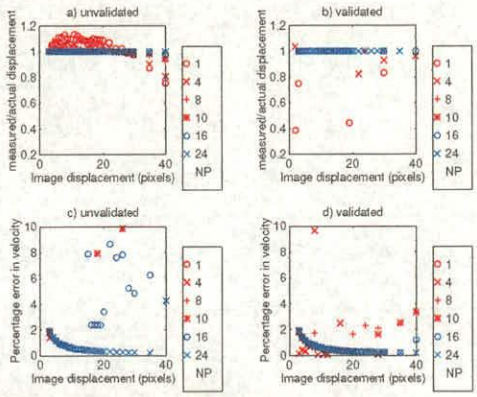


Figure A.9: Results for three pulses and an image diameter of 1 pixel.

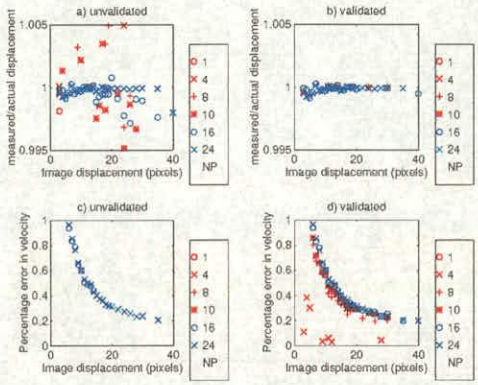


Figure A.10: Results for three pulses and an image diameter of 1 pixel. (Magnified view)

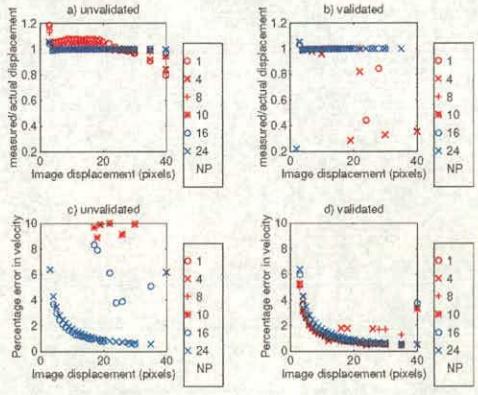


Figure A.11: Results for three pulses and an image diameter of 2 pixels.

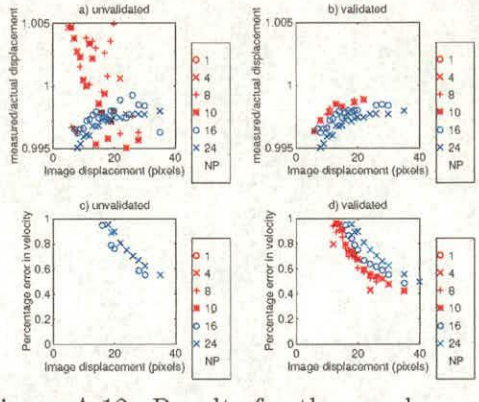


Figure A.12: Results for three pulses and an image diameter of 2 pixels. (Magnified view)

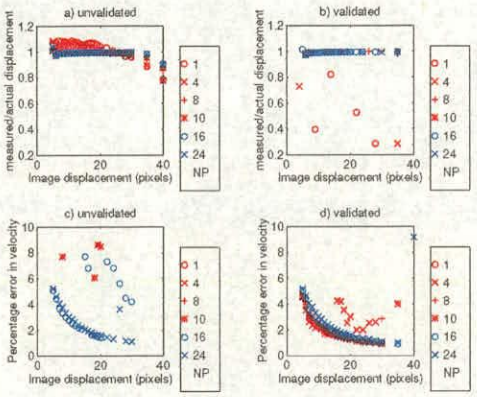


Figure A.13: Results for three pulses and an image diameter of 4 pixels.

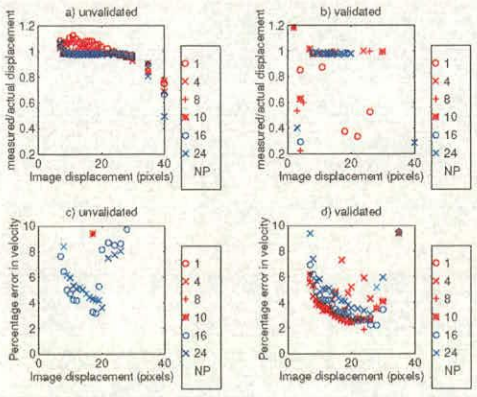


Figure A.14: Results for three pulses and an image diameter of 6 pixels.

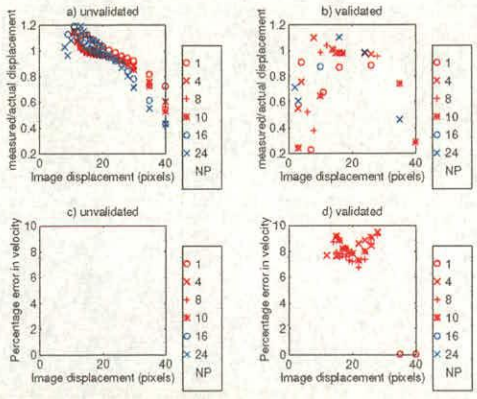


Figure A.15: Results for three pulses and an image diameter of 10 pixels.

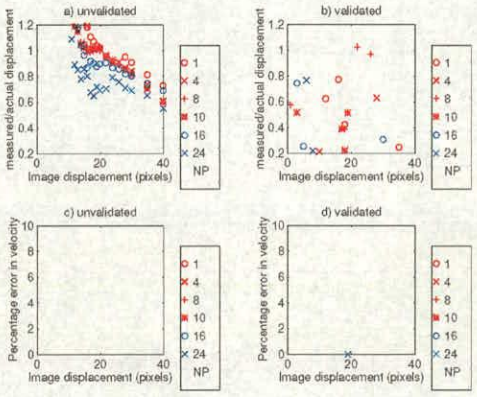


Figure A.16: Results for three pulses and an image diameter of 16 pixels.

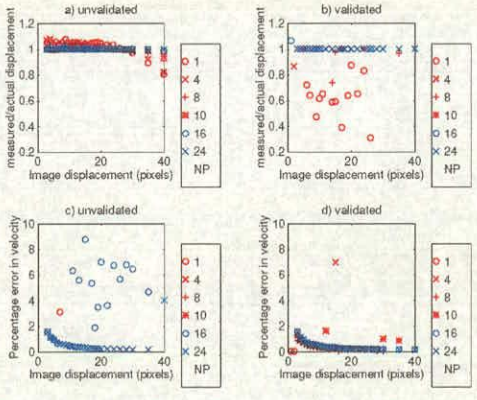


Figure A.17: Results for four pulses and an image diameter of 1 pixel.

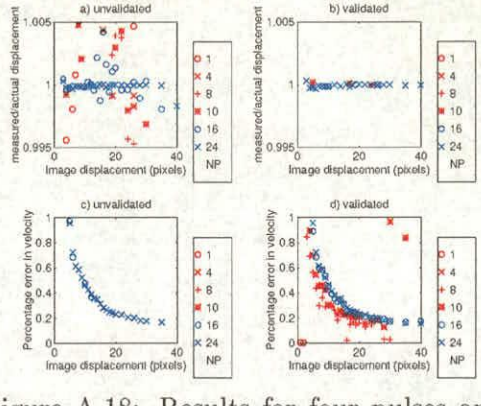


Figure A.18: Results for four pulses and an image diameter of 1 pixel. (Magnified view)

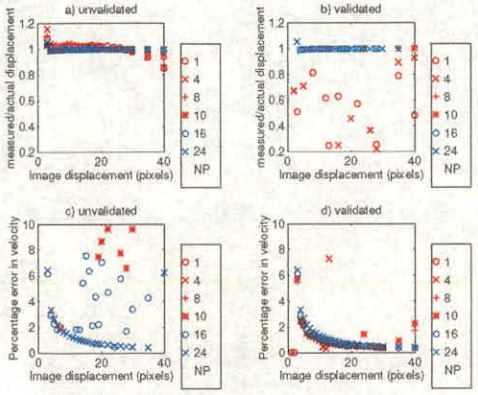


Figure A.19: Results for four pulses and an image diameter of 2 pixels.

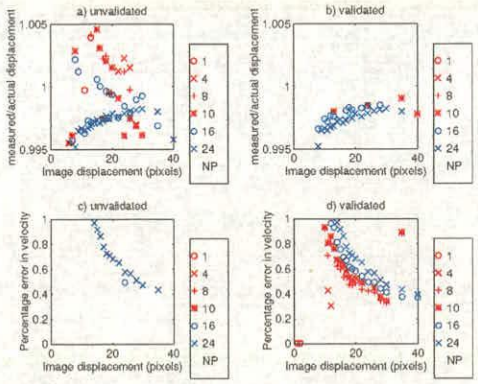


Figure A.20: Results for four pulses and an image diameter of 2 pixels. (Magnified view)

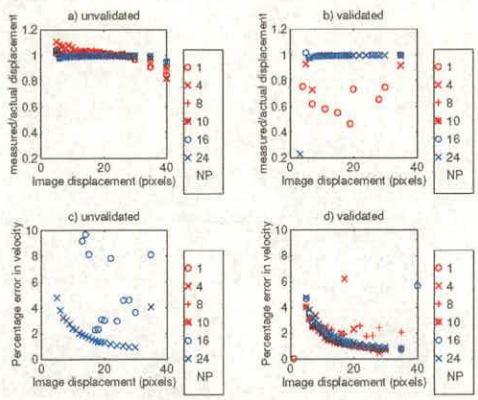


Figure A.21: Results for four pulses and an image diameter of 4 pixels.

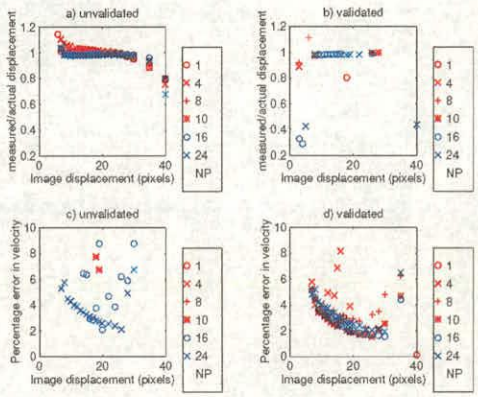


Figure A.22: Results for four pulses and an image diameter of 6 pixels.

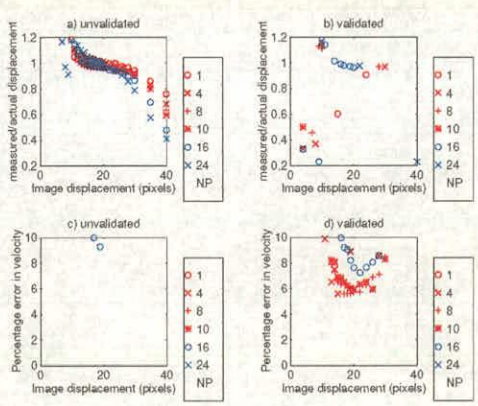


Figure A.23: Results for four pulses and an image diameter of 10 pixels.

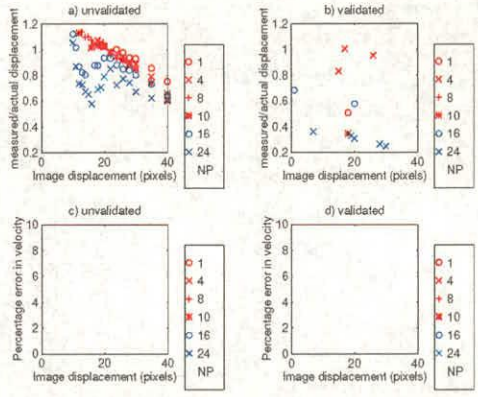


Figure A.24: Results for four pulses and an image diameter of 16 pixels.

A.3 Gaussian moment peak location method

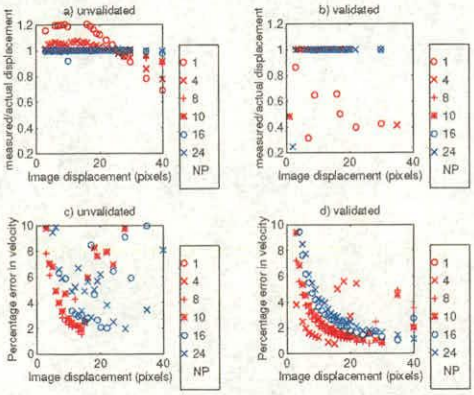


Figure A.25: Results for two pulses and an image diameter of 1 pixel.

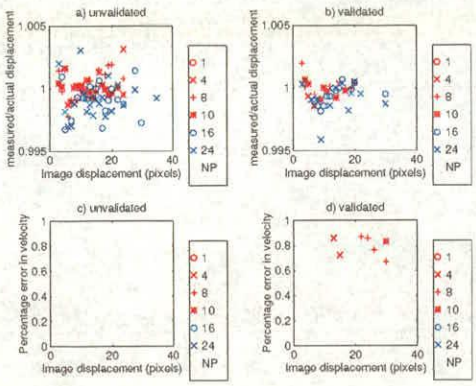


Figure A.26: Results for two pulses and an image diameter of 1 pixel. (Magnified view)

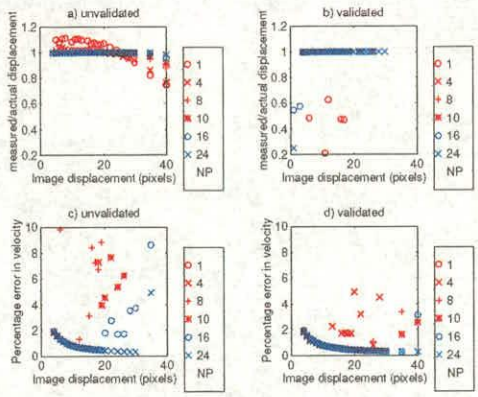


Figure A.27: Results for two pulses and an image diameter of 2 pixels.

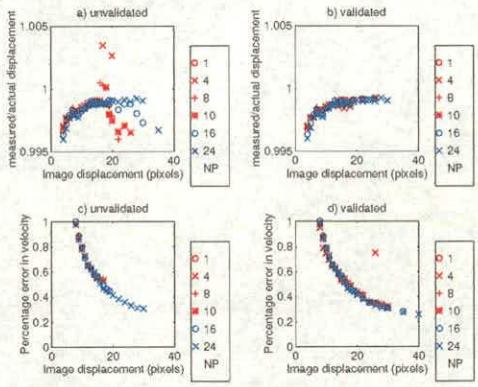


Figure A.28: Results for two pulses and an image diameter of 2 pixels. (Magnified view)

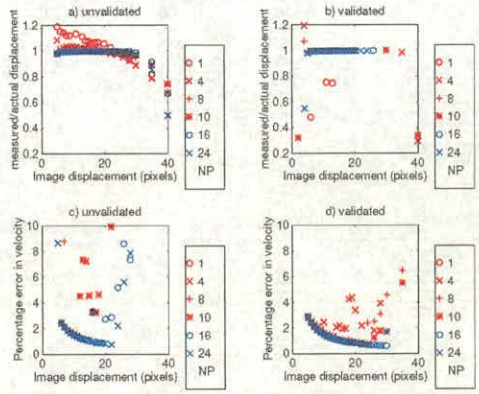


Figure A.29: Results for two pulses and an image diameter of 4 pixels.

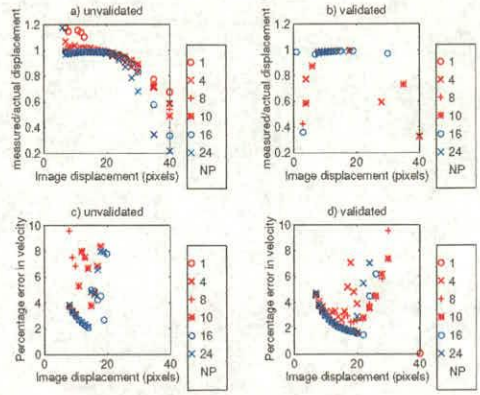


Figure A.30: Results for two pulses and an image diameter of 6 pixels.

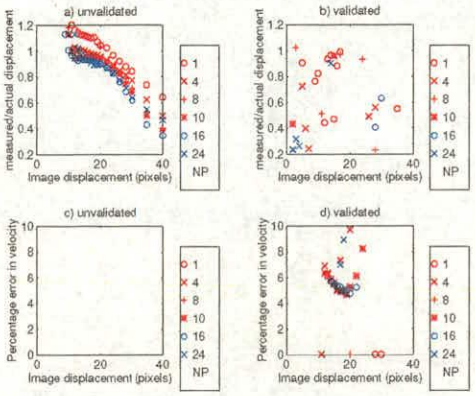


Figure A.31: Results for two pulses and an image diameter of 10 pixels.

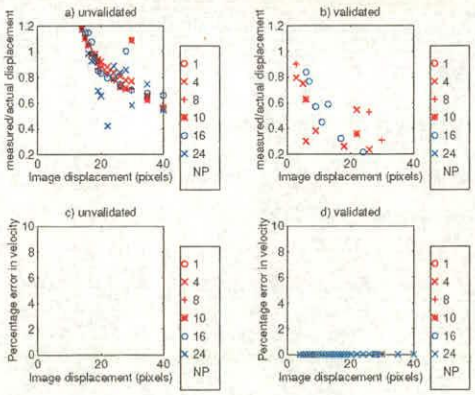


Figure A.32: Results for two pulses and an image diameter of 16 pixels.

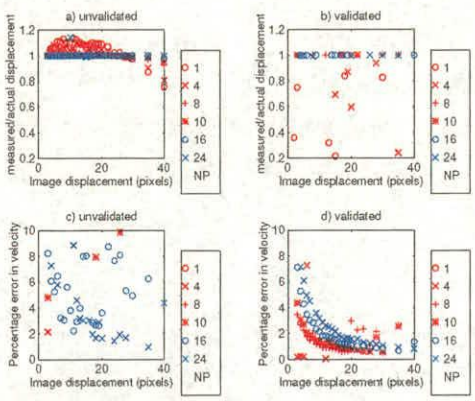


Figure A.33: Results for three pulses and an image diameter of 1 pixel.

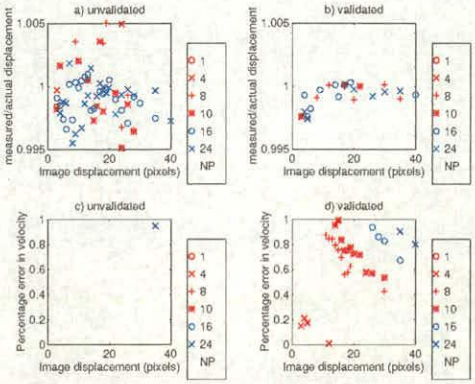


Figure A.34: Results for three pulses and an image diameter of 1 pixel. (Magnified view)

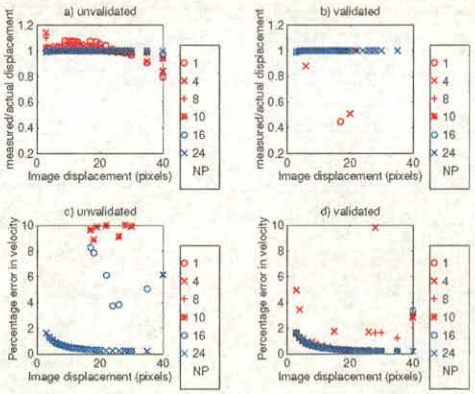


Figure A.35: Results for three pulses and an image diameter of 2 pixels.

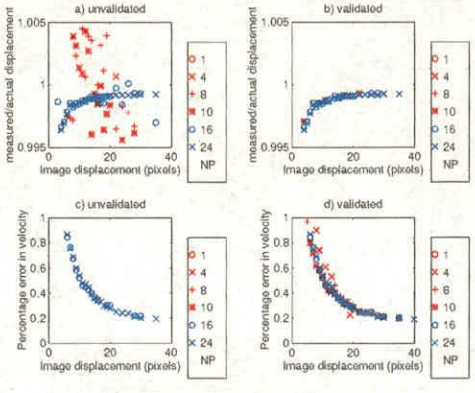


Figure A.36: Results for three pulses and an image diameter of 2 pixels. (Magnified view)

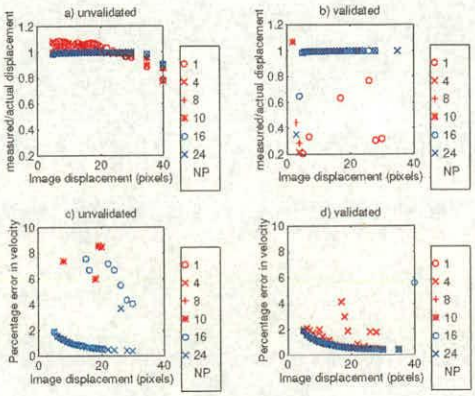


Figure A.37: Results for three pulses and an image diameter of 4 pixels.

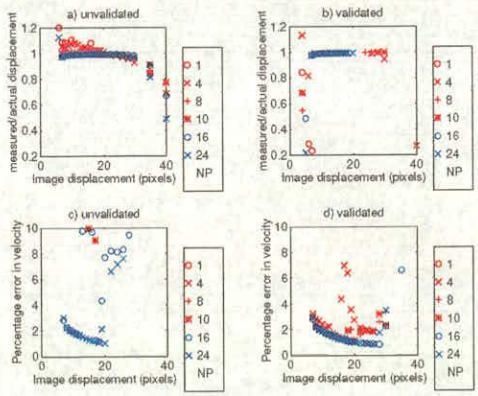


Figure A.38: Results for three pulses and an image diameter of 6 pixels.

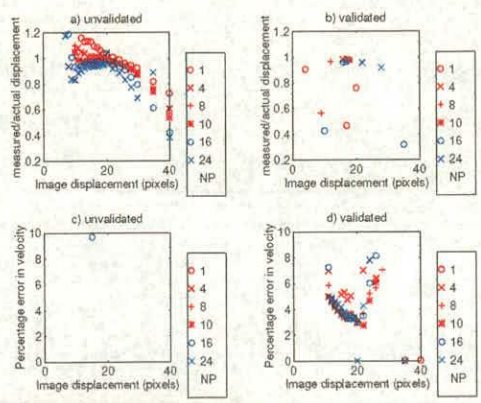


Figure A.39: Results for three pulses and an image diameter of 10 pixels.

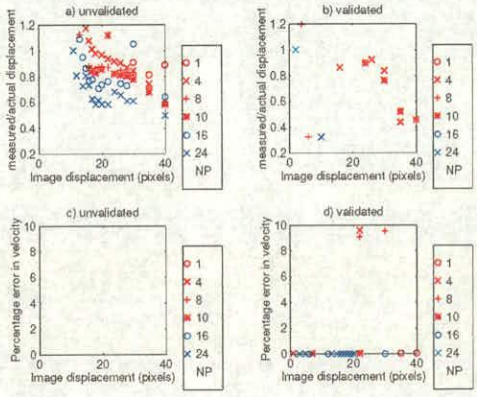


Figure A.40: Results for three pulses and an image diameter of 16 pixels.

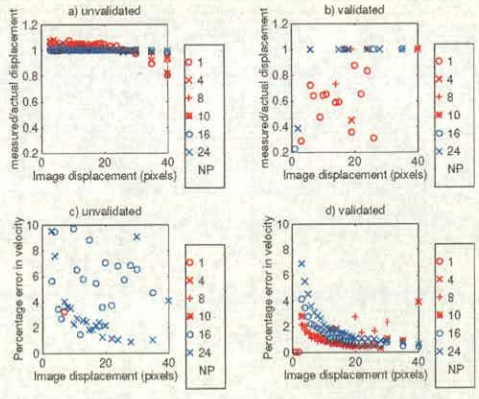


Figure A.41: Results for four pulses and an image diameter of 1 pixel.

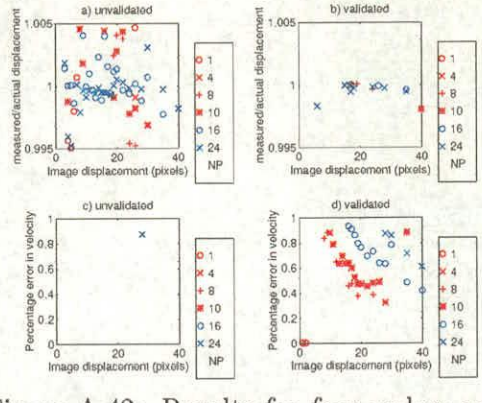


Figure A.42: Results for four pulses and an image diameter of 1 pixel. (Magnified view)

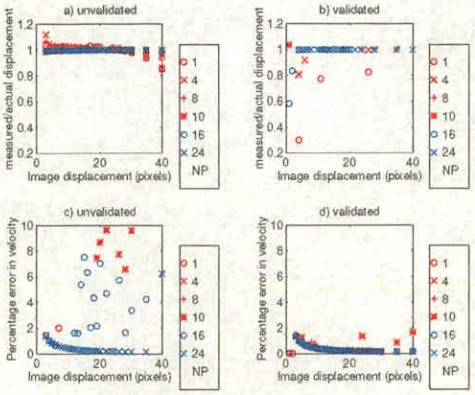


Figure A.43: Results for four pulses and an image diameter of 2 pixels.

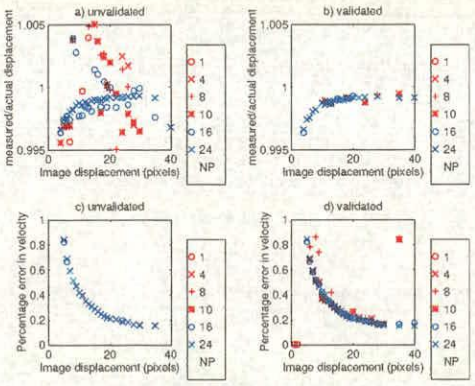


Figure A.44: Results for four pulses and an image diameter of 2 pixels. (Magnified view)

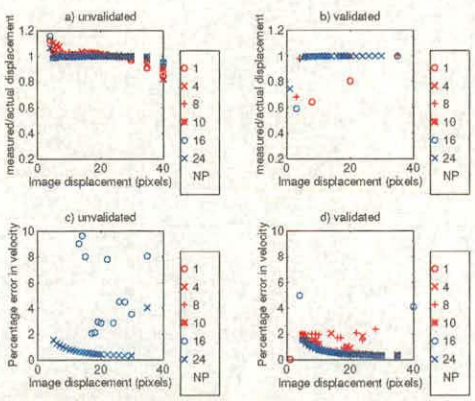


Figure A.45: Results for four pulses and an image diameter of 4 pixels.

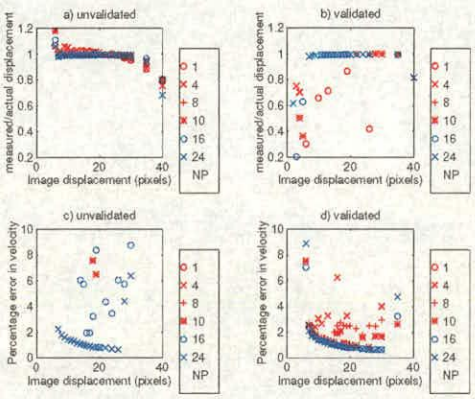


Figure A.46: Results for four pulses and an image diameter of 6 pixels.

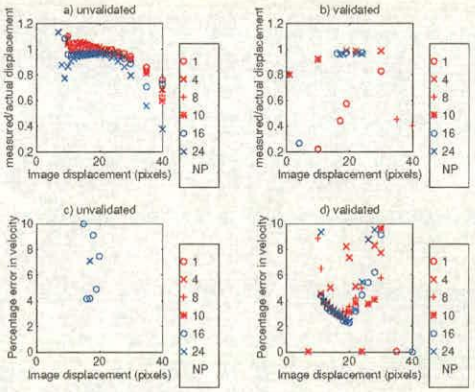


Figure A.47: Results for four pulses and an image diameter of 10 pixels.

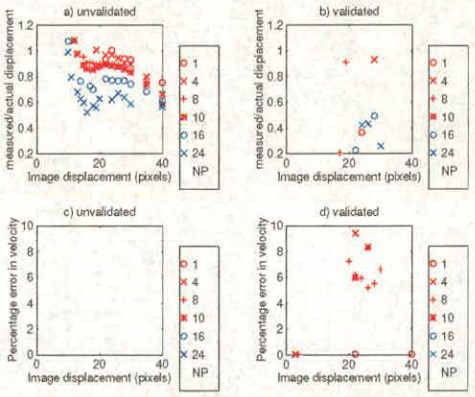


Figure A.48: Results for four pulses and an image diameter of 16 pixels.

A.4 Whittaker's method for peak location

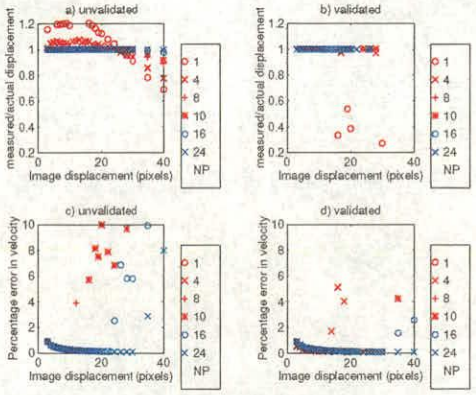


Figure A.49: Results for two pulses and an image diameter of 1 pixel.

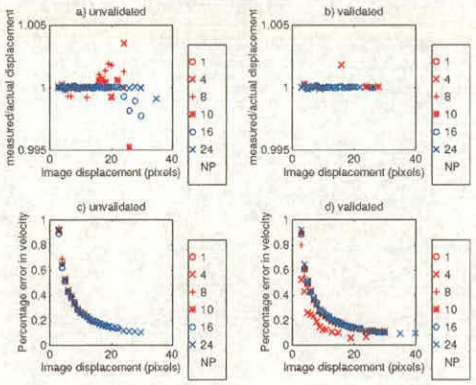


Figure A.50: Results for two pulses and an image diameter of 1 pixel. (Magnified view)

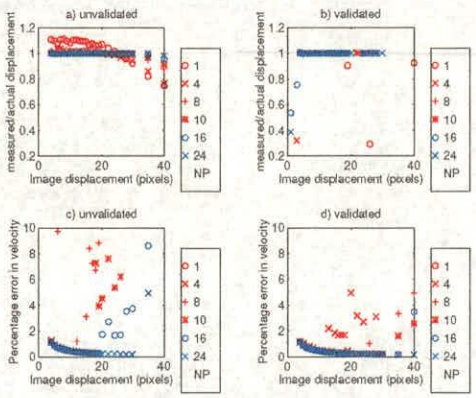


Figure A.51: Results for two pulses and an image diameter of 2 pixels.

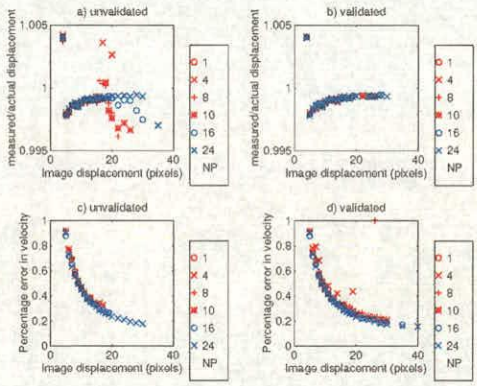


Figure A.52: Results for two pulses and an image diameter of 2 pixels. (Magnified view)

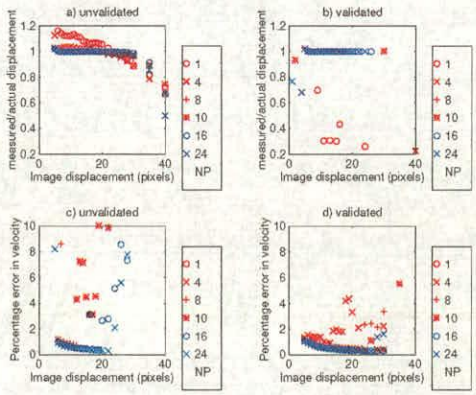


Figure A.53: Results for two pulses and an image diameter of 4 pixels.

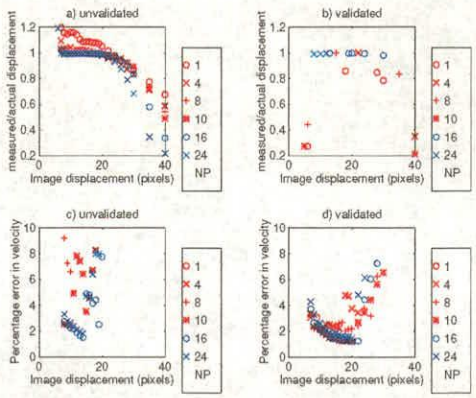


Figure A.54: Results for two pulses and an image diameter of 6 pixels.

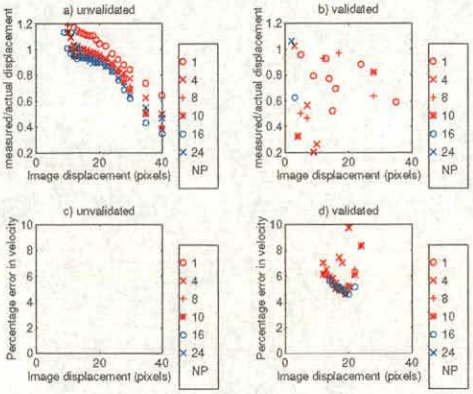


Figure A.55: Results for two pulses and an image diameter of 10 pixels.

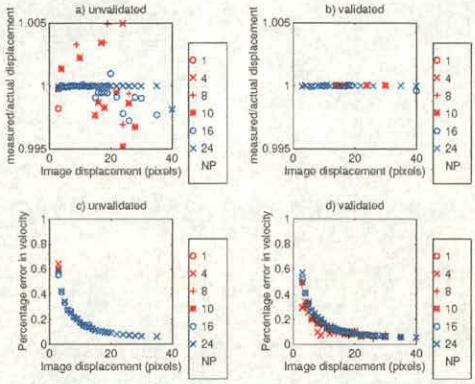


Figure A.58: Results for three pulses and an image diameter of 1 pixel. (Magnified view)

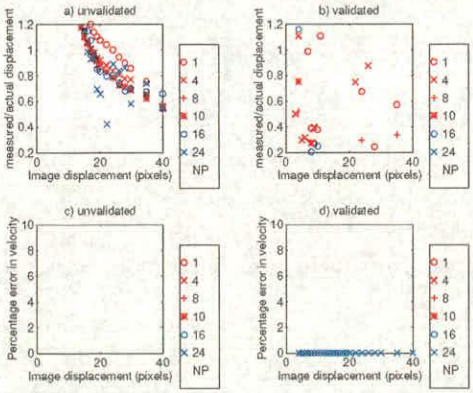


Figure A.56: Results for two pulses and an image diameter of 16 pixels.

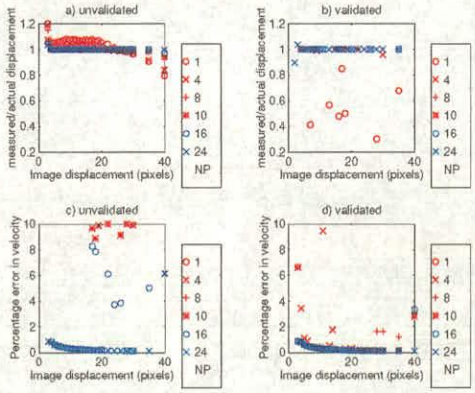


Figure A.59: Results for three pulses and an image diameter of 2 pixels.

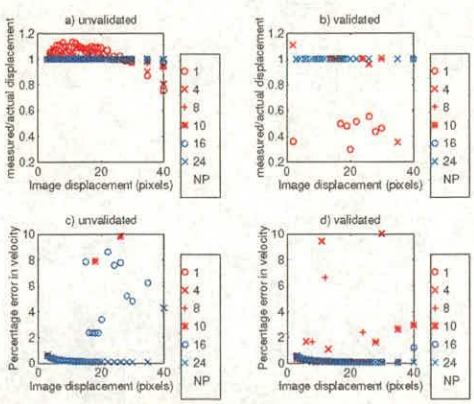


Figure A.57: Results for three pulses and an image diameter of 1 pixel.

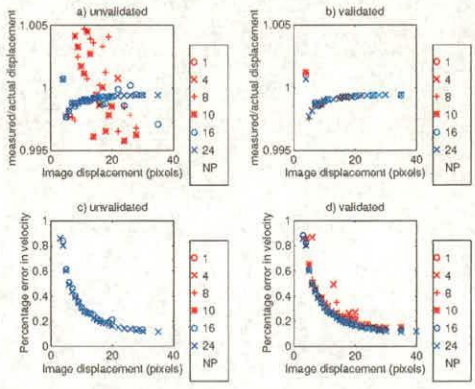


Figure A.60: Results for three pulses and an image diameter of 2 pixels. (Magnified view)

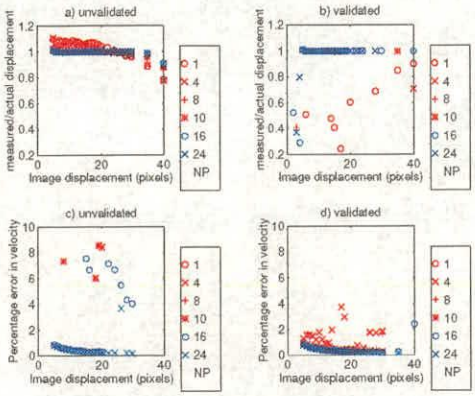


Figure A.61: Results for three pulses and an image diameter of 4 pixels.

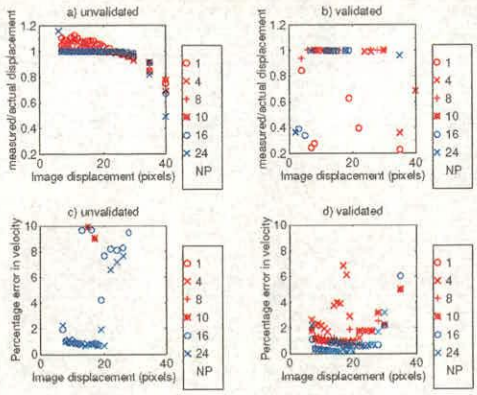


Figure A.62: Results for three pulses and an image diameter of 6 pixels.

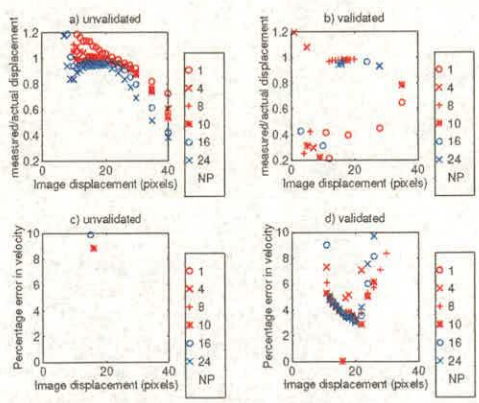


Figure A.63: Results for three pulses and an image diameter of 10 pixels.

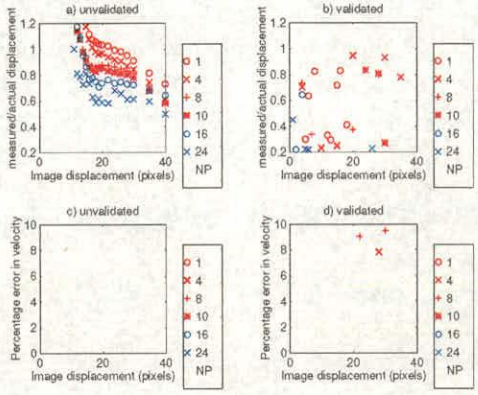


Figure A.64: Results for three pulses and an image diameter of 16 pixels.

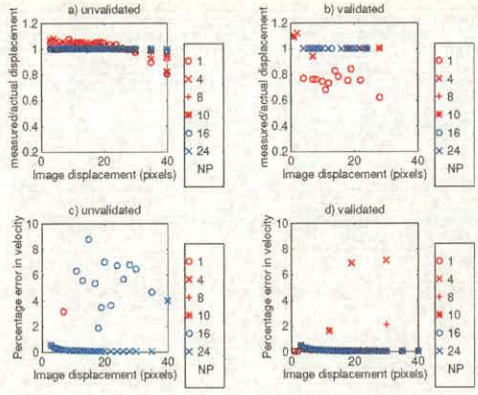


Figure A.65: Results for four pulses and an image diameter of 1 pixel.

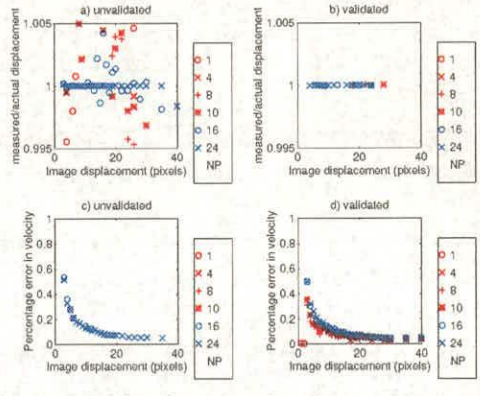


Figure A.66: Results for four pulses and an image diameter of 1 pixel. (Magnified view)

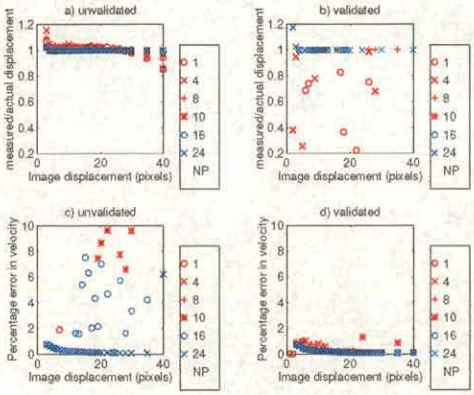


Figure A.67: Results for four pulses and an image diameter of 2 pixels.

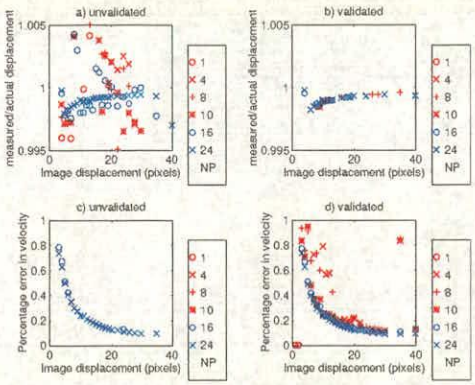


Figure A.68: Results for four pulses and an image diameter of 2 pixels. (Magnified view)

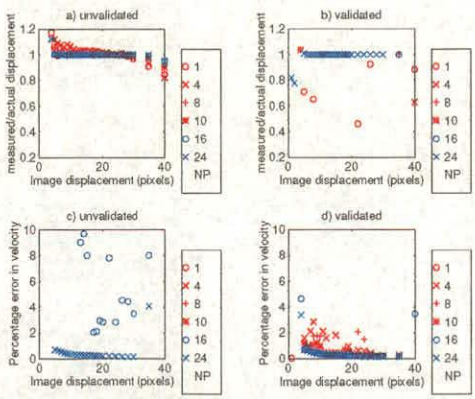


Figure A.69: Results for four pulses and an image diameter of 4 pixels.

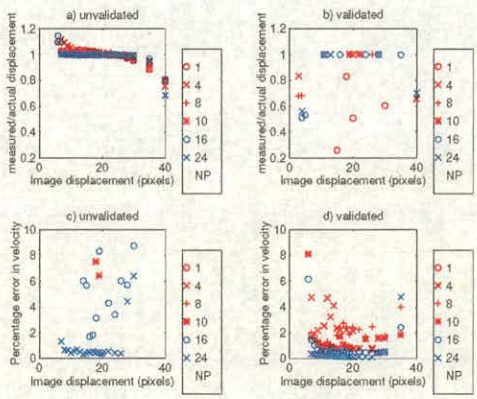


Figure A.70: Results for four pulses and an image diameter of 6 pixels.

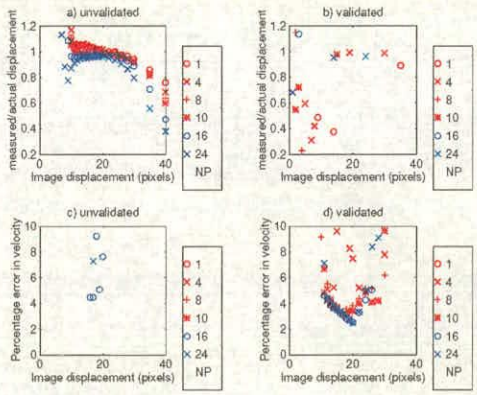


Figure A.71: Results for four pulses and an image diameter of 10 pixels.

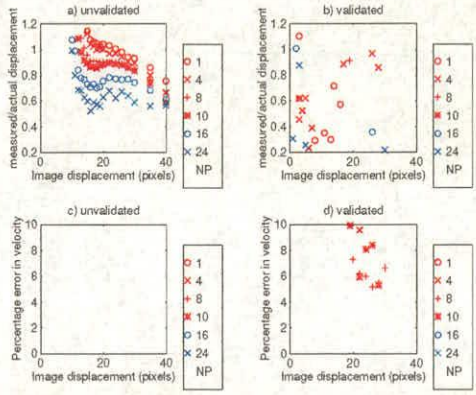


Figure A.72: Results for four pulses and an image diameter of 16 pixels.

Appendix B

B.1 Bias in the measurement of fractional displacements

The results of a series of simulations of PIV recordings with velocities in the range 10 to 11 pixels/s are presented here to illustrate and quantify the bias associated with different methods used to estimate the position of the signal peak in the autocorrelation function. PIV recordings have been simulated with particle image diameters (measured at the e^{-2} value of intensity) of 1, 2, and 3 pixels with pairs of particle images equal to 10, 16, and 24. In all other respects the images are identical to those produced in the results reported in appendix A.

The simulated images were analysed using real fast Fourier transforms of 64 by 64 pixel adjacent analysis areas. The position of the signal peak was estimated using volume moments (for which the results are encoded in red), a Gaussian least squares fit (for which the results are encoded green), and interpolated using Whittaker's reconstruction(for which the results are encoded blue). The results from simulations with an image pair density of 10 are indicated by a "+", those for an image pair density of 16 by a "*", and those for an image pair density of 24 by a "o".

The results have all been corrected for velocity bias according to the method suggested by Keane and Adrian[215,216]. That is, the measured displacement has been multiplied by $1 + (\frac{d_p}{d_I})^2$.

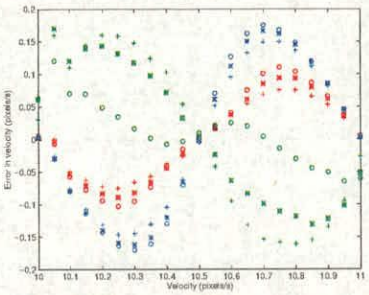


Figure B.1: Bias for two pulse recordings with images of diameter 1 pixel and analysed with no padding of the data in the analysis region.

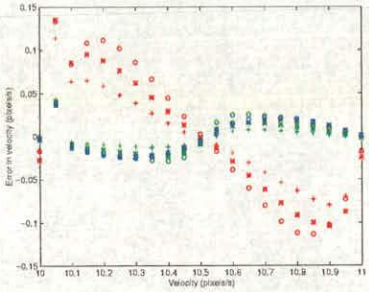


Figure B.2: Bias for two pulse recordings with images of diameter 2 pixel and analysed with no padding of the data in the analysis region.

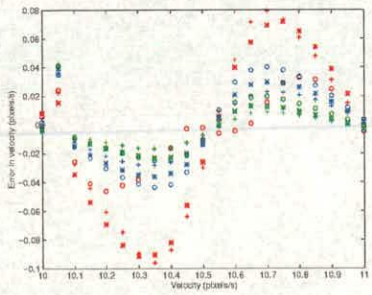


Figure B.3: Bias for two pulse recordings with images of diameter 3 pixel and analysed with no padding of the data in the analysis region.

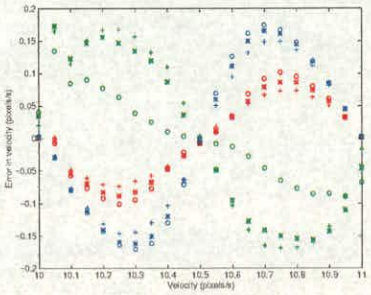


Figure B.4: Bias for two pulse recordings with images of diameter 1 pixel and analysed with padding equal to half the length of analysis size added to the data in the analysis region.

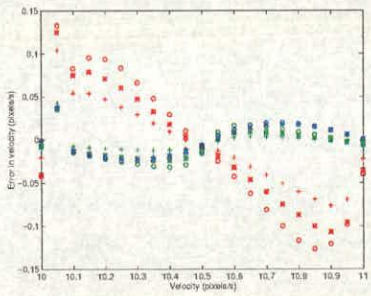


Figure B.5: Bias for two pulse recordings with images of diameter 2 pixel and analysed with padding equal to half the length of analysis size added to the data in the analysis region.

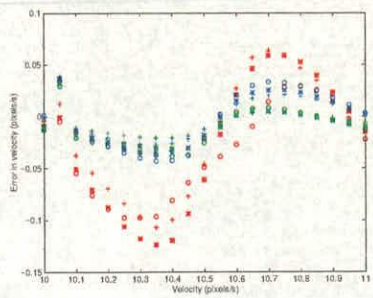


Figure B.6: Bias for two pulse recordings with images of diameter 3 pixel and analysed with padding equal to half the length of analysis size added to the data in the analysis region.

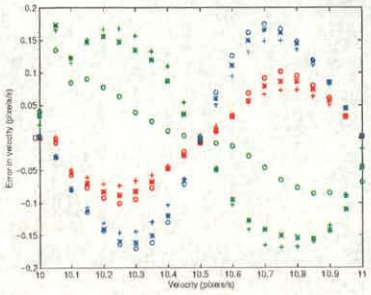


Figure B.7: Bias for two pulse recordings with images of diameter 1 pixel and analysed with padding equal the length of analysis size added to the data in the analysis region.

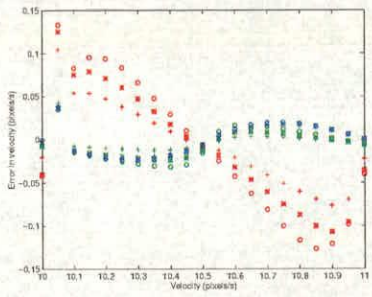


Figure B.8: Bias for two pulse recordings with images of diameter 2 pixel and analysed with padding equal the length of analysis size added to the data in the analysis region.

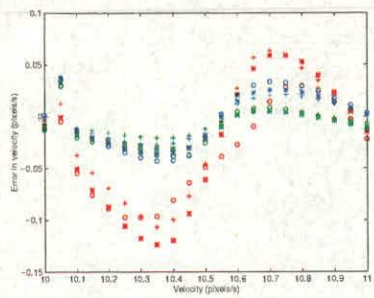


Figure B.9: Bias for two pulse recordings with images of diameter 3 pixel and analysed with padding equal the length of analysis size added to the data in the analysis region.

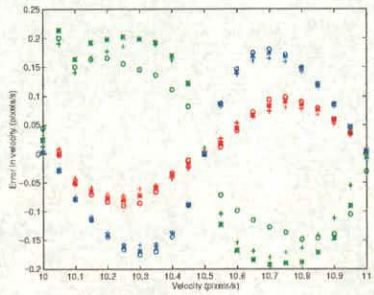


Figure B.10: Bias for three pulse recordings with images of diameter 1 pixel and analysed with no padding of the data in the analysis region.

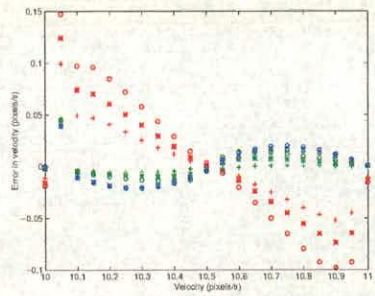


Figure B.11: Bias for three pulse recordings with images of diameter 2 pixel and analysed with no padding of the data in the analysis region.

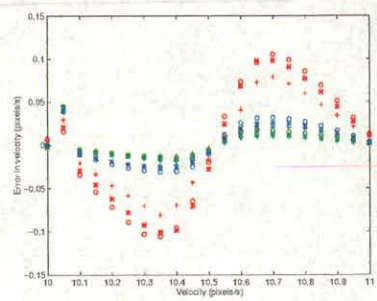


Figure B.12: Bias for three pulse recordings with images of diameter 3 pixel and analysed with no padding of the data in the analysis region.

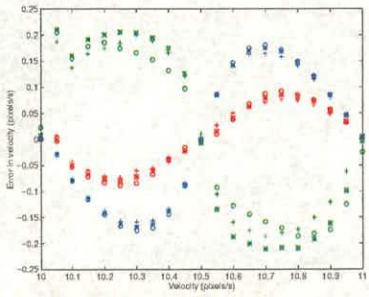


Figure B.13: Bias for three pulse recordings with images of diameter 1 pixel and analysed with padding equal to half the length of analysis size added to the data in the analysis region.

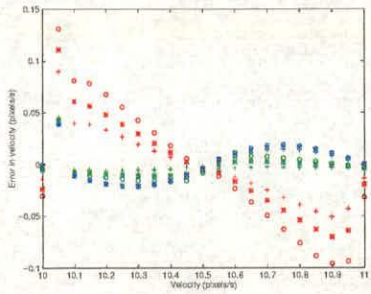


Figure B.14: Bias for three pulse recordings with images of diameter 2 pixel and analysed with padding equal to half the length of analysis size added to the data in the analysis region.

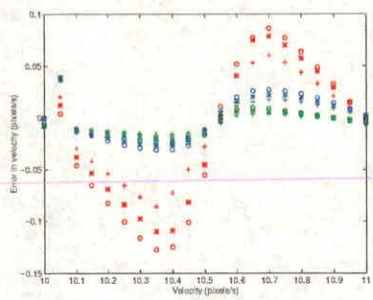


Figure B.15: Bias for three pulse recordings with images of diameter 3 pixel and analysed with padding equal to half the length of analysis size added to the data in the analysis region.

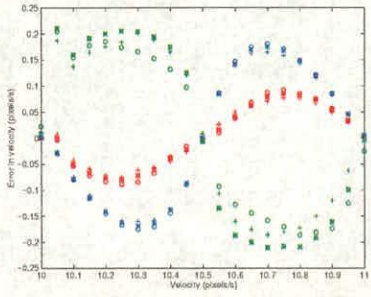


Figure B.16: Bias for three pulse recordings with images of diameter 1 pixel and analysed with padding equal the length of analysis size added to the data in the analysis region.

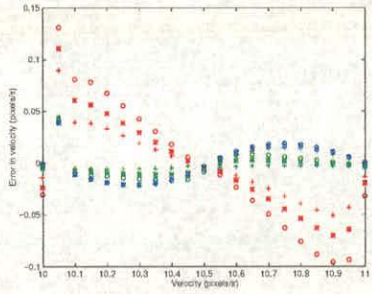


Figure B.17: Bias for three pulse recordings with images of diameter 2 pixel and analysed with padding equal the length of analysis size added to the data in the analysis region.

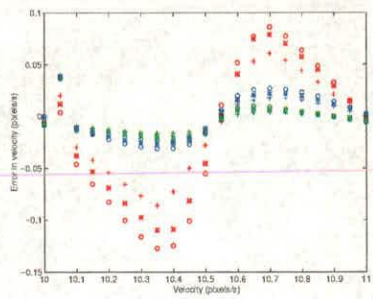


Figure B.18: Bias for three pulse recordings with images of diameter 3 pixel and analysed with padding equal the length of analysis size added to the data in the analysis region.

B.2 Bias arising from an alternative calculation of the volume moment

Here the volume moment is calculated as described in section 2.2.7 but the extent of the area over which the volume moment is determined by finding the limits where the value of the autocorrelation function falls below 13% of the maximum value for the signal peak or the autocorrelation function starts to increase.

An "x" represents images simulated with 1 effective particle pair per interrogation region and a "."represents images simulated with 2 effective particle pairs per interrogation region

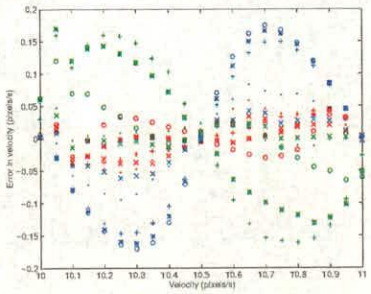


Figure B.19: Bias for two pulse recordings with images of diameter 1 pixel and analysed with no padding of the analysis region. The area for the volume moment calculations extended as described at the start of the chapter.

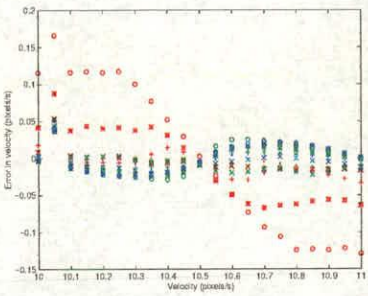


Figure B.20: Bias for two pulse recordings with images of diameter 2 pixel and analysed with no padding of the analysis region. The area for the volume moment calculations extended as described at the start of the chapter.

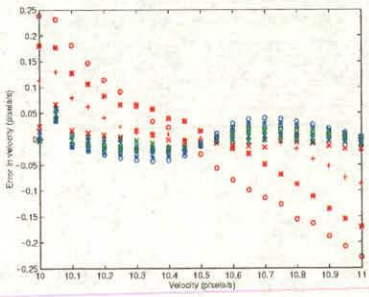


Figure B.21: Bias for two pulse recordings with images of diameter 3 pixel and analysed with no padding of the analysis region. The area for the volume moment calculations extended as described at the start of the chapter.

B.3 Bias in the measurement of fractional displacements, including the bias from loss of pairs

As section B.1 but without correction for the bias arising from the loss of image pairs.

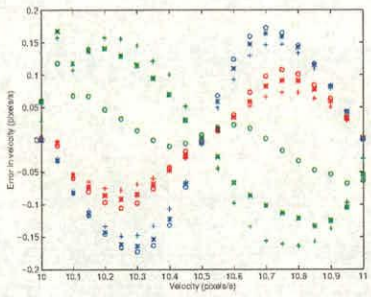


Figure B.22: Bias for two pulse recordings with images of diameter 1 pixel and analysed with no padding of the analysis region. The velocity is not corrected for the bias arising from loss of image pairs.

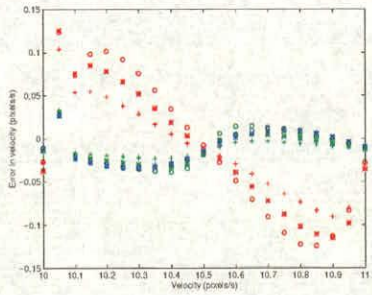


Figure B.23: Bias for two pulse recordings with images of diameter 2 pixel and analysed with no padding of the analysis region. The velocity is not corrected for the bias arising from loss of image pairs.

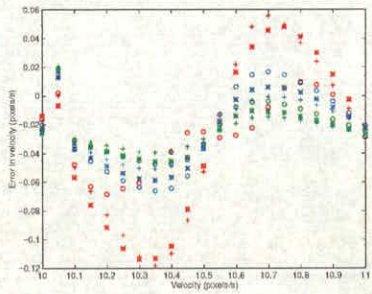


Figure B.24: Bias for two pulse recordings with images of diameter 3 pixel and analysed with no padding of the analysis region. The velocity is not corrected for the bias arising from loss of image pairs.

Appendix C

C.1 Maple script showing the derivation of the methods used to correct velocity gradients

```
> restart;
```

To determine:

1) the factor to correct the x position in PIV recordings

2) the deformed x component of the stream function

Define the expected displacement in terms of the displacement at the centre of the interrogation region modified according to the linear variation in displacement over the area. The displacement is calculated using the mean particle position. It is assumed that the axes have been oriented so that the 'x' axis aligns with the displacement vector.

(x1, y1) = Initial particle position (x2, y2) = Final particle position (delx0, 0) = Central particle displacement

```
> {a=Diff(delx0,x),b=Diff(delx0,y),c=Diff(dely0,x),d=Diff(dely0,y)};
```

$$\left\{a = \frac{\partial}{\partial x}\, delx0, b = \frac{\partial}{\partial y}\, delx0, c = \frac{\partial}{\partial x}\, dely0, d = \frac{\partial}{\partial y}\, dely0\right\}$$

```
> eqn1:=(x2-x1)=delx0+a/2*(x1+x2)+b/2*(y1+y2);
```

$$eqn1 := x2 - x1 = delx0 + \frac{1}{2}\, a\,(\, x1 + x2\,) + \frac{1}{2}\, b\,(\, y1 + y2\,)$$

```
> eqn2:=(y2-y1)=c/2*(x1+x2)+d/2*(y1+y2);
```

$$eqn2 := y2 - y1 = \frac{1}{2}\, c\,(\, x1 + x2\,) + \frac{1}{2}\, d\,(\, y1 + y2\,)$$

Now solve these equations to determine x2 and y2 in terms of the constant values and x1 and y1. x2s and y2s are assigned the answers.

```
> ans:=solve({eqn1,eqn2},{x2,y2});
```

$$ans := \left\{x2 = -(2\,d\,x1 + 2\,d\,delx0 - c\,x1\,b + x1\,a\,d - 2\,a\,x1 - 4\,b\,y1 - 4\,x1 - 4\,delx0)\Big/(-c\,b + 4 - 2\,d - 2\,a + a\,d),\ y2 = \frac{4\,c\,x1 + 2\,c\,delx0 + c\,b\,y1 + 4\,y1 + 2\,d\,y1 - 2\,a\,y1 - a\,d\,y1}{-c\,b + 4 - 2\,d - 2\,a + a\,d}\right\}$$

```
> x2s:=subs(ans,x2);
```

$$x2s := -(2\,d\,x1 + 2\,d\,delx0 - c\,x1\,b + x1\,a\,d - 2\,a\,x1 - 4\,b\,y1 - 4\,x1 - 4\,delx0)\Big/(-c\,b + 4 - 2\,d - 2\,a + a\,d)$$

```
> y2s:=subs(ans,y2);
```

$$y2s := \frac{4\,c\,x1 + 2\,c\,delx0 + c\,b\,y1 + 4\,y1 + 2\,d\,y1 - 2\,a\,y1 - a\,d\,y1}{-c\,b + 4 - 2\,d - 2\,a + a\,d}$$

We now look for a function f which we can use to reposition the first and second particle images to x2n and x1n in an analysis area deformed only in the x-direction.

```
> x2n:=x2s*f;
```

$$x2n := -(2\,d\,x1 + 2\,d\,delx0 - c\,x1\,b + x1\,a\,d - 2\,a\,x1 - 4\,b\,y1 - 4\,x1 - 4\,delx0)f\Big/(-c\,b + 4 - 2\,d - 2\,a + a\,d)$$

```
> x1n:=x1*f;
```

$$x1n := x1\,f$$

The difference between the two particle position should now be independent of x1 and y1 and equal to the displacement at the centre of the analysis area.

```
> difference:=delx0=x2n-x1n;
```

$$difference := delx0 = -(2\,d\,x1 + 2\,d\,delx0 - c\,x1\,b + x1\,a\,d - 2\,a\,x1 - 4\,b\,y1 - 4\,x1 - 4\,delx0)f\Big/(-c\,b + 4 - 2\,d - 2\,a + a\,d) - x1\,f$$

We now solve for f and simplify the result.

```
> ans:=solve(difference,f);
```

$$ans := -delx0 \Big/ \left(2\frac{d\,x1}{\%1} + 2\frac{d\,delx0}{\%1} - \frac{c\,x1\,b}{\%1} + \frac{x1\,a\,d}{\%1} - 2\frac{a\,x1}{\%1} - 4\frac{b\,y1}{\%1} - 4\frac{x1}{\%1} - 4\frac{delx0}{\%1} + x1\right)$$

$$\%1 := -c\,b + 4 - 2\,d - 2\,a + a\,d$$

```
> ans2:=simplify(ans);
```

$$ans2 := -\frac{1}{2}\frac{delx0\,(-c\,b+4-2\,d-2\,a+a\,d)}{d\,delx0 - c\,x1\,b + x1\,a\,d - 2\,a\,x1 - 2\,b\,y1 - 2\,delx0}$$

```
> collect(ans2,delx0);
```

$$-\frac{1}{2}\frac{delx0\,(-c\,b+4-2\,d-2\,a+a\,d)}{(-2+d)\,delx0 - c\,x1\,b + x1\,a\,d - 2\,a\,x1 - 2\,b\,y1}$$

We would like to express the correction factor in terms of the mid-point of the displacement as this will give the best correction for all particles at a particular point with out bias towards the beginning of the displacement as would be the case if we used x1 and y1.

We define xm and ym to be the mid points of our particle displacement and then solve for x1 and y1 in terms of these values.

```
> xmeqn1:=xm=(x1+x2s)/2;xmeqn2:=ym=(y1+y2s)/2;
```

$$xmeqn1 := xm = \frac{1}{2}x1 - \frac{1}{2}(2\,d\,x1 + 2\,d\,delx0 - c\,x1\,b + x1\,a\,d - 2\,a\,x1 - 4\,b\,y1 - 4\,x1 - 4\,delx0) \Big/ (-c\,b + 4 - 2\,d - 2\,a + a\,d)$$

$$xmeqn2 := ym = \frac{1}{2}y1 + \frac{1}{2}\frac{4\,c\,x1 + 2\,c\,delx0 + c\,b\,y1 + 4\,y1 + 2\,d\,y1 - 2\,a\,y1 - a\,d\,y1}{-c\,b + 4 - 2\,d - 2\,a + a\,d}$$

```
> ans4:=solve({xmeqn1,xmeqn2},{x1,y1});
```

$$ans4 := \left\{y1 = -\frac{1}{2}ym\,d - \frac{1}{2}c\,xm + ym,\ x1 = xm - \frac{1}{2}xm\,a - \frac{1}{2}b\,ym - \frac{1}{2}delx0\right\}$$

```
> x1xm:=x1=subs(ans4,x1);y1ym:=y1=subs(ans4,y1);
```

$$x1xm := x1 = xm - \frac{1}{2}xm\,a - \frac{1}{2}b\,ym - \frac{1}{2}delx0$$

$$y1ym := y1 = -\frac{1}{2}ym\,d - \frac{1}{2}c\,xm + ym$$

```
> simplify(x1xm);
```

$$x1 = xm - \frac{1}{2}\,xm\,a - \frac{1}{2}\,b\,ym - \frac{1}{2}\,delx0$$

We now find our correction factor, f, expressed in terms of the mean position of the particle and simplify the result.

```
> eqn4:=subs({x1xm,y1ym},ans2);
```

$$eqn4 := -\frac{1}{2}\,delx0\,(-c\,b + 4 - 2\,d - 2\,a + a\,d)\Big/\Big(d\,delx0 - c\,\%1\,b + \%1\,a\,d$$

$$- 2\,a\,\%1 - 2\,b\left(-\frac{1}{2}\,ym\,d - \frac{1}{2}\,c\,xm + ym\right) - 2\,delx0\Big)$$

$$\%1 := xm - \frac{1}{2}\,xm\,a - \frac{1}{2}\,b\,ym - \frac{1}{2}\,delx0$$

When simplified the answer is equal to that expected intuitively! That is, "scale the local separation in relation to the central and local velocity" - QED

```
> eqn5:=xp=xm*collect(simplify(eqn4),{xm,ym,delx0});
```

$$eqn5 := xp = \frac{xm\,delx0}{xm\,a + b\,ym + delx0}$$

We now want to determine:

```
> Int(c*x,xun=0..xun);
```

$$\int_0^{xun} c\,x\,dxun$$

so that the stream function can be evaluated. We need x in terms of the now distorted x-axis:

```
> xasxp:=collect(solve(eqn5,xm),xp);
```

$$xasxp := -\frac{(b\,ym + delx0)\,xp}{xp\,a - delx0}$$

We now integrate to find the required solution and generate the appropriate FORTRAN

```
> ans5:=int(c*xasxp,xp=0..xun);
```

$$ans5 := -c(b\,ym\,a\,xun + delx0\,a\,xun + delx0\ln(-a\,xun + delx0)\,b\,ym + delx0^2\ln(-a\,xun + delx0))\Big/a^2 + \frac{c\,delx0\ln(delx0)\,(b\,ym + delx0)}{a^2}$$

```
> simplify(ans5);
```

$$-c(b\,ym\,a\,xun + delx0\,a\,xun + delx0\ln(-a\,xun + delx0)\,b\,ym + delx0^2\ln(-a\,xun + delx0) - delx0^2\ln(delx0) - delx0\ln(delx0)\,b\,ym)\Big/a^2$$

```
> fortran(",optimized);
      t1 = b*ym
      t2 = a*xun
      t7 = alog(-t2+delx0)
      t10 = delx0**2
      t12 = alog(delx0)
      t18 = a**2
      t21 = -c*(t1*t2+delx0*a*xun+delx0*t7*t1+t10*t7-t10*t12-delx0*t12*t
     #1)/t18
```

Appendix D

D.1 The flow patterns downstream of the Björk-Shiley valve in steady flow

This appendix presents the results obtained downstream of the Björk-Shiley valve in a steady flow of 2×10^{-5} m^3/s. The flow was seeded with conifer pollen and illuminated with a light sheet pulsed at 75 Hz. Figure (D.1) shows the location of the valve and the direction of flow. Recordings were made at one second intervals and are shown in figure (D.2) with time increasing left to right and then from top to bottom. The Reynolds number based on the pipe diameter was 800.

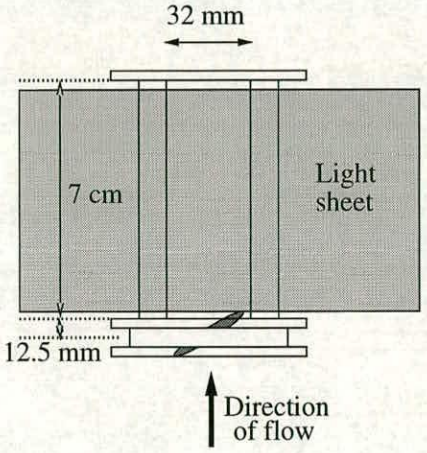


Figure D.1: A schematic indicating the location of the PIV recordings.

D.1.1 Iterative analysis of the first image

The figure (D.3) shows the velocity field produced after the initial analysis of the first (top left) PIV recording of the series shown in figure (D.2). The velocity field was validated using the method described by Meinhart *et al.*[269] modified to allow for directional ambiguity. Any vector with a component more than five standard deviations away from the mean of that component - taken over the velocity field - was deleted.

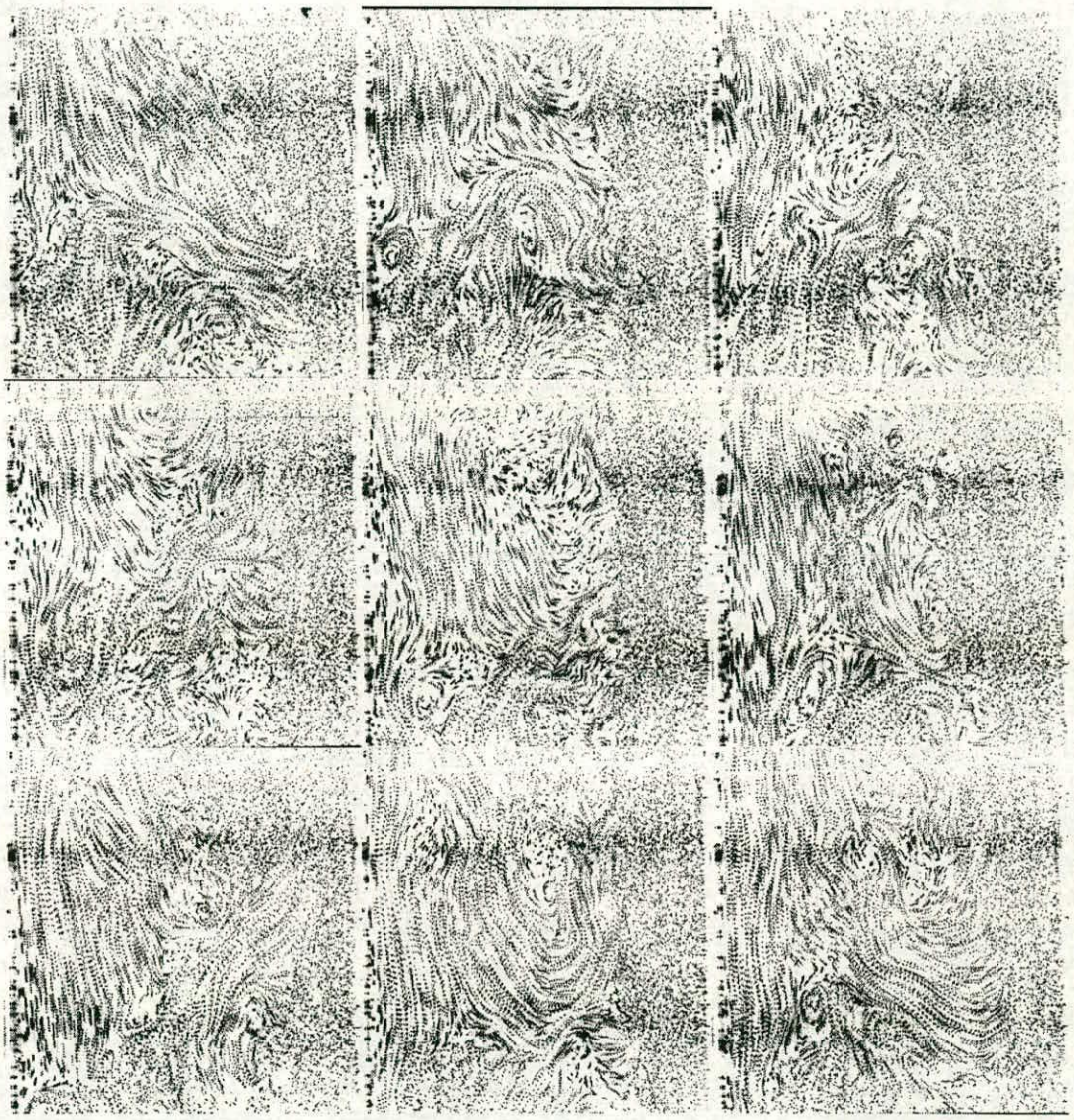


Figure D.2: A series of nine PIV recordings made distal to the mount of the Björk-Shiley Valve. The recordings were made at one second intervals. The number in each figure indicates the time at which each recording was made. Re=800 (based on the pipe diameter).

From trial and error, vectors were deleted if the L_2 norm of the median vector minus the central vector was greater than nine pixels. A relative test was also made using the same norm divided by the median vector: the central vector was deleted if this value was greater than one. Figure (D.4) shows the effect of correcting for velocity gradients in the analysis of the first image and the validated results after zero, one, two and three iterations of the correction procedure. Figure (D.5) shows the results obtained at the final and fifth iteration stage and compares the results with the initial unvalidated vector field. An interpolated velocity field is also shown. The remaining figures show the sequence of PIV images at one second time intervals with the validated velocity field produced after five iterations to correct for velocity gradients. Note that the third image produced no valid vectors after one iteration of the correction procedure and

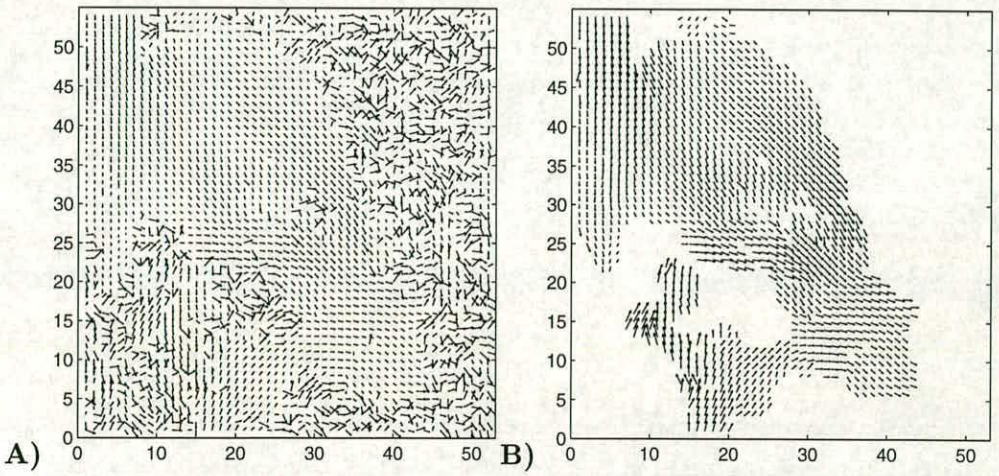


Figure D.3: **A)** The vector field produced by analysing the first image. **B)** The vector field produced after validating the vector field shown in A) using the method described in the text.

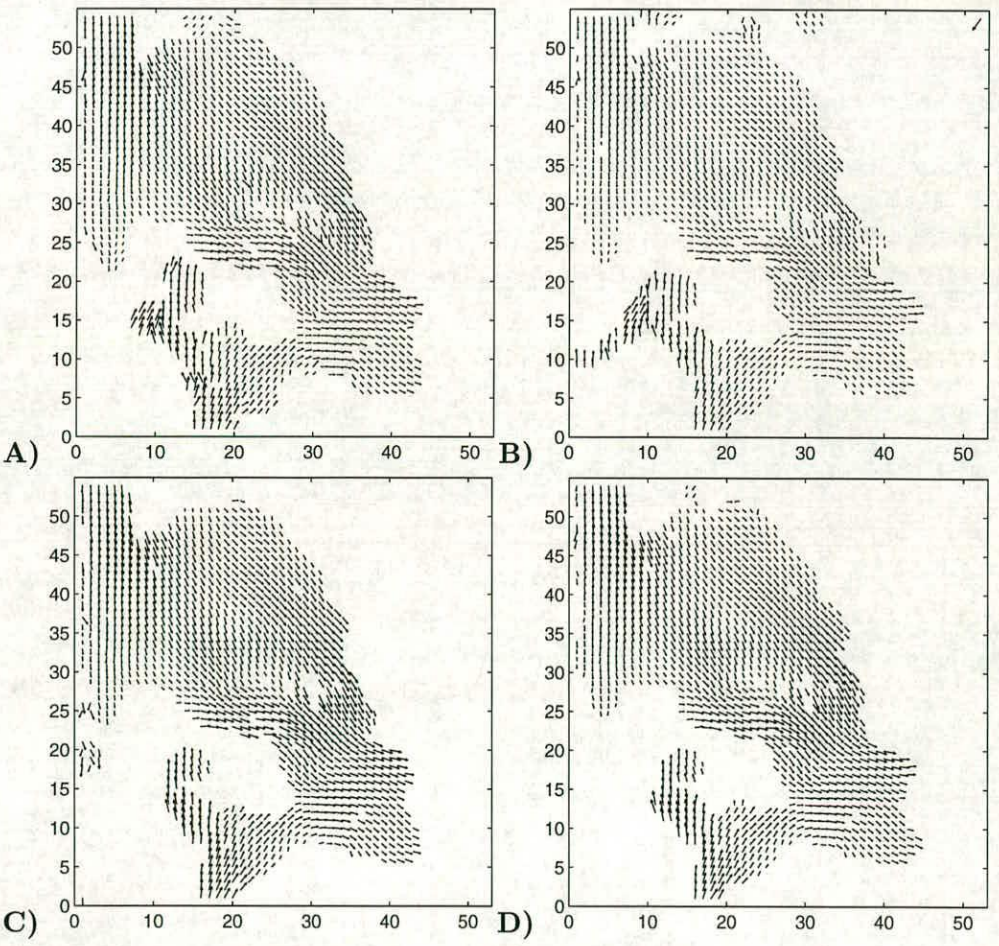


Figure D.4: **A)** The validated velocity field after no iterations; **B)** after one iteration **C)** after two iterations; **D)** and after three iterations.

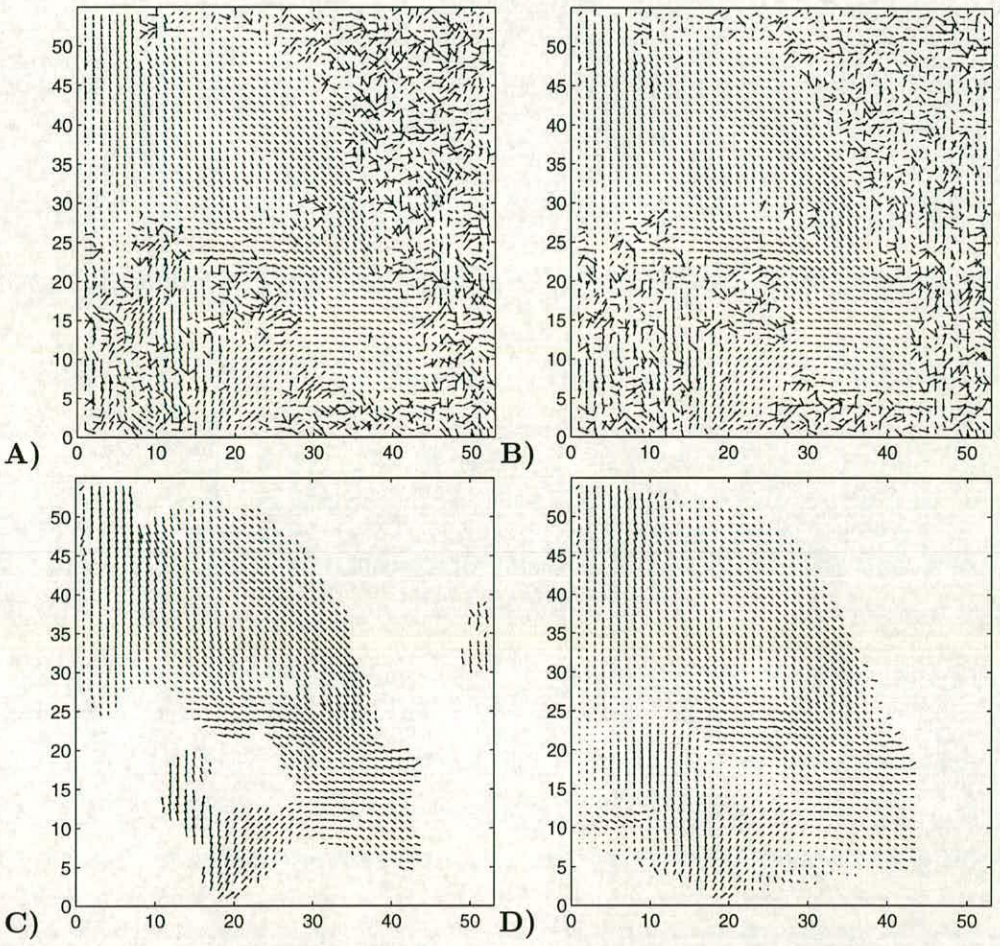


Figure D.5: **A)** The unvalidated velocity field after no iterations; **B)** after five iterations; **C)** the validated velocity field after five iterations; **D)** and the interpolated and validated velocity field after five iterations.

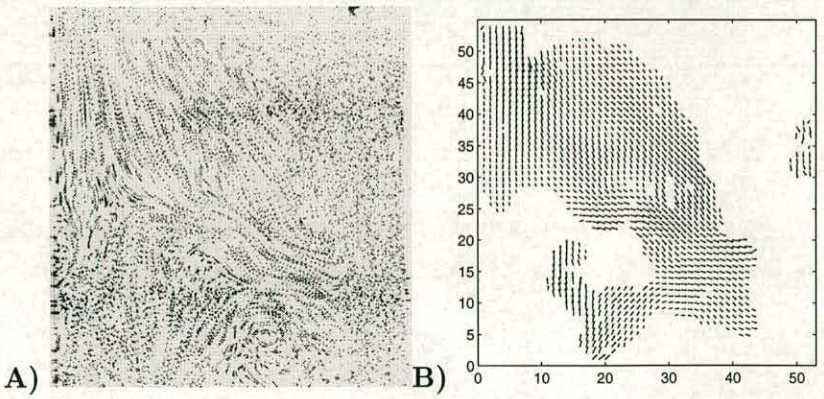


Figure D.6: **A)** PIV recording at time 0 s. **B)** The vector field produced after five iterations to correct for velocity gradients and validation. The maximum velocity vector represents 0.0620 m/s: the maximum shear stress is 0.023 N/m^2.

only the initial analysis results are presented.

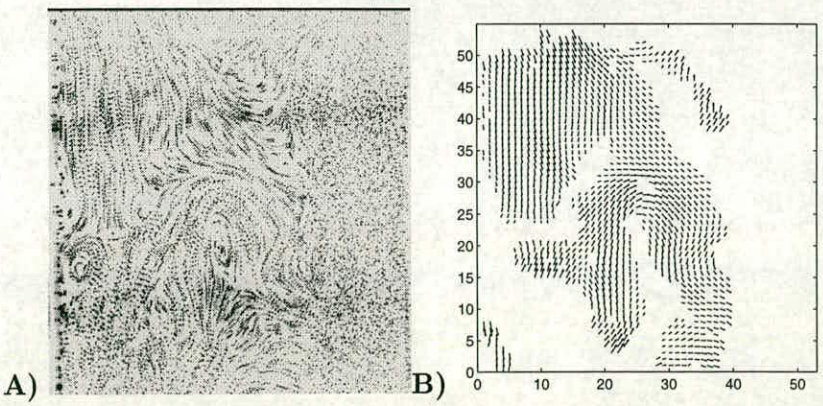


Figure D.7: **A)** PIV recording at time 1 s. **B)** The vector field produced after five iterations to correct for velocity gradients and validation. The maximum velocity vector represents 0.0528 m/s: the maximum shear stress is 0.018 N/m^2.

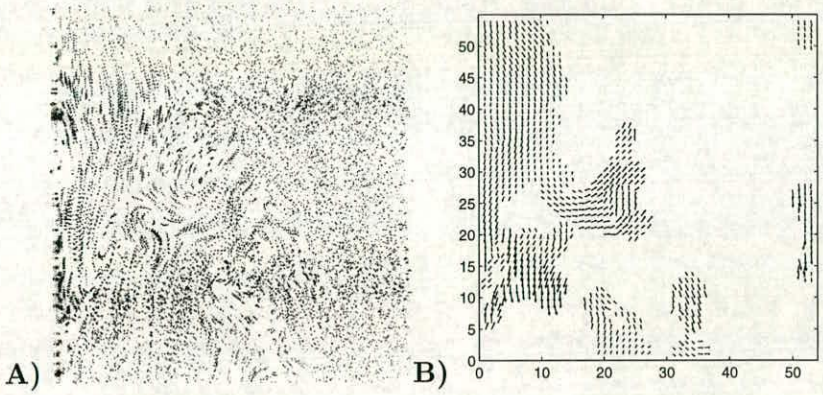


Figure D.8: **A)** PIV recording at time 2 s. **B)** The vector field produced after the initial analysis. The maximum velocity vector represents 0.0529 m/s: the maximum shear stress is 0.035 N/m^2.

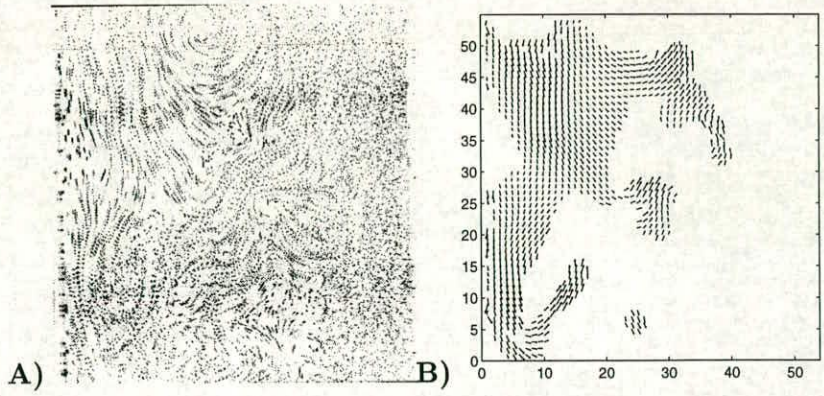


Figure D.9: **A)** PIV recording at time 3 s. **B)** The vector field produced after five iterations to correct for velocity gradients and validation. The maximum velocity vector represents 0.0479 m/s: the maximum shear stress is 0.020 N/m^2.

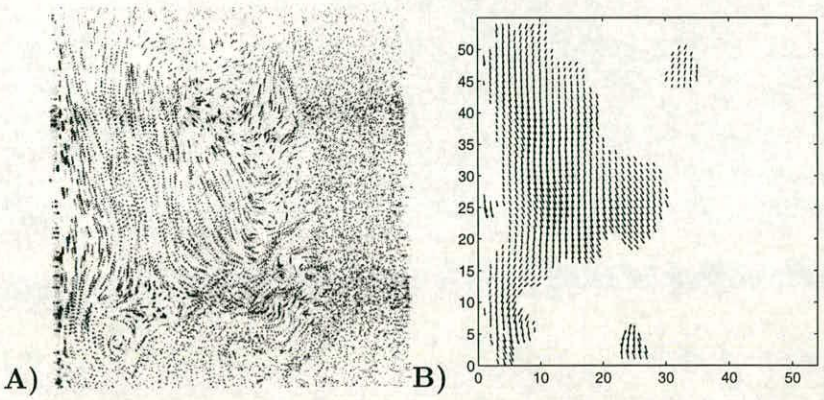


Figure D.10: **A)** PIV recording at time 4 s. **B)** The vector field produced after five iterations to correct for velocity gradients and validation. The maximum velocity vector represents 0.0393 m/s: the maximum shear stress is 0.012 N/m^2.

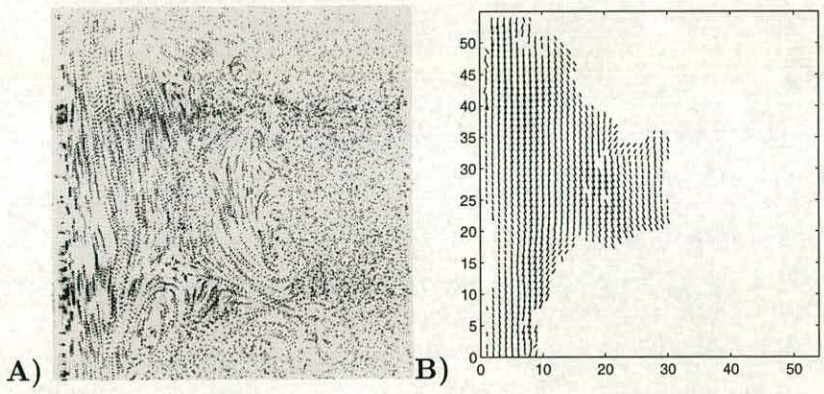


Figure D.11: **A)** PIV recording at time 5 s. **B)** The vector field produced after five iterations to correct for velocity gradients and validation. The maximum velocity vector represents 0.0419 m/s: the maximum shear stress is 0.014 N/m^2.

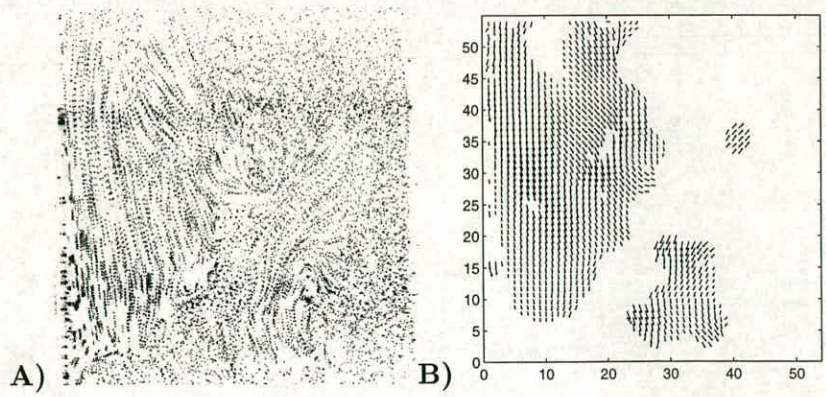


Figure D.12: **A)** PIV recording at time 6 s. **B)** The vector field produced after five iterations to correct for velocity gradients and validation. The maximum velocity vector represents 0.0511 m/s: the maximum shear stress is 0.017 N/m^2.

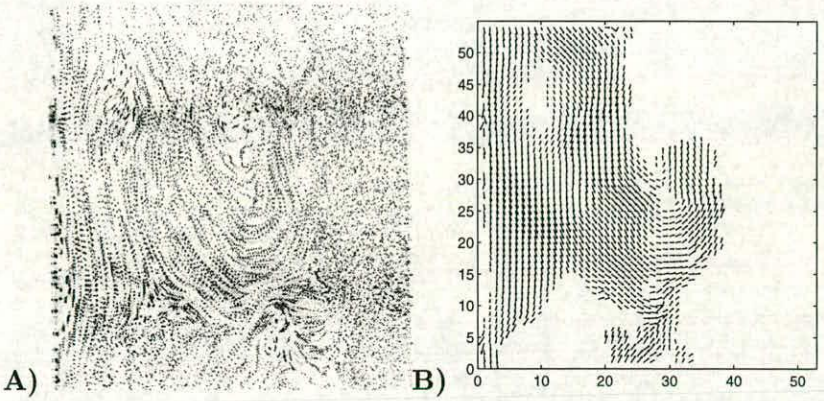


Figure D.13: **A)** PIV recording at time 7 s. **B)** The vector field produced after five iterations to correct for velocity gradients and validation. The maximum velocity vector represents 0.0472 m/s: the maximum shear stress is 0.025 N/m^2.

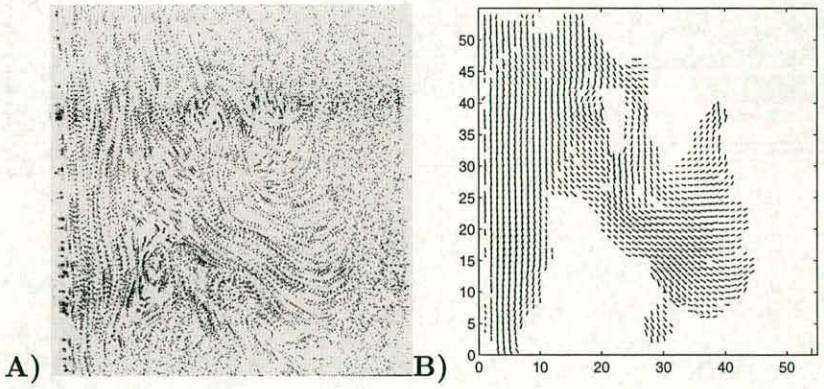


Figure D.14: **A)** PIV recording at time 8 s. **B)** The vector field produced after five iterations to correct for velocity gradients and validation. The maximum velocity vector represents 0.0564 m/s: the maximum shear stress is 0.019 N/m^2.

Appendix E

E.1 The flow patterns downstream of Dr. Norman Macleod's valve in pulsatile flow

This appendix presents the PIV recordings and results made over two pulse cycles downstream of the valve designed by Dr. Norman Macleod. The mean volumetric flowrate was 1.6×10^{-5} m^3/s and the pulse frequency was 0.4 Hz. The Reynolds number based on the pipe diameter was 530 and frequency parameter, α=25. The flow was seeded with 6 μm aluminium oxide particles and illuminated using the scanning beam system with the 35 mW HeNe laser. The light sheet was pulsed at 40 Hz. Two sets of eight recordings were made in which each recording was separated by a dimensionless time of 1/8 representing 1/8 of a cycle. The photographs were taken using an aperture of f/2.8 and a shutter speed of 1/8 of a second and recorded on 400 ASA film. The light sheet was aligned perpendicular to the axis of rotation of the disk and along the centreline of the flow, as described in chapter 4.

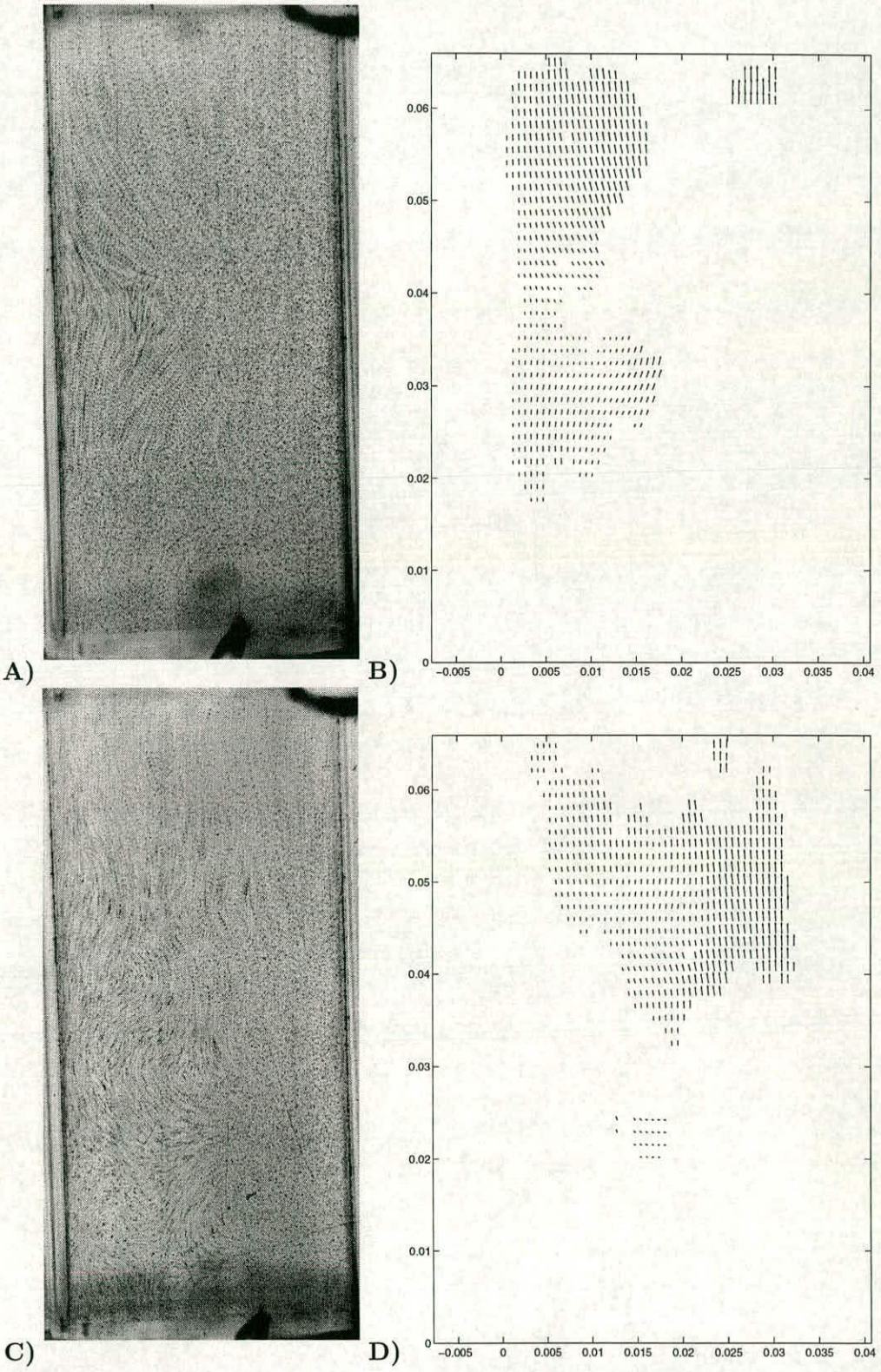


Figure E.1: **A)** PIV recording at a dimensionless time of 0/8 **B)** The vector field produced after five iterations to correct for velocity gradients and validation. The maximum velocity vector represents 0.0242 m/s. **C)** PIV recording at a dimensionless time of 0/8 **D)** The vector field produced after five iterations to correct for velocity gradients and validation. The maximum velocity vector represents 0.0223 m/s.

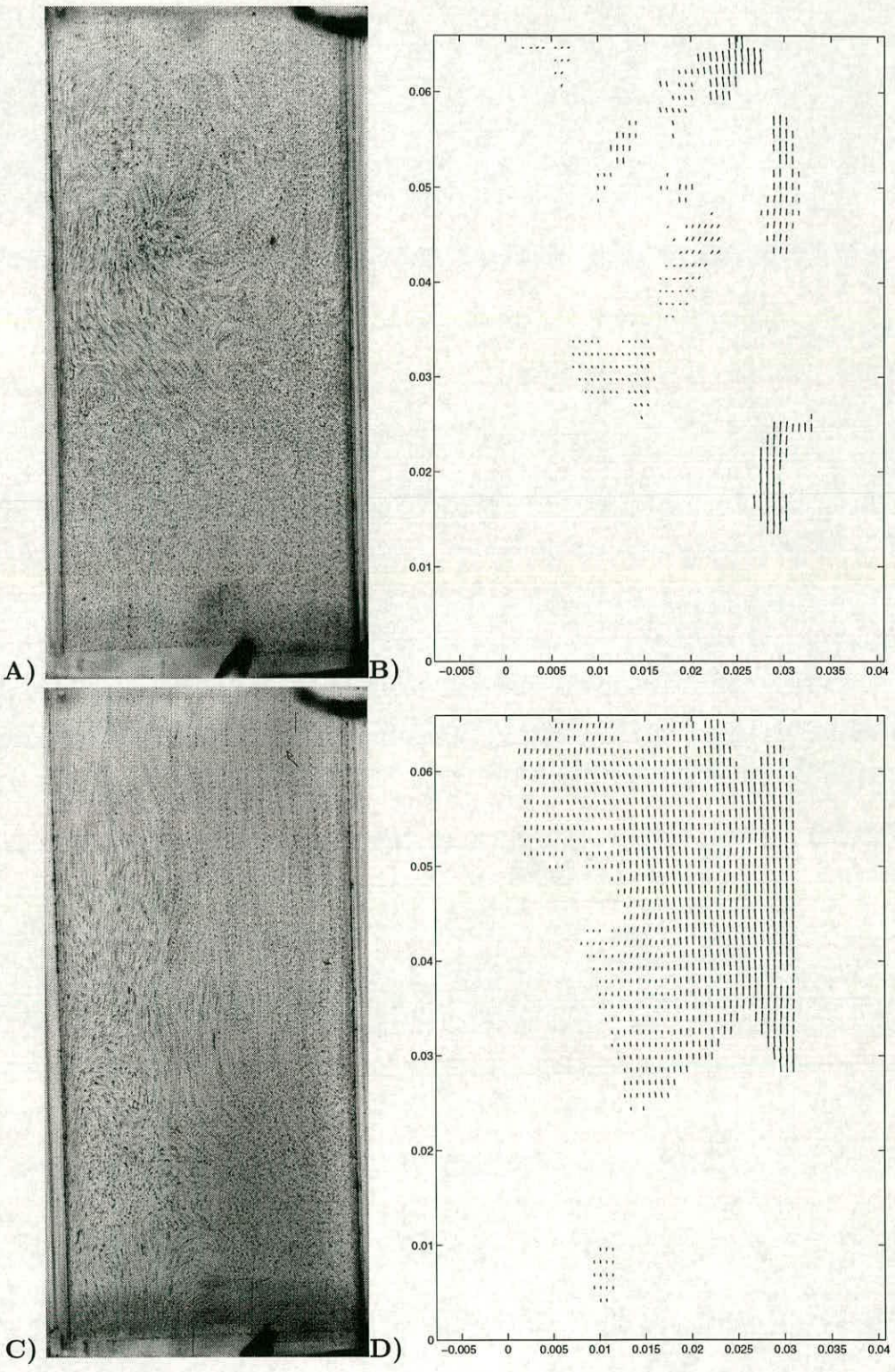


Figure E.2: **A)** PIV recording at a dimensionless time of 1/8 **B)** The vector field produced after five iterations to correct for velocity gradients and validation. The maximum velocity vector represents 0.0298 m/s. **C)** PIV recording at a dimensionless time of 1/8 **D)** The vector field produced after five iterations to correct for velocity gradients and validation. The maximum velocity vector represents 0.0250 m/s.

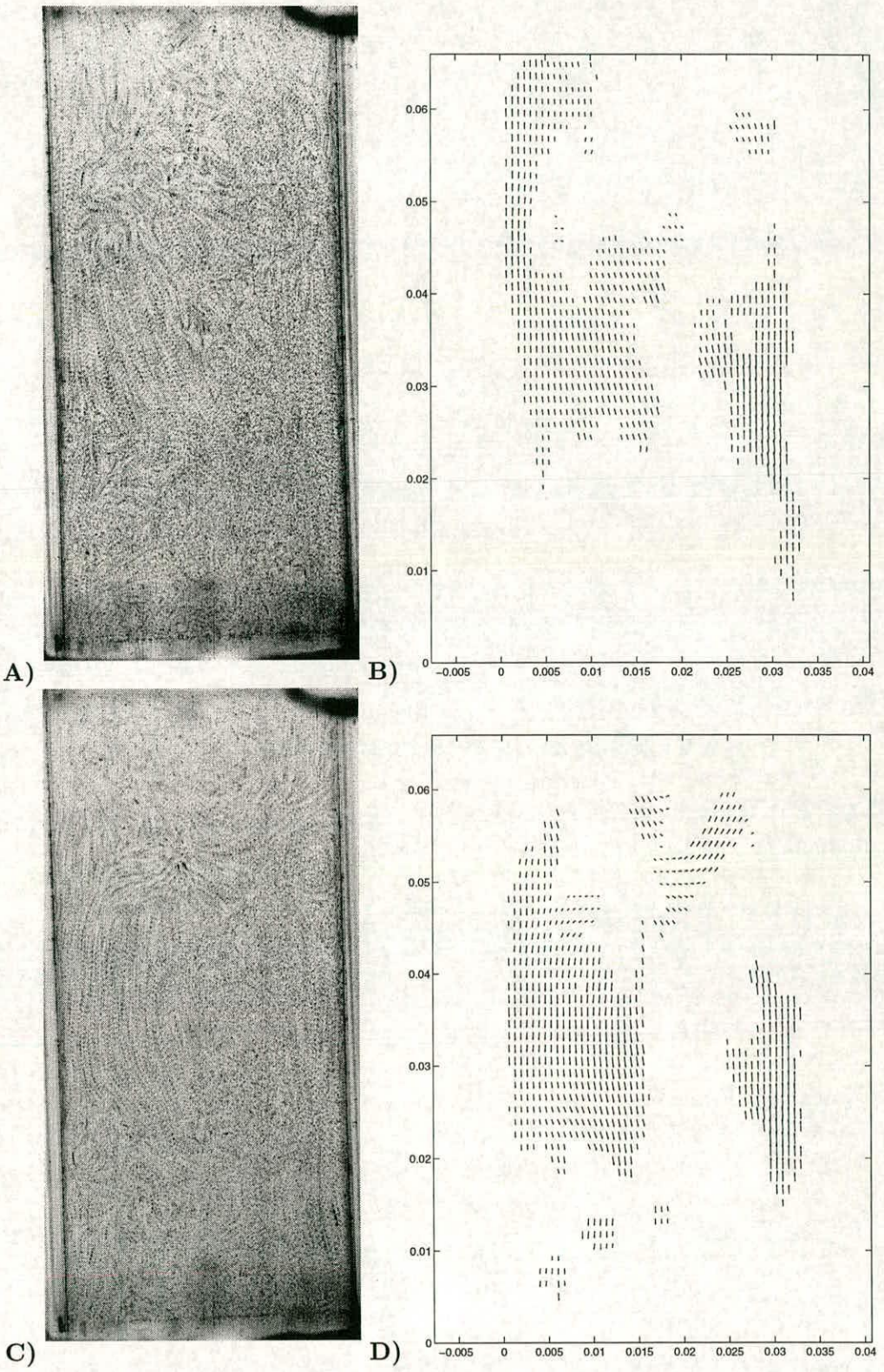


Figure E.3: **A)** PIV recording at a dimensionless time of 2/8 **B)** The vector field produced after five iterations to correct for velocity gradients and validation. The maximum velocity vector represents 0.0221 m/s. **C)** PIV recording at a dimensionless time of 2/8 **D)** The vector field produced after five iterations to correct for velocity gradients and validation. The maximum velocity vector represents 0.0181 m/s.

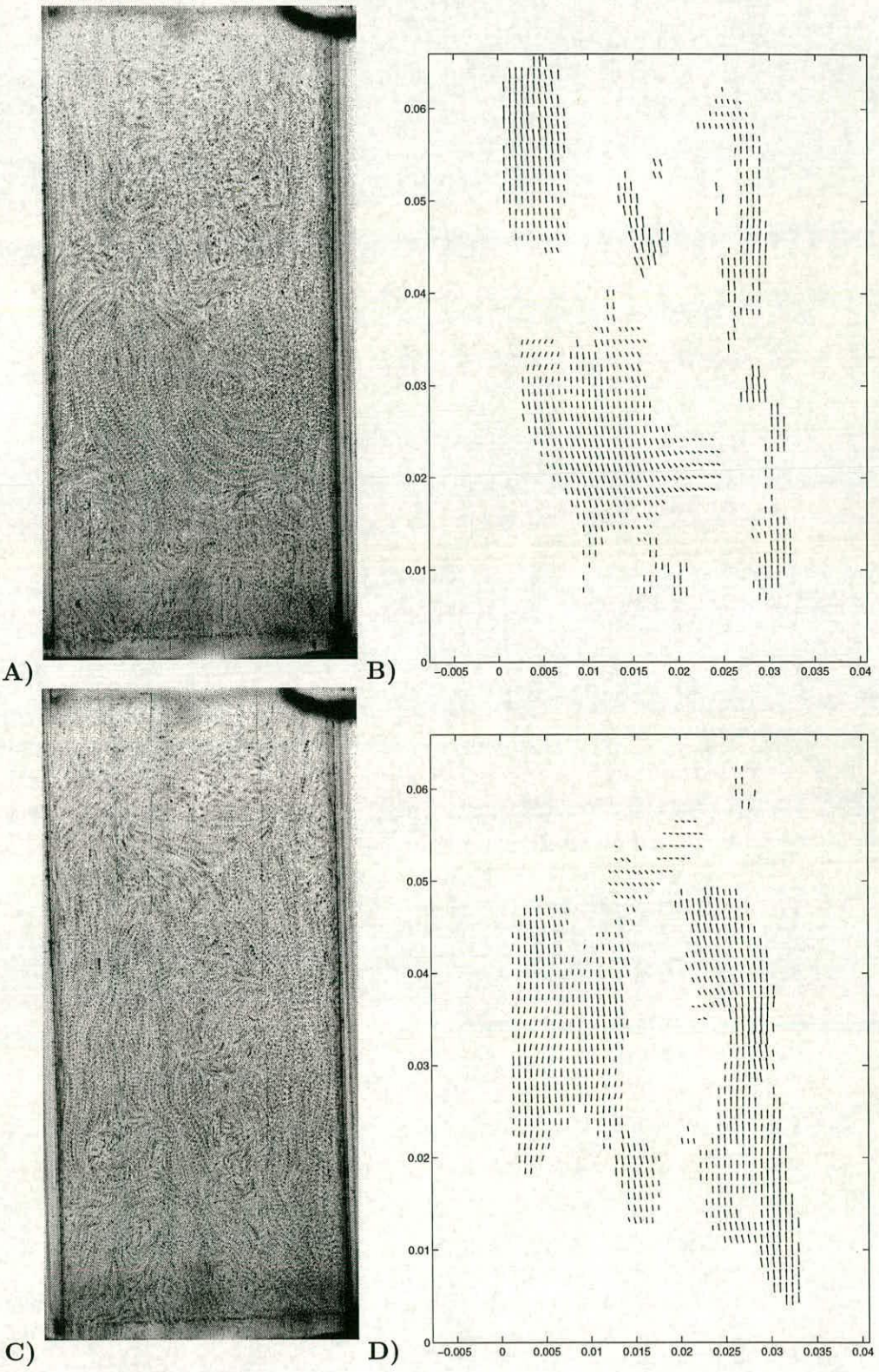


Figure E.4: **A)** PIV recording at a dimensionless time of 3/8 **B)** The vector field produced after five iterations to correct for velocity gradients and validation. The maximum velocity vector represents 0.0176 m/s. **C)** PIV recording at a dimensionless time of 3/8 **D)** The vector field produced after five iterations to correct for velocity gradients and validation. The maximum velocity vector represents 0.0164 m/s.

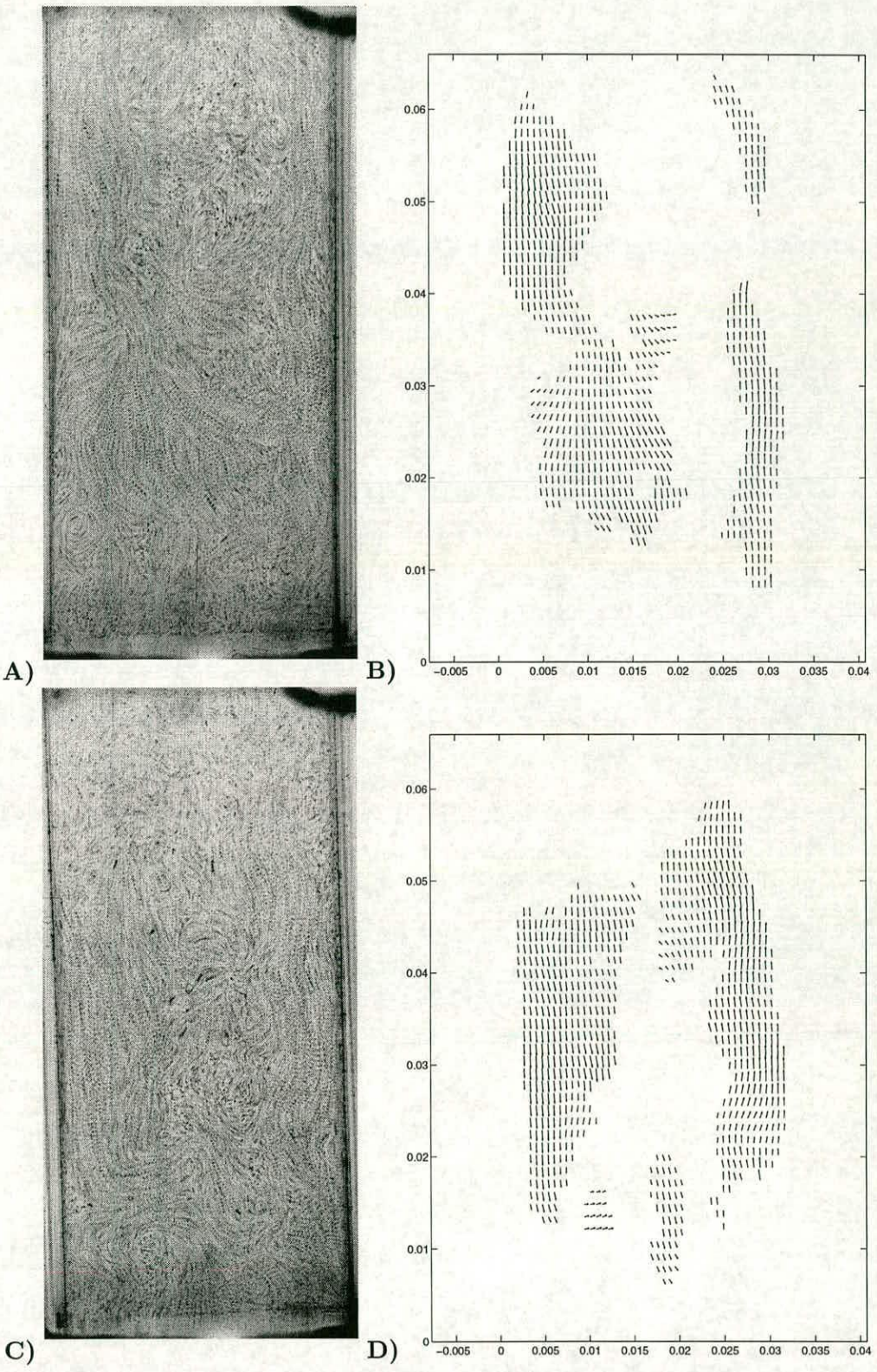


Figure E.5: **A)** PIV recording at a dimensionless time of 4/8 **B)** The vector field produced after five iterations to correct for velocity gradients and validation. The maximum velocity vector represents 0.0130 m/s. **C)** PIV recording at a dimensionless time of 4/8 **D)** The vector field produced after five iterations to correct for velocity gradients and validation. The maximum velocity vector represents 0.0126 m/s.

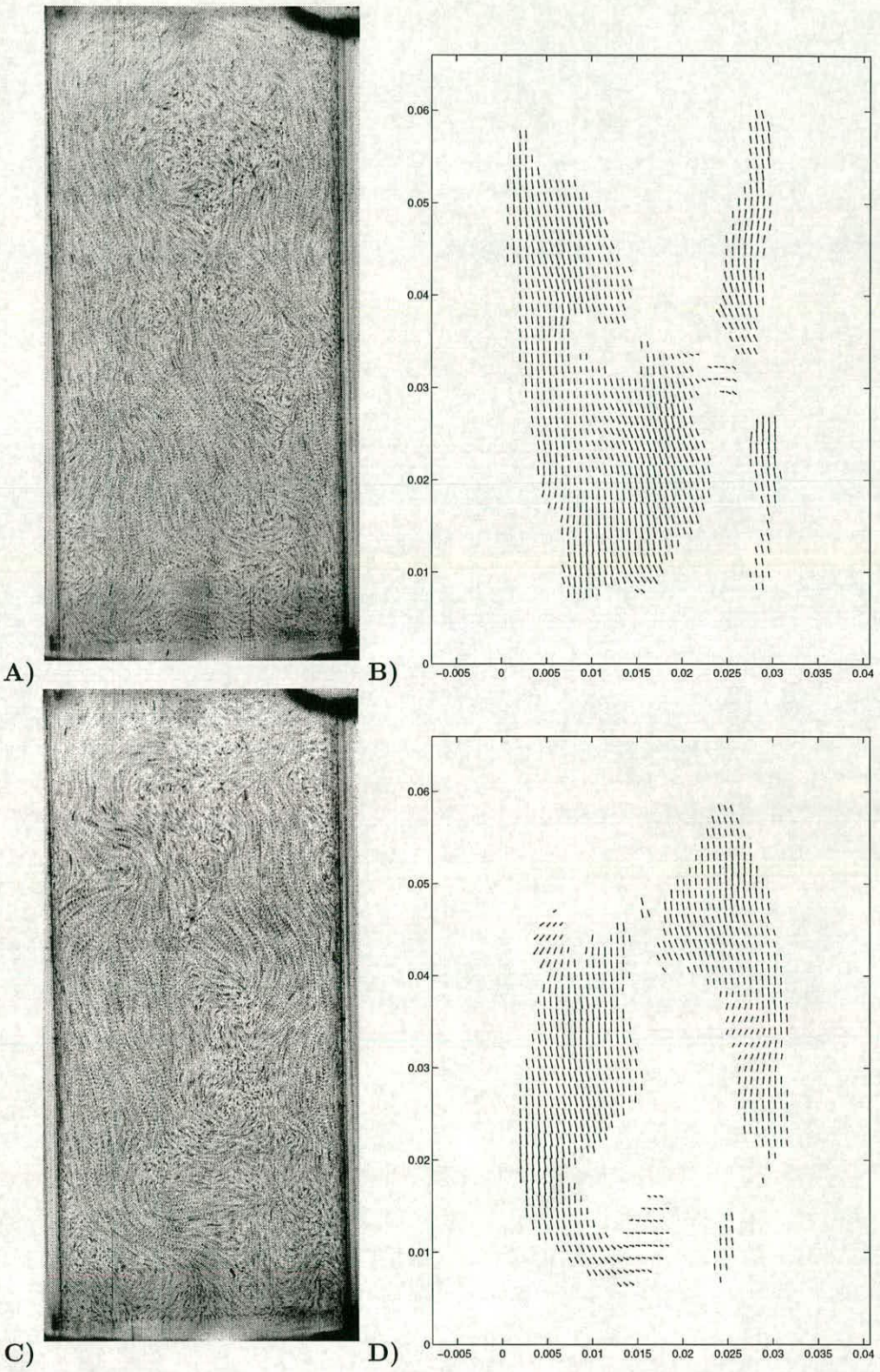


Figure E.6: **A)** PIV recording at a dimensionless time of 5/8 **B)** The vector field produced after five iterations to correct for velocity gradients and validation. The maximum velocity vector represents 0.0105 m/s. **C)** PIV recording at a dimensionless time of 5/8 **D)** The vector field produced after five iterations to correct for velocity gradients and validation. The maximum velocity vector represents 0.0117 m/s.

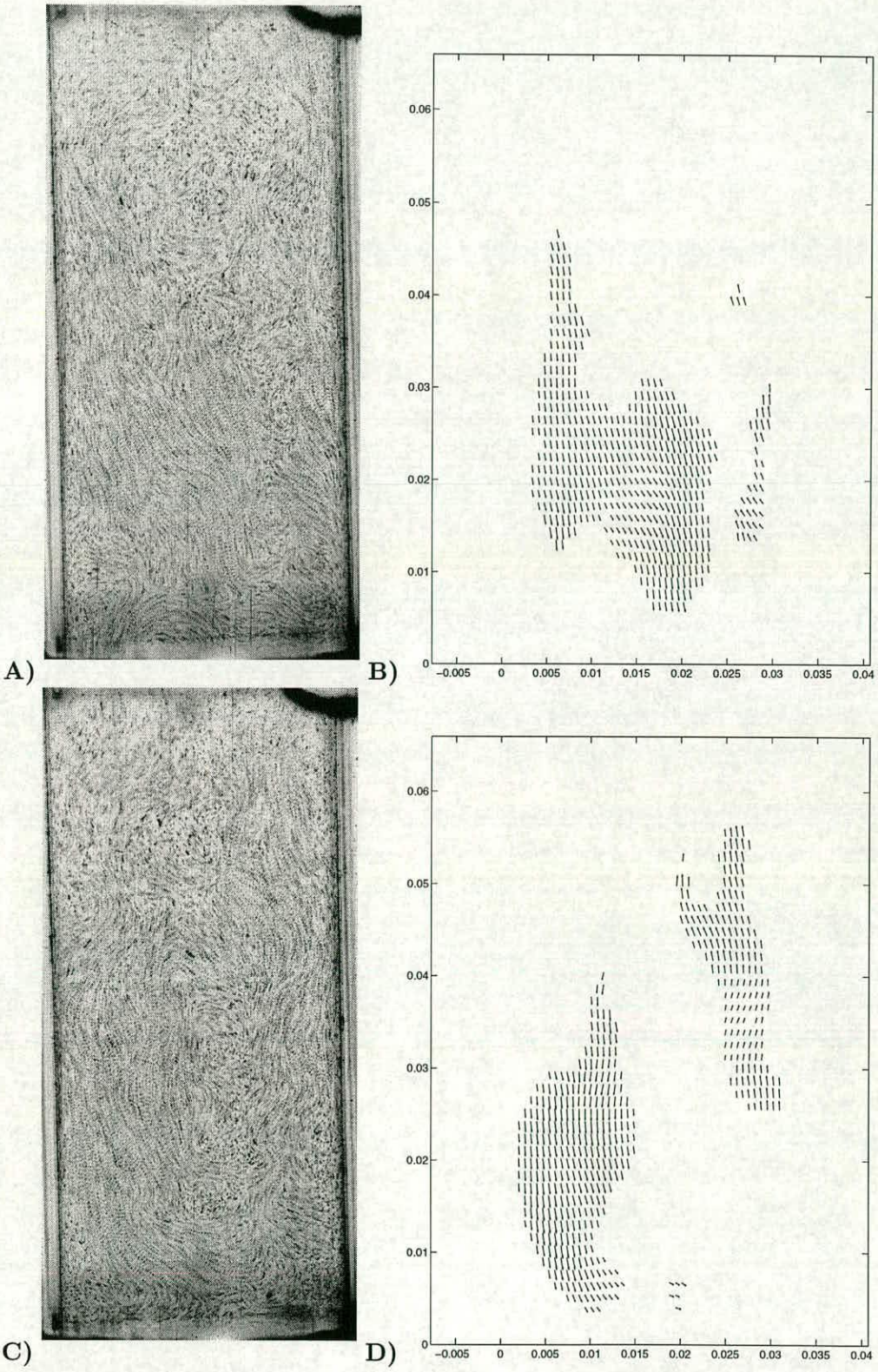


Figure E.7: **A)** PIV recording at a dimensionless time of 6/8 **B)** The vector field produced after five iterations to correct for velocity gradients and validation. The maximum velocity vector represents 0.0090 m/s. **C)** PIV recording at a dimensionless time of 6/8 **D)** The vector field produced after five iterations to correct for velocity gradients and validation. The maximum velocity vector represents 0.0101 m/s.

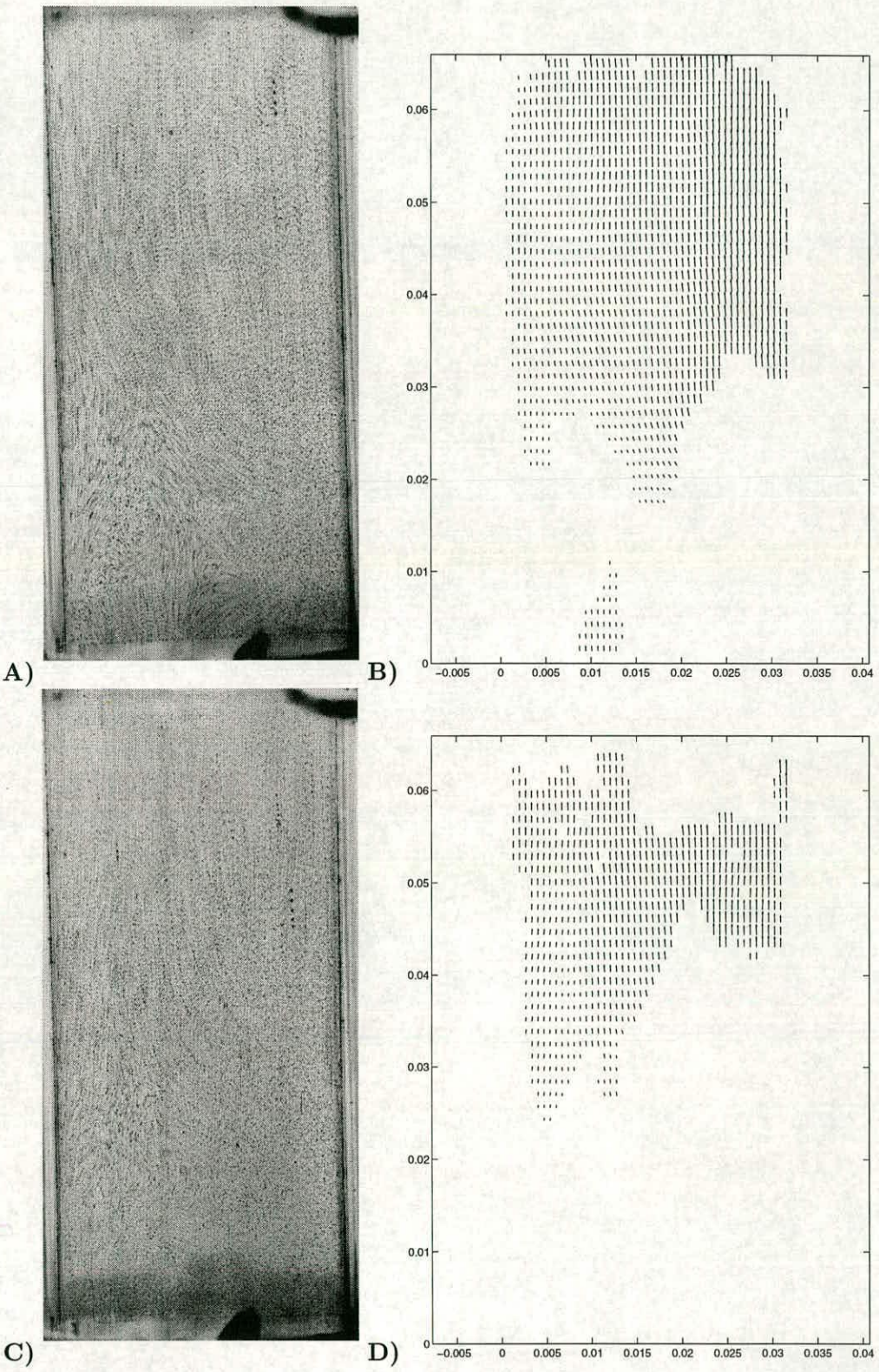


Figure E.8: **A)** PIV recording at a dimensionless time of 7/8 **B)** The vector field produced after five iterations to correct for velocity gradients and validation. The maximum velocity vector represents 0.0243 m/s. **C)** PIV recording at a dimensionless time of 7/8 **D)** The vector field produced after five iterations to correct for velocity gradients and validation. The maximum velocity vector represents 0.0292 m/s.

References

[1] J. R. E. Christy. *An investigation of fluid mechanical influences on the clotting of a blood analogue fluid.* PhD thesis, The University of Edinburgh, 1988.

[2] R. J. Adrian. Particle-imaging techniques for experimental fluid mechanics. *Ann. Rev. Fluid Mech.*, 23:261–304, 1991.

[3] J. C. Agüé and J. Jiménez. On the performance of particle tracking. *J. Fluid Mech.*, 185:447–468, 1987.

[4] W. L. Lim, Y. T. Chew, and H. T. Low. Improving the dynamic range of particle tracking velocimetry systems. *Experiments in Fluids*, 17:282–289, 1994.

[5] D. J. Wheatley. Clinical and laboratory assessment of prosthetic heart valves. In J.C Barnabel, editor, *Blood Flow in Artificial Organs and Cardiovascular Prosthesis.* Oxford University Press, 1989.

[6] Keith W. Marosek. *An investigation of the clot deposition from a flowing blood analogue by means of ultrasound imaging.* PhD thesis, University of Edinburgh, 1995.

[7] M. Giersiepen, L. J. Wurzinger, R. Opitz, and H. Reul. Estimation of shear stress-related blood damage in heart valve prostheses- *in vitro* comparison of 25 aortic valves. *Int. J. Artificial Organs*, 13(5):300–306, 1990.

[8] S. A. Jones. A relationship between Reynolds stresses and viscous dissipation:implications to red cell damage. *Annals of Biomedical Engineering*, 23:21–28, 1995.

[9] L. J. Wurzinger, P. Blasberg, and H. Schmid-Schönbein. Towards a concept of thrombosis in accelerated flow: rheology, fluid dynamics, and biochemistry. *Biorheology*, 22:437–449, 1985.

[10] G. D. Tansley, R. J. Edwards, and C. R. Gentle. Role of computational fluid mechanics in the analysis of prosthetic heart valve flow. *Med & Biol. Eng. & Comp.*, 26:175–185, 1988.

[11] A. P. Yoganathan, Y. R. Woo, and H. W. Sung. Turbulent shear stress measurements in the vicinity of aortic heart valve prostheses. *J. Biomechanics*, 19(6):433–442, 1986.

[12] Y. R. Woo and A. P. Yoganathan. Pulsatile flow velocity and shear stress measurements on the st. jude bileaflet valve prosthesis. *Scand. J. Thor. Cardiovasc. Surg.*, 20:15–28, 1986.

[13] H. Nygaard, M. Giersiepen, J. M. Hasenkam, H. Reul, P. K. Paulsen, P. E. Rovsing, and D. Westphal. Two-dimensional color-mapping of turbulent shear stress distribution downstream of two aortic bioprosthetic valves *in vitro*. *J. Biomechanics*, 25(4):429–440, 1992.

[14] D. L. Fry. Certain histological and chemical responses of the vascular interface to acutely induced mechanical stress in the aorta of the dog. *Circulation Research*, 24:93–108, 1969.

[15] J. M. O. Lewis and N. Macleod. A blood analogue for the experimental study of flow-related thrombosis at prosthetic heart valves. *Cardiovasc. Res.*, 17:466–475, 1983.

[16] P. Jollès. Structural aspects of the milk clotting process. Comparative features with the blood clotting process. *Molecular & Cellular Biochemistry*, 7(2):73–85, 1975.

[17] C. C. Landreth and R. J. Adrian. Impingement of a low Reynolds number turbulent circular jet onto a flat plate at normal incidence. *Experiments in Fluids*, 9:74–84, 1990.

[18] T. Utami and T. Ueno. Experimental study on the coherent structure of turbulent open-channel flow using visualisation and picture processing. *J. Fluid Mech*, 174:399–440, 1987.

[19] P. G. Lynch, A. Saylor, B. Ha, C. Lucas, G. W. Henry, J. I. Ferreiro, and A. P. Yoganathan. The effects of curvature on fluid flow fields in pulmonary artery models: flow visualisation studies. *J. Biomechanical eng.*, 115:97–103, 1993.

[20] A. K. Hind and J. R. E. Christy. Digital PIV applied to the flows around artificial heart valves: analysis by autocorrelation. In F.T.M. Nieuwstadt, editor, *Flow Visualization and Image Analysis*, pages 259–271. Kluwer, 1993.

[21] A. K. Hind, D. R. McCluskey, J. R. E. Christy, W. J. Easson, C. A. Greated, and D. H. Glass. PIV analysis of two-phase air particle flows. In *Optical Methods and Data Processing in Heat and Fluid Flow, 2-3 April, City University.* The Institution of Mechanical Engineers, London, 1992.

[22] D. R. McCluskey, A. K. Hind, S. L. J. Rix, M. L. Jacobsen, J. R. E. Christy, W. J. Easson, D. H. Glass, and C. A. Greated. Development and application of a simultaneous two phase PIV system for the analysis of air-particle flow fields. In *Optical Methods and Data Processing in Heat and Fluid Flow II, City University, London, April 1994*, 1994.

[23] M. Yianneskis, K. C. Lee, W. J. Easson, D. R. McCluskey, and A. K. Hind. Investigation of flow variations in inlet ports with particle image and laser velocimetry techniques. In *Experimental and Predictive Methods in Engine Research and Development, Birmingham, 17-18 Nov, 1993.* The Institute of Mechanical Engineers, 1993.

[24] A. K. Hind and J. R. E. Christy. Particle image velocimetry (PIV): Otaining instantaneous, multi-point velocity measurements through out a 2D plane in a time varying flow downstream of an artificial heart valve. In *The IChemE Research Event, UMIST, Manchester, 9-10 January*, pages 494–496. The Institution of Chemical Engineers, 1992.

[25] A. K. Hind and J. R. E. Christy. Flow field measurements around bluff bodies and artificial heart valves in pulsatile flows. In *The 1995 IChemE Research Event*, volume 2, pages 686–688. The Institution of Chemical Engineers ISBN 0 85295 359 3, 1995.

[26] J. R. E. Christy and A. K. Hind. Prediction of the thrombosis in flowing blood using particle image velocimetry. *Innovation and Technology in Biology and Medicine*, 15(3):337–350, 1994.

[27] A. K. Hind and J. R. E. Christy. A method to correct for velocity gradients in the analysis of PIV recordings. In *Optical Methods and Data Processing in Heat and Fluid Flow, 18-19 April*, volume C516 of *IMechE Conference Transactions 1996-3*, pages 201–210. Mechanical Engineering Publications Limited, 1996.

[28] C. R. McKay. Prosthetic heart valve thrombosis "What can be done with regard to treatment?". *Circulation*, 87(1):294–296, 1993.

[29] F. J. Schoen and R. J. Levy. Pathology of substitute heart valves: New concepts and developments. *J. Card. Surg.*, 9:222–227, 1994.

[30] V. O. Björk. Development of an artificial heart valve. *Ann. Thorac. Surg.*, 50:151–154, 1990.

[31] R. B. More. An examination of two retrieved long-term human implant Björk-Shiley valves. *Medical Progress through Technology*, 20:195–200, 1994.

[32] S. S. Kaplan. Biomaterial-host interactions: consequences, determined by implant retrieval analysis. *Medical Progress through Technology*, 20:209–230, 1994.

[33] D. S. Coulshed, M. A. Fitzpatrick, and C. H. Lee. Drug treatment associated with heart valve replacement. *Drugs*, 49(6):897–911, 1995.

[34] C. S. Peskin. The fluid dynamics of heart valves: experimental, theoretical and computational methods. *Ann. Rev. Fluid Mech.*, 14:235–259, 1982.

[35] E. Knott, H. Reul, M. Knoch, U. Steinseifer, and G. Rau. *In vitro* comparison of aortic heart valve prostheses. *J. Thorac. Cardiovasc. Surg.*, 96:952–961, 1988.

[36] H. Reul, M. Giersiepen, and E. Knott. *In vitro* testing of bioprostheses. *Trans. Am. Soc. Artif. Intern. Organs*, 34:1033–1039, 1988.

[37] J. Fisher, D. J. Wheatley, G. R. Jack, and L. Cathcart. Leaflet design and manufacture in pericardial heart valves. In J.C Barnabel, editor, *Blood flow in artificial organs and cardiovascular prosthesis*, pages 22–30. Oxford University Press, 1989.

[38] A. P. Yoganathan and W. H. Corcoran. Pressure drops across prosthetic aortic heart valves under steady and pulsatile flow - *in vitro* measurements. *J. Biomech.*, 12:153–164, 1979.

[39] W. B. Tindale and E. A. Trowbridge. The hydrodynamic performance of heart valve substitutes: The importance of standardisation. In J.C Barnabel, editor, *Blood Flow in Artificial Organs and Cardiovascular Prosthesis.* Oxford University Press, 1989.

[40] P. Willshaw, M. Biagetti, and R. H. Pichel. A comparative in vitro study of the closing charateristics of Björk-Shiley and Bicer-Val tilting disc mitral valve protheses. *J. Biomed. Eng.*, 8:43–48, 1986.

[41] C. S. Lee and K. B. Chandran. Instantaneous back flow through peripheral clearance of Medtronic Hall tilting disc valve at the moment of closure. *Annals of Biomedical Engineering*, 22:371–380, 1994.

[42] M. O. Wendt, M. Pohl, and D. Lerche. Leakage of mechanical heart valve prostheses of Björk-Shiley type: *in vitro* investigations using Newtionian fluids. *J. Biomed. Eng.*, 13:126–132, 1991.

[43] J. She, M. Li, L. Huan, and Y. Yu. Dynamic characteristics of prosthetic heart valves. *Med. Eng. Phys.*, 17(4):273–281, 1995.

[44] K. Köhler and R. Wirtz. Cinematics and sticking of heart valves in pulsatile flow test. *Int. J. Artificial Organs*, 14(5):290–294, 1991.

[45] C. D. Forbes, J. M. Courtney, G. D. O. Lowe, and M. Travers. Thrombosis and artificial surfaces. In J.C Barnabel, editor, *Blood flow in artificial organs and cardiovascular prosthesis*, pages 89–103. Oxford University Press, 1989.

[46] M. Otaki. Prosthetic valve endocarditis: An analysis of the outcome of 32 cases. *ASAIO Journal*, pages 176–180, 1994.

[47] A. D. Haubold. On the durability of pyrolytic carbon in vivo. *Medical Progress through Technology*, 20:201–208, 1994.

[48] P. Arru, S. Rinaldi, C. Stacchino, and F. Vallana. Relationship between some design characteristics and wear in the bicarbon heart valve prosthesis. *Int. J. Artifical Organs*, 17(5):280–293, 1994.

[49] G. S Bhuvaneshwar, C. V. Muraleedharan, A. V. Ramani, and M. S. Valiathan. Evaluation of materials for artificial heart valves. *Bull. Mater. Sci.*, 14(6):1363–1374, 1991.

[50] P. L. Blackshear and G. L. Blackshear. Mechanical hemolysis. In R. Skalak and S. Chien, editors, *Handbook of Bioengineering*, chapter 15, pages 15.1–15.19. McGraw Hill, 1987.

[51] L. J. Wurzinger, R. Opitz, and H. Eckstein. Mechanical blood trauma. An overview. *Angéiologie*, 38(3):81–97, 1986.

[52] C. Meneveau and K. R. Sreenivasan. The multifractal nature of turbulent energy dissipation. *J. Fluid Mech.*, 224:429–484, 1991.

[53] G. Häussinger, H. Reul, and U. Essers. In-vitro measurement of hemolysis and thrombosis: A comparative study of a ball-, disc-, and leaflet-aortic-valve. In *Proc. ESAO*, volume 6, pages 243–247, 1979.

[54] M. O. Wendt, M. Pohl, S. Pratsch, and D. Lerche. *In vitro* hemolysis by mechanical heart valve prostheses with tilting disc. *Int. J. Artificial Organs*, 15(11):681–685, 1992.

[55] H. Barmada and A. Starr. Clinical hemolysis with the St. Jude heart valve without paravalvular leak. *Medical Progress through Technology*, 20:191–194, 1994.

[56] R. T. Knapp, J. W. Daily, and F. G. Hammitt. *Cavitation.* McGraw-Hill, 1970.

[57] The Japan Society of Mechanical Engineers, editor. *Visualized Flow.* Pergamon Press, 1988.

[58] T. Graf, H. Fischer, H. Reul, and G. Rau. Cavitation potential of mechanical heart valve prostheses. *Int. J. Artificial Organs*, 14(3):169–174, 1991.

[59] C. S. Lee, K. B. Chandran, and L. D. Chen. Cavitation dynamics of mechanical heart valve prostheses. *Artificial Organs*, 18(10):758–767, 1994.

[60] C. M. Zapanta, E. G Liszka Jr., T. C. Lamson, D. R. Stinebring, S. Deutsch, D. B. Geselowitz, and J. M. Tarbell. A method for real time *in vitro* observation of cavitation on prosthetic heart valves. *Journal of Biomechanical Engineering*, 116:460–468, 1994.

[61] C. F. Dewey, S. R. Bussolari, M. A. Gimbrone, and P. F. Davies. The dynamic response of vascular endothelial cells to fluid shear stress. *J. Biomech. Eng.*, 103:177–185, 1981.

[62] W. H. Herkes and J. R. Lloyd. Experimental measurements of the flow-induced shear stress distribution in the vicinity of, prosthetic heart valves. *J. Biomech. Eng.*, 103:267–274, 1981.

[63] W. Tillmann, H. Reul, M. Herold, K. H. Bruss, and J. van Gilse. *In vitro* wall shear measurements at aortic valve prostheses. *J. Biomechanics*, 17(4):263–279, 1984.

[64] J. R. E. Christy and N. Macleod. The role of stasis in the clotting of blood and milk flows around solid objects. *Cardiovascular Research*, 23(11):949–959, 1989.

[65] W. Merzkirch. *Flow Visualisation.* Academic Press, 1974.

[66] M. van Dyke. *An Album of Fluid Motion.* Parabolic Press, Stanford, Calafornia, 1982.

[67] M. Gad el Hak. Visualization techniques for unsteady flows: An overview. *J. Fluids Eng.*, 110:231–243, 1988.

[68] W. Lauterborn and A. Vogel. Modern optical techniques in fluid mechanics. *Ann. Rev. Fluid Mech.*, 16:223–244, 1984.

[69] L. Hesselink. Digital image processing in flow visualization. *Ann. Rev. Fluid Mech.*, 20:421–485, 1988.

[70] R. S. Figliola and T. J. Mueller. Fluid stresses in the vicinity of disk, ball, and tilting disk prosthetic heart valves from in-vitro measurements. *J. Biomech. Eng.*, pages 173–177, 1977.

[71] K. B. Chandran, T. L. Yearwood, C. J. Chen, and H. L. Falsetti. Pulsatile flow measurements on heart valve prostheses. *Med. & Biol. Eng. & Comput.*, 21:529–537, 1983.

[72] J. M. Hasenkam, H. Nygaard, M. Giersiepen, H. Reul, and H. Stødkilde-Jørgensen. Turbulent stress measurements downstream of six mechanical aortic valves in a pulsatile flow model. *J. Biomechanics*, 21(8):631–645, 1988.

[73] V. N. Yurechko, Y. S. Ryazantsey, E. S. Shtengold, and V. N. Ilminsky. Photochromic visualisation for investigation of artificial heart valves. *Trans. Am. Soc. Artif. Intern. Organs*, 35:218–221, 1989.

[74] K. Affeld, P. Walker, and K. Schichl. The use of image processing in the investigation of artificial heart valve flow. *Trans. Am. Soc. Artif. Intern. Organs*, 35:294–298, 1989.

[75] F. Cassot, R. Pelissier, and G. Tonietto. Vorticity formation and transport from mechanical heart valve prostheses experimental and numerical simulations. In F. Mosora, editor, *Biomechanical Transport Processes*, volume 193, chapter 40, pages 105–114. Plenum Press, 1990.

[76] F. Hirt, E. Jud, and Z. Zhang. Investigation of the local flow topology in the vicinity of a prosthetic heart valve by using particle image velocimetry. In *Seventh International Symposium on Applications of Laser Techniques to Fluid Mechanics, July 11th to 14th 1994, Lisbon, Portugal.*, volume II, pages 37.3.1–37.3.7, 1994.

[77] M. S. Chong, A. E. Perry, and B. J. Cantwell. A general classification of three-dimensional flow fields. *Phys. Fluids A*, 2(5):765–777, 1990.

[78] R. Chevray and J. Mathieu. *Topics in Fluid Mechanics.* Cambridge University Press, 1993.

[79] W. L. Lim, Y. T. Chew, T. C. Chew, and H. T. Low. Particle image velocimetry in the investigation of flow past artificial heart valves. *Annals of Biomedical Engineering*, 22:307–318, 1994.

[80] M. Ojha, R. S. C. Cobbold, K. W. Johnston, and R. L. Hummel. Detailed visualization of pulsatile flow fields produced by modelled arterial stenoses. *J. Biomed. Eng.*, 12:463–469, 1990.

[81] D. Farahifar, H. Bodard, F. Cassot, and R. Pelissier. Velocity field of a Björk - Shiley valve prosthesis: influence of the disc orientation. *Cardiovascular Research*, 21:90–98, 1987.

[82] T. David, J. Clamp, and J. Fisher. Analysis of regurgitant jets in natural and bio-prosthetic heart valves. *J. Biomechanics*, 25(4):457–462, 1992.

[83] K. Chao, V. A. Moises, R. Shandas, T. Elkadi, D. J. Sahn, and R. Weintraub. Influence of the Coanda effect on color doppler jet area and colour encoding. *Circulation*, 85(1):333–341, 1992.

[84] J. C. Mohan, R. Agrawal, R. Arora, and M. Khalilullah. Improved Doppler assessment of the Bjork-Shiley mitral prosthesis using the continuity equation. *Int. J. Cardiology*, 43:321–326, 1994.

[85] H. Nygaard, P. K. Paulson, J. M. Hasenkam, E. M. Pederson, and P. E. Rovsing. Turbulent stresses downstream of three mechanical aortic valve prostheses in human beings. *Journal of Thoracic and Cardivascular Surgery*, 107(2):438–446, 1994.

[86] F. L. Galanga and J. R. Lloyd. An experimental study of the flow-induced mass transfer distribution in the vicinity of prosthetic heart valves. *J. Biomech. Eng.*, 103:1–10, 1981.

[87] D. J. Tritton. *Physical Fluid Dynamics.* Clarendon Press, Oxford, 1988.

[88] L. E. Drain. *The laser doppler technique.* John Wiley and Sons, 1980.

[89] F. Durst, A. Melling, and Whitelaw. *Principles and practice of Laser Doppler Anemometry.* Academic Press, 1976.

[90] A. P. Yoganathan, W. H. Corcoran, and E. C. Harrison. *In vitro* velocity measurements in the vicinity of aortic prostheses. *J. Biomech.*, 12:135–152, 1979.

[91] R. S. Figliola and T. J. Mueller. On the hemolytic and thrombogenic potential of occluder prosthetic heart valves from in-vitro measurements. *J. Biomechanical Engineering*, 103:83–90, 1981.

[92] K. B. Chandran, T. V. Ferguson, C. J. Chen, and B. Khalighi. Experimental study of flow dynamics behind valve prostheses. *ASAIO Journal*, 6(3):146–152, 1983.

[93] M. Lei, A. A. van Steenhoven, and D. H. van Campen. Experimental and numerical analyses of the steady flow field around an aortic Björk-Shiley standard valve prosthesis. *J. Biomechanics*, 25(3):213–222, 1992.

[94] B. Thwaites. *Incompressible Aerodynamics.* Oxford University Press, Oxford, 1960.

[95] K. B. Chandran, R. Fatemi, L. F. Haratzka, and C. Harris. Effect of wedging on the flow characteristics past tilting disc aortic valve prosthesis. *J. Biomechanics*, 19(3):181–186, 1986.

[96] W. G. Tiederman, M. J. Steinle, and W. M. Phillips. Two-component laser velocimeter measurements downstream of heart valve prostheses in pulsatile flow. *J. Biomech. Eng.*, 108:59–64, 1986.

[97] Y. T. Chew, H. T. Low, C. N. Lee, and S. S. Kwa. Laser anemometry measurements of steady flow past aortic valve prostheses. *J. Biomech. Eng.*, 115:290–298, 1993.

[98] F. J. Walburn, H. N. Sabbah, and P. D. Stein. Turbulent stresses in the region of a Hancock porcine bioprosthetic aortic valve. *J. Biomech. Eng.*, 107:200–205, 1985.

[99] Y. R. Woo and A. P. Yoganathan. Two-component laser doppler anemometer for measurment of velocity and turbulent shear stress near prosthetic heart valves. *Medical Instumentation*, 19(5):224–231, 1985.

[100] Y. R. Woo and A. P. Yoganathan. *In vitro* pulsatile flow velocity and shear stress measurements in the vicinity of mechanical mitral heart valve prostheses. *J. Biomechanics*, 19(1):39–51, 1986.

[101] A. C. Schwarz, W. G. Tiederman, and W. M. Phillips. Influence of cardiac flow rate on turbulent shear stress from a prosthetic heart valve. *J. Biomechanical Eng.*, 110:123–128, 1988.

[102] M. Giersiepen, U. Krause, E. Knott, H. Reul, and G. Rau. Velocity and shear stress distribution downstream of mechanical heart valves in pulsatile flow. *Int. J. Artificial Organs*, 12(4):261–269, 1989.

[103] P. G. Walker and A. P. Yoganathan. In vitro pusatile flow heamodynamics of five mechanical aortic heart valve prostheses. *Eur. J. Cardio-thorac. Surg.*, 6(Suppl 1):S113–S123, 1992.

[104] J. A. M. van Son, H. Reul, U. Steinseifer, B. Schmitz, A. Schmid, C. Schmitz, and G. Rau. Systolic sequential flow velocity profiles in four currently used bileaflet heart valve prostheses. *European Journal of Cardio-thoracic Surgery*, 7:107–108, 1993.

[105] J. T. Baldwin, S. Deutsch, H. L. Petrie, and J. M. Tarbell. Determination of principle Reynolds stresses in pulsatile flows after elliptical filtering of discrete velocity measurements. *Trans. AMSE*, 115:396–403, 1993.

[106] L. C. Cheng, M. E. Clark, and J. M. Robertson. Numerical calculations of oscillating flow in the vicinity of square wall obstacles in plane conduits. *J. Biomech.*, 5:467–484, 1972.

[107] L. C. Cheng, J. M. Robertson, and M. E. Clark. Calaulation of plane pulsatile flow past wall obstacles. *Computers & Fluids*, 2:363–380, 1974.

[108] T. H. Reif. A numerical analysis of the backflow between the leaflets of a St. Jude medical cardiac valve prosthesis. *J. Biomechanics*, 24(8):733–741, 1991.

[109] K. Thalassoudis, J. Mazumdar, B. J. Noye, and I. H. Craig. Numerical study of turbulent blood flow through a caged-ball prosthetic heart valve using a boundary-fitted co-ordinate system. *Med. & Biol. Eng. & Comp.*, 25:173–180, 1987.

[110] S. E. Rogers, D. Kwak, and C. Kiris. Numerical solution of the incompressible Navier-Stokes equations for steady-state and time-dependent problems. *AIAA Paper 89-0463*, 89.

[111] S. Rogers, P. Kutler, D. Kwak, and C. Kiris. Numerical simulation of flow through an artificial heart. *Cray Channels*, pages 16–19, Winter 1990.

[112] I. Peterson. Heart flow. *Science News*, 130:204–206, 1986.

[113] T. Cheng and C. S. Peskin. Stability and instability in the computation of flows with moving immersed boundaries: a comparison of three methods. *SIAM J. Sci. Stat. Comput.*, 13(6):1361–1376, 1992.

[114] C. C. Vesier and A. P. Yoganathan. A computer method for simulation of cardiovascular flow fields: Validation of approach. *J. Comp. Phys.*, 99:271–287, 1992.

[115] C. S. Peskin and D. M. McQueen. Cardiac fluid dynamics. *Critical Reviews in Biomedical Engineering*, 20(5-6):451–459, 1992.

[116] R. J. Adrian. Multi-point optical measurements of simultaneous vectors in unsteady flow - a review. *Int. J. Heat & Fluid Flow*, 7(2):127–145, 1986.

[117] T. D. Dudderar, R. Meynart, and P. G. Simpkins. Full-field laser metrology for fluid velocity measurement. *Optics and Lasers in Engineering*, 9:163–199, 1988.

[118] I. Grant and G. H. Smith. Modern developments in particle image velocimetry. *Optics and Lasers in Engineering*, 9:245–264, 1988.

[119] P. Buchhave. Particle image velocimetry - status and trends. *Experimental Thermal and Fluid Science*, 5:586–604, 1992.

[120] Ian Grant, editor. *Selected papers on Particle Image Velocimetry*, volume MS 99 of *SPIE Milestone Series*. SPIE, 1994.

[121] J. C. Dainty. Some statistical properties of random speckle patterns in coherent and partially coherent illumination. *Optica Acta*, 17(10):761–772, 1970.

[122] G. E. Willis and J. W. Deardorff. A laboratory model of the unstable planetary boundary layer. *J. Atmos. Sci.*, 31:1297–1307, 1974.

[123] D. B. Barker and M. E. Fourney. Measuring fluid velocities with speckle patterns. *Opt. Lett.*, 1(4):135–137, 1977.

[124] R. Grousson and S. Mallick. Study of flow pattern in a fluid by scattered laser light. *Appl. Opt.*, 16(9):2334–2337, 1977.

[125] T. D. Dudderar and P. G. Simpkins. Laser speckle photography in a fluid medium. *Nature*, 270:45–47, 1977.

[126] J. M. Burch and J. M. J. Tokarski. Production of multiple beam fringes from photographic scatterers. *Optica Acta*, 15(2):101–111, 1968.

[127] E. Archbold and A. E. Ennos. Displacement measurement from double-exposure laser photographs. *Optica Acta*, 19(4):253–271, 1972.

[128] K. A. Stetson. A review of speckle photography and interferometry. *Opt. Eng.*, 14:482–489, 1975.

[129] L. Celaya, J. M. Jonathan, and S. Mallick. Velocity contours by speckle photography. *Opt. Comm.*, 18(4):496–498, 1976.

[130] R. K. Erf. Application of laser speckle to measurement. In J.W. Goodman and M. Ross, editors, *Laser Applications*, volume 4. Academic Press, 1980.

[131] B. Ineichen, P. Eglin, and R. Dändliker. Hybrid optical and electronic image processing for strain measurements by speckle photography. *Appl. Opt.*, 19(13):2191–2195, 1980.

[132] G. H. Kaufmann. On the numerical processing of speckle photograph fringes. *Optics and Laser Technology*, pages 207–209, August 1980.

[133] E. Hecht. *Optics.* Addison-Wesley Publishing Company, Inc, 2nd edition, 1987.

[134] K. Iwata, T. Hakoshima, and R. Nagata. Measurement of flow velocity distribution by multiple-exposure speckle photography. *Opt. Comm*, 25(3):311–314, 1978.

[135] B. C. R. Ewan. Particle velocity distribution measurement by holography. *Appl. Opt.*, 18(18):3156–3160, 1979.

[136] R. Meynart. Equal velocity fringes in a Rayleigh-Benard flow by a speckle method. *Appl. Opt.*, 19(9):1385–1386, 1980.

[137] P. L. Baker, F. Ninio, G. J. Troup, and R. Bryant. Velocity measurements with speckle and speckle-like photography. *Aust. J. Phys.*, 33:601–605, 1980.

[138] R. Jones and C. Wykes. *Holographic and speckle interferometry.* Number ISBN 0-521-23268-6. Cambridge University Press, 1983.

[139] J. Georgieva. Removing the diffraction halo effect in speckle photography. *Appl. Opt.*, 28(1):21–22, 1989.

[140] G. H. Kaufmann, A. E. Ennos, B. Gale, and D. J. Pugh. An electro-optical read-out system for analysis of speckle photogrphs. *J. Phys. E: Sci. Instrum.*, 13:579–584, 1980.

[141] G. H. Kaufmann. Numerical processing of speckle photography data by Fourier transform. *Appl. Opt.*, 20(24):4277–4280, 1981.

[142] R. Meynart. Digital image processing for speckle flow velocimetry. *Rev. Sci. Instrum.*, 53(1):110–111, 1982.

[143] R. Meynart. Instantaneous velocity field measurements in unsteady gas flow by speckle velocimetry. *Appl. Opt.*, 22(4):535–540, 1983.

[144] R. Meynart. Speckle velocimetry: An application of image analysis techniques to the measurement of instantaneous velocity fields in unsteady flow. In *International Congress on Instrumentation in Aerospace Simulation Facilities*, pages 30–36. IEEE, 1983.

[145] D. W. Robinson. Automatic fringe analysis with a computer image-processing system. *Applied Optics*, 22(14):2169–2176, 1983.

[146] R. Meynart. Diffraction halo in speckle photography. *Appl. Opt.*, 23(14):2235–2236, 1984.

[147] I. Yamaguchi. Fringe formation in speckle photography. *J. Opt. Soc. Am. A*, 1(1):81–86, 1984.

[148] C. J. D. Pickering and N. A. Halliwell. Particle image velocimetry: fringe visibility and pedestal removal. *Appl. Opt.*, 24(16):2474–2476, 1985.

[149] R. Erbeck. Fast image processing with a microcomputer applied to speckle photography. *Appl. Opt.*, 24(22):3838–3841, 1985.

[150] S. H. Collicott and L. Hesselink. Anamorphic optical processing of mutiple-exposure speckle photographs. *Opt. Lett.*, 11(7):410–412, 1986.

[151] C. J. D. Pickering and N. A. Halliwell. Particle image velocimetry: data reduction by fringe analysis. In *Internatioanl Symposium on Application of Laser Anemometry to Fluid Mechanics, 3rd, July 7-9, Lisbon, Potugal*, 1986.

[152] A. Kirita, C. J. D. PIckering, and N. A. Halliwell. Particle image velocimetery: automatic fringe analysis by cross-correlation. *Opt. Eng.*, 27(3):188–192, 1988.

[153] A. Kirita, C. J. D. Pickering, and N. A. Halliwell. Particle image velocimetry: A new approach to fringe analysis. *Optics and Lasers in Engineering*, 7:137–147, 1987.

[154] J. M. Huntley. Speckle photography fringe analysis: assessment of current algorithms. *Appl. Opt.*, 28(20):4316–4323, 1989.

[155] W. H. Press, S. A. Teukolsky, W. T. Vetterling, and B. P. Flannery. *Numerical recipes in C: the art of scientific computing.* Cambridge University Press, 2nd edition, 1994.

[156] J. S. Kim. Range and accuracy of speckle displacement measurement in double-exposure speckle photography. *J. Opt. Soc. Am. A*, 6(5):675–681, 1989.

[157] N. Takai and T. Asakura. Displacement measurement of speckles using a 2-D level-crossing technique. *Appl. Opt.*, 22(22):3514–3519, 1983.

[158] R. J. Adrian and C. S. Yao. Development of pulsed laser velocimetry (PLV) for measurement of turbulent flow. In *Symposium on Turbulence*, pages 170–186. Curators of the University of Missouri, 1984.

[159] C. J. D. Pickering and N. A. Halliwell. Laser speckle photography and particle image velocimetry: photographic film noise. *Appl. Opt.*, 23(17):2961–2969, 1984.

[160] C. J. D. Pickering and N. A. Halliwell. Speckle photography in fluid flows: signal recovery with two step processing. *Appl. Opt.*, 23(8):1128–1129, 1984.

[161] C. J. D. Pickering and N. A. Halliwell. Particle image velociemtry: improving signal-to-noise ratio with a two step photographic process. Part II. *J. Opt. Soc. Am. A*, 2(10):1721–1724, 1985.

[162] C. J. D. Pickering and N. A. Halliwell. Particle image velocimetry: improving fringe signal-to-noise ratio with a two-step photographic process. *J. Opt. Soc. Am. A*, 2(4):610–615, 1985.

[163] A. R. Ganesan, P. Meinlschmidt, H. Hinrichs, and K. D. Hinsch. Particle image velocimetry: improving fringe quality with a negative-mask method. *Applied Optics*, 34(11):1763–1768, 1995.

[164] J. B. Pearson, B. Hilko, H. Houtman, and F. L. Curzon. Laser speckle velocity measurements of flow velocity in a simplified gas jet. *Rev. Sci. Instrum.*, 57(3):374–376, 1986.

[165] K. Hinsch, W. Schipper, and D. Mach. Fringe visibility in speckle velocimetry and the analysis of random flow components. *Appl. Opt.*, 23(4):4460–4462, 1984.

[166] W. Arnold, K. D. Hinsch, and D. Mach. Turbulence level measurements by speckle velocimetry. *Applied Optics*, 25(3):330–331, 1986.

[167] R. Erbeck and W. Merzkirch. Speckle photographic measurement of turbulence in an air stream with fluctuating temperature. *Experiments in Fluids*, 6:89–93, 1988.

[168] I. Grant, E. H. Owens, and G. H. Smith. Particle image velocimetry fringe visibility as a means of turbulence estimation. *Applied Optics*, 28(15):2982–2984, 1989.

[169] I. Grant, E. H. Owens, and G. H. Smith. The effect of flow turbulence and interrogating beam profile on particle image velocimetry fringes. *Optics and Lasers in Engineering*, 11:115–128, 1989.

[170] P. Jacquot and P. K. Rastogi. Influence of out-of-plane defermation and its elimination in white light speckle photography. *Optics and Lasers in Engineering*, 2:33–55, 1981.

[171] R. Meynart. Non-Gaussian statistics of speckle noise of Young's fringes in speckle velocimetry. *Appl. Opt.*, 24(10):1448–1453, 1985.

[172] R. J. Binnington, D. V. Boger, G. Troup, and R. G Turner. Point velocity measurement in slow flows using laser speckle photography. *Atti della Fondazione Giorgio Roncho*, 36:665–672, 1981.

[173] R. J. Binnington, G. J. Troup, and D. V. Boger. A low cost laser-speckle photographic technique for velocity measurements in slow flows. *J. Non-Newtonian Fluid Mech.*, 12:255–267, 1983.

[174] E. Bernabeu, J. C. Amaré, and M. P. Arroyo. White-light speckle method of measurement of flow velocity distribution. *Appl. opt.*, 21(14):2583–2586, 1982.

[175] G. H. Kaufmann. Double-pulsed white-light speckle photography. *Appl. Opt.*, 23(2):194–196, 1984.

[176] U. Gärtner, U. Wernikinck, and W. Merzkirch. Velocity measurements in the field of an internal gravity wave by means of speckle photography. *Exp. Fluids*, 4:283–287, 1986.

[177] R. Meynart, P. G. Simpkins, and T. D. Dudderar. Speckle measurements of convection in a liquid cooled from above. *J. Fluid Mech.*, 182:235–254, 1987.

[178] M. Kawahashi and K. Hosoi. Beam-sweep laser speckle velocimetry. *Exp. Fluids*, 8:109–111, 1989.

[179] M. R. Maxey and J. J. Riley. Equation of motion for a small rigid sphere in a nonuniform flow. *Phys. Fluids*, 26(4):883–889, 1983.

[180] D. J. Brown and P. Hutchinson. The interaction of solid or liquid particles and turbulent flow fields - a numerical simulation. *Journal of Fluids Engineering*, 101:265–269, 1979.

[181] M. Dadi, M. Stanislas, O. Rodriguez, and A. Dyment. A study by holographic velocimetry of the behaviour of free small particles in a flow. *Experiments in Fluids*, 10:285–294, 1991.

[182] R. J. Adrian. Scattering power of seed materials Mie scattering calculations. In *Particle Image Displacement Velocimetry, Lecture series 1988-06.* Von Karman Institute for Fluid Dynamics, March 12-25, Belgium 1988.

[183] R. J. Adrian and C. S. Yao. Pulsed laser technique appplication to liquid and gaseous flows and the scattering power of seed materials. *Applied Optics*, 24(1):44–52, 1985.

[184] R. J. Adrian. Scattering particle characteristics and their effect on pulsed laser measurements of fluid flow: speckle velocimetry v.s. particle image velocimetry. *Applied Optics*, 23(11):1690–1691, 1984.

[185] T. Schmitt, J. N. Koster, and H. Hamacher. Particle design for displacement tracking velocimetry. *Meas. Sci. Technol.*, 6(6):682–689, 1995.

[186] H. C. van de Hulst. *Light Scattering by Small Particles.* Dover, 1981.

[187] D. J. Anderson, R. D. Morgan, D. R. McCluskey, J. D. C. Jones, W. J. Easson, and C. A. Greated. An optical fibre delivery system for pulsed laser particle image velocimetry illumination. *Meas. Sci. Technol.*, 6(6):809–814, 1995.

[188] M. Grobel and W. Merzkirch. White-light speckle velocimetry applied to plane free convective flow. *Experimental Heat Transfer*, 4:253–262, 1991.

[189] S. Ashforth-Frost, K. Jambunathan, X. Y. Ju, and X. Wu. Application of liquid crystals to particle image velocimetry. In *Optical methods and data processing in heat and fluid flow, 18-19 April*, volume C516 of *IMechE Conference Transactions 1996-3*, pages 81–90. Mechanical Engineering Publications Limited, 1996.

[190] C. Gray, C. A. Greated, D. R. McCluskey, and W. J. Easson. An analysis of the scanning beam PIV illumination system. *Meas. Sci. Technol.*, 2:717–724, 1991.

[191] D. Rockwell, C. Magness, J. Towfighi, O. Akin, and T. Corcoran. High image-density particle image velocimetry using laser scanning techniques. *Experiments in Fluids*, 14:181–192, 1993.

[192] M. E. Post, D. D. Trump, L. P. Goss, and R. D. Hancock. Two-color particle-imaging velocimetry using a single argon-ion laser. *Experiments in Fluids*, 16:263–272, 1994.

[193] C. Brücker. A new method for the determination of the out-of-plane component in three-dimensional PIV using a colour-coded light sheet and spatial correlation: simulation and feasibility study for three dimensional scanning PIV. In *Optical methods and data processing in heat and fluid flow, 18-19 April*, volume C516 of *IMechE Conference Transactions 1996-3*, pages 189–200. Mechanical Engineering Publications Limited, 1996.

[194] Kodak Limited, PO Box 66, Station Road, Hemel Hempstead, Herts, HP1 1JU. *Kodak Publication No. F-32(H): Kodak T-Max professional films.*

[195] Kodak Limited, PO Box 66, Station Road, Hemel Hempstead, Herts, HP1 1JU. *Kodak Publication No. P-255: Kodac Technical Pan Films.*

[196] L. Lourenco and A. Krothapalli. The role of photographic parameters in laser speckle or particle image displacement velocimetry. *Exp. Fluids*, 5:29–32, 1987.

[197] M. P. Arroyo, T. Yonte, M. Quintanilla, and J. M. Savirón. Particle image velocimetry in Rayleigh-Bénard convection: Photographs with a high number of exposures. *Optics and Lasers in Engineering*, 9:295–316, 1988.

[198] M. P. Arroyo, T. Yonte, M. Quintanilla, and J. M. Savirón. Velocity measurements in convective flows by particle image velocimetry using a low powered laser. *Opt. Eng.*, 27(8):641–649, 1988.

[199] M. P. Arroyo and J. M. Savirón. Rayleigh-Bénard convection in a small box: spatial features and thermal dependance of the velocity field. *J. Fluid Mech.*, 235:325–348, 1992.

[200] Kodak. Kodak home page. http://www.kodak.com/homePage.shtml.

[201] J. Westerweel, A. A. Draad, J. G. Th. van der Hoeven, and J. van Oord. A fast data acquisition system for digital PIV: Application to fully-developed and transition turbulent pipe flow. In *Seventh International Symposium on Applications of Laser Techniques to Fluid Mechanics, July 11th to 14th 1994, Lisbon, Portugal.*, volume II, pages 35.1.1–35.1.8, 1994.

[202] I. Grant and X. Wang. Directionally-unambiguous, digital particle image velocimetry studies using a image intensifier camera. *Experiments in Fluids*, 18:358–362, 1995.

[203] H. J. Nussbaumer. *Fast Fourier transforms and convolution algorithms.* ISBN 0-387-10159-4. Springer-Verlag, 1981.

[204] G. E. J. Bold. A comparison of the time involved in computing fast Hartley and fast Fourier transforms. *Proc. IEEE*, 73(12):1863–1964, 1985.

[205] A. B. Watson and A. Poirson. Separable two-dimensional discrete Hartley transfrom. *J. Opt. Soc. Am. A*, 3(12):2001–2004, 1986.

[206] S. E. Reichenbach, J. C. Burton, and K. W. Miller. Comparison of algorithms for computing the two-dimensional discrete Hartley transform. *J. Opt. Soc. Am. A*, 6(6):818–822, 1989.

[207] R. Kumaresan and P. K. Gupta. Vector-radix algorithm for a 2-D discrete Hartley transform. *Proc. IEEE*, 74(5):755–757, 1986.

[208] H. Hao and R. N. Bracewell. A three-dimensional DFT algorithm using the fast Hartley transform. *Proc. IEEE*, 75(2):264–266, 1987.

[209] O. Buneman. Conversion of FFT's to fast Hartley transforms. *SIAM J. Sci. Stat. Comput.*, 7(2):624–638, 1986.

[210] O. Buneman. Multidimensional Hartley transforms. *Proc. IEEE*, 75(2):267, 1987.

[211] J. Prado. Comments on the fast Hartley transform. *Proc. IEEE*, 73(12):1862–1863, 1985.

[212] R. N. Bracewell. Discrete Hartley transform. *J. Opt. Soc. Am.*, 73(12):1832–1835, 1983.

[213] R. N. Bracewell. The fast Hartley transform. *Proc. IEEE*, 72(8):1010–1018, 1984.

[214] R. N. Bracewell, O. Buneman, H. Hao, and J. Villasenor. Fast two-dimensional Hartley transform. *Proc. IEEE*, 74(9):1282–1283, 1986.

[215] R. D. Keane and R. J. Adrian. Optimization of particle image velocimeters. Part I: Double pulsed systems. *Meas. Sci. Technol.*, 1:1202–1220, 1990.

[216] R. D. Keane and R. J. Adrian. Optimization of particle image velocimeters. Part II: Multiple pulsed systems. *Meas. Sci. Technol.*, 2(10):963–974, 1991.

[217] L. Lourenco and A. Krothapalli. On the accuracy of velocity and vorticity measurements with PIV. *Experiments in Fluids*, 18:421–428, 1995.

[218] C. E. Willert and M. Gharib. Digital particle image velocimetry. *Exp. Fluids*, 10:181–193, 1991.

[219] J. M. Coupland and N. A. Halliwell. Particle image velocimetry: rapid transparency analysis using optical correlation. *Appl. Opt.*, 27(10):1919–1921, 1988.

[220] M. P. Wernet and R. V. Edwards. Real time optical correlator using a magneto-optical device applied to particle imaging velocimetry. *Applied Optics*, 27(5):813–815, 1988.

[221] J. Kompenhans, J. Reichmuth, and R. Höcker. Data evaluation in particle image velocimetry by means of a spacial light modulator. *Proc. LIA*, 68:121–129, 1989.

[222] P. V. Farrell and D. Goetsch. Optical liquid-crystal-television correlator for particle-image-velocimetry processing. *Optics Letters*, 14(18):978–980, 1989.

[223] P. V. Farrell and D. Goetsch. Optical analysis of particle image velocimetry data. *Proc. LIA*, 68:82–91, 1989.

[224] J. M. Coupland and N. A. Halliwell. Automated optical analysis of Young's fringes - optical autocorrelation. *Optics and Lasers in Engineering*, 14:351–361, 1991.

[225] W. Arnold and K. Hinsch. Purley optical parallel processing in particle image velocimetry and the study of flow structures. *Proc. LIA*, 67:157–165, 1988.

[226] W. Arnold and K. D. Hinsch. Parallel optical evaluation of double-exposure records in optical metrology. *Applied Optics*, 28(4):726–729, 1989.

[227] P. V. Farrell. Optical evaluation methods in particle image velocimetry. *Optics and Lasers in Engineering*, 17:187–207, 1992.

[228] J. M. Huntley, H. T. Goldrein, and L. R. Benckert. Parallel processing system for rapid analysis of speckle-photography and particle-image-velocimetry data. *Applied Optics*, 32(17):3152–3155, 1993.

[229] A. Voght, M. Raffel, and J. Kompenhaus. Parallel digital processor system for particle image velocimetry. In *Sixth Int. Symp. Applications of Laser techniques to Fluid Mechanics*, pages 27.4.1–27.4.6, 1992.

[230] A. Vogt, F. Reichel, and J. Kompernhans. A compact and simple all optical evaluation method for PIV recordings. In *Seventh International Symposium on Applications of Laser Techniques to Fluid Mechanics, July 11th to 14th 1994, Lisbon, Portugal.*, volume II, pages 35.2.1–35.2.8, 1994.

[231] T. Morck, P. E. Anderson, and C. H. Westergaard. Processing speed of photorefractive optical correlators in PIV processing. In *Sixth Int. Symp. Applications of Laser Techniques to Fluid Mechanics*, pages 27.2.1–27.2.6, 1992.

[232] P. M. Petersen, B. Edvold, P. Buchhave, P. E. Anderson, and A. Marrakchi. Photorefractive particle image velocimetry: performance enhancement with bismuth silicon oxide crystals. *Optics Lett.*, 17(8):619–61, 1992.

[233] M. L. Jacobsen, D. R. McCluskey, W. J. Easson, D. H. Glass, and C. A. Greated. Pneumatic particle conveyance in pipe bend: simultaneous two phase PIV measurements of the slip velocity between the air and particle. In *Seventh International Symposium on Applications of Laser Techniques to Fluid Mechanics, July 11th to 14th 1994, Lisbon, Portugal.*, volume II, pages 31.4.1–31.4.5, 1994.

[234] R. D. Keane and R. J. Adrian. Theory of cross-correlation analysis of PIV images. In F.Y.M. Nieuwstadt, editor, *Flow visualization and image analysis*, pages 1–26. Klewer, 1993.

[235] H. T. Huang, H. E. Fielder, and J. J. Wang. Limitation and improvement of PIV. Part I: Limitation of conventional techniques due to deformation of particle image patterns. *Exp. Fluids*, 15:168–174, 1993.

[236] H. T. Huang, H. E. Fielder, and J. J. Wang. Limitation and improvement of PIV. Part II: Particle image distortion, a novel technique. *Exp. Fluids*, 15:263–273, 1993.

[237] K. Jambunathan, X. Y. Ju, B. N. Dobbins, and S. Ashforth-Frost. An improved cross correlation technique for particle image velocimetry. *Meas. Sci. Technol.*, 6:507–514, 1995.

[238] R. D. Keane and R. J. Adrian. Theory and simulation of particle image velocimetry. In J.M. Bessom, R. Booij, H.W.H.E Godefroy, P.J. de Groot, K. Krishna Prasad, F.F.M. de Mul, and E.J. Nijhof, editors, *Laser Anemometry: Advances and Applications - Proceedings of the Fifth International Conference*, volume 2052 of *Proc. SPIE*, pages 477–492, 1993.

[239] A. K. Prasad, R. J. Adrian, C. C. Landreth, and P. W. Offutt. Effect of resolution on the speed and accuracy of particle image velocimetry interrogation. *Experiments in Fluids*, 13:105–116, 1992.

[240] C. D. Meinhart, A. K. Prasad, and R. J. Adrian. Parallel digital processor system for particle image velocimetry. In *Sixth Int. Symp. Applications of laser techniques to fluid mechanics*, pages 30.1.1–30.1.6, 1992.

[241] C. D. Meinhart, A. K. Prasad, and R. J. Adrian. A parallel digital processor system for particle image velocimetry. *Meas. Sci. Technol.*, 4:619–626, 1993.

[242] J. Westerweel. Analysis of PIV interrogation with low pixel resolution. *Proc. SPIE*, 2005:624–635, 1993.

[243] J. Westerweel, A. A. Draad, J. G. Th. van der Hoeven, and J. van Oord. Measurement of fully-developed turbulent pipe flow with digital particle image velocimetry. *Experiments in Fluids*, 20:165–177, 1996.

[244] R. J. Adrian. Image shifting technique to resolve directional ambiguity in double pulsed velocimetry. *Applied Optics*, 25(21):3855–3858, 1986.

[245] J. Stefanini, G. Cognet, J. C. Vila, and Y. Brenier. A new colored method for particle tracking velocimetry. In *Sixth Int. Symp. Applications of Laser Techniques to Fluid Mechanics*, pages 3.6.1–3.6.4, 1992.

[246] J. Stefanini, G. Cognet, J. C. Vila, and Y. Brenier. The use of a CCD camera for a colored PIV technique. In *Optical Methods and Data Processing in Heat and Fluid Flow, 2-3 April, City University*. The Institution of Mechanical Engineers, London, 1992.

[247] J. Stefanini, G. Cognet, J. C. Vila, B. Merite, and Y. Brenier. A colored method for PIV technique. In F.T.M. Nieuwstadt, editor, *Flow Visualization and Image Analysis*, pages 247–258. Kluwer, 1993.

[248] I. Grant, S. Fu, X. Pan, X. Wang, and A. Aroussi. An in-line stereoscopic, colour PIV system for 3-component velocity measurements with ambiguity resolution. In *Seventh International Symposium on Applications of Laser Techniques to Fluid Mechanics, July 11th to 14th 1994, Lisbon, Portugal.*, volume II, pages 26.3.1–26.3.8, 1994.

[249] M. Reeves, N. J. Lawson, N. A. Halliwell, and J. M. Coupland. Particle image velocimetry: image labeling using encoding of the point-spread function by application of a polarization-sensitive pupil mask. *Applied Optics*, 34(1):194–200, 1995.

[250] I. Grant and A. Liu. Directional ambiguity resolution in particle image velocimetry by pulse tagging. *Exp. Fluids*, 10:71–76, 1990.

[251] I. Grant, X. Pan, and A. Aroussi. The application of the neural network technique to the analysis of particle tracking (PIV) images obtained in flows with a directional ambiguity. In *Seventh International Symposium on Applications of Laser Techniques to Fluid Mechanics, July 11th to 14th 1994, Lisbon, Portugal.*, volume II, pages 35.4.1–35.4.8, 1994.

[252] I. Grant and X. Pan. An investigation of the performance of multi layer, neural networks applied to the anlysis of PIV images. *Experiments in Fluids*, 19:159–166, 1995.

[253] P. Guibert, Q. C. Duan, M. Murat, and J. Jullien. Development of particle image velocimetry: A new computation method with directional resolution. In F.T.M. Nieuwstadt, editor, *Flow Visualization and Image Analysis*, pages 101–116. Kluwer, 1993.

[254] J. M. Coupland, C. J. D. Pickering, and N. A. Halliwell. Particle image velocimetry: Theory of directional ambiguity removal using holographic image separation. *Appl. Opt.*, 26(9):1576–1579, 1987.

[255] J. M. Coupland, C. J. D. Pickering, and N. A. Halliwell. Particle image velocimetry: The ambiguity problem. *Opt. Eng.*, 27(3):193–198, 1988.

[256] V. Gauthier and M. L. Riethmuller. Application of DPIV to complex flows: resolution of directional ambiguity. In *Particle Image Velocimetry, Lecture series 1988-06.* von Karman Institute for Fluid Dynamics, March 12-25, Belgium 1988.

[257] I. Grant, G. H. Smith, and E. H. Owens. A directionally sensitive particle image velocimeter. *J. Phys. E:Sci. Instrum.*, 21:1190–1195, 1988.

[258] C. C. Landreth, R. J. Adrian, and C. S. Yao. Double pulsed particle image velocimeter with directional resolution for complex flows. *Exp. Fluids*, 6:119–128, 1988.

[259] J. Kompenhans and M. Raffel. The importance of image shifting to the applicability of the PIV technique for aerodynamic investigations. In *Seventh International Symposium on Applications of Laser Techniques to Fluid Mechanics, July 11th to 14th 1994, Lisbon, Portugal.*, volume II, pages 35.6.1–35.6.6, 1994.

[260] M. Raffel and J. Kompenhans. Error analysis for PIV recording utilizing image shifting. In *Seventh International Symposium on Applications of Laser Techniques to Fluid Mechanics, July 11th to 14th 1994, Lisbon, Portugal.*, volume II, pages 35.5.1–35.5.5, 1994.

[261] M. Oschwald, S. Bechle, and S. Welke. Systematic errors in PIV by realizing velocity offsets with the rotating mirror method. *Experiments in Fluids*, 18:329–334, 1995.

[262] Z. Zhang and K. Eisele. The two-dimensional velocity shift caused by the use of a rotating mirror in PIV flow field measurements. *Experiments in Fluids*, 20:106–111, 1995.

[263] M. Raffel and J. Kompenhans. Theoretical and experimental aspects of image-shifting by means of a rotating mirror system for particle image velocimetry. *Meas. Sci. Technol.*, 6(6):795–808, 1995.

[264] C. C. Landreth and R. J. Adrian. Electrooptical image shifting for particle image velocimetry. *Appl. Opt.*, 27(20):4216–4220, 1988.

[265] L. Lourenco. Recent advances in LSV, PIV and PTV. In *Image Analysis as Measuring Technique in Flows. Euromech Colloquium 279, 2-5th July, T.U.U Delft*, 1991.

[266] L. Lourenco. Recent advances in LSV, PIV and PTV. In F.T.M. Nieuwstadt, editor, *Flow Visualization and Image Analysis*, pages 81–100. Kluwer, 1993.

[267] J. Westerweel. Efficient detection of spurious vectors in particle image velocimetry data. *Exp. in Fluids*, 16:236–247, 1994.

[268] M. Raffel, B. Leitl, and J. Kompenhans. Data validation for particle image velocimetery. In *Sixth Int. Symp. Applications of Laser Techniques to Fluid Mechanics*, pages 30.2.1–30.2.6, 1992.

[269] C. D. Meinhart, D. H. Barnhart, and R. J. Adrian. A high-speed processinng system for holographic particle image velocimetry. In *Seventh International Symposium on Applications of Laser Techniques to Fluid Mechanics, July 11th to 14th 1994, Lisbon, Portugal.*, volume I, pages 1.4.1–1.4.6, 1994.

[270] J. Westerweel, F. T. M. Nieuwstadt, and J. B. Flōr. Measurement of dynamics of coherent flow strauctures using particle image velocimetry. In *Applications of Laser Techniques to Fluid Mechanics*. Springer-Verlag, 1990.

[271] J. Hartmann, J. Köhler, W. Stolz, and H. H. Flögel. Evaluation of instationary flow fields using crosscorrealtion in image sequences. *Experiments in Fluids*, 20:210–217, 1996.

[272] J. Astola, P. Haavisto, and Y. Neuvo. Vector median filters. *Proc. IEEE*, 78(4):678–689, 1990.

[273] Numeric Algorithms Group. *NAG Fortran Library Manual*, mark 12 edition.

[274] K. Imaichi and K. Ohmi. Numerical processing of flow-visualisation pictures - measurement of two-dimensional vortex flow. *J. Fluid Mech.*, 129:283–311, 1983.

[275] J. Jiménez and J. C. Agüí. Approximate reconstruction of randomly sampled signals. *Signal Processing*, 12:153–168, 1987.

[276] R. G. Spedding and E. J. M. Rignot. Performance analysis and applications of grid interpolation techniques for fluid flows. *Experiments in Fluids*, 15:417–430, 1993.

[277] Q. Wang, P. W. Bearman, and J. K. Harvey. A study of the instantaneous flow structure behind a car by particle image velocimetry. In *Optical methods and data processing in heat and fluid flow, 18-19 April*, volume C516 of *IMechE Conference Transactions 1996-3*, pages 179–188. Mechanical Engineering Publications Limited, 1996.

[278] A. Shekarriz, T. C. Fu, J. Katz, H. L. Liu, and T. T. Huang. Study of junction and tip vortices using particle displacement velocimetry. *AIAA Journal*, 30(1):145–152, January 1992.

[279] C. V. Seal, C. R. Smith, O. Akin, and D. Rockwell. Quantitative characteristics of a laminar, unsteady necklace vortex system at a rectangular block-flat plate juncture. *J. Fluid Mech.*, 286:117–135, 1995.

[280] J. H. Ferziger and M. Perić. *Computational Methods for Fluid Dynamics.* Springer, 1996.

[281] S. Abrahamson and S. Lonnes. Uncertainty in calculating vorticity from 2D velocity fields using circulation and least-squares approaches. *Experiments in Fluids*, 20:10–20, 1995.

[282] I. Grant and E. H. Owens. Confidence interval estimates in PIV measurements of turbulent flows. *Appl. Opt.*, 29(10):1400–1402, 1990.

[283] Z. C. liu, C. C. Landreth, R. J. Adrian, and T. J. Hanratty. High resolution measurement of turbulent structure in a channel with particle image velocimetry. *Exp. Fluids*, 10:301–312, 1991.

[284] D. R. McCluskey, C. Elgaard, W. J. Easson, and C. A. Greated. The application of PIV to turbulent two phase flow. In F.T.M. Nieuwstadt, editor, *Flow Visualization and Image Analysis*, pages 207–226. Kluwer, 1993.

[285] K. Hinsch, W. Arnold, and W. Platen. Turbulence measurements by particle image velocimetry. *Proc. LIA*, 63:127–134, 1987.

[286] Y. Hassan and T. Blanchat. Full-field bubbly flow velocity measurements by digital image pulsed laser velocimetry. *Experiments in Fluids*, 11:293–301, 1991.

[287] B. R. Frieden and C. K. Zoltani. Fast tracking algorithm for multiframe particle image velocimetry data. *Applied Optics*, 28(4):652–655, 1989.

[288] M. P. Wernet. Two-dimensional particle displacement tracking in particle imaging velocimetry. *Applied Optics*, 30(14):1839–1846, 1991.

[289] Y. Hassan and T. Blanchat. Flow velocity measurements using digital pulsed laser velocimetry. *Opt. Eng.*, 30(8):1220–1227, 1991.

[290] Y. A. Hassan, T. K. Blanchat, and C. H. Seeley Jr. PIV flow visualization using particle tracking techniques. *Meas. Sci. Technol.*, 3:633–642, 1992.

[291] M. P. Wernet and A. Pline. Particle displacement tracking technique and Cramer-Rao lower bound error in centroid estimates from CCD imagery. *Exp. in Fluids*, 15:295–307, 1993.

[292] S. Ushijima and N. Tanaka. Particle tracking velocimetry using laser-beam scanning and its application to transient flows driven by a rotating disk. *Journal of Fluids Engineering*, 116:265–272, 1994.

[293] I. Grant and A. Liu. Method for the efficient incoherent analysis of particle image velocimetry images. *Applied Optics*, 28(10):1745–1748, 1989.

[294] C. Brückur and W. Althas. Study of vortex breakdown by particloe tracking velocimetry (PTV). Part 1: Bubble-type vortex breakdown. *Experiments in Fluids*, 13:339–349, 1992.

[295] C. Brücker. Study of vortex breakdown by particle tracking velocimetry (PTV). Part 2: Spiral-type vortex breakdown. *Experiments in Fluids*, 14:133–139, 1993.

[296] C. Brücker and W. Althaus. Study of vortex breakdown by particle tracking velocimtry (PTV): Part 3: Time-dependent structure and development of breakdown-modes. *Experiments in Fluids*, 18:174–186, 1995.

[297] P. E. Dimotakis and F. D. Debussy amd M. M. Koochesfahani. Particle streak velocity field measurements in a two-dimensional mixing layer. *Phys. Fluids*, 24(6):995–999, 1981.

[298] A. A. Adamczyk and L. Rimai. 2-Dimensional particle tracking velocimetry (PTV): Technique and image processing algorithms. *Experiments in Fluids*, 6:373–380, 1988.

[299] B. Khalighi and Y. H. Lee. Particle tracking velocimetry: an automatic image processing algorithm. *Appl. Opt.*, 28(20):4328–4332, 1989.

[300] C. E. Camp, W. B. Kolb, K. L. Sublette, and R. J. Cerro. The measurement of square channel velocity profiles using a microcomputer-based image analysis system. *Experiments in Fluids*, 10:87–92, 1990.

[301] E. R. Ramer and F. D. Shaffer. Automated analysis of multiple-pulse particle image velocimetry data. *Appl. Opt.*, 31(6):779–784, 1992.

[302] M. S. Pervez and T. H. Solomon. Long-term tracking of neutrally bouyant tracer particles in two dimensional fluid flows. *Experiments in Fluids*, 17(3):135–140, 1994.

[303] S. B. Dalziel. Decay of rotating turbulence: some particle tracking experiments. In F.Y.M. Nieuwstadt, editor, *Flow visualization and image analysis*, pages 27–54. Klewer, 1993.

[304] Y. H. E. Sheu, T. P. K. Chang, and G. B. Tatterson. A three-dimensional measurement technique for turbulent flows. *Chem. Eng. Commun.*, 17:67–83, 1982.

[305] T. P. Chang, N. A. Wilcox, and G. B. Tatterson. Application of image processing to the analysis of three-dimensional flow fields. *Opt. Eng.*, 23(3):283–287, 1984.

[306] T. P. K. Chang, A. T. Watson, and G. B. Tatterson. Image processing of tracer particle motions as applied to mixing and turbulent flow - I. The technique. *Chem. Eng. Sci*, 40(2):269–275, 1985.

[307] T. P. K. Chang, A. T. Watson, and G. B. Tatterson. Image processing of tracer particle motions as applied to mixing and turbulent flow - II Results and discussion. *Chem. Eng. Sci*, 40(2):277–285, 1985.

[308] R. G. Racca and J. M. Dewey. A method for automatic tracking in a three-dimensional flow field. *Exp. Fluids*, 6(1):25–32, 1988.

[309] K. Nishino, N. Kasagi, and M. Hirata. Three-dimensional particle tracking velocimetry based on automated digital image processing. *Trans. AMSE*, 111:384–391, 1989.

[310] J. A. Liburdy and E. F. Young. Processing of three-dimensional particle tracking velocimetry data. *Optics and Lasers in Engineering*, 17:209–227, 1992.

[311] S. K. Sinha and P. S. Kuhlman. Investigating the use of stereoscopic particle streak velocimetry for estimating the three-dimensional vorticity field. *Experiments in Fluids*, 12:377–384, 1992.

[312] H. G. Maas, A. Gruen, and D. Papantoniou. Particle tracking velocimetry in three-dimensional flows: Part I. Photogrammetric determination of particle coordinates. *Experiments in Fluids*, 15:133–146, 1993.

[313] N. A. Malik, Th. Dracos, and D. A. Papantoniou. Particle tracking velocimetry in three-dimensional flows. Part II: Particle tracking. *Exp. in Fluids*, 15:279–294, 1993.

[314] O. Robinson and D. Rockwell. Construction of three-dimensional images of flow structure via particle tracking techniques. *Experiments in Fluids*, 14:257–270, 1993.

[315] Y. G. Guezennec, R. S. Brodkey, N. Trigui, and J. C. Kent. Algorithms for fully automated three-dimensional particle tracking velocimetry. *Experiments in Fluids*, 17:209–219, 1994.

[316] A. Cenedese, G. P. Romano, A. Paglialunga, and M. Terlizzi. Neural net for trajectories recognition in a flow. In *Sixth Int. Symp. Applications of laser techniques to fluid mechanics*, pages 27.1.1–27.1.5, 1992.

[317] D. Derou and L. Herault. A new paradigm for particle tracking velocimetry, based on graph theory and pulsed neural network. In *Seventh International Symposium on Applications of Laser Techniques to Fluid Mechanics, July 11th to 14th 1994, Lisbon, Portugal.*, volume II, pages 35.3.1–35.3.8, 1994.

[318] M. P. Arroyo and C. A. Greated. Stereoscopic particle image velocimetry. *Meas. Sci. Technol*, 2:1181–1186, 1991.

[319] I. Grant, Y. Zhao, Y. Tan, and J. N. Stewart. Three component flow mapping; experiments in stereoscopic PIV and holographic velocimetry. In *Fourth International conference on Laser Anemometry, Advances and Applications*, pages 365–371. ASME, 1991.

[320] A. K. Prasad and R. J. Adrian. Stereoscopic particle image velocimetry applied to liquid flows. In *Sixth Int. Symp. Applications of Laser Techniques to Fluid Mechanics*, pages 6.1.1–6.1.7, 1992.

[321] A. K. Prasad and R. J. Adrian. Stereoscopic particle image velocimetry applied to liquid flows. *Experiments in Fluids*, 15:49–60, 1993.

[322] D. H. Barnhart, R. J. Adrian, and G. C. Papen. Phase-conjugate holographic system for high-resolution particle-image velocimetry. *Applied Optics*, 33(30):7159–7170, 1994.

[323] P. J. Bryanston-Cross, M. Funes-Gallanzi, C. Quan, and T. R. Judge. Holographic particle image velocimetry (HPIV). *Optics & Laser Technology*, 24(5):251–256, 1992.

[324] J. M. Coupland and N. A. Halliwell. Particle image velocimetry: three dimensional fluid velocity measurements using holographic recording and optical correlation. *Appl. Opt.*, 31(8):1005–1007, 1992.

[325] J. M. Coupland and N. A. Halliwell. Three dimensional particle image velocimetry. In *Optical methods and data processing in heat and fluid flow, 2-3 April, City University.* The Institution of Mechanical Engineers, London, 1992.

[326] P. H. Malyak and B. J. Thompson. Particle displacement and velocity measurement using holography. *Optical Engineering*, 23(5):567–576, 1984.

[327] N. Andrès, M. P. Arroyo, and M. Quintanilla. Three component velocity measurements in a convective flow by holographic interferometry. In *Seventh International Symposium on Applications of Laser Techniques to Fluid Mechanics, July 11th to 14th 1994, Lisbon, Portugal.*, volume II, pages 32.4.1–32.4.6, 1994.

[328] C. Gray and C. A. Greated. Three-dimensional correlation analysis for particle field hologram velocimetry. In *Optical Methods and Data Processing in Heat and Fluid Flow, 14-15th April, City University, London*, 1994.

[329] M. Funes-Gallanzi and P. J. Bryanston-Cross. High accuracy techniques applied to the extraction of absolute position estimation in 3d piv. In *Seventh International Symposium on Applications of Laser Techniques to Fluid Mechanics, July 11th to 14th 1994, Lisbon, Portugal.*, volume II, pages 35.7.1–35.7.8, 1994.

[330] C. S. Moraitis and P. Buchhave. Three dimensional instantaneous velocity measurements by optical processing of holographic records. In *Sixth Int. Symp. Applications of Laser Techniques to Fluid Mechanics*, pages 6.4.1–6.4.8, 1992.

[331] K. Hinsch, H. Hinrichs, G. Kuhfahl, and P. Meinlschmidt. Holography with controlled coherence for 3-D particle image velocimetry (PIV). *Holographics*, pages 51–57, 1990.

[332] R. D. Keane, R. J. Adrian, and Y. Zhang. Super-resolution particle imaging velocimetry. *Meas. Sci. Technol.*, 6(6):754–768, 1995.

[333] D. R. McCluskey, W. J. Easson, D. H. Glass, and C. A. Greated. The characterisation of particle jet dispersion. In *Sixth Int. Symp. Applications of Laser Techniques to Fluid Mechanics*, pages 9.2.1–9.2.7, 1992.

[334] S. J. L. Rix, D. H. Glass, and C. A. Greated. Preliminary studies of elutriation from gas-fluidised beds using particle image velocimetry. *Chem. Eng. Sci.*, 51(13):3479–3489, 1996.

[335] J. M. Kay and R. M. Nedderman. *Fluid Mechanics and Transfer Processes.* Cambridge University Press, 1985.

[336] Y. A. Hassan, T. K. Blanchat, C. H. Seeley, and R. E. Canaan. Simultaneous velocity measurements of both components of a two-phase flow using particle image velocimetry. *Int. J. Multiphase Flow*, 18(3):371–395, 1992.

[337] K. W. Marosek. Private comment.

[338] J. A. Szymczyk, J. Siekmann, C. H. Chun, and K. Wozniak. Liquid crystal tracers as a method for thermocapillary flow diagnostics. *Arch. Mech.*, 41(2-3):351–360, 1989.

[339] M. Treuner, H. J. Rath, U. Duda, and J. Siekmann. Thermocapillary flow in drops under low gravity analysed by the use of liquid crystals. *Experiments in Fluids*, 19:264–273, 1995.

[340] G. Wozniak and K. Wozniak. Buoyancy and thermocapillary flow analysis by the combined use of liquid crystals and PIV. *Experiments in Fluids*, 17:141–146, 1994.

[341] G. Wozniak, K. Wozniak, and H. Bergelt. On the influence of buoyancy on the surface tension driven flow around a bubble on a heated wall. *Experiments in Fluids*, 21, 181-186 1996.

[342] D. J. Farina, J. M. Hacker, R. J. Moffat, and J. K. Eaton. Illuminant invariant calibration of thermochromic liquid crystals. *Experimental Thermal and Fluid Science*, 9:1–12, 1994.

[343] M. Dzodzo, M. J. Braun, and S. B. Lattime. A non-intrusive computer automated investigation of natural convection using thermochromic liquid crystals and comparison with numerical simulation. In G.F. Hewitt, editor, *Heat Transfer 94*, volume 2, chapter 2-MT-6, pages 225–230. The Institution of Chemical Engineers, UK, 1994.

ISSN 0243 - 7228

INNOVATION ET TECHNOLOGIE EN BIOLOGIE ET MEDECINE

UN JOURNAL EUROPEEN DE GENIE BIOLOGIQUE ET MEDICAL POUR LA PROMOTION DES APPLICATIONS DE LA RECHERCHE.

TIRAGE A PART

CONTENTS
VOL. 15, N° 3, 1994

THEMATIC ISSUE
MOTION ANALYSIS IN BIOMEDICAL IMAGES

- PREDICTION OF THE THROMBOSIS IN FLOWING BLOOD USING PARTICLE IMAGE VELOCIMETRY.
CHRISTY J.R.E., HIND A.K., ...337

Innovation et Technologie en Biologie et Médecine est indexée ou répertoriée par BIOMEDICAL ENGINEERING CITATION INDEX TM édité par l'ISI (Institute for Scientific Information R) et par PASCAL (CNRS) édité par l'INIST.

Innovation and Technology in Biology and Medicine is indexed or listed by BIOMEDICAL ENGINEERING CITATION INDEX TM edited by ISI (Institute for Scientific Information R) and by PASCAL (CNRS) edited by INIST

REPRINTED FROM

INNOVATION AND TECHNOLOGY IN BIOLOGY AND MEDICINE

INNOVATION ET TECHNOLOGIE EN BIOLOGIE ET MEDECINE

CONTENTS

VOL. 15, N° 3, 1994

THEMATIC ISSUE
MOTION ANALYSIS IN BIOMEDICAL IMAGES

- ON MOTION ANALYSIS IN MEDICAL IMAGING.
COATRIEUX J.L., GARREAU M., RUAN S., MAO F., ...253

- TISSUE CHARACTERIZATION FROM ECHOGRAPHIC SPECKLE MOTION.
MEUNIER J., BERTRAND M., ...268

- ESTIMATING EPICARDIAL DYNAMICS FROM THE CORONARY ARTERIAL TREE MOTION IN CINEANGIOGRAPHY.
MEUNIER J., VERREAULT M., LESPERANCE J., BERTRAND M., ...282

- MIXED-FINITE ELEMENT BASED MOTION ESTIMATION.
SUTER D., ...292

- NON-RIGID MOTION ANALYSIS OF THE GROWTH CONE USING CONTINUITY SPLINES.
GWYDIR S.H., BUETTNER H.M., DUNN S.M., ...308

- ANALYSIS OF HUMAN ORGANS MOVEMENTS IN BIOIMAGES.
TISTARELLI M., MARCERANO G., BELTRAME F., ...322

- PREDICTION OF THE THROMBOSIS IN FLOWING BLOOD USING PARTICLE IMAGE VELOCIMETRY.
CHRISTY J.R.E., HIND A.K., ...337

- OPTICAL FLOW METHODS IN ANGIOGRAPHY : A COMPARATIVE STUDY USING SIMULATED IMAGE SEQUENCES.
MONGRAIN R., BERTRAND M., GARON A., TOROUSSIAN V., ...351

- COMPUTING OPTICAL FLOW IN COLOR IMAGES SEQUENCES.
LAI J., GAUCH J., CRISMAN J., ...374

Subscriptions to I.T.B.M. are available from :

ITBM

I.T.B.M. - C.R.D.P.
3, Rue Jean Bart - B.P. 199 - 59018 LILLE CEDEX - FRANCE
FAX : (33) 20.85.11.14.

1994 PRICES (6 ISSUES) : FRANCE : 420 FRENCH FRANCS
: ELSEWHERE : 450 FF or U.S. $85

PRÉDICTION DE LA THROMBOSE DANS LE SANG EN MOUVEMENT PAR VÉLOCIMÉTRIE DE PARTICULES

J.R.E. CHRISTY, A.K. HIND

RÉSUMÉ :
Ce article porte sur l'étude de relations entre la dynamique des fluides et la thrombose. Pour ce faire, on a utilisé un fluide analogue au sang et avec lequel il est possible de recréer plus facilement les conditions de déposition. On rapporte les résultats d'une étude d'écoulements autour de corps de forme simple, utilisant des débits pulsatiles et stationnaires et pour lesquels le régime d'écoulement est soit bien connu, soit facilement identifiable. Cette étude a révélé une forte corrélation entre les régions de stases et les sites de déposition.
On rapporte deux autres études portant sur la modélisation de la croissance du dépôt. Dans la première, l'échographie a permis d'observer en temps réel la croissance de dépôts de caillots, alors que dans la seconde, la technique par vélocimétrie de particules (PIV) a permis d'obtenir une information quantitative du champ de vitesse de l'écoulement. En utilisant une technique PIV adaptée, il a été possible d'estimer la durée du séjour dans le voisinage immédiat des corps tests rigides. En faisant appel à un simple modèle de réaction, il a aussi été possible de prédire le temps de déposition du caillot dans le sillage de l'un des corps tests. Les temps prédits concordent avec les temps observés pour la croissance de tels dépôts en utilisant l'échographie.

Mots clés: Thrombose; Valves cardiaques; Coagulation du lait; Vélocimétrie de particules; Ultrason

PREDICTION OF THE THROMBOSIS IN FLOWING BLOOD USING PARTICLE IMAGE VELOCIMETRY

ABSTRACT :
To facilitate study of the relationship between fluid dynamics and thrombosis, a blood analogue fluid has been used in studies of deposition around bodies of simple shape in steady and pulsatile flows where the nature of the flow is known or can be determined easily. This study revealed a strong correlation between regions of stasis and sites of deposition, although the extent of deposition and the shape of deposit are not immediately apparent from a knowledge of the regions of stasis.
Two further studies, reported here, have been conducted in an attempt to model the growth deposit. In one ultrasonic imaging has provided a means of observing in real time the growth of clot deposit, whilst in the other, particle image velocimetry (PIV) has enabled quantitative information from the field to be determined. Using an adaptation of the PIV technique, it has been possible to predict the residence time distribution in the immediate vicinity of the solid test bodies. This along with some simple reaction theory has enabled prediction of the time for clot to deposit in the wake of one of the test bodies. The times predicted are consistent with times observed for the growth of such deposit using ultrasound.

Key words: Thrombosis, Cardiac Valves, Milk Clotting, Particle Image Velocimetry, Ultrasound

PREDICTION OF THROMBOSIS IN FLOWING BLOOD USING PARTICLE IMAGE VELOCIMETRY

CHRISTY J.R.E., HIND A.K. - University of Edinburgh, Scotland [1]

Introduction

Research (1,2) into the hydrodynamic correlates of thrombosis in the vicinity of prosthetic cardiac valves has revealed that high shear stress may damage blood platelets and erythrocytes leading to the release of clotting agents and that stasis in the vicinity of the valve may allow thrombus deposition. However, although there is some knowledge as to the extent of damage caused by shear, the effect of flow on the subsequent reaction and clot deposition is still not fully understood. The problem is compounded by the complexity arising from the pulsatile flow interacting with a moving valve, and from the chemical reaction cascade involved in clotting. We are therefore still unable to predict whether or not the potential exists for radical improvements in valve design in relation to thrombosis.

The aim of our work is to study the fluid mechanical determinants of thrombus formation to enable the design of artificial heart valves and other blood handling equipment whose local flow characteristics are inherently less thrombogenic. To this end we have studied hydrodynamic phenomena and coagulation under similar determinable flow conditions, using a blood analogue for coagulation studies. We have applied some simple reaction theory to our findings as a first stage in the development of a technique for prediction of thrombosis in blood flows.

Since the time of Virchow (3), it has been known that blood chemistry, surface properties of blood interfaces and haemodynamics all contribute to thrombosis. Blood chemistry can be altered using anticoagulants which block one or more of the reactions in the sequence leading to thrombosis. However, anticoagulation therapy has side effects such as risk of haemorrhage and, over extended periods, damage of the liver and kidneys, and so is undesirable as a long-term means of preventing thrombosis.

Early work of Gott(4) and Petschek(5) concentrated on the choice of material for valve construction. However, as less inherently thombogenic materials were discovered the principal problem shifted from the material of construction of the valve towards the nature of the blood flow. To design valves with inherently athrombogenic haemodynamic features it is first necessary to understand the effect of the flow on the blood clotting process.

As research shifted towards characterising the relationship between flow and coagulation, a variety of approaches were adopted. Clinical studies of thrombosis either involved insertion of devices into the cardiovascular system of various species of animal(4,6) or drawing blood from an animal into an external device(5,7). Other experiments were conducted in-vitro using citrated heparinised blood(8). The devices

[1]Correspondence to: Dr J.R.E. Christy, Department of Chemical Engineering, University of Edinburgh, The King's Buildings. Mayfield Rd., Edinburgh EH9 3JL, Scotland.
The authors wish to thank Shell Expro UK for funding Mr Hind's salary.

employed in such studies were generally simple in design so that flow characteristics could often be inferred, though the impact of the flow was not always foremost in the mind of the experimenters. The fluid dynamicists, on the other hand, developed mock circulatory systems, observing flow phenomena using hot film/wire anemometry or laser based velocimetry techniques(9,10). Here, observations of flow phenomena were correlated with reports of thrombus deposition in clinical practice.

The work carried out in the clinical studies relies on knowledge of the probable flow patterns for its interpretation, whereas that of the fluid dynamicists relies on the mock in-vitro circulatory loop being sufficiently similar to the human heart and aortic root for conclusions based on flow measurement in-vitro to have a direct bearing on observed thrombosis in-vivo.

Our approach has been to study both flow characteristics and clot deposition in the same in-vitro apparatus using a blood analogue for deposition studies. This allows closer correlation between the measured flow and the deposition observed.

The blood analogue fluid chosen is bovine milk (normally unpasteurised, although pasteurised and reconstituted dried milk powder have both been used successfully) to which cheese-makers' Rennet, containing the enzyme Chymosin, and saturated aqueous calcium chloride are added. This mixture was used first by Lewis(11), who investigated its performance both microscopically and macroscopically as a blood analogue before assessing its usefulness in valve testing.

Chemically, the final stages of the blood and milk clotting reactions are similar(12), both involving the enzymic cleavage of a soluble protein to yield an insoluble protein and soluble glycopeptides, the insoluble protein undergoing what is thought to be a second order polymerisation reaction to form a gel. On the macroscopic scale both reactions exhibit an induction period, during which no soluble material is visible, followed by the appearance of particles which rapidly coagulate to form a structured clot.

Lewis observed microscopically the solid deposition arising from a laminar submerged jet of milk impinging on a glass slide(13) and compared the results obtained with those from similar work of Petschek(5) using fresh arterial canine blood. The correspondence in terms of an initial apparently homogeneous deposit followed by by deposition of small particles and the ultimate formation of either a circular deposit or wedge-shaped deposits was remarkable. Further study revealed that, as with blood, calcium is concentrated in the latter stages of milk deposition.

Two experiments on the macroscale provided further evidence of the analogous deposition behaviour of blood and milk coagulum. In a version of the Lee White test commonly applied to blood, the gross rheological behaviour of milk during the clotting reaction was studied. As is expected when using this test with blood, a sharp end point was observed after which the clot would no longer flow. Milk was then tested in an apparatus similar to that used by Hladovec(8) to study the growth of thrombus in flowing blood. Here the liquid under test is pumped round in a closed circuit, at one point of which the flow issues from a nozzle across the end of

which is stretched a metal gauze or net. With both blood and milk, clot forms on the downstream side of the net, indicating that coagulum is preferentially forming in this region rather than being sieved out from the bulk flow.

Deposition studies with pulsatile milk flows through Starr-Edwards and Bjork-Shiley prosthetic valves mounted in an artificial heart also yielded patterns of deposition remarkably similar to those found on such valves removed during autopsy.

Lewis, in making these observations of the similarity between clotting of blood and milk flows, postulated that enhanced mass transfer in the liquid flow may shorten the observed lag time in the clotting reaction, thus leading to greater deposition in disturbed regions of the flow.

In an attempt to verify this hypothesis, milk coagulation was studied further in situations were flow patterns were already known or could be easily determined(14). The experimental test-chamber comprised a cylinder, on the axis of which a test body could be mounted by means of a metal spigot or sting inserted from the rear. The chosen test objects were bodies of revolution; these being a cone, disc, sphere and tear-drop. Experiments involved flowing milk either steadily or in pulsatile manner through the test chamber with a mean Reynolds number of 220 (based on the diameter of the test body). The extent and location of deposition was measured at the end of an experiment of fixed duration.

For all of the test bodies in steady flow conditions, deposition led to a conical clot in the wake of the test object. In pulsatile flow, however, the wake of the disc and cone remained substantially free of deposited coagulum and a thin azimuthal band of clot was found to deposit just downstream of the widest point of the body in the case of the sphere and tear-drop. Using a dye injection technique, it was discovered that a trapped vortex forms under the pulsatile flow conditions of our milk study for both the sphere and the tear-drop, but not for the cone and disc. In steady flow, as expected, a trapped vortex formed in the wake of all of the test bodies. It was thus concluded that stasis is a necesary condition for milk clot deposition.

The shape of the deposit formed downstream of the sphere and tear-drop in pulsatile flow is not readily explained by a knowledge of stasis. During the pulsatile cycle the trapped vortex oscillates along the length of these test bodies, but, deposition is not uniform along the region covered by this oscillation, ranging from zero in some areas to a thick deposit at the upstream extremity of the vortex movement. Following Lewis's hypothesis that enhanced mass transfer might play a role in determining the favoured site of deposition, a simple set of experiments was conducted, based on the Lee White test, in which the coagulable milk solution was vigorously agitated for a short duration whilst clotting proceeded: the time, following addition of the enzyme, at which this agitation occurred was varied from one experiment to the next. Agitation was found to have no measurable influence on the length of the lag phase of the clotting reaction, but could greatly influence the adhesivity of clot deposit to the test tube surface if applied at the start of visible coagulation.

We have thus concluded that the fluid must reside in contact with the test body for

long enough, following addition of the enzyme, for the lag phase to reach completion and that enhanced mass transfer at this stage may lead to preferential deposition on certain regions of the surface.

In order to establish whether mass transfer is indeed responsible for the deposition patterns observed, two further studies have been conducted. In one, ultrasound is used to locate the boundary between the deposited milk curd and the milk flow, thus enabling measurement of the rate of growth of the deposited layer. In the other, particle image velocimetry (PIV) techniques are used to characterise the behaviour of the flow around one of the axisymmetrical test bodies in the cylindrical test chamber.

Methods

In all of the experiments reported here, a tear-drop shaped test body of diameter 10mm and length 28mm was employed. This was supported by means of a spigot on the axis of a cylindrical test chamber of internal diameter 32mm (Fig 1).

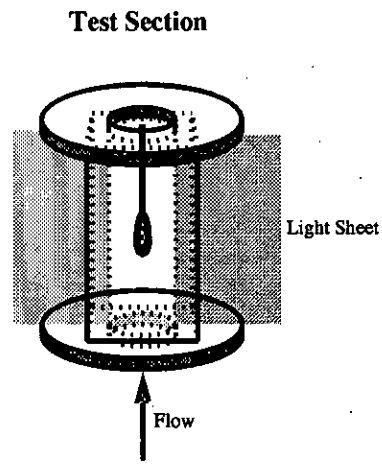


Figure 1: Diagram of experimental test section.

The studies of milk clotting employed the same experimental procedure as detailed in (14). However, the section of test chamber immediately surrounding the test body was replaced with one of the same diameter fabricated from polypropylene to reduce ultrasonic scattering from the wall-fluid interface, and the metal sting was replaced with one fabricated from perspex. A Dynamic Imaging Concept 2000 L/C Linear/Convex ultrasound scanner with a 7.5MHz linear array transducer was employed to enable observation of deposition in the opaque fluid during the course of the experiment. The transducer was supported firmly against the outside wall of the test chamber by means of a rotatable holder. Gel was used to exclude air from the contact zone, but no stand-off was required. The holder allowed the transducer to be rotated around the axis of the cylindrical test chamber, enabling the test body to be viewed from all angles. The focal length of the ultrasound beam was adjusted to give greatest resolution of the clot on the proximal side of the test body. Images were recorded both on video-tape and on paper using a Sony Video-Printer.

For the laser imaging experiments a cylindrical perspex test chamber of the same

bore (32mm) as that for the milk clotting experiments was employed. To avoid refractive distortion of the image, viewed perpendicularly to the illuminated diametrical plane, the test chamber segment is surrounded by a square duct, the cavity in between being filled with water. Water seeded with 7μm aluminium oxide particles is illuminated with a pulsed plane of light from a 35mW He-Ne laser(15). A Nikon F3 camera with a 105mm f/2.8 micro lens is used to record multiply exposed images on Kodak Tri-X 400 film. Typically, recordings of four exposures are taken giving a sequence of up to four point images per particle. A motor wind and trigger allow photographs to be taken at up to 4.5 frames per second. A steady flowrate of 1.2l/min was used giving a test body Reynolds number of 220, as for the milk clotting experiments.

Two methods were used to seed the water flow around the tear-drop shaped body. For velocimetry experiments, the whole water flow is seeded with aluminium oxide particles, whereas for study of the boundary layer and residence time distribution a seeded water flow was injected isokinetically along the axis of the test chamber into the unseeded main flow a short distance upstream of the test body.

The photographic negative of the experimental recording is enlarged to give an A4 print. The print is digitised using a flat bed scanner, giving a resolution of 300 dots/inch with 256 grey scale values.

In PIV, the digitised image is divided into small sections, each to be analysed using autocorrelation techniques(16) to determine the average displacement of particle images between illumination pulses. From the particles' displacement, velocity vectors can be determined. These vectors are validated using parameters obtained from the autocorrelation routine. After the vectors have been determined a NAG routine [2] is used to interpolate missing data points over the investigation plane. The surface of the test body and test-chamber wall are also located on the image to allow the no-slip condition to be incorporated into the interpolation. Spatial derivatives of the velocity at each point can then be estimated and used to calculate the derived quantities, vorticity and shear stress.

To study the locus of the boundary layer and its separation from the test body surface, seeding particles are injected for a short period of time along the axis of an unseeded main flow. Some particles enter the boundary layer leading to significant light scattering from this region once the particle injection has ceased. Separation of the boundary layer from the surface is revealed by the high density of scattering centres in the separated fluid. The locus of the boundary layer and its break away, along with that of the test body, can be determined from the digitised image and used to estimate the volume of the recirculation zone if axial symmetry is assumed.

Residence time distribution measurement is conducted in a similar manner by injecting a large pulse of seeding particles so as to swamp the recirculation zone with particles. A sequence of photographs is recorded as particles are washed out of this region. Processing of the negatives is the same as before except that the digitised

[2]National Algorithms Group, Oxford, UK. (Tel +44 865 311744; email: infodesk@nag.co.uk)

image is analysed to determine the particle concentration in the recirculation zone. The image is first reduced to a black and white representation, from which the percentage of white points can be determined. The radial nature of the flow can be accounted for by weighting the intensity proportional to radius before reducing the image to a black and white representation. This assumes that the scattered light intensity is proportional to the number of scattering particles. A more complicated approach would be to locate all of the particle image centres and weight them by radius to give concentration.

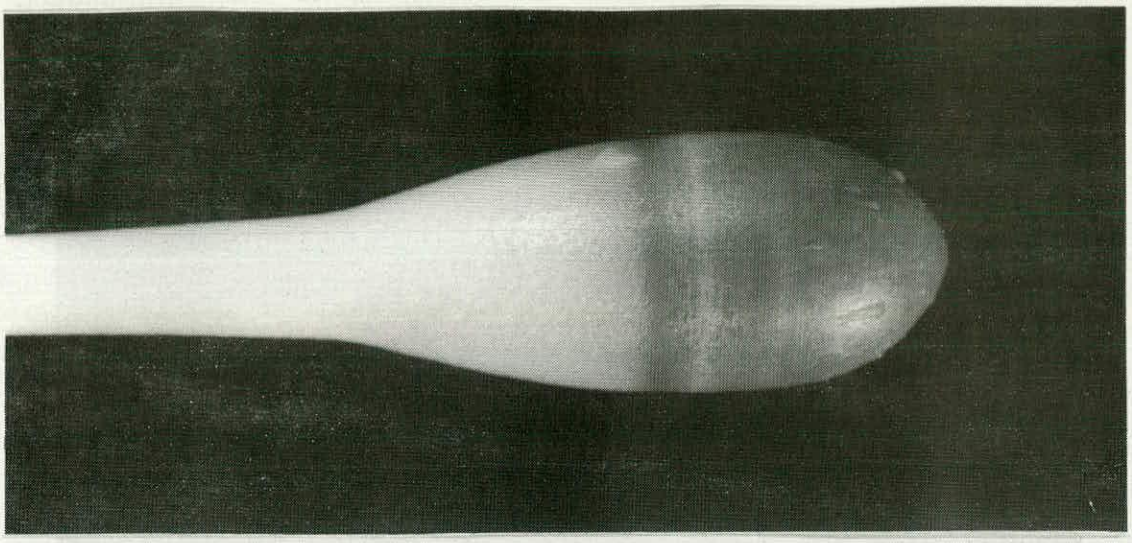


Figure 2: Photograph showing clot deposited on tear-drop test body in steady flow. Re = 220 based on test body diameter.

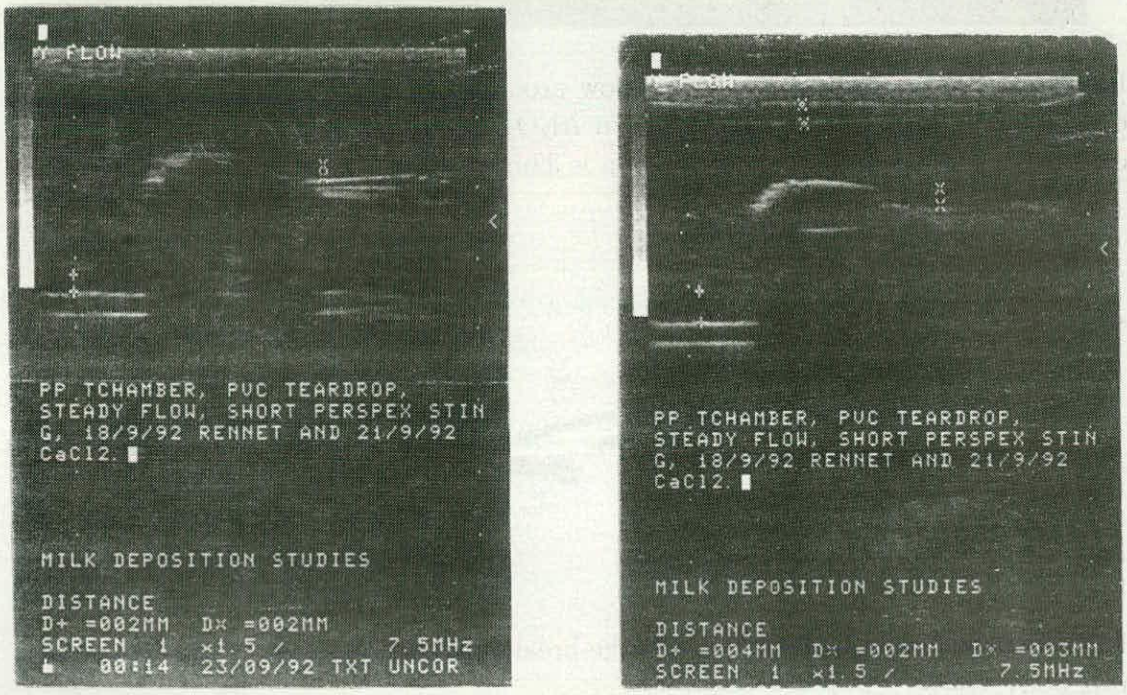


Figure 3: Ultrasonic image of test body during coagulation: after 14 and 25 mins.

Results

A photograph of the tear-drop removed from the apparatus at the end of a 35 minute experiment in the work reported in (14) is shown in figure 2. Figure 3 shows a typical ultrasound image of clot around the same test body, 14 minutes and 25 minutes after the start of an experimental run. In the photograph, the clot deposit shows up as a white layer on top of the grey PVC test body. This clot forms a smooth layer along the downstream half of the body and the sting. The clot adhering to the sting is approximately 1mm thick. In the case of the ultrasound images, the paper record lacks the clarity of the image on the scanner screen. The white markers for determining distances between visible interfaces on the ultrasound image were positioned using the on-line image of higher quality. Here the apparent thickness of the layer of clot on the sting reached a maximum of about 2mm after a period of approximately 10 minutes.

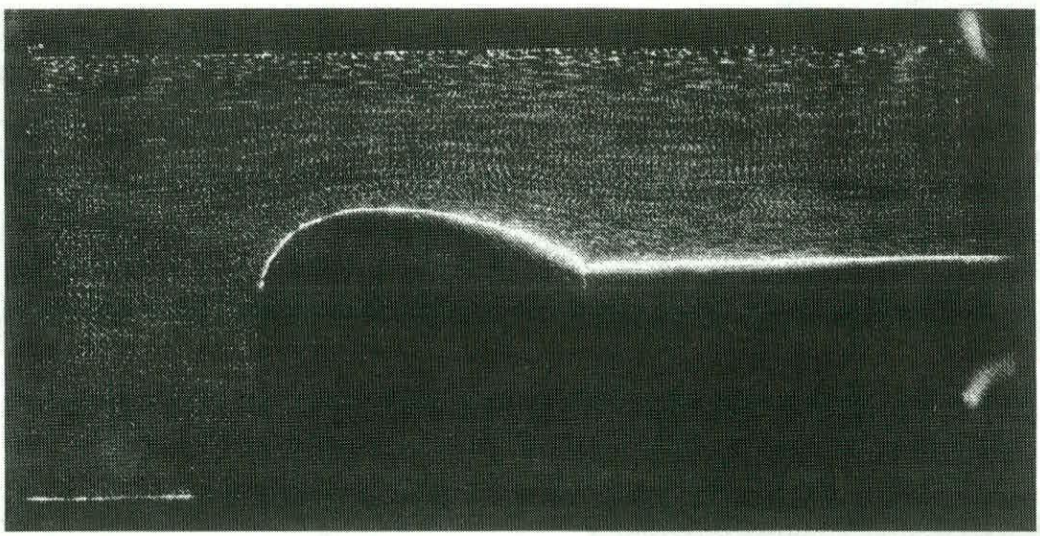


Figure 4: PIV recording of a water flow around a tear drop shaped body of revolution. The water is seeded with 7μm Al_2O_3. Re = 220 based on the test body diameter. The width of the test section is 32mm

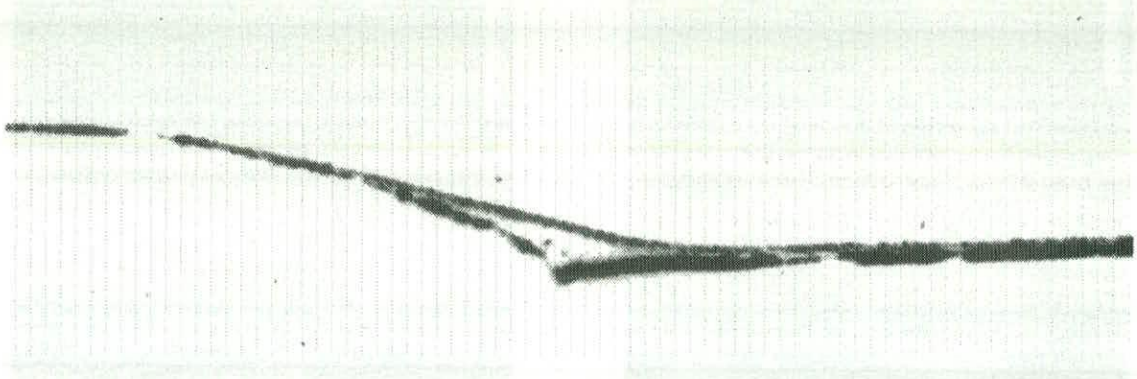


Figure 6: Flow visualisation showing the breakaway of the boundary layer from the test body

Figures 4 and 5 show the PIV image obtained from a steady flow of seeded water

around the tear drop and the velocity map and shear stress distribution derived from this data. The resolution of the analysis technique is finer than 1% of the maximum velocity measured. The pattern of relatively streamline flow with a small recirculation zone is in line with expectations for steady flows in the Reynolds number range for this test body. The analysis enabled the maximum shear stress, in the region where the test body reaches its greatest width, to be evaluated as $0.096 Nm^{-2}$. The values for milk and blood would be higher as their viscosities relative to that of water are 2 and 4 respectively (ignoring slight non-Newtonian behaviour).

Figure 6 reveals the boundary layer and the edge of the recirculation zone behind the test body. From this image, the volume of the recirculation zone was estimated as $170 mm^3$. The decay of particle concentration over time is revealed in the sequence of photographic images in figure 7. The photographs were recorded at one second intervals with the sequence starting at the top lefthand corner and reading left to right, down through the rows. Not only is it possible to see the reduction in particle concentration with time, but movement of the region of highest particle concentration is also apparent. A graph of the radius-weighted light intensity against time is shown in figure 8. If the wake region were to behave as a continuously stirred tank with a mean residence time, τ, the particle concentration, c, at time t would decay exponentially according to the relation

$$c = c_o e^{-\frac{t}{\tau}} \tag{1}$$

where c_o is the concentration at time t=0. The curve representing equation 1 with τ=20 seconds is plotted in figure 8, showing reasonable fit with the decay of particle concentration.

Knowing that the induction period is around 30 second duration under the conditions pertaining in the milk clotting experiments, a simple model was devised to predict the rate of growth of clot in the wake of the test object. If it is assumed that all of the clot forms inside the circulation zone and that any material entering and remaining within the circulation zone for 30 seconds will clot, then the following equation should govern clot growth:

$$-\frac{dV}{dt} = \frac{V}{\tau} e^{-\frac{30}{\tau}} \tag{2}$$

where V is the volume of the recirculation zone.

fraction of wake filled with clot	predicted time (seconds)
0.5	60
0.9	200
0.95	260
0.99	380
0.999	600

Table 1: Predicted times for fractional filling of the recirculation zone with clot

Integration of equation 2 using the values determined previously will yield predictions of the time taken for given fractions of the wake to fill with clot (Table 1).

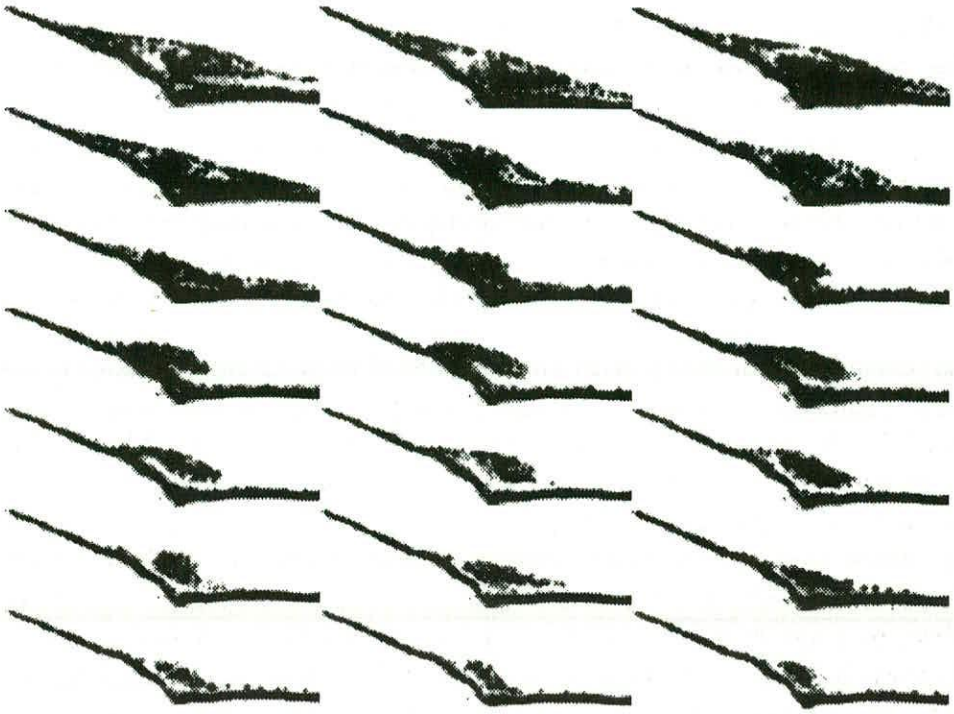


Figure 7: Decay of particle concentration in the recirculation zone behind the test body. Images are recorded every second reading left to right and top to bottom

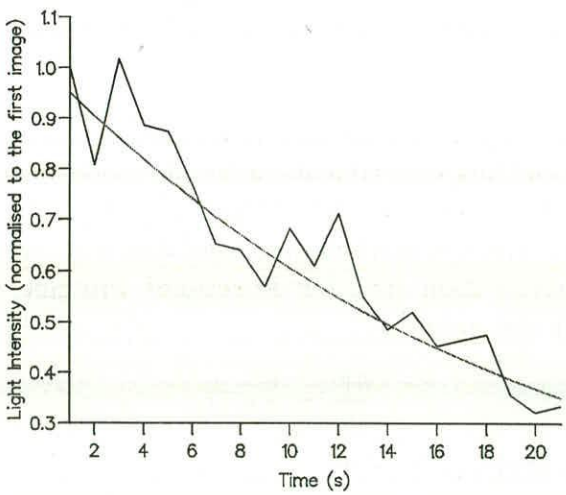


Figure 8: Scattered light intensity from the recirculation area, weighted by radius and plotted against time. The best fit line for CSTR behaviour is also plotted.

Discussion

The PIV observations of steady flow around the tear-drop shaped test object are in agreement with the expected streamline flow for Re=220. The curvature of the downstream surface is sufficient to induce separation of the boundary layer, but reattachment is seen to occur a short length along the spigot. The measured residence time distribution shows that this recirculation zone is stable since there is only a small exchange of material with the surrounding fluid. The maximum shear stresses in the flow past this body are low, indicating that shear stress is unlikely to be a dominant feature in determining the extent of deposition. The maximum stress recorded here, $0.096 Nm^{-2}$, is significantly lower than the value of $42 Nm^{-2}$ reported by Fry (17) as being responsible for endothelial damage. It should be noted, however, that this maximum value will be an underestimate due to velocity averaging effects close to the test body surface.

There appears to be a close correlation between the shape of clot deposited on the test body under steady flow conditions, as revealed in Fig 2, and the measured recirculation zone downstream of this body (Fig 6). This supports the hypothesis put forward in (14) that stasis is a necessary condition for thrombus formation. It would appear that prolonged residence times in the boundary layer around the test body and the recirculation zone allow some of the fluid time to reach completion of the induction phase of the reaction, with clot then being formed on the test body. Since the flow pattern will evolve as clot deposits on the surface, growth will be difficult to model accurately. Here it has been assumed that any major changes to the flow will act to remove areas conducive to deposition as the clot grows, reducing circulation and creating the optimum streamlined flow. That is, clot deposition occurs until the region bounded by the separation and reattachment of the boundary layer is filled.

In more complicated flows situations, with no reattachment of the boundary layer, the final shape of deposit would require a detailed knowledge of the development of the flow during deposition. Indeed, it is possible in such cases that clot growth will be halted, not from elimination of the recirculation region, but instead from some other factor such as the shear stress on the surface of the deposited curd rising to a value sufficient to remove any further clot which deposits. It is our intention to test this hypothesis using PIV with a new set of test bodies fabricated to represent the different stages of clot deposition around one of our original test pieces.

The residence time distribution results (figures 7 and 8) give only an estimation of τ based on the assumption that the recirculation zone is behaving as a continuously stirred reactor. The observed fluctuations in particle concentration may arise from several sources; particle overlap, concentration variations within the recirculation zone, inaccuracy in aligning the images. Structures can clearly be seen within the recirculation zone as the seeding particles clump and move around in images 10-14. Whilst the large scale investigation of the flow could not resolve the detail in the recirculation area, it is clear from these observed structures that our assumption of the zone behaving as a continuously stirred tank is only partly justified. The flow in this region could have been examined at greater magnification with PIV to

determine the detailed flow pattern, but this was deemed unnecessary at this stage.

The ultrasonic analysis of the growth of clot indicates that deposition reaches its maximum extent after less than 10 minutes. The thickness of deposit measured using ultrasound is slightly greater than that observed on removal of the test piece (2mm as compared to 1 – 1.5mm). This discrepancy is largely due to difficulties in resolving the precise absolute position of the interface from the ultrasound image. However, this slight magnification of the thickness of the clot should not affect the time at which completion of deposition is observed.

A crude prediction of clot growth has been made, based on a simple reaction model, that appears to agree with the ultrasound observations of clot growth. The model predicts a slightly greater rate of deposition than is actually observed. There are a number of features of the model that would account for the accelerated growth predicted.

- It is assumed at the start of the reaction that the recirculation zone already contains fluid in the process of coagulating. This is not the case, coagulating species having to be convected into this region. Since the mean residence time is only 20 seconds, it is unlikely that the clotting time predicted would be extended by much more than a minute if the initial conditions were altered.
- Perfect mixing is assumed within the recirculation zone so that mass transfer effects are ignored. As discussed earlier there is evidence from the residence time studies to suggest that segregation does occur.
- The reaction is assumed to occur instantaneously once the end of the induction period has been reached. In 'Lee White' experiments using milk, however, the coagulation stage takes place over a period lasting up to half as long as the induction phase. It should be noted that in such a batch system the coagulation rate is probably diffusion limited, which is not necessarily the case here.
- All clot formed in the recirculation zone is deemed to adhere to the surface. Some convection of coagulum out of the recirculation zone might be expected in practice.
- The composition of the clot is deemed to be identical to that of the fluid. In the model this alters the way in which the remaining volume of the recirculation zone is calculated. The clot formed in flowing milk appears to contain less water than that formed in batch experiments such as the 'Lee White' test. Therefore the predicted decrease in volume of the recirculation region is exaggerated.

Two other features of the model should be mentioned:

- The model assumes that growth of clot alters the size of the recirculation zone without affecting mixing within it or extending the zone into the main

flow. This assumption is reasonable in that if clot is forming on the test body and spigot, this thickening surface layer will squeeze the recirculation zone radially outwards and back along the sting without appreciably changing its shape. Also if clot formation is due to stasis, further deposition is unlikely to occur if the deposit grows to reach the fast moving separated boundary layer. Deposition might, however continue to occur in the boundary layer over the streamlined clot but this should be slow as the boundary layer is very thin. Indeed, the absence of appreciable clot on the upstream surface of the test body in fig 2 would confirm that clot growth is slow in the boundary layer itself.

- Milk that has not reached the end of the induction phase is assumed to be incapable of clotting. There is biochemical evidence (18) to suggest that this may not be the case, although the coagulation times were proportionally greater when fresh milk was added to the milk treated with enzyme.

It is clear that the reaction model has significant limitations, but it does form a first step towards predicting clot growth around artificial heart valves. The velocities around the test bodies are clearly measurable and with a more complex reaction model could be used to make more accurate predictions

To be of use in the design of heart valves, extension of the model to pulsatile flows would be required. This will lead to additional problems in that the recirculating pockets of fluid will no longer remain in a fixed location and deposition at one part of the cycle will alter the flow development later in that and subsequent cycles. To this end we propose to investigate the flow around a series of bodies shaped to match the developing clot.

Conclusions

Particle image velocimetry and a novel residence time study have revealed that the extent of clot deposition from flowing milk around a tear-drop shaped test body correlates closely with the location and size of the recirculation zone in its wake.

A simplified reaction model, used to predict coagulation growth in the recirculation zone, yields clotting times that are only marginally shorter than those determined using ultrasonic analysis of the growth of clot.

The reaction model is not immediately applicable to pulsatile flows in that no allowance is made for the change in flow arising from previous deposition.

References

1–LEVERETT, L.B., HELLUMS, J.D., ALFREY, C.P., LYNCH, E.C. Red blood cell damage by shear stress. Biophys J 12, 257-273 (1972)

2–GIERSIEPEN, M., WURZINGER, L.J., OPITZ, R., RUEL, H. Estimation of shear stress-related blood damage in heart valve prostheses - in vitro comparison of 25 aortic valves. Int J Artif Organs 13:5, 300-306 (1990)

3–VIRCHOW, R. Gesammelte abhandlung zur wissenschaftlichen medzin. Frankfurt: Meidinger (1856)

4–GOTT, V.L., RAMOS, M.D., NAJJAR, F.B., ALLEN, J.L., BECKER, K.E. The in vivo screening of potential thromboresistant materials. Proc Artif Heart Prog Conf, Washington 181-191 (1969)
5–MADRAS, P.N., MORTON, W.A., PETSCHEK, H.E. Dynamics of thrombus formation. Fed Proc 30, 1665-1676 (1971)
6–VORHAUER, B.W., M^{c}ETHANEY, J.H. Discussion on flow patterns through artificial valves. In "Prosthetic heart valves", ed Brewer, L.A. Springfield, Ill.: Thomas (1969)
7–STEIN, P.D., SABBAH, H.N. Measured turbulence and its effect on thrombus formation. Circ Res 35, 608-614 (1974)
8–HLADOVEC, J., RIHA, P. The model of thrombosis and thrombolysis in vitro. Thromb Res 7, 743-752 (1975)
9–FIGLIOLA, R.S., MUELLER, T.J. On the haemolytic and thrombogenic potential of occluder prosthetic heart valves from in vitro measurements. J Biomech Eng 103, 83-90 (1981)
10–WOO, Y., YOGANATHAN, A.P. In vitro pulsatile flow velocity and turbulent shear stress measurements in the vicinity of mechanical aortic heart valve prostheses. Life Supp Syst 3, 283-312 (1985)
11–LEWIS, J.M.O., MACLEOD, N. A blood analogue for the experimental study of flow-related thrombosis at prosthetic heart valves. Cardiovasc Res, 17, 466-475 (1983)
12–JOLLES, P. Structural aspects of the milk clotting process. Comparative features with the blood clotting process. Mol Cell Biochem 7, 73-85 (1975)
13–LEWIS, J.M.O., MACLEOD, N., TAYLOR, W.D. A critical investigation of the fluid mechanical factors associated with clotting in Petschek's stagnation point flow chamber experiments. Proc Eur Soc Artif Organs 5, 124-127 (1978)
14–CHRISTY, J.R.E., MACLEOD N. The Role of Stasis in the Clotting of Blood and Milk Flows around Solid Objects. Cardiovasc Res, 23, 949-959 (1989)
15–HIND, A.K., CHRISTY, J.R.E. Particle Image Velocimetry (PIV): Obtaining instantaneous, multi-point velocity measurements throughout a 2-D plane in a time varying flow downstream of an artificial heart valve. IChemE Research Event, ISBN 0 85295 290, 491-493 (1992)
16–HIND, A.K., CHRISTY, J.R.E. Digital PIV applied to flows around artificial heart valves: analysis by autocorrelation. In "Flow visualisation and image analysis", ed. Nieuwstand, F.T.M. Kluwer (1993)
17–FRY, D.L. Certain histological and chemical responses of the vascular interface to acutely induced mechanical stress in the aorta of the dog. Circulation Res, 24, 93-108 (1969)
18–CHERYAN, M., VAN WYK, P.J., OLSON, N.F., RICHARDSON, T. Secondary phase and mechanism of enzymic milk coagulation. J Dairy Sci 58, 477-481 (1974)

C516/018/96

A method to correct for velocity gradients in the analysis of PIV recordings

A K HIND MA, MEng and J R E CHRISTY MA, PhD, MIChemE
Department of Chemical Engineering, University of Edinburgh, UK

Abstract

A method is presented that reduces the error introduced by velocity gradients in the analysis of PIV images using digital auto-correlation. The PIV recording is analysed initially using regular shaped analysis regions and the resulting velocity field used to calculate velocity gradients within the flow, these are then used to deform individual analysis areas in further analysis steps. Assuming linear velocity gradients, after deforming the analysis area the spacing between particle centres will be constant across the analysis area improving the signal-to-noise ratio and reducing measurement bias. The deformation method and its application to a PIV recording from a simulated Oseen vortex are presented. The error in the velocity vectors produced after iteration is significantly reduced using the algorithm and previously unanalysable areas of the PIV recording give reasonable vectors. Previous criteria limiting the velocity gradients in analysis areas can be relaxed using this analysis technique.

1 Introduction

Particle image velocimetry (PIV) is an increasingly popular technique for the quantitative measurement of instantaneous velocity fields in experimental fluid mechanics [1–10]. A pulsed plane of light is used to illuminate a flow seeded with small, light-scattering particles that accurately follow the fluid motion. Viewed perpendicular to the light sheet, streak lines followed by the particles are recorded as a series of dots. For analysis by auto-correlation, this time series of particle images is captured on one PIV recording. A choice of processing stages may then be used to determine the mean particle separation in a small area of the recording, which yields a local velocity if the frequency of the illumination is known. Repeated over the PIV recording, this procedure gives an instantaneous 2D velocity map.

Errors associated with the technique are minimised by careful choice of experimental and analysis parameters [11–17]. In particular, Keane and Adrian [13,15] addressed the errors arising from velocity gradients within PIV analysis areas, recommending that experimental parameters be chosen to meet the following inequality

$$\frac{M \mid \Delta \mathbf{u} \mid \Delta t}{d_I} < 0.05 \qquad (1)$$

to give an RMS error in the measured displacement of less than 0.8% of the interrogation area diameter. M is the magnification used in making the recording, $\Delta \mathbf{u}$ the change in velocity across a typical analysis area in m/s, Δt the time interval between pulses in seconds, and d_I the interrogation area diameter in m. In effect, the change in displacement should be less than 5% of a characteristic length associated with the interrogation area.

For digital recordings Prasad *et al*[16] recommend that

$$\frac{d_\tau}{d_{pix}} \approx 4 \tag{2}$$

where d_τ is the e^{-2} diameter of a particle image and d_{pix} the characteristic pixel size of digitisation. When this criterion is met the bias error associated with digitisation is less than one fifth of the random error.

Keane and Adrian [13] introduce two terms: *gradient bias*, referring to bias against the larger velocities in the interrogation area, and *detection bias*, referring to the reduction in amplitude of the signal peak and the associated lowering of the probability that it is correctly detected amongst the noise peaks in the auto-correlation function. Peak broadening and peak splintering are discussed as additional factors increasing the likelihood of detection bias. The conclusions drawn from this work show that velocity gradients place a fundamental limit on the measurements that can be made using PIV, along with the limit to the size of seeding particles that can be recorded and the smallest scales of motion that can be resolved.

These constraints are expressed by the authors in recommending:

$$\frac{\Delta u}{u} < 4\frac{d_\tau}{d_I} \tag{3}$$

where u is the mean velocity in a typical analysis area in m/s. Meeting this inequality limits the bias to around 6% and gives a detection probability of 92% or greater. There will always be flows of interest which give recordings that can not be analysed without appreciable velocity gradients in some analysis areas. In these areas the above inequality is difficult to achieve and is in conflict with other recommendations. It is suggested that the appropriate way to reduce bias arising from velocity gradients is to find an appropriate compromise between reducing the interval between illumination pulses and the increasing error associated with measuring small displacements. Image shifting techniques increase the range of time intervals between illumination pulses that can be used to make acceptable PIV recordings. Correcting for velocity gradients using a simple formula was also suggested. Alternatively the size of the interrogation area can be reduced but this will reduce the number of effective image pairs. Detection bias can be reduced by using a multi-pulsed system although gradient bias remains the same [15].

Correction of these errors by formula, as suggested by Keane and Adrian [13], does not improve the signal-to-noise ratio in the auto-correlation function but tries to correct the measured displacement. It is proposed here that a correction technique based on deforming the analysis area from a multi-pulse recording will improve the signal-to-noise ratio and correct for both detection bias and gradient bias. A technique for correcting the same errors in cross-correlation analysis methods has been presented by Huang *et al*[18, 19]. The analysis image from the second recording is deformed according to the velocity gradients detected after an initial conventional PIV analysis stage. An iterative procedure is then used to reduce the errors from velocity gradients. Missing velocity vectors are interpolated in order to estimate the velocity gradients in unanalysable areas of the flow. With this information, initially unanalysable areas yield PIV data after the iterative analysis stages. Unfortunately, the approach adopted in the cross-correlation case is not readily extended to auto-correlation analysis and an alternative method is required.

2 Method

2.1 Principle

An ideal PIV image would be divisible into small analysis areas in which particle images are separated by the same displacement and the PIV recording has been made taking into account the criteria described earlier. The aim of this section is to develop an algorithm that will take a PIV analysis area meeting all the usual recording and analysis recommendations, but containing velocity gradients, and transform this image to give something closer to the ideal. Such an ideal image is essentially of a one dimensional flow and would have equally spaced parallel streamlines. In contrast, the image requiring correction may have apparent variations in velocity across the analysis area arising from spacial velocity gradients, accelerating motion, compressible flow, three dimensional flow, and noise. Correcting for the apparent velocity gradients redresses all these factors.

© IMechE 1996 C516/01

For a two dimensional flow, the stream function is defined as follows[20]:

$$\frac{\partial \psi}{\partial y} = \frac{\partial u}{\partial x}x + \frac{\partial u}{\partial y}y + u_0 \tag{4}$$

$$-\frac{\partial \psi}{\partial x} = \frac{\partial v}{\partial x}x + \frac{\partial v}{\partial y}y + v_0 \tag{5}$$

where u and v are the x and y components of the velocity vector which can be expressed as functions relative to the components of the velocity at the centre of the analysis area (u_0 and v_0) assuming a linear velocity gradient. The stream function defined in this way represents in incompressible flow that obeys continuity. On integration equations (4) and (5) give:

$$\psi = \frac{\partial u}{\partial x}xy + \frac{\partial u}{\partial y}\frac{y^2}{2} + u_0 y + 0 \tag{6}$$

$$\psi = -\frac{\partial v}{\partial x}\frac{x^2}{2} - \frac{\partial v}{\partial y}xy + v_0 x - 0 \tag{7}$$

if $\psi = 0$ at (0,0). Clearly these equations are only compatible for incompressible flows, where $\frac{\partial u}{\partial x} = -\frac{\partial v}{\partial y}$. However, if the velocity gradients affecting the u component of velocity were corrected then equation (6) represents streamlines equally spaced in the x direction and the appropriate expression for the stream function can be used to correct for apparent velocity gradients involving v.

2.2 Deforming the analysis area

Consider an arbitrary point (x, y) in the analysis area, the spacing between particle images in the x direction at this point is proportional to the x component of velocity, u, at this point. If this velocity is compared with the velocity at the centre of the analysis area, u_0, then this point should be moved to x_{un} in a scaling process that equalises the separation of particles in the x direction. That is:

$$\frac{x}{x_{un}} = \frac{\frac{\partial u}{\partial x}x + \frac{\partial u}{\partial y}y + u_0}{u_0} \tag{8}$$

$$x_{un} = \frac{u_0 x}{\frac{\partial u}{\partial x}x + \frac{\partial u}{\partial y}y + u_0} \tag{9}$$

Problems with division by zero can be avoided by an initial rotation of axes and re-calculation of the velocity gradients in the new coordinate frame. If the x axis is aligned with the velocity vector there is least likelihood that the x component of velocity will change sign in the analysis area. $\frac{\partial v}{\partial x_{un}}$ is now a function of x_{un}. If all the points were transformed at once this would give an intermediate image where $\frac{\partial u}{\partial x_{un}}$ and $\frac{\partial u}{\partial y}$ are both zero. The stream function in this intermediate analysis area is now defined by:

$$\frac{\partial \psi}{\partial y} = u_0 \tag{10}$$

$$-\frac{\partial \psi}{\partial x_{un}} = \int_0^{x_{un}} \frac{\partial v}{\partial x_{un}}\partial x_{un} + \frac{\partial v}{\partial y}y \tag{11}$$

$$\psi = u_0 y - \int_0^{x_{un}}\int_0^{x_{un}} \frac{\partial v}{\partial x_{un}}\partial x_{un}\partial x_{un} - \frac{\partial v}{\partial y}x_{un}y \tag{12}$$

Noting that as a result of the change of axes v_0 will be zero. The value of $\frac{\partial v}{\partial x_{un}}$ at x_{un} is given by:

$$\frac{\partial v}{\partial x_{un}} = \frac{\partial v}{\partial x}\frac{x}{x_{un}} \tag{13}$$

and can be used in changing the variable in the double integral to x to allow an analytic solution or in a numerical estimate of the integral. It should be noted that if the flow were two dimensional, steady, and incompressible then the last term in equation (12) would be zero and differentiation with respect to y would give the expected answer. Here this term is retained and equation (12) used to give a

function that can be used for correcting velocity gradients arising, for example, from density changes in the flow. In this work, Maple, a symbolic mathematical package, was used to carry out the integration and generate suitable code to calculate the exact value of the integral.

The steam function at the point in the transformed area (x_{un}, y) is calculated using equations (12) and (13), this must then be equal to the stream function in the analysis area when $\frac{\partial v}{\partial x_{un}}$ and $\frac{\partial v}{\partial y}$ are zero. That is:

$$u_0 y_{un} = \psi = u_0 y - \int_0^{x_{un}} \int_0^{x_{un}} \frac{\partial v}{\partial x_{un}} \partial x_{un} \partial x_{un} - \frac{\partial v}{\partial y} x_{un} y \tag{14}$$

The point (x_{un}, y_{un}) has now been deformed from the point (x, y) and can be transformed back to the original coordinate frame. The coordinates for the point in the deformed analysis area in the original coordinate frame (x', y') will generally not correspond to an exact pixel location and the intensity is conventionally divided between four neighbouring pixels as adopted by Huang *et al*[19]. Supposing

$$x' = x_0 + \delta x \tag{15}$$

$$y' = y_0 + \delta y \tag{16}$$

where x_0 and y_0 are the integer parts of x' and y', and δx and δy are the real remainders, then if the intensity of the point is $I(x', y')$ then

$$I(x_0, y_0) = I(x', y')(1 - \delta x)(1 - \delta y) \tag{17}$$

$$I(x_0, y_0 + 1) = I(x', y')(1 - \delta x)\delta y \tag{18}$$

$$I(x_0 + 1, y_0) = I(x', y')\delta x(1 - \delta y) \tag{19}$$

$$I(x_0 + 1, y_0 + 1) = I(x', y')\delta x \delta y \tag{20}$$

Particle images may overlap in the distorted image as the deformation effectively broadens particle images. The intensity at a point in the deformed analysis area must be the sum of all contributing intensities calculated using the above method considering all points in the original area. Points that are deformed to positions outside the original analysis area are ignored.

This procedure should give an interrogation area with no velocity gradients that can be processed by conventional analysis methods.

2.3 Determination of velocity gradients

Velocity gradients were calculated using the NAG interpolation routine E01SAF that implements Shepard's algorithm for interpolation given a set of randomly located data points. This routine calculates and uses the velocity gradients at each data point. The routine was also used to extrapolate velocities in unanalysable regions and thus estimates the velocity gradients in these areas.

2.4 Iteration

A reliable method for validating and orienting velocity vectors is required after each analysis stage. Validation can be based on the properties of the auto-correlation plane [13] or in a post-processing validation step based in global-mean, local-mean, and local-median tests [21]. Directional ambiguity has been resolved in a number of ways based on image shifting techniques [22–24], pulse tagging [25] or a knowledge of the flow. It may be that the flow field from the first analysis can be used to fix the orientation of those from subsequent analysis steps. Iteration should give progressively better estimates of the velocity field with convergence assumed when successive velocity measurements differ by less than a given threshold.

3 Applying the technique to a simulated Oseen vortex

A similar example flow field has been chosen to that used by Huang *et al*[19]. The velocity distribution for an Oseen vortex located at the origin of a polar coordinate system is give by:

© IMechE 1996 C516/018

$$u_\theta = \frac{\Gamma}{2\pi r}\left(1 - e^{\frac{-r^2}{4vt}}\right) \quad (21)$$

$$u_r = 0 \quad (22)$$

and the vorticity is

$$\Omega = \frac{\Gamma}{4\pi vt} e^{\frac{-r^2}{4vt}} \quad (23)$$

where Γ is the circulation, v the flow kinematic viscosity, and t the time in appropriate units. The only non-zero derivative of velocity is given by

$$\frac{\partial u_\theta}{\partial r} = -\frac{\Gamma\left(1 - e^{-\frac{r^2}{4vt}}\right)}{2\pi r^2} + \frac{\Gamma e^{-\frac{r^2}{4vt}}}{4\pi vt} \quad (24)$$

A PIV image 693 by 693 pixels was generated using a Monte-Carlo technique with the centre of the vortex at the centre of the recording, a circulation, $\Gamma = 5000[pixel]^2/s$, and $vt = 2000[pixel]^2$. 1200 particles were recorded as a series of four images of e^{-2} diameter four pixels, 4 seconds apart, and with a Gaussian intensity profile. The simulated image is shown in figure(1).

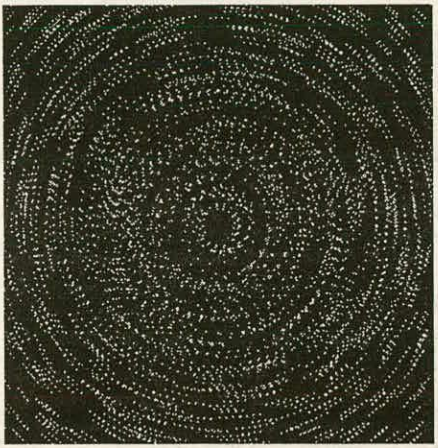


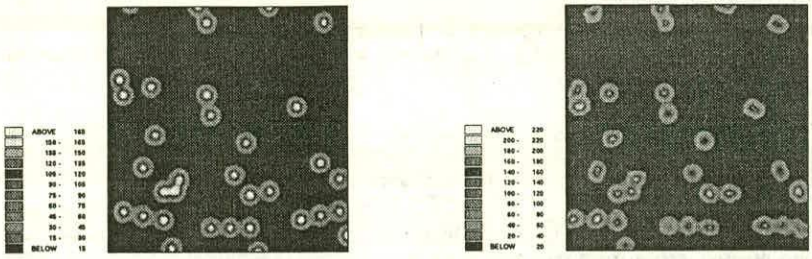
Figure 1: A simulated PIV image of an Oseen vortex - see text for details

Figure (2a) shows a typical analysis area containing velocity gradients and figure (2b) the resulting analysis area after correcting for velocity gradients. Figures (3a) and (3b) show the respective auto-correlation functions.

The results of a conventional PIV analysis are shown in figure (4). Figure (4a) shows the unvalidated vector map. Figure (4b) this velocity map after removing vectors 3 standard deviations away from the global mean velocity or 1.4 standard deviations away from the local median velocity, and vectors which are oriented at an angle greater than $\frac{\pi}{8}$ from the local median velocity. Figure (4c) shows the variation in u_r as a function of r, the distance from the centre of the vortex. Figure (4d) shows the variation of u_θ with r. Analysis was carried out using standard digital techniques [26] with an analysis area of 63 by 63 pixels with a 21 pixel spacing between areas. It is clear that the inequalities discussed in the introduction are not always met.

Figure (5) shows the same set of information after five iterations of the deformation analysis technique.

C516/018 © IMechE 1996



a) b)

Figure 2: a) A PIV analysis area before correction for velocity gradients and b) the analysis area after correction



a) b)

Figure 3: a) The auto-correlation function from the PIV analysis area before correction for velocity gradients and b) the auto-correlation function after correction

4 Discussion

The auto-correlation functions for analysis areas before and after correction for velocity gradients show that when velocity gradients have been removed from the area the peaks are clearer. The signal peak is slightly larger after correction and the second harmonic peak is much larger. The deformed analysis area shows that the particle tracks have been aligned with the mean velocity at the centre (along the horizontal) and the spacing between particle images is more uniform.

Even with one iteration where the analysis area is deformed there is a significant increase in the number of valid vectors detected and a decrease in the spread of results. The effect is more pronounced for five iterations of the deformation analysis algorithm and ten iterations gives little further improvement. These results agree well with those produced by Huang *et al*[19] for their correction to the cross-correlation analysis technique for a similar simulated flow.

The assumption of a linear velocity gradient is obviously incorrect in many analysis areas although a reasonable correction is still achieved. More complicated expressions could be incorporated into the deformation algorithm. The overhead in performing the deformation of the analysis area is about 20% of the time required to calculate the auto-correlation function for a 63 by 63 area. So five iterations of the analysis including deformation would increase the total time for analysis six fold. In this case each analysis step required about 1 minutes on a SUN SPARC station 20 (analysed using fully padded FFTs

© IMechE 1996 C516/01

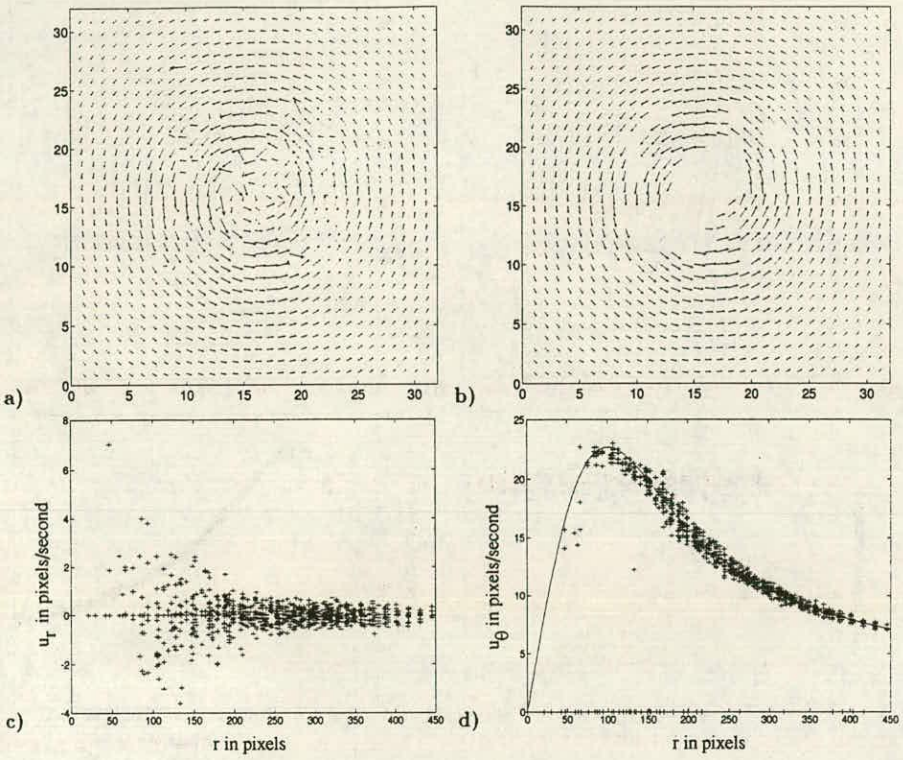


Figure 4: The result of conventional PIV analysis: **a)** the raw velocity field, **b)** the velocity field after validation, **c)** the variation of u_r with r, and **d)** the variation of u_θ with r.

on one 100MHz HyperSPARC processor). This estimate will obviously depend on the nature of the flow. An improvement in speed could be achieved by direct calculation of the auto-correlation function around the area where a valid signal peak was found in the previous analysis step.

A reliable computational method for validating velocity vectors is required between analysis steps that should err on the side of caution to avoid any invalid vectors. Such erroneous vectors would introduce incorrect velocity gradients and lead to a much reduced signal peak. The number of iterations required for the vector field to converge will be increased if incorrect vectors are not removed and they may inhibit convergence.

After correcting for velocity gradients there is still bias in the measured results that is greatest for high velocities, as can be seen in figure (5). The use of a simple smoothing scheme will introduce bias into measurements in areas where the velocity gradient is high, to some extent negating the improvement produced by deforming the analysis area. A plot of 'u_θ measured' over 'u_θ expected' as a function of the dimensionless velocity gradient, figure (6), shows that the measurement bias remains within 6% up to values of the dimensionless velocity gradient of 0.4. This is a significant improvement over the results obtained by Keane and Adrian[13] where it is recommended that this dimensionless velocity gradient be less than 0.05 to limit the bias to 6%. After normal PIV analysis the mean value of $\frac{u_\theta\ measured}{u_\theta\ expected}$ is 0.99 with a standard deviation of 0.41. After ten iteration steps this value remains 0.99 with a standard deviation of 0.024. This compares well with the accuracy expected from typical PIV recordings of about 2.5% [13]. Application of the deformation algorithm gives measurements in flows containing appreciable velocity

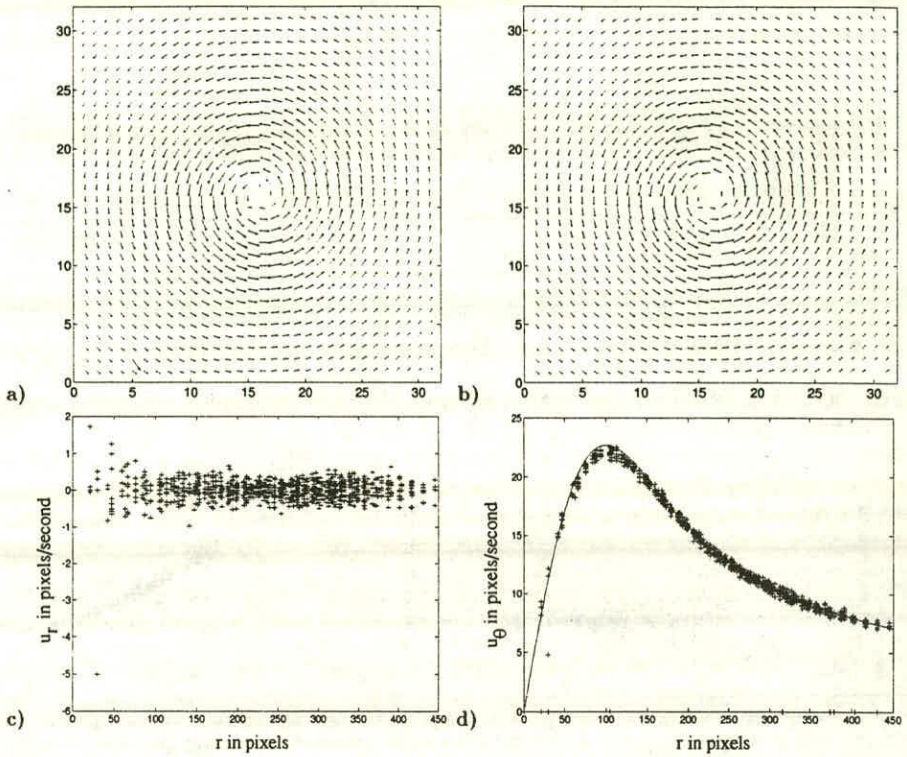


Figure 5: The results after five iterations of the analysis method including deformation: **a)** the raw velocity field, **b)** the velocity field after validation, **c)** the variation of u_r with r, and **d)** the variation of u_θ with r.

gradients with almost the same accuracy as investigations where the flow contains velocity gradients recorded meeting previous criteria.

5 Conclusions

An algorithm has been presented that deforms analysis areas used in the auto-correlation analysis of PIV images to remove velocity gradients from the analysis area. This is an iterative procedure using the results from previous analysis stages and requires a reliable validation and orientation step between iterations. Removal of velocity gradients improves signal quality and yields velocity data from previously unanalysable areas. The bias in velocity measurement is also reduced. PIV recordings of flows that can not be made and analysed without including velocity gradients can be more reliably analysed relaxing the recommendations made by [13]. Analysis areas with $\frac{M|\Delta \mathbf{u}|\Delta t}{d_I} < 0.4$ gave results within 6% of those expected as opposed to $\frac{M|\Delta \mathbf{u}|\Delta t}{d_I} < 0.05$ as recommended for conventional analysis. The use of a simple smoothing algorithm can increase the errors in regions where there are appreciable velocity gradients.

© IMechE 1996 C516/018

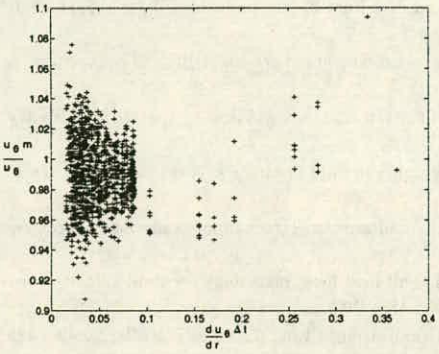


Figure 6: The variation in the detected value for u_θ divided by the expected value as a function of the dimensionless velocity gradient

6 List of symbols

M	magnification of PIV recording
Δu	the change in velocity across an analysis area (m/s)
Δt	time interval between illumination pulses (s)
d_I	characteristic length of the analysis area (m)
d_τ	e^{-2} particle diameter (m)
d_{pix}	A characteristic length for a pixel in a digitised PIV image (m)
u	mean of component of velocity in a PIV analysis area when used with Δu(m/s) or the x component of velocity in an analysis area (m/s)
v	the y component of velocity in an analysis area (m/s)
u_0	the mean x component of velocity in a PIV analysis area (m/s)
v_0	the mean y component of velocity in a PIV analysis area (m/s)
ψ	the stream function (m^3/s)
(x, y)	a point in an undeformed analysis area
(x_{un}, y)	a point in an analysis area in which the velocity in the u direction has been corrected
(x_{un}, y_{un})	A general point after correcting all velocity gradients
(x', y')	a point after correcting for velocity gradients in the original coordinate frame
x_0	the integer part of x'
y_0	the integer part of y'
δx	the fractional part of x'
δy	the fractional part of y'
$I(x', y')$	the intensity at pixel (x', y')
u_θ	the θ component of velocity for the Oseen vortex (pixels/s)
u_r	the r component of velocity for the Oseen vortex (pixels/s)
r	the distance from the origin of the Oseen vortex (pixels)
Γ	the circulation of the Oseen vortex ($[pixel]^2/s$)
νt	the flow viscosity multiplied by time ($[pixel]^2$)

References

[1] D.B. Barker and M.E. Fourney. Measuring fluid velocity with speckle patterns. *Opt. Lett.*, 1(4):135–137, 1977.

C516/018 © IMechE 1996

[2] R. Grousson and S. Mallick. Study of flow pattern in a fluid by scattered laser light. *Appl. Opt.*, 16(9):2334–2337, 1977.

[3] P.G. Simpkins and T.D. Dudderar. Laser speckle measurements of transient Bénard convection. *J. Fluid Mech.*, 89(4):665–671, 1978.

[4] R. Meynart. Instantaneous velocity field measurements in unsteady gas flow by speckle velocimetry. *Appl. Opt.*, 22(4):535–540, 1983.

[5] W. Lauterborn and A. Vogel. Modern optical techniques in fluid mechanics. *Ann. Rev. Fluid Mech.*, 16:223–244, 1984.

[6] R.J. Adrian. Multi-point optical measurements of simultaneous vectors in unsteady flow - a review. *Int. J. Heat & Fluid Flow*, 2:127–145, 1986.

[7] T.D. Dudderar, R. Meynart, and P.G. Simpkins. Full-field laser metrology for fluid velocity measurement. *Optics and Lasers in Engineering*, 9:163–199, 1988.

[8] L. Hesselink. Digital image processing in flow visualization. *Ann. Rev. Fluid Mech.*, 20:421–485, 1988.

[9] I. Grant and G.H. Smith. Modern developments in particle image velocimetry. *Optics and Lasers in Engineering*, 9:245–264, 1988.

[10] R.J. Adrian. Particle-imaging techniques for experimental fluid mechanics. *Ann. Rev. Fluid Mech.*, 23:261–304, 1991.

[11] R.J. Adrian and C-S. Yao. Pulsed laser technique appplication to liquid and gaseous flows and the scattering power of seed materials. *Applied Optics*, 24(1):44–52, 1985.

[12] L. Lourenco and A. Krothapalli. The role of photographic parameters in laser speckle or particle image displacement velocimetry. *Exp. Fluids*, 5:29–32, 1987.

[13] R.D. Keane and R.J. Adrian. Optimization of particle image velocimeters. Part I: Double pulsed systems. *Meas. Sci. Technol.*, 1:1202–1220, 1990.

[14] Y.G. Guezennec and N. Kiritsis. Statistical investigation of errors in particle image velocimetry. *Exp. Fluids.*, 10:138–146, 1990.

[15] R.D. Keane and R.J. Adrian. Optimization of particle image velocimeters. Part II: Multiple pulsed systems. *Meas. Sci. Technol.*, 2(10):963–974, 1991.

[16] A.K. Prasad, R.J. Adrian, C.C. Landreth, and P.W. Offutt. Effect of resolution on the speed and accuracy of particle image velocimetry interrogation. *Experiments in Fluids*, 13:105–116, 1992.

[17] M.P. Wernet and A. Pline. Particle displacement tracking technique and Cramer-Rao lower bound error in centroid estimates from CCD imagery. *Exp. in Fluids*, 15:295–307, 1993.

[18] H.T. Huang, H.E. Fielder, and J.J. Wang. Limitation and improvement of PIV. Part I: Limitation of conventional techniques due to deformation of particle image patterns. *Exp. Fluids*, 15:168–174, 1993.

[19] H.T. Huang, H.E. Fielder, and J.J. Wang. Limitation and improvement of PIV. Part II: Particle image distortion, a novel technique. *Exp. Fluids*, 15:263–273, 1993.

[20] J.M. Kay and R.M. Nedderman. *Fluid mechanics and transfer processes*, chapter 4, page 94ff. Cambridge University Press, 1985.

[21] J. Westerweel. Efficient detection of spurious vectors in particle image velocimetry data. *Exp. in Fluids*, 16:236–247, 1994.

[22] R.J. Adrian. Image shifting technique to resolve directional ambiguity in double pulsed velocimetry. *Applied Optics*, 25(21):3855–3858, 1986.

[23] C.C. Landreth and R.J. Adrian. Electro-optical image shifting for particle image velocimetry. *Appl. Opt.*, 27(20):4216–4220, 1988.

[24] L. Lourenco. Recent advances in LSV, PIV and PTV. In F.Y.M. Nieuwstadt, editor, *Flow visualization and image analysis*, pages 81–100. Klewer, 1993.

[25] I. Grant and A. Liu. Directional ambiguity resolution in particle image velocimetey by pulse tagging. *Exp. Fluids*, 10:71–76, 1990.

[26] C.E. Willert and M. Gharib. Digital particle image velocimetry. *Exp. Fluids*, 10:181–193, 1991.

© IMechE 1996 C516/01